ON THE CHEMICAL COMPOSITION OF INTERSTELLAR MOLECULAR CLOUDS: A MILLIMETER AND SUBMILLIMETER SPECTRAL LINE SURVEY OF OMC-1

Thesis by

Geoffrey A. Blake

In Partial Fulfillment of the Requirements

for the Degree of

Doctor of Philosophy

California Institute of Technology

Pasadena, California

1986

(Submitted July 2, 1985)

Acknowledgments

Having worked in spectroscopy labs on both coasts and at observatories from California to the tropopause, I have, of course, encountered many people who are, as much as I, responsible for the present work. To thank even those who have been most helpful would take pages, but it's my thesis, so I'll try anyway.

To all of you at Duke, my heartiest thanks. It is with pride that I consider myself a Duke microwaver. Paul Helminger, David Skatrud, and K. Sastry taught me much of what I know about experimental spectroscopy, and graciously allowed me to work on their projects. I would especially like to thank fellow graduate student Grant Plummer, with whom much of the spectroscopic work at Duke was done, and who put in long hours at the Durham Bulls games and at the Hideaway with me when things didn't go so well! I am also deeply indebted to Frank De Lucia and Eric Herbst for letting me work there, and to Eric for introducing me to interstellar chemistry in the first place. Both Frank and Eric served as my advisors away from home during my summers at Duke, and it was a pleasure to have worked with them.

Closer to home, many people at JPL have been quite helpful during this work. Wes Huntress and Sheo Prasad taught me the "guts" of interstellar chemistry, and Vince Anicich performed most of the ICR measurements on Cl. In the spectroscopy lab, Ed Cohen has always been helpful, as has Mark Schaefer. I would also like to thank my advisor at JPL, Herb Pickett, for his continual support and guidance, and most especially Jam Farhoomand, who basically built the laser sideband source and let me tag along, and who also taught me to be ever alert for a simple twist of fate.

For the staff at OVRO and at the KAO, you all deserve my gratitude for your consistently excellent support. Particular thanks go to Dave Woody and Steve

Scott at OVRO for making everything run so well.

To those at Caltech who have contributed to my appreciation of *haute cuisine*, and incidentally to my development as a scientist, I'm glad I had a chance to work with you. Thanks to Ed Sutton for building the receiver, reducing the line search data, and the pears bocuse, to Colin Masson for building the AOS and for all of your bread at 4 AM, and to Dr. Bob Leighton for building the superb telescopes at OVRO, and, soon, at Mauna Kea. I would also like to thank Jocelyn Keene for putting up with me during the long hours getting ready for the KAO runs and on the often hectic flights, for teaching this uninformed chemist about telescopes, and for reminding me that other sources do exist in the sky besides Orion. My fellow inmates Mike Wengler, Erich Grossman, Elliott Brown, and Jeff Stern taught me a lot and helped make graduate school a lot of fun, and I wish you all well. To all the members of the dreaded Downs Syndrome softball team, this certainly wasn't what Alexander Doubleday had in mind!

Dan Watson was an endless fount of knowledge on matters both social and scientific, and he did a marvelous job with the thankless task of reading an early version of this thesis, as did my advisor Tom Phillips. I would especially like to thank Tom for allowing me to follow those projects which I found most interesting, and for his thoughtful advice and guidance. And, of course, a most special thanks goes to Anneila Sargent for Paris and the jacuzzi.

Finally, my greatest debt is certainly to my wife and family, whose continual support and love have made this work possible. To Mom, Dad, Mark, Karen, and all the rest, may your lives be as rich as you have helped make mine.

ABSTRACT

The same basic principles govern the chemical and physical evolution of systems throughout the universe. However, the dissimilar conditions on the Earth and in the interstellar medium lead to remarkably different chemical compositions for these two environments. While less familiar than terrestrial chemistry, the study of the chemical composition of the interstellar medium is important because it bears directly on the understanding of phenomena as diverse as star formation, galactic structure and dynamics, and the cosmological origin of the universe, in addition to providing a unique opportunity to investigate a number of fundamental chemical and physical processes.

We present here results from a millimeter and submillimeter spectral line survey of the core of the Orion molecular cloud (OMC-1). The millimeter-wave survey, conducted at the Owens Valley Radio Observatory (OVRO), covers a 55 GHz interval in the 1.3 mm (230 GHz) atmospheric window and contains emission from 29 molecules. Together with the frequency selective submillimeter observations of H_2D^+ (372.4 GHz), CI (492.2 GHz), NH_3 (572.5 GHz), and HCl (625.9 GHz) performed aboard NASA's Kuiper Airborne Observatory, over 800 emission lines have been detected from 33 chemically distinct species during the course of this work. The uniformly calibrated results from the unique and extensive OVRO spectral line survey place significant constraints on models of interstellar chemistry, and have allowed the chemical composition of the various regions in OMC-1 to be definitively characterized.

A global analysis of the observed abundances has shown that the markedly different chemical compositions of the kinematically distinct Orion subsources may be simply interpreted in the framework of an evolving, initially quiescent, gas-phase chemistry influenced by the process of massive star formation. The chemical composition of the extended Orion cloud complex is similar to that

found in a number of other objects, but the central regions of OMC-1 have had their chemistry selectively altered by the high velocity outflow from the young star(s) embedded deep within the interior of the molecular cloud. Detailed arguments are presented in this thesis which relate the seemingly disparate chemical compositions of the individual regions to each other and to the expected physical manifestations of the circumstellar mass loss, and which suggest that similar mechanisms may operate in other molecular clouds as well.

By performing supporting laboratory spectroscopy to supplement existing millimeter-wave catalogues only 33 of the over 800 lines remain unidentified, in contradiction to earlier expectations which had predicted that the near millimeter-wave spectrum of molecular clouds would contain hundreds of strong, unidentifiable emission features. It is probable that a number of the unidentified lines left in the OVRO survey are due to transitions between states of either isotopically substituted or highly excited abundant and complex molecules such as CH_3OH, CH_3OCH_3, and $HCOOCH_3$ whose rotational spectra are poorly known at present. The very small percentage and weak strength of the unidentified lines implies that the dominant chemical constituents visible at millimeter wavelengths have been identified in the Orion molecular cloud.

Also presented are high resolution laboratory millimeter, submillimeter, and far-infrared absorption spectra of the transient molecular species OH, CN, HOC^+, and HCO. The zero-field pure rotational spectrum of the OH radical was observed, for the first time, with a frequency agile far-infrared laser sideband spectrometer which promises to revolutionize high resolution spectroscopy at submillimeter and far-infrared wavelengths, while the HOC^+ molecular ion was synthesized in a novel glow discharge cell that increases ion abundances by roughly two orders of magnitude as compared with those produced by previously reported methods. Studies of several ions produced in the new discharge

cell have provided a theory of the mechanism responsible for the ion enhancement. Sixty-five transitions of CN in its first four vibrational states have been observed, allowing a detailed examination of vibrational and electronic effects in this astrophysically important free radical. The investigation of HCO is the first extensive zero-field analysis of the formyl radical, and is one of the very few millimeter and submillimeter laboratory studies of a non-linear free radical performed to date.

Table of Contents

Illustrations

Tables

For Karen.

1. MOLECULES IN THE INTERSTELLAR MEDIUM

1.1 Introduction and Early History

As compared with the lengthy history of traditional astronomical observations, the study of interstellar molecules, and thereby interstellar chemistry, is still in its infancy. While much has been learned about stellar structure, evolution, and chemistry, considerably less is known about the interstellar matter from which stars form and to which they return mass at the end of their lives. The interplay of matter between stars and the interstellar medium is a complex process, but its investigation is vital to our complete understanding of the structure and dynamics of galaxies, including our own. As matter is cycled between stellar interiors and the interstellar gas, its chemical composition is affected by both environments, and, besides being of interest in its own right, the characterization of interstellar chemistry will therefore eventually lead to a more comprehensive analysis of galactic composition and evolution. In addition, the exotic conditions prevailing in the interstellar medium have made it possible to examine fundamental chemical and physical processes such as the formation and destruction of molecules at pressures, temperatures, and time scales that would be impossible to reproduce in the laboratory.

The interaction of matter with radiation is, currently, the most informative tool we have available to examine the physical condition and chemical composition of material outside our own solar system. Until quite recently only the visible portion of the electromagnetic spectrum has been accessible to investigation. Most of the visible radiation in our galaxy emanates from very hot regions such as the surfaces of stars where molecules, if they existed, would not survive for long. However, the radiation emitted by stars must also traverse the dilute gas permeating the interstellar medium before it reaches the Earth, and will

therefore interact with whatever species are present there. Given the dominance of optical methods throughout the history of astronomy, it is not surprising that the first interstellar molecular spectra were found near 4000 Å as an initially unidentified triplet of narrow visible absorption features along the lines of sight towards several reddened stars (Dunham and Adams 1937), subsequently identified as CH and CH^+ by Swings and Rosenfield (1937) and Douglas and Herzberg (1941). The identification of CH and CH^+ was soon followed by that of the CN radical (McKellar 1941), firmly establishing the existence of interstellar molecules. These identifications came as quite a surprise as at that time and for many years thereafter most theories of the physical conditions prevailing in and the chemical composition of the interstellar medium had predicted that the molecular content of the tenuous mixture of gas and dust along the lines of sight towards visible stars would be negligible due to the (presumed) slow formation and rapid photodissociation rates of most known species. Indeed, the detectable abundances of CH, CH^+, and CN were not interpreted as evidence of an active interstellar chemistry, but rather as residual products left over from the destruction of interstellar dust grains released by stars.

That stars should be invoked as a source of molecules in the interstellar medium is natural in that they have produced most of the heavier elements in our galaxy. Only H, He, and Li were generated by the Big Bang from which the universe began, and as these primordial elements are processed by stellar nucleosynthesis the heavier species are produced. Circumstellar mass loss or stellar explosions then return some of this matter enriched in heavier elements to the interstellar medium and to the next generation of stars. Even so, hydrogen, either as H^+ (HII), H (HI), or H_2, dominates the cosmic elemental abundances both by number and mass, with most of the remaining material present as He. By number, the heavier elements comprise only $\sim 10^{-4}$ of the matter in the galaxy. Thus, the chemistry we will discuss here occurs between elements

that may be considered trace contaminants of the interstellar medium. Molecular species have even lower abundances, as is evidenced by the fact that, combined, the optically detected CH, CH^+, and CN molecules contained only 0.1% of the cosmically available carbon. The remaining material, including hydrogen, was assumed to exist in atomic form.

Of the more highly obscured and presumably denser regions of gas visible on optical plates as dark "holes" against a brighter stellar background very little was known. The dust associated with these objects strongly scatters and severely attenuates visible and ultraviolet (UV) radiation rendering sensitive optical absorption techniques useless, but also protects any gas-phase species within from photodissociation or photoionization. Thus, the abundances of molecular species, in particular H_2, might be expected to rise considerably. Unlike optical studies, experiments using radio frequency radiation are able to easily penetrate even the densest regions of the interstellar medium because the dust is optically thin at these wavelengths. Spurred on by the development of microwave instrumentation and spectroscopy during and immediately following World War II, an intensive effort was therefore mounted to detect low frequency rotational or fine structure lines of simple molecules such as CH and OH (Shklovskii 1949, Townes 1954). After many negative results Weinreb *et al.* (1963) reported the first detection of a radio frequency molecular spectral line, the ground state lambda doubling transition of OH, toward the supernova remnant Cassiopeia A using a newly developed autocorrelation spectrometer. Some five years later rotational lines of the familiar and more complex water (H_2O), ammonia (NH_3), and formaldehyde (H_2CO) molecules were discovered with similar instrumentation (Cheung *et al.* 1969, 1968; Snyder *et al.* 1969), and the field of molecular astrophysics was born.

The rapid advances in radio and millimeter-wave technology in the twenty-

two years since the discovery of interstellar OH have revolutionized our concepts about the nature of the neutral gas in our galaxy. Astronomical observations at these wavelengths have revealed an entirely new type of object, the so-called dense molecular cloud, in which over sixty atomic and molecular species have now been identified -- a richness and complexity totally unexpected even a decade ago. As their name implies, molecular clouds contain little atomic material, but are a crucial component of many galaxies in that they may constitute the dominant mass phase of the neutral interstellar gas and, perhaps most importantly, because they are sites of star formation. Various studies have shown that different types of dense molecular clouds exist, from relatively small ($\sim 10^3$ $M_\odot$) and quiescent dark "dust" clouds characterized by kinetic temperatures on the order of 10 K to extremely massive ($\sim 10^6$ $M_\odot$) "giant" molecular clouds which typically have regions with somewhat higher temperatures up to ~100 K and which often contain newly formed stars embedded deeply within them.

It is only recently that we have begun to understand how molecules can be created so efficiently in such a hostile environment, and why in some cases the chemical composition of the various types of molecular clouds should differ so radically. As an illustration of this chemical diversity and the equally diverse methods that have been used to study it, a list of the molecular species identified in the interstellar medium at the time of this writing (7/1/85) is presented in Table 1.1 along with the technique used to detect them. Various mechanisms have been proposed to account for the chemical composition of interstellar molecular clouds, but, as we will later show, it now appears as if networks of bimolecular ion-molecule reactions are primarily responsible for the efficiency and diversity of interstellar chemistry.

Table 1.1
A List of Known Interstellar Molecules (as of 7/1/85)

Chemical Formula	Name	Detection Wavelength	Chemical Formula	Name	Detection Wavelength
H_2	Hydrogen	UV,IR	C_3H	Propynylidyne radical	MW
CH	Methyladine radical	Vis,MW	C_3N	Cyanoethynyl radical	MM
CH^+	Methyladine ion	Vis	C_3O	Tricarbon monoxide	MW
OH	Hydroxyl radical	UV,MW	HNCO	Isocyanic acid	MW,MM
		SMM	HNCS	Thioisocyanic acid	MM
HCl	Hydrogen chloride	SMM	H_2CO	Formaldehyde	MW,MM
CC	Diatomic carbon	Vis	H_2CS	Thioformaldehyde	MW,MM
CN	Cyanogen radical	Vis,MM	$HOCO^+$	Protonated carbon dioxide	MM
CO	Carbon monoxide	UV,IR	CH_4	Methane	IR
		MM,SMM	SiH_4	Silane	IR
CS	Carbon monosulfide	MM	C_4H	Butadiynyl radical	MM
NO	Nitric oxide	MM	C_3H_2	Cyclopropenylidene radical	MW,MM
NS	Nitric sulfide	MM	HC_3N	Cyanoacetylene	MM
SiO	Silicon monoxide	MM	NH_2CN	Cyanamide	MW,MM
SiS	Silicon monosulfide	MM	H_2CNH	Methylenimine	MW,MM
SO	Sulfur monoxide	MM	H_2CCO	Ketene	MW,MM
H_2D^+	Protonated HD	SMM	HCOOH	Formic acid	MW,MM
CCH	Ethynyl radical	MM	C_2H_4	Ethylene	IR
HCN	Hydrogen cyanide	MM	CH_3CN	Methyl cyanide	MM
HNC	Hydrogen isocyanide	MM	CH_3OH	Methanol	MW,MM
HNO (?)	Nitroxyl radical	MM	CH_3SH	Methyl mercaptan	MM
HNN^+	Diazenylium	MM	NH_2CHO	Formamide	MW,MM
HCO	Formyl radical	MM	HC_5N	Cyanodiacetylene	MW
HCO^+	Formyl ion	MM	CH_3CCH	Methyl acetylene	MM
HOC^+	Isoformyl ion	MM	CH_3NH_2	Methylamine	MW,MM
HCS^+	Thioformyl ion	MM	CH_3CHO	Acetaldehyde	MW,MM
OCS	Carbonyl sulfide	MM	C_2H_3CN	Vinyl cyanide	MW,MM
NaOH (?)	Sodium hydroxide	MW	CH_3C_3N	Methyl cyanoacetylene	MW
H_2O	Water	UV,MW	$HCOOCH_3$	Methyl formate	MW,MM
		MM,SMM	HC_7N	Cyanohexatriyne	MW
H_2S	Hydrogen sulfide	MM	CH_3C_4H	Methyl diacetylene	MW
SO_2	Sulfur dioxide	MW,MM	CH_3OCH_3	Dimethyl ether	MW,MM
SiC_2	Silacyclopropyne	MM	C_2H_5OH	Ethanol	MW,MM
HCCH	Acetylene	IR	C_2H_5CN	Ethyl cyanide	MW,MM
NH_3	Ammonia	IR,MW	HC_8N	Cyanooctatetrayne	MW
		SMM	$HC_{11}N$	Cyanodecapentyne	MW

UV = Ultraviolet Vis = Visible IR = Infrared
SMM = Submillimeter-wave and FIR MM = Millimeter-wave MW = Microwave

1.2. Millimeter and Submillimeter Spectral Lines

Because the gas and dust in "typical" molecular clouds has a temperature on the order of 10 - 100 K, the bulk of the radiation emitted by such objects lies at millimeter (10-1 mm), submillimeter (1-0.2 mm), and far-infrared (200-30 μm) (FIR) wavelengths where the interaction of electromagnetic radiation with the rotational motion of simple molecules is at a maximum. As noted above, radiation at these frequencies also passes virtually unattenuated through the interstellar medium, and it is for these reasons that most of the species listed in Table 1.1 have been detected using rotational spectroscopic methods at microwave and millimeter wavelengths. Observations at higher frequencies are more difficult but are equally important because the pure rotational transitions of molecular hydrides, which constitute many of the fundamental interstellar molecules due to the universal predominance of hydrogen, lie exclusively at submillimeter or far-infrared wavelengths. The fine structure ground state lines of the lighter atoms also lie in the submillimeter and far-infrared. Because of their large rotational constants and dipole moments, line emission from simple hydrides is also a potentially large source of energy loss from molecular clouds. Figure 1.1 illustrates the optimum frequency ranges for the interaction of millimeter and FIR radiation with interstellar molecules by presenting the fully excited rotational envelopes of OCS, one of the heavier detected species, CO, a molecule of intermediate mass, and HCl, which is more characteristic of the light molecular hydrides, for a kinetic temperature of 100 K. As this figure shows, the OCS envelope has its maximum strength near 150 GHz while the strongest HCl rotational transition lies near 1250 GHz. Many interstellar molecules have rotational constants somewhere in between these extremes, and therefore absorb radiation most strongly in the 100-1000 GHz range, sometimes called the *near millimeter-wave* region. Densities in molecular clouds are often insufficient to maintain a fully thermalized population distribution in many

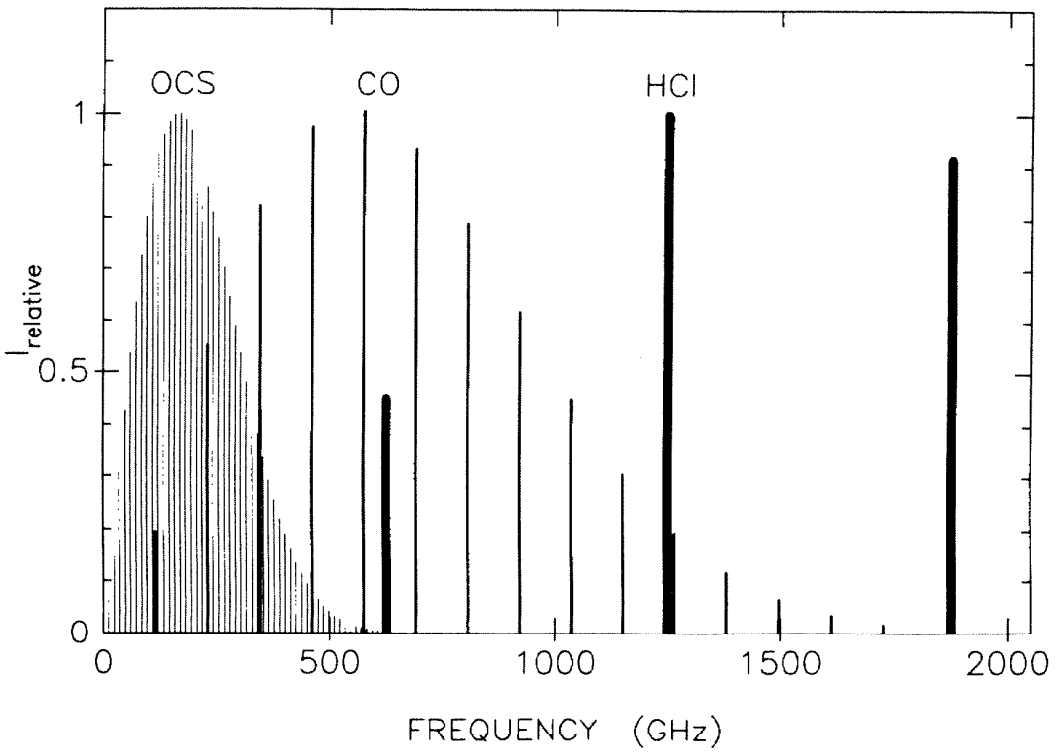

Figure 1.1: The rotational envelopes of OCS ($J_{max}=14\rightarrow13$), CO ($J_{max}=5\rightarrow4$), *and* HCl ($J_{max}=2\rightarrow1$) *for a kinetic temperature of 100 K.*

molecular hydrides because of their rapid spontaneous decay rates, and for such species the ground state transition will be strongest. A more quantitative listing of the rotational envelope maxima and fundamental transition frequencies for some abundant interstellar molecules is presented in Table 1.2.

Observations of spectral lines in the relatively unexplored region above 200 GHz are therefore quite important because they provide powerful, and often unique, probes into the chemical and physical nature of the interstellar gas. In addition to producing some of the most accurate estimates of the chemical abundances, temperatures, and densities within molecular clouds near millimeter-wave spectral lines also contribute substantially to the energy balance in these objects and are therefore important in their own right. The amount of energy lost from rotational emission lines determines, in part, the

Table 1.2
LTE Rotational Envelope Maxima and Low-Lying Transition Frequencies of Some of the More Abundant Interstellar Molecules

Molecule, envelope maximum	ν (GHz)	Hydride, lowest transition	ν (GHz)
CO $J=5\rightarrow4$	576.3	NaH $J=1\rightarrow0$	289.9
HCO^+ $J=6\rightarrow5$	535.1	H_3O^+ $J_K=2_1\rightarrow1_1$ (ortho)	307.2
HCN $J=6\rightarrow5$	531.7	MgH $^2\Sigma^+$ $J=1/2$, $N=1\rightarrow0$	343.0
H_2CO $J_{K_pK_o}=6_{06}\rightarrow5_{05}$	434.5	H_2D^+ $J_{K_pK_o}=1_{10}\rightarrow1_{11}$ (ortho)	372.4
CS $J=8\rightarrow7$	391.8	LiH $J=1\rightarrow0$	444.0
CH_3OH $J_K=8_0\rightarrow7_0$ A,E	386.7	H_2S $J_{K_pK_o}=1_{11}\rightarrow0_{00}$	452.4
SiO $J=8\rightarrow7$	347.3	CH $^2\Pi_{3/2}$, $J=3/2\rightarrow{}^2\Pi_{1/2}$, $J=1/2$	532.7
HCS^+ $J=8\rightarrow7$	341.3	NH_3 $J_K=1_0\rightarrow0_0$	572.5
SO $N_J=8_8\rightarrow7_7$	337.6	HCl $J=1\rightarrow0$	625.9
H_2CS $J_{K_pK_o}=9_{09}\rightarrow8_{08}$	308.7	SiH $^2\Pi_{1/2}$, $J=3/2\rightarrow1/2$	660.0
H_2CCO $J_{K_pK_o}=11_{0,11}\rightarrow10_{0,10}$	222.2	CH^+ $J=1\rightarrow0$	835.1
SO_2 $J_{K_pK_o}=11_{1,11}\rightarrow10_{0,10}$	222.0	NH $^3\Sigma^-$ $N=1\rightarrow0$	974.5
CH_3CN $J_K=12_0\rightarrow11_0$	220.7	H_3O^+ $J_K=1_0\rightarrow0_0$ (para)	984.6
SiS $J=12\rightarrow11$	217.8	H_2O $J_{K_pK_o}=1_{11}\rightarrow0_{00}$	1113.3
CH_3OCH_3 $J_{K_pK_o}=11_{1,11}\rightarrow10_{0,10}$	209.5	H_2D^+ $J_{K_pK_o}=1_{01}\rightarrow0_{00}$ (para)	1374.2
OCS $J=14\rightarrow13$	170.3	SH $^2\Pi_{3/2}$ $J=5/2\rightarrow3/2$	1382.9
HC_3N $J=16\rightarrow15$	145.6	HeH^+ $J=1\rightarrow0$	2010.1
$HCOOCH_3$ $J_{K_pK_o}=13_{0,13}\rightarrow12_{0,12}$	142.8	CH_2 $J_{K_pK_o}=1_{11}\rightarrow0_{00}$	2344.7
C_2H_5CN $J_{K_pK_o}=16_{0,16}\rightarrow15_{0,15}$	139.3	OH $^2\Pi_{3/2}$ $J=5/2\rightarrow3/2$	2509.9
HC_5N $J=29\rightarrow28$	77.2	HD $J=1\rightarrow0$	2675.0

rates of collapse and ultimately the efficiency of star formation in molecular clouds, and is very sensitive to the exact chemical composition of the gas.

However, the particular scope of rotational spectroscopy brings with it certain observational selection effects. For example, rotational spectral lines from molecular clouds can be extremely narrow and therefore provide useful information about the velocity fields of these objects, especially in the cold quiescent clouds where the velocity line widths can be less than 0.3 km s^{-1} (~100 kHz at 100 GHz) -- smaller than that achieved in all but the most exacting molecular beam experiments. Since astronomical heterodyne spectrometers can easily achieve this resolution, it is desirable to know to an equivalent accuracy the exact transition frequency of the assigned molecular rotational line in order to

most positively identify a given feature. Thus, searches for and definitive identification of interstellar molecules have relied almost exclusively on existing laboratory data to furnish the required rest frequencies, and Table 1.1 therefore contains a natural bias towards simpler and terrestrially stable species such as CO and OCS for which accurate spectra exist. The exotic conditions prevailing in the interstellar medium are such, however, that large amounts of highly unusual and reactive species may exist whose spectra are not presently known. Indeed, the laboratory spectra of several terrestrially reactive species like CN, CCH and HCO^+ were recorded only *after* they had been identified in the interstellar medium through an ingenious combination of astronomical spectroscopy and *ab initio* quantum mechanical structural calculations. The detection of such unusual molecules in the interstellar medium has provided a new and urgent impetus for the laboratory study of the rotational spectra of both complex and short-lived species, particularly in the near millimeter-wave spectral region.

The elucidation of the HCO^+ rotational spectrum was particularly important to the development of molecular astrophysics in that it stimulated progress in a number of experimental and theoretical disciplines. The $J = 1 \rightarrow 0$ line was initially detected as an intense unidentified feature at 89.2 GHz labeled X-ogen by Buhl and Snyder (1970), and Klemperer (1970) was the first of many to suggest that X-ogen was, in fact, HCO^+. Klemperer's insightful suggestion was based on simple structural calculations and chemical intuition, but some five years would pass before it was unequivocally verified. By 1973, refined quantum mechanical calculations on the structure of the formyl ion had reproduced the X-ogen frequency to within 200 MHz (Wahlgren *et al.* 1973), and had provided the rest frequency necessary for a detection of the interstellar $H^{13}CO^+$ $J = 1 \rightarrow 0$ transition (Snyder *et al.* 1976). Nearly simultaneously, Woods *et al.* (1975) observed the parent and ^{13}C and ^{18}O isotopes in the laboratory for the first time, verifying

both the astronomical and theoretical results. Chemical models of the interstellar medium were also modified to include the presence of ion-molecule reactions (Herbst and Klemperer 1973), and had shown that such reactions could, in principle, account for the abundances of nearly all of the species detected in dense molecular clouds at that time. Thus, the early work on HCO^+ is at least partially responsible for the fields of interstellar chemical modeling and high resolution ion spectroscopy as we know them today.

A second and certainly more constraining observational selection effect is that, regardless of their abundance, only molecules possessing a permanent dipole moment may be studied by means of their rotational spectra. Fundamental and most certainly otherwise detectable molecules such as H_2 (the most abundant interstellar molecule), H_3^+, CO_2, C_2H_2, and CH_4 will therefore never be observed in the millimeter-wave spectrum of molecular clouds. Fortunately, most of these molecules posses an active vibrational spectrum and may be studied, albeit in somewhat less detail and generality, with high resolution infrared techniques. Some species like N_2, however, have no strongly allowed rotational or vibrational transitions, and their abundances must be inferred from chemical models or from chemically related molecules such as HN_2^+. Also, some very important astronomical species, such as O_2 and H_2O, cannot be easily observed with current technology because of their presence in the Earth's atmosphere (cf. Section 1.3).

Finally, a more subtle selection effect arises from the rotational spectra of larger molecules. As a rotor increases in size and complexity the number of rotational states populated grows dramatically, particularly if the energy levels contain splittings induced by electronic fine structure interactions or internal rotation. Thus, although it may be possible to obtain meaningful upper limits to the populations of individual levels in a complex molecule, the overall sensitivity

may be quite low since so many states are occupied. Another way of saying this is that even at the low temperatures characterizing molecular clouds the rotational partition functions of heavy, complex molecules can become quite large. Because of these restrictions the currently identified interstellar species listed in Table 1.1 are dominated by simple, light molecules whose terrestrial stability and dipole moments are appreciable.

1.3. Astronomical Observations at Millimeter and Submillimeter Wavelengths

Like many types of astronomy, ground-based observations at millimeter and submillimeter wavelengths must be undertaken within spectral "windows" where the atmospheric transmission is relatively high. As Figure 1.2 shows, water vapor in the atmosphere imposes boundaries for most of these windows at millimeter wavelengths via its strongly allowed rotational transitions which become particularly opaque at the shorter FIR wavelengths. Atmospheric oxygen also contributes strongly at certain frequencies, particularly via its band of fine structure transitions near 60 GHz. For this reason, most of the observations of interstellar molecules have been conducted at frequencies below 200 GHz. Even in this region, however, early observations were conducted on a "line-by-line" basis because of the low sensitivity of existing telescopes and detectors and the small bandwidths of the back end spectrometers. The basic impression from these observations was that, even though large numbers of individual molecules existed in molecular clouds, the overall spectra of these objects were not nearly so rich in features as were those of stellar atmospheres so crucial to our understanding of stellar structure and evolution.

Whereas only limited observations of selected species were previously possible, the improved performance of new large aperture telescopes and low-noise broad-band receivers has recently allowed unbiased millimeter-wave surveys of

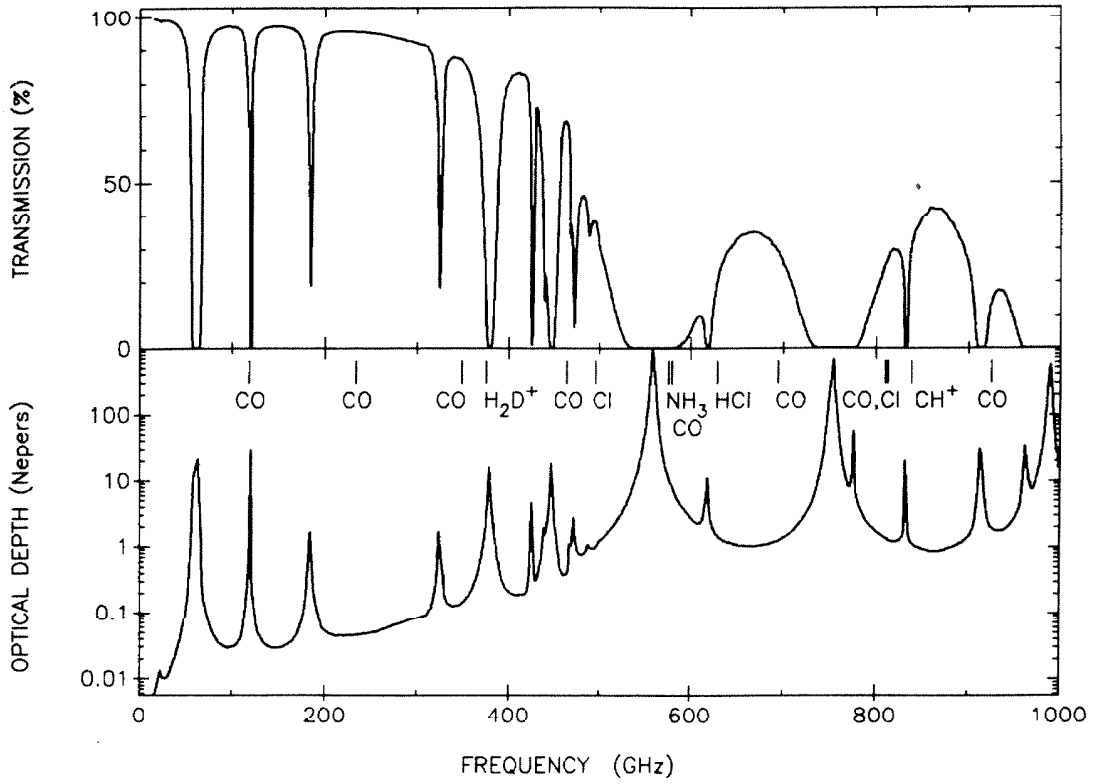

Figure 1.2: Atmospheric transmission and optical depth vs. frequency for a precipitable water vapor column of 1.5 mm. The positions of some important astronomical emission lines are indicated by the vertical bars.

molecular line emission to be conducted on a number of objects (Johansson *et al.* 1984; Cummins, Linke, and Thaddeus 1985). The most extensive spectral line survey of this type is that of the Orion molecular cloud (OMC-1) conducted at the Owens Valley Radio Observatory (OVRO) which constitutes the major portion of this thesis (Sutton *et al.* 1985; Blake *et al.* 1986). The great strength and number density of rotational emission lines from OMC-1 near 1.3 mm is dramatically illustrated in the compressed view of the OVRO spectral line survey presented in Figure 1.3. This figure shows that the millimeter-wave spectra of molecular clouds can become as dense as those of stellar atmospheres, and that only now is the sensitivity sufficient to begin a comprehensive investigation of the broad-band spectral properties of molecular clouds. In fact, large portions

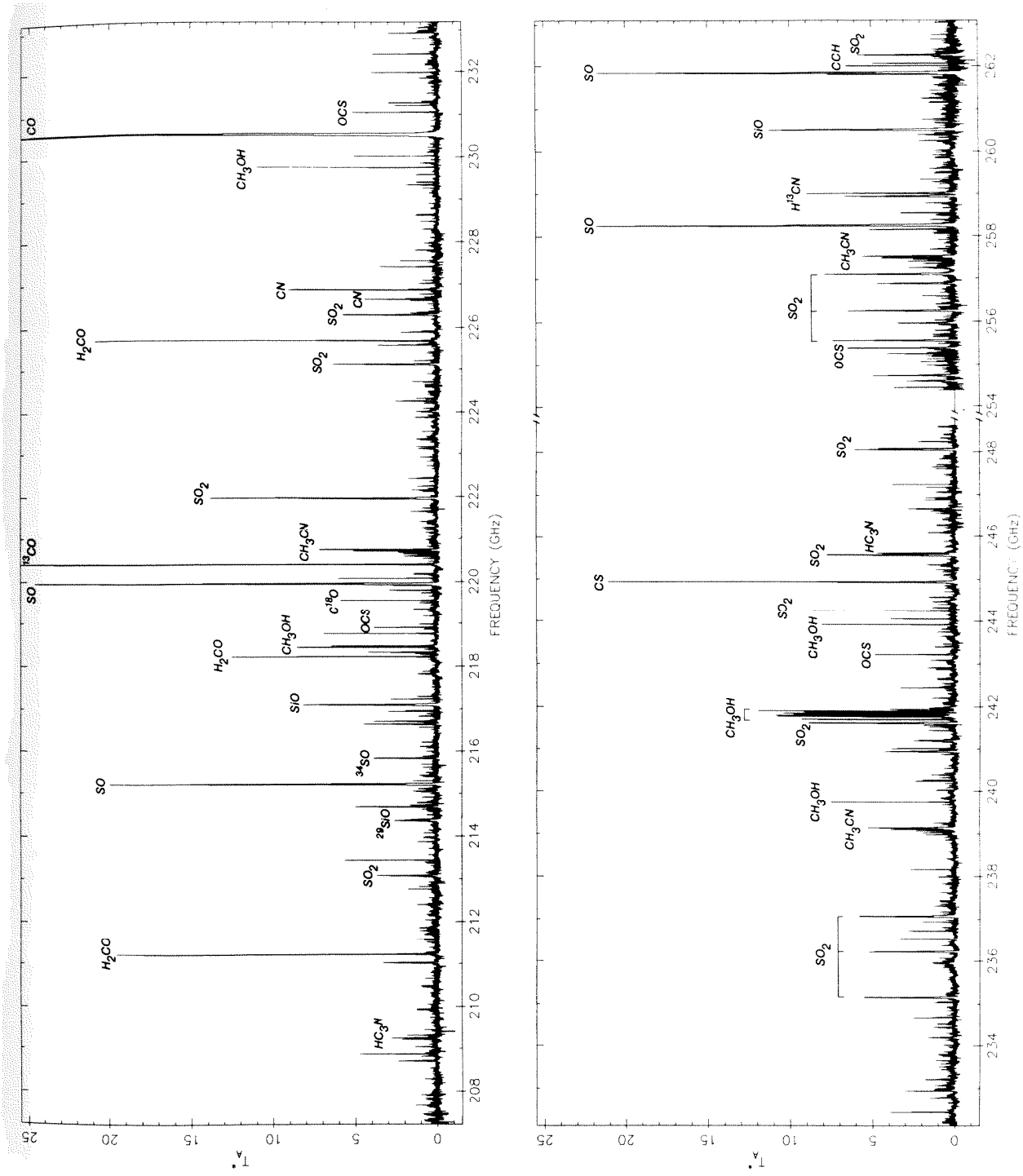

Figure 1.3: A compressed view of the OVRO spectral line survey of OMC-1.

of the OVRO survey are "confusion-limited" in that rotational emission lines stronger than the anticipated noise level occupy the entire baseline. The examination of large parts of the millimeter-wave spectrum has several advantages over isolated, single line measurements, some of which are:

(1) *New Species:* In the early days of molecular line astronomy the detection of a single transition was usually all that was available to identify a new molecule in the interstellar medium. Naturally, several mistakes were made. Today, however, unless the lines are very strong the identification of new species relies on the detection of several transitions because the near millimeter-wave spectrum is so congested with lines of known molecules (cf. Figure 1.3). Thus, either several different observations must be made with narrow-band devices, or a large region of the spectrum must be recorded. Since most of the new lines will be weak (almost all of the strong emitters have been identified), good sensitivity is a must.

(2) *Chemical and Physical Properties:* By examining molecular line emission from several sources of differing type, it may be possible to "classify" molecular clouds and their chemistry just as stars are now classified according to their optical spectra. Such an approach demands spectrometers with large bandwidth and high sensitivity so that extensive regions of the rotational spectrum may be covered with great dynamic range in order to insure a complete sampling of the species present in the source. In addition, the improved relative and absolute calibration provided by observations taken with a single instrument produces much more accurate estimates of the temperatures, densities, and chemical composition of molecular clouds than would observations conducted with several different telescopes.

(3) *Far-infrared characteristics:* Energy loss through their total radiative output is the principal cooling mechanism of molecular clouds. To date it has been assumed that the "continuum" millimeter and submillimeter radiation emitted by molecular clouds arises nearly exclusively from dust grains associated with these objects. If the rotational line density is large, however, the *integrated* molecular line emission may account for a substantial fraction of the near millimeter-wave continuum output of molecular clouds and circumstellar shells as measured by broad-band detectors. Spectroscopic instruments that combine large bandwidth with high resolution are required to separate the line and true continuum contributions to the energy balance in molecular clouds because of the narrow line widths of the emission features.

Observations at submillimeter wavelengths are currently hampered by lower instrumental sensitivity as compared with lower frequency studies, and by the increased atmospheric attenuation shown in Figure 1.2 as well. However, most of the water vapor in our atmosphere is trapped below the tropopause, which lies near 35000 ft at most latitudes. Balloon or airborne platforms are therefore able to operate above most of the atmospheric attenuation and can allow many astronomical observations to be conducted that would be impossible from the ground. The largest such telescope is the Gerard P. Kuiper Airborne Observatory (KAO) operated by the National Aeronautics and Space Administration (NASA), shown in Figure 1.4. A converted C-141 military transport aircraft, the KAO houses a full flight crew and several observers in a shirt-sleeve environment and its highly stabilized 91.4 cm optical quality telescope while flying at an operational altitude of about 12.5 km (Cameron, Bader, and Mobley 1971; Gillespie 1981). The KAO has been the leading far-infrared and submillimeter astronomical observatory since it inaugural flights over a decade ago, and has

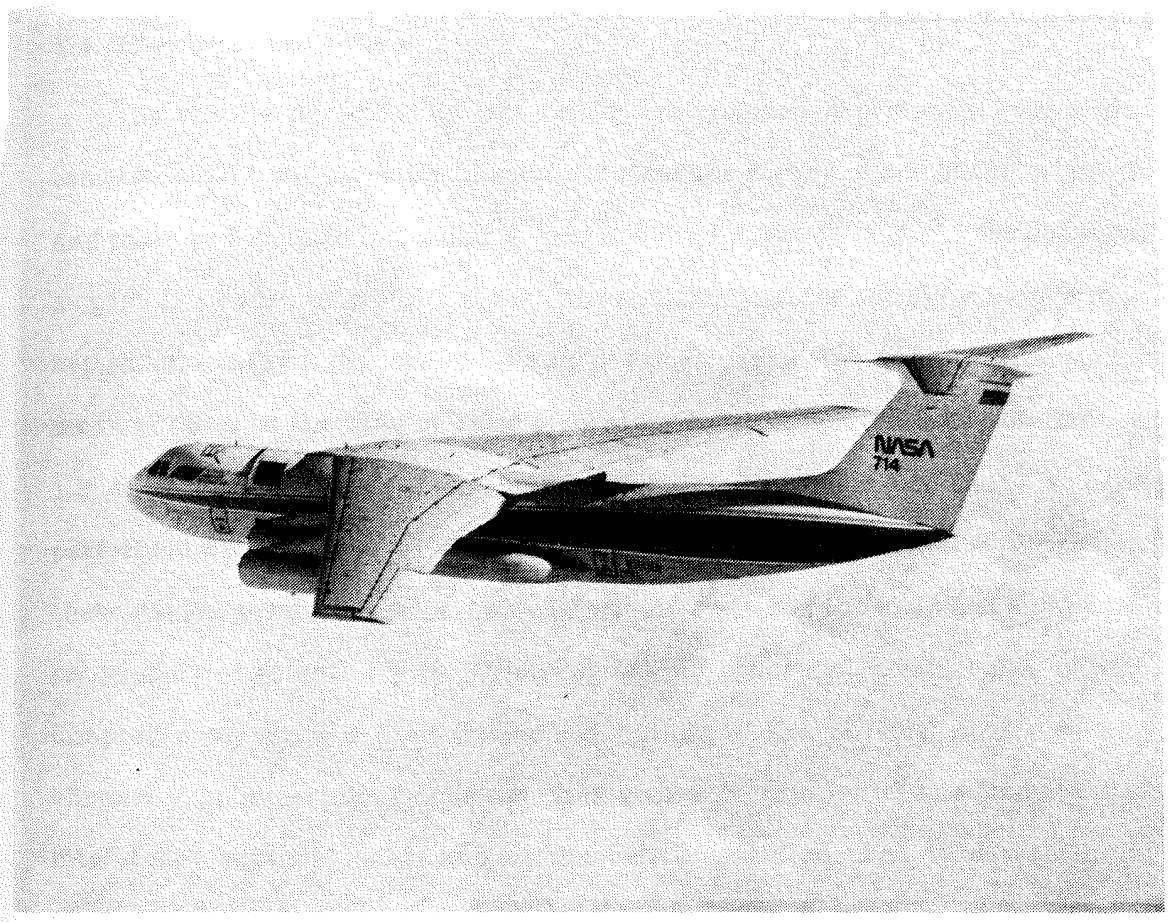

Figure 1.4: The C-141 Gerard P. Kuiper Airborne Observatory (KAO) operated by NASA. The 91.5 cm telescope is situated just forward of the wings, visible as the black square in the photograph.

been used for all of the submillimeter measurements described here. Nevertheless, the decreased instrumental sensitivity at these wavelengths coupled with the limited observing time available on an airborne platform means that only exploratory observations of those lines expected to be the strongest or of the greatest interest can be attempted, a general submillimeter spectral line survey will not be feasible until the next generation of ground-based telescopes becomes operational.

1.4. Preview of the Thesis

The results described in this thesis are concerned primarily with a systematic millimeter and submillimeter spectral line survey of one of the brightest and most well-studied molecular clouds in our galaxy, OMC-1, and were collected as part of a continuing effort of the Caltech Submillimeter Astrophysics group to better understand the chemical and physical parameters of the interstellar medium. Due to the lack of basic laboratory information alluded to in Section 1.2, a considerable amount of supporting laboratory spectroscopy has also been performed on a number of stable and transient interstellar species. Together, these results produce a remarkably informative atlas of the chemical and physical properties of not only the Orion region, but other molecular clouds as well. Chapter 2 presents a brief theoretical outline of the physical structure and chemistry of molecular clouds together with a description of the formation of interstellar spectral lines, and of the instrumentation used to detect them. Chapter 3 contains a summary of the basic results of the laboratory and astronomical observations, while Chapter 4 is devoted to a more detailed discussion of the chemistry of the various regions of OMC-1. Because of the large body of data obtained, a detailed presentation of the astronomical and laboratory data is included in two Appendices which follow the main text.

So, Geoff, do you think you'll
like working under two women?

-Anneila I. Sargent

2. THEORETICAL OVERVIEW AND INSTRUMENTATION

2.1 The Physical Structure of Dense Molecular Clouds

Consider the idealized representation of a giant molecular cloud such as OMC-1 depicted in Figure 2.1. As this figure shows, molecular clouds are often closely associated with HII regions and other manifestations arising from the young stars born within them. A general feature observed in most large clouds, and also in many theoretical models of their dynamics, is a well-defined "core-halo" structure in which an extended (~50 pc) and cooler region of gas surrounds a warmer, compact (~1-5 pc) cloud core that may contain embedded stellar or protostellar objects (Thaddeus 1982; Sanders, Solomon, and Scoville 1984; Falgarone and Puget 1985). The extended material is of fairly low density (n_{H_2}~100-1000 cm^{-3}) and temperature ($T \gtrsim 10$ K) and contains most of the mass of the cloud, while the cores are often considerably warmer (T~30-100 K) and more dense ($n_{H_2} \gtrsim 10^4$ cm^{-3}). Cocoons of gas adjacent to embedded stars can become very warm and dense (T~100-300 K, $n_{H_2} \gtrsim 10^7$ cm^{-3}), and may have chemical properties significantly different from the rest of the cloud. This is particularly true for "active" cloud cores such as Orion, where mass loss from embedded sources can accelerate large amounts of material, driving shock waves into much of the cloud core and beyond.

Scattered rather evenly throughout the cloud complex is a distribution of small particulate matter known as dust grains, whose exact composition remains a topic of considerable debate. While grain sizes may vary greatly, most are approximately 0.1 μm in diameter. Taken together they contain ~1% of the cloud mass and provide nearly all of the attenuation of visible and near-UV radiation associated with dense interstellar clouds. Their abundance is insufficient to prevent significant photochemical processing in the extended

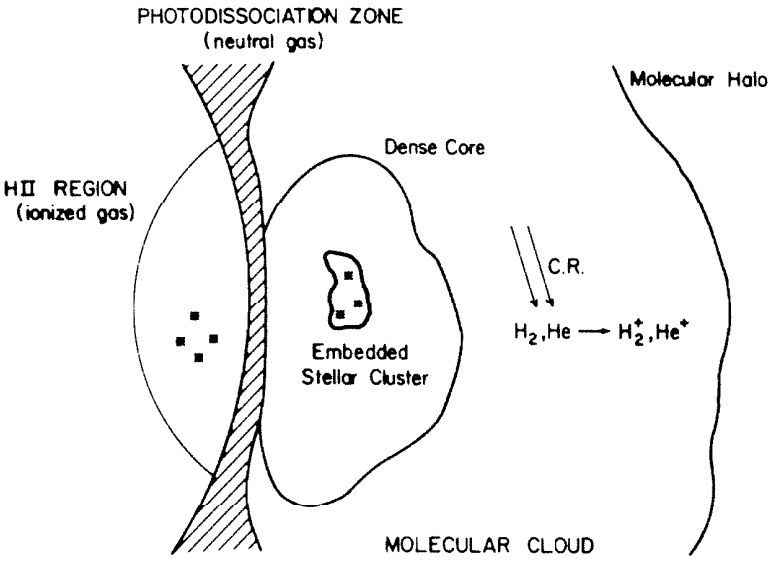

Figure 2.1: Idealized representation of a "typical" giant molecular cloud and its surroundings (after Zuckerman 1973).

halo component of molecular clouds, but is high enough to insure that photodissociation and other photon-assisted processes may be safely ignored in cloud cores, except in those small regions immediately surrounding embedded stars and dissociative shock fronts. In addition to "shielding" interstellar molecules from harmful radiation, dust grains are also intimately involved in the chemistry of molecular clouds, as we shall see.

2.2. A Brief Description of Interstellar Chemistry

Hydrogen dominates the relative cosmic elemental abundances and, by inference, interstellar chemistry as well. The quantitative abundances presented in Table 2.1 show that, except for helium, all other elements may be considered trace constituents. In fact, astronomical objects are often classified according to which of the three states of hydrogen, H(HI), H^+(HII), and H_2, is most prevalent. As mentioned above, molecular hydrogen is not generally observable in dense interstellar clouds, and its abundance must be inferred

Table 2.1
Relative Cosmic Abundances for Some of the Lighter Elements

Species	Relative Abundance
H	1.00
He	0.15
C	3.0×10^{-4}
N	9.0×10^{-5}
O	7.0×10^{-4}
Ne	8.3×10^{-5}
Si	3.0×10^{-5}
S	1.6×10^{-5}
Cl	3.0×10^{-7}

from the trace molecular constituents that can be detected. Numerous such studies on a wide range of objects have concluded that nearly all of the hydrogen is in the form of H_2 in molecular clouds (Spitzer 1978). Because of its symmetry, H_2 cannot be dissociated by the absorption of a single photon, nor can it be formed efficiently via gas-phase radiative association reactions. Put another way, the photodissociation of molecular hydrogen is dominated by *line* rather than continuum absorption, and H_2 is therefore able to protect, or "self-shield," itself against destruction once its column density in the outer regions of the cloud is sufficient to render the initial transitions in the two-step dissociation sequence optically opaque (Stecher and Williams 1967; Hollenbach, Werner, and Salpeter 1971). Except for the reaction

$$H^- + H \rightarrow H_2 + e^- \ ,$$

no rapid gas-phase production mechanisms of H_2 exist, and it is therefore inferred that molecular hydrogen must be formed via the recombination of hydrogen atoms on the mantles of interstellar dust grains (Hollenbach, Werner, and Salpeter 1971), a process known to occur on many surfaces in the laboratory (Lee 1972). From the measured H^- + H rate constant (Schmeltekopf, Fehsenfeld, and Ferguson 1967) and the estimated H_2 formation efficiency on

grains, it is found that a fractional ionization in excess of 10^{-2} is required to equalize the gas-phase and grain surface formation rates, which, except for ionization fronts, is orders of magnitude above that inferred to exist in in the molecular interstellar gas (Hill and Silk 1975). The relative H/H_2 content of interstellar gas varies sharply as a function of depth into the cloud and is determined by the balance between photodissociation and surface recombination. Of the other molecular species in dense interstellar clouds, it now appears as if most or all of them, unlike H_2, can be formed by chemical reactions in the gas-phase. Grains still play an important role in the chemistry of the trace elements, however, as many of these species may be selectively removed from the gas-phase and subsequently chemically processed by condensation onto grain surfaces.

Of the plethora of gas-phase reactions known to chemistry, only a handful of them are important in the interstellar medium. The low density of molecular clouds is such that three body collisions are exceedingly rare; only bimolecular reactions involving the ground electronic and vibrational states of the reactants have appreciable probability. Secondly, the low temperatures in most quiescent molecular clouds prove to be extremely restrictive. Few endothermic reactions can proceed, and even most exothermic reactions are extraordinarily slow because of their associated activation energies. Except for a few radical-atom or radical-molecule reactions, the overwhelming majority of neutral-neutral reactions have activation barriers much larger than the typical kT values in dense molecular clouds. In contrast, ion-molecule reactions usually posses no activation energy and therefore have little or no temperature dependence. Indeed, the rates of some ion-molecule reactions such as radiative association actually increase as the temperature decreases. Ion-molecule cross sections and reaction rates are among the largest known, with many reactions occurring at or near the Langevin (collisional) frequency of $k = \langle \sigma v \rangle \sim 10^{-9}$ $cm^3 s^{-1}$. The

identification of molecular ions like HCO^+ and HN_2^+ in the interstellar medium (cf. Table 1.1) certainly implies that ion-molecule reactions occur. Can they produce the observed chemical diversity of molecular clouds? After all, the creation of appreciable concentrations of molecular ions in the cores of dense, quiescent clouds would require a great deal of energy that cannot be provided internally. That such an energy source is available is clearly demonstrated by the chemical composition of molecular clouds, however.

For example, the lifetimes of most interstellar molecules are significantly shorter than those of the clouds in which they exist, and such molecules must therefore be perpetually created and destroyed *in situ*. Moreover, the presence of highly unusual and reactive species like HNC, CN, and various molecular ions illustrate that the chemistry in molecular clouds is not at equilibrium, and that some continual energy input is required to maintain this disequilibrium. As indicated in Figure 2.1, a nearly constant flux of galactic high energy cosmic rays penetrates even to the cores of dense molecular clouds, thereby producing a small amount of ionization. The energy liberated by this process is now thought to be the driving force behind the gas-phase chemistry in molecular clouds. In dense clouds, molecular chemistry is initiated by the ionization of H_2 and He to produce H_2^+ and He^+. Ionized molecular hydrogen may then react with the ever present H_2 to produce H_3^+, the cornerstone of gas-phase interstellar chemistry. As shown by Herbst and Klemperer (1973) and Watson (1973) in their pioneering studies of dense interstellar clouds, secondary reactions of H_3^+ with trace atomic constituents like C and O unleash a complex network of chemical reactions that proceed until the lowest ionization potential products, the "metals," are formed. (Astronomers usually define all those elements heavier than He to be "metals"; we use the term here to identify abundant species such as Na, Mg, or Fe whose low ionization potentials make them natural carriers of the positive charge in interstellar clouds.) In this way, the energy carried by high energy

cosmic rays is used to synthesize successively more complex molecular ions, which then produce the observed neutral species by charge transfer or recombination with electrons. A schematic diagram of this process is illustrated in Figure 2.2. In an effort to more accurately characterize the chemistry of dense molecular clouds, large-scale theoretical calculations incorporating thousands of ion-molecule reactions ranging from simple charge or proton transfer processes to complex radiative association pathways, as well as the few neutral-neutral reactions expected to be important, have now been performed. Current models follow the abundances of over a hundred species and reproduce, for the most part, the observed values rather well and provide a useful and detailed outline of interstellar chemistry and of the similarities and differences between the various chemical families (carbon, oxygen, nitrogen, etc.), but a few notable problems remain (Prasad and Huntress 1980; Leung, Herbst, and Huebner 1984). An exhaustive description of the reaction types and model predictions is beyond the scope of this discussion, but a more detailed comparison of the results of large-scale theoretical calculations with our observed abundances will be presented in Chapter 4.

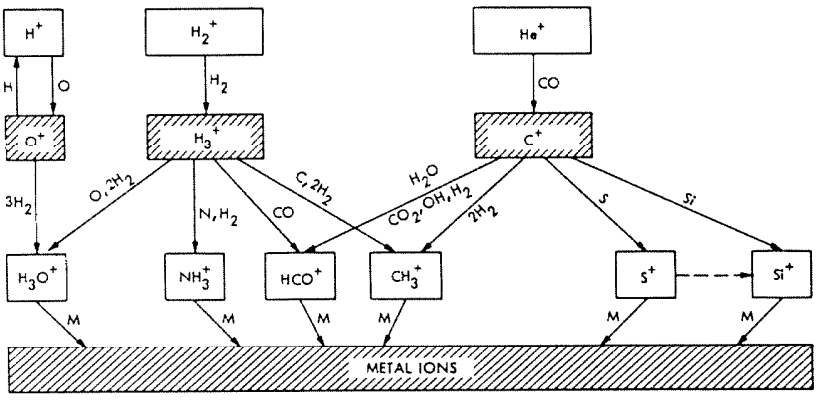

Figure 2.2: The flow of ionization and the initiation of molecular chemistry in dense interstellar clouds (Prasad and Huntress 1980).

2.3. The Formation of Interstellar Spectral Lines

The determination of molecular abundances from the rotational spectra of interstellar clouds is an involved, and sometimes quite uncertain, process. We shall first consider the two-level problem depicted in Figure 2.3, which shows that the relative level populations are determined not only by the familiar spontaneous and induced radiative transitions, but through collisional processes as well. In both space and the laboratory the quantitative radiative transfer equation

$$dI_\nu / ds = j_\nu - \kappa_\nu I_\nu \tag{2.1}$$

governs the detailed interaction of matter with spectral line radiation, where I_ν is the specific intensity at frequency ν, j_ν is the emissivity, and κ_ν is the absorption coefficient of the gas. For our simple case, the emissivity treats spontaneous emission from the upper level k to the lower level j, while the absorption coefficient describes the overall effect of induced absorption and emission. In terms of the Einstein A and B coefficients, the level population densities n_k and n_j, and the normalized line profile $\Phi(\nu)$ these functions are given by

$$j_\nu = \frac{h\nu\, n_k A_{kj}}{4\pi} \Phi(\nu) \tag{2.2a}$$

$$\kappa_\nu = \frac{h\nu}{4\pi} (n_j B_{jk} - n_k B_{kj})\, \Phi(\nu)\,. \tag{2.2b}$$

The Einstein coefficients are not independent, but are related to each other by the expressions

$$A_{kj} = \frac{64\pi^4\nu^2}{3hc^2} |\mu_{kj}|^2 = \frac{64\pi^4\nu^2\mu^2 S}{3hc^2 g_k} \tag{2.3a}$$

$$g_j B_{jk} = g_k B_{kj} = \frac{c^2}{2h\nu^3} g_k A_{kj} \tag{2.3b}$$

obtained from detailed balancing, where the rotational transition matrix element $|\mu_{kj}|^2$

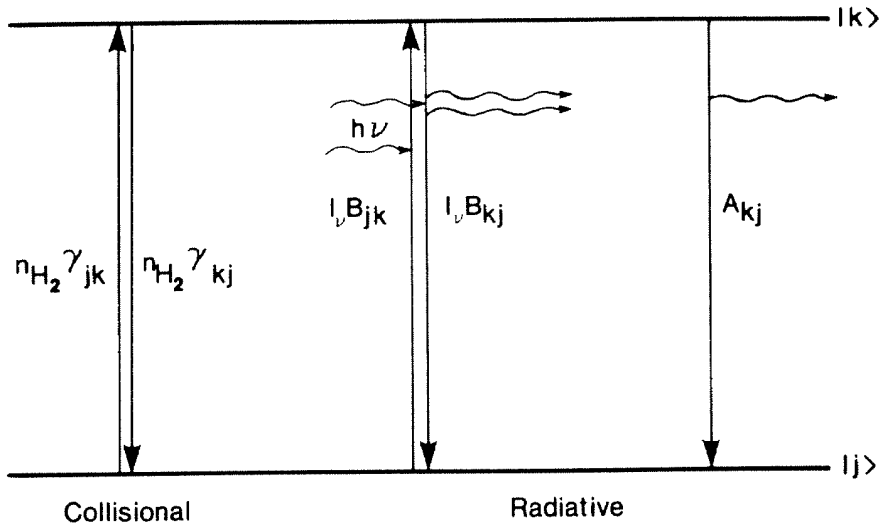

Figure 2.3: An illustration of the relative radiative and collisional rates for a two-level system.

is simply the permanent electric dipole moment, μ, times the reduced line strength, S/g_k.

The line width function $\Phi(\nu)$ is composed of several parts which may be divided into homogeneous and inhomogeneous broadening processes. Homogeneous processes are those for which every molecule in a system may absorb or emit photons across the entire line profile, and occur because the upper state lifetime is finite. Example of processes which create homogeneous broadening are the natural radiative lifetime (related to A_{kj}), collisional or pressure broadening, and saturation (optical depth) broadening. The low values of A_{kj} at millimeter wavelengths and the low n_{H_2} density in molecular clouds are such that the natural line width and collision broadened line widths are less than 100 Hz, while saturation broadening is important only for those species whose abundances are very high (see below). Inhomogeneous broadening occurs when, because of their environments, the molecules may absorb or emit photons at slightly different frequencies, of which the most familiar example is Doppler broadening. The low kinetic temperatures prevailing in the interstellar medium insure that the random, or microturbulent, broadening is only about

100-500 kHz for most species in the near millimeter-wave region. This microturbulent, or thermal, broadening defines the lower limit for interstellar spectral line widths. More often, however, it is found that molecular clouds have associated with them large-scale motions of the gas, either as rotation, collapse, or expansion. The velocity of such motion is typically 1-10 km s^{-1}, which at millimeter and submillimeter wavelengths corresponds to at least a few MHz. Since all other processes have line widths of $\Delta\nu \lesssim$ 100-500 kHz, it is this systematic large-scale motion of molecular clouds which dominates line profiles in the interstellar medium.

As is often the case, a simple change of variable recasts eq. (2.1) into the more easily integrable form

$$dI_\nu / d\tau_\nu = S_\nu - I_\nu \tag{2.4}$$

in which $\tau_\nu = \int_0^l \kappa_\nu \, ds$ is the total transition optical depth, l is the cloud thickness, and $S_\nu = j_\nu / \kappa_\nu$ is the so-called source function. From eqs. (2.2) and (2.3) we see that S_ν may also be written as

$$S_\nu = \frac{2h\nu^3}{c^2} \left(\frac{n_j g_k}{n_k g_j} - 1 \right)^{-1} . \tag{2.5}$$

A more transparent form of the source function is obtained if we define an excitation temperature T_{ex} that determines the relative level populations in terms of the Boltzmann relation

$$\frac{n_k}{n_j} = \frac{g_k}{g_j} e^{-h\nu / kT_{ex}} .$$

thereby reducing S_ν to the Planck function $B_\nu(T_{ex})$:

$$S_\nu = B_\nu(T_{ex}) = \frac{2h\nu^3}{c^2} \left(e^{h\nu / kT_{ex}} - 1 \right)^{-1} . \tag{2.6}$$

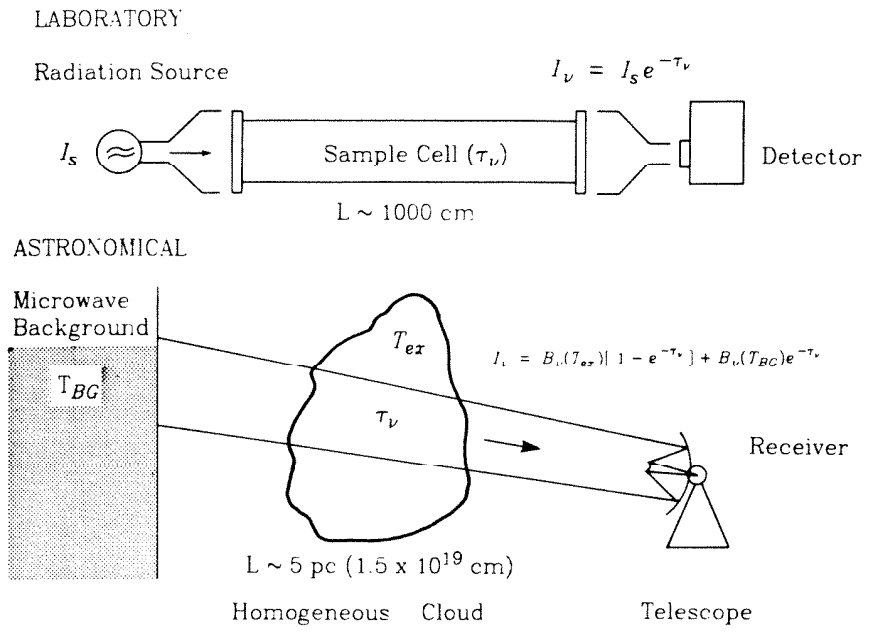

Figure 2.4: A comparison between interstellar clouds and laboratory absorption cells, and the basic integration geometry of eq. (2.10). In each case, the minimum detectable column density is on the order of 10^{11} cm^{-2}. After Winnewisser, Churchwell, and Walmsley (1979).

For a line of sight through a homogeneous cloud uniformly filling the telescope beam the integration of eq. (2.4) yields

$$I_\nu = \int_0^{\tau_\nu} S_\nu e^{(t_\nu - \tau_\nu)} dt_\nu + I_{cont} e^{-\tau_\nu} , \qquad (2.7)$$

where I_{cont} represents the contribution of any background continuum sources to the measured intensity. Figure 2.4 presents the the basic integration geometry for both the laboratory and astronomical environments and shows that, except for the huge difference in scale, the situations are remarkably similar. The high spectral brightness of tunable monochromatic sources available in the laboratory insures that the second term in eq. (2.7) dominates high resolution rotational spectroscopy; while at millimeter wavelengths in the interstellar medium only the 2.7 K cosmic microwave background, which we denote by $B_\nu(T_{BG})$, has

appreciable magnitude, except for the somewhat special geometry in which a cold cloud lies along the line of sight toward a warmer background cloud.

If the excitation temperature is constant throughout the cloud then eq. (2.7) becomes

$$I_\nu = B_\nu(T_{ex})[1 - e^{-\tau_\nu}] + B_\nu(T_{BG})e^{-\tau_\nu} \quad . \tag{2.8}$$

It is sometimes difficult in practice to measure the true continuum level accurately using spectroscopic systems, but the excess, or line, intensity $\Delta I = I_\nu - I_{BG}$ given by

$$\Delta I = [B_\nu(T_{ex}) - B_\nu(T_{BG})][1 - e^{-\tau_\nu}] \tag{2.9}$$

is rather more easily measured and still contains all of the relevant spectral line information. As we shall see, temperature is often a more convenient measure of the line strength than intensity, and it is now customary to define a line "brightness" temperature T_b via the Rayleigh-Jeans formula $T_b = c^2\Delta I/2k\nu^2$ to rewrite eq. (2.9) as

$$T_b = \frac{h\nu}{k}[1 - e^{-\tau_\nu}]\left[\frac{1}{e^{h\nu/kT_{ex}} - 1} - \frac{1}{e^{h\nu/kT_{BG}} - 1}\right] \quad . \tag{2.10}$$

the basic radio frequency radiative transport equation found in many textbooks. Thus, in addition to the brightness temperature, T_b, the optical depth, τ_ν, and the excitation temperature, T_{ex}, are also required to fully characterize interstellar spectral lines.

Several classes or types of lines exist, and are most easily delineated according to their optical depth, which from eqs. (2.3) and (2.4) is just

$$\tau_\nu = \frac{c^2 A_{kj} N_k}{8\pi\nu^2}[e^{h\nu/kT_{ex}} - 1]\Phi(\nu) \quad . \tag{2.11}$$

In the optically thin limit where $\tau << 1$ eqs. (2.10) and (2.11) show that the line brightness temperature is proportional to the column density of the upper (or lower) transition state and therefore gives useful column density estimates, while for the optically thick case ($\tau >> 1$) the line brightness saturates at $T_{ex} - T_{BG}$ when $T_{ex}, T_{BG} >> h\nu/k$. In each limit the line will appear either in absorption or emission depending on whether T_{ex} is less than or greater than T_{BG}. For the rather unusual case where the level populations are inverted, both τ_ν and T_{ex} are less than zero and an interstellar maser results.

In steady state the level populations do not change with time and the number of transitions into and out of each state must balance, or for our two-level case

$$n_j(n_{H_2}\gamma_{jk} + B_{jk}I_\nu) = n_k(n_{H_2}\gamma_{kj} + B_{kj}I_\nu) + A_{kj} \quad , \tag{2.12}$$

where I_ν is the radiation intensity present within the cloud. Of course, many levels exist in real life and for a given level j eq. (2.12) must be modified to include the sum over all levels k with which it is connected, or

$$n_j[\sum_k(n_{H_2}\gamma_{jk} + B_{jk}I_\nu) + \sum_{k<j}A_{jk}] = \sum_k n_k(n_{H_2}\gamma_{kj} + B_{kj}I_\nu) + \sum_{k>j}A_{kj} \tag{2.13}$$

subject to the restriction $n_{total} = \sum n_j$. In general, the equations relating the level populations and line intensities are coupled, and therefore require a detailed knowledge of both the radiative and collisional excitation rates. For optically thin lines the radiative and collisional problems are separable, but for the fully generalized case simplifying approximations are required to reduce eqs. (2.4) and (2.13) to a more tractable form. The simple two-level problem can be solved in closed form, however, and illustrates many of the salient features of more complicated numerical calculations.

By combining the solutions to eq. (2.4) and (2.12) we find that in the optically thin limit the excitation, kinetic, and background temperatures T_{ex}, T_{kin}, and T_{BG} are related to each other and to the collisional and radiative rates A_{kj} and γ_{kj} by

$$e^{-h\nu/kT_{ex}} = e^{h\nu/kT_{BG}} \frac{1 + (n_{H_2}\gamma_{kj}/A_{kj})e^{-h\nu/kT_{kin}}[e^{-h\nu/kT_{BG}} - 1]}{1 + (n_{H_2}\gamma_{kj}/A_{kj})[1 - e^{-h\nu/kT_{BG}}]} \quad . \qquad (2.14)$$

Thus, T_{ex} and thereby the line brightness temperature T_b is seen to depend critically on the ratio of the collisional and radiative rates $A_{kj}/n_{H_2}\gamma_{kj}$. As this ratio runs from values much greater than one to much less than one, T_{ex} varies smoothly between T_{BG} and T_{kin}, but is never less than T_{BG} or negative. This is perhaps more easily seen if we allow $T_{BG} \to 0$ (or for $T_{ex} >> T_{BG}$), in which case eq. (2.14) simplifies to

$$T_{ex} = \frac{T_{kin}}{1 + (kT_{kin}/h\nu)\ln[1 + (A_{kj}/n_{H_2}\gamma_{kj})]} \quad . \qquad (2.15)$$

Interstellar absorption lines and masers must therefore be treated in a more general fashion. Eq. (2.15) is valid at millimeter wavelengths, however, since the 2.7 K background temperature is always much less than the cloud kinetic temperature and the lines must appear in emission. Even so, the density must still exceed a critical value n_c such that the collisional and radiative rates are approximately equal, or, as eq. (2.10) shows, the upper level will be strongly underpopulated and the line will disappear, that is as $T_{ex} \to T_{BG}$, $T_b \to 0$. Thus, in addition to producing information about cloud abundances and temperatures, optically thin line strengths also serve as good indicators of variations in density. Lines with large spontaneous emission coefficients, that is, with large dipole moments or transition frequencies, generally require the highest cloud densities for excitation and trace out the cloud cores, while lower dipole

moment species may be used to examine the more extended and diffuse cloud regions. As the densities become high enough to equate T_{ex} and T_{kin} for all the energy levels, the population distribution approaches that expected for thermal equilibrium. We note that except for some special cases (masers, lasers, etc.), densities in the laboratory are always sufficient to produce thermalized energy distributions.

Much the same situation exists for optically thick lines, but a detailed examination of their physics in even our simplest case is greatly complicated by the fact that the line intensity by itself may contribute substantially to I_ν, which now depends on n_j. However, for clouds with large internal velocity gradients even the optically thick case becomes tractable if the escape probability formalism is employed (Sobolev 1963). A full description of this LVG approach is not warranted here, and we simply outline the results below. Basically, whereas in the optically thin case every upward collisional transition results in an emitted line photon that may leave the cloud unhindered, photons at optically thick frequencies are generally absorbed and reemitted many times before they actually leave the cloud. The absorption and reemission processes are formally treated by multiplying the Einstein A coefficients by the direct photon escape probabilities β, which causes the calculation to be geometry-dependent. One finds (Scoville and Solomon 1974; de Jong, Chu, and Dalgarno 1975) for most geometries that β is roughly proportional to $1/\tau$, and that for the limit where $T_{BG} \to 0$ the excitation temperature is given by

$$T_{ex} = \frac{T_{kin}}{1 + (kT_{kin}/h\nu)\ln[1 + (\beta A_{kj}/n_{H_2}\gamma_{kj})]} \qquad (2.16)$$

Once again, T_{ex} varies between 0 and T_{kin}, but the critical density is now reduced to $n_{cr} = \beta A_{kj}/n_{H_2}\gamma_{kj}$ by the "trapping" of photons within the cloud. The line brightness temperature of fully excited optically thick transitions therefore

directly measures the cloud kinetic temperature. Armed with this insight, astronomers are now able to probe cloud temperatures by using thermalized and optically thick transitions such as those of ^{12}CO, while density and abundance information are obtained from other less saturated species, including isotopic variants.

For clouds without large internal velocity gradients optically thick line profiles are sometimes inverted, or "self-absorbed," because molecules in the cooler cloud halo can absorb much of energy radiatively transported outward from the warmer cloud core, giving rise to a larger excitation temperature (and thereby line intensity) in the line wings. Extensive numerical calculations on such microturbulent line profiles have shown self-absorption to be an unavoidable consequence of high line optical depths in quiescent molecular clouds (Leung and Liszt 1976). Self-absorption is somewhat rare in "active" molecular clouds such as Orion, however, so much so that the simpler LVG approach is almost always used in the interpretation of optically thick molecular lines.

It can be difficult to estimate the line excitation and optical depth from the observation of a single line, but when many transitions of an individual molecule can be observed it is possible to estimate any deviations from thermal excitation along with the transition optical depths, particularly if the lines are not strongly saturated. For example, if we assume that the lines are optically thin and that the excitation temperature is such that $T_{ex} >> T_{BG}$ and $T_{ex} >> h\nu/k$, then the integration of eqs. (2.10) and (2.11) shows that

$$\frac{N_k}{g_k} = \frac{3kc\int T_b d\nu}{8\pi^3\mu^2\nu^2} \quad , \tag{2.17}$$

where N_k is the column density of the upper transition state. If we further assume that the population distribution is thermalized at a single rotational temperature T_{ROT}, then N_k/g_k may be replaced by

$$\frac{N_k}{g_k} = \frac{N_T}{Q(T_{ROT})} e^{-E_u/kT_{ROT}} ,$$

where N_T is the total molecular column density summed over all the levels, E_u is the energy of the upper transition state, and $Q(T_{ROT})$ is the rotational partition function at temperature T_{ROT}. The natural log of eq. (2.17) is therefore

$$ln\left(\frac{3kc\int T_b d\nu}{8\pi^3\mu^2\nu^2 S}\right) = ln\frac{N_T}{Q(T_{ROT})} - \frac{E_l}{kT_{ROT}} \qquad (2.18)$$

and a plot of the log of the integrated line strength versus energy should produce a straight line whose intercept is proportional to the log of the total molecular column density and whose slope gives T_{ROT}, provided the assumptions listed above are met. Such "rotation diagrams" have been utilized in a number of previous studies (Linke, Frerking, and Thaddeus 1978; Johansson *et al.* 1984), and will be extensively applied in Ch. 3 and Ch. 4. Figures 2.5a and 2.5b present the rotation diagrams for two of the molecules in the OVRO survey, dimethyl ether (CH_3OCH_3) and isocyanic acid (HNCO). The CH_3OCH_3 rotation diagram shows that the procedure can be quite accurate, and that in the best cases the errors may approach 15 - 20%. The HNCO rotation diagram indicates, however, that care must be taken and that considerable deviations from local thermodynamic equilibrium (LTE) may often occur. Most often these deviations arise from the large density and temperature gradients present in active molecular cloud cores, but subthermal excitation, opacity effects, radiative pumping, and other non-LTE mechanisms may also render this single temperature approach inadequate. A great advantage of the OVRO spectral line survey is that for most species a large number of rotational states have been observed and it is therefore possible to examine the relative excitation and abundance of these species in considerable detail. In addition to the above uncertainties, instrumental calibration problems can also be quite serious.

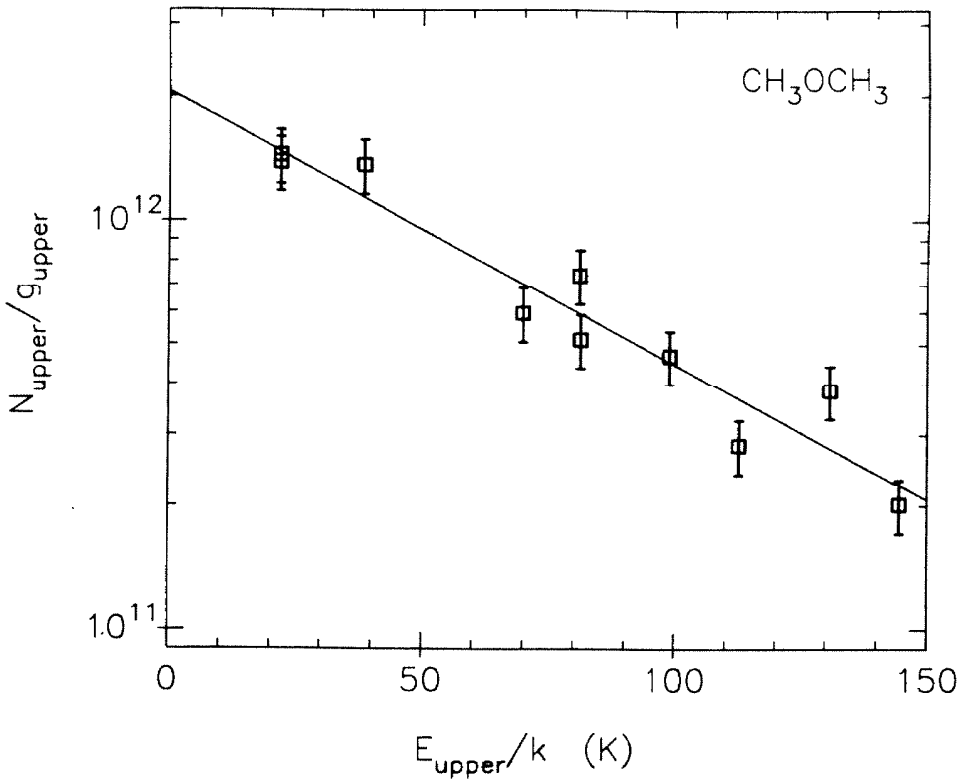

Figure 2.5a: The rotation diagram of CH_3OCH_3 *which illustrates the potential accuracy of the LTE approach.*

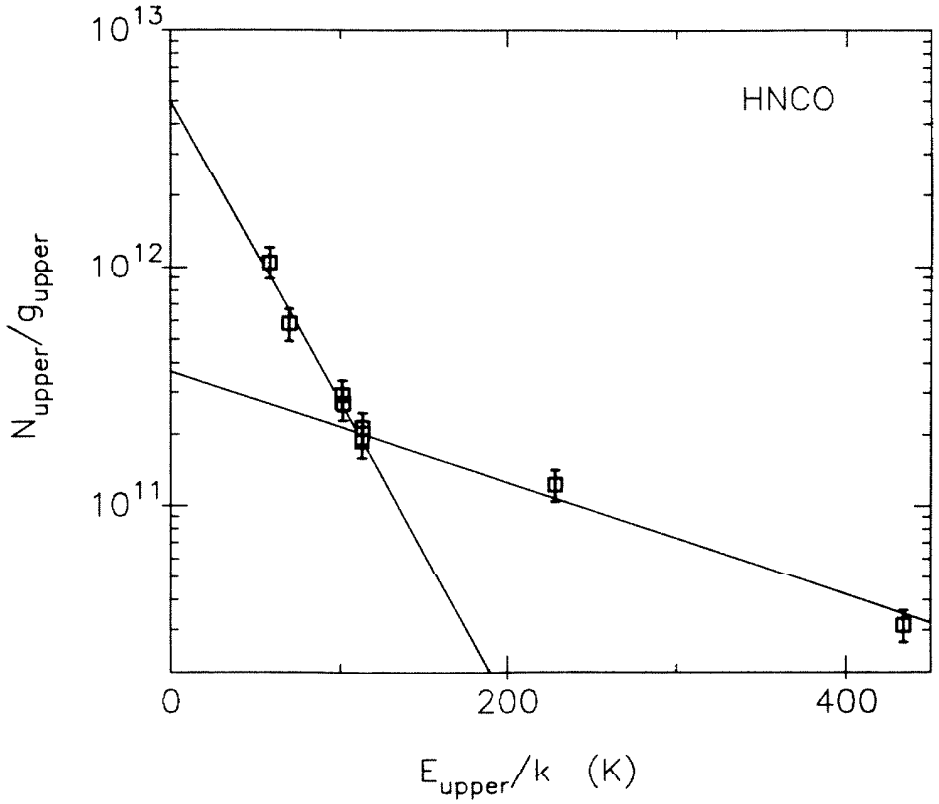

Figure 2.5b: The rotation diagram of HNCO. *The highest energy levels are populated via radiative pumping and are therefore not in thermal equilibrium with the lower energy states.*

2.4. Astronomical Instrumentation

A. Telescopes

The preceding discussion assumed that the observed cloud was homogeneous and that it filled the entire beam, which is fine for a telescope with infinite spatial resolution. However, sources often occupy a much smaller angular extent on the sky than the telescope beam. The width of the far-field antenna pattern of radio telescopes is limited by diffraction of the aperture field distribution, a result of the fact that the local oscillator radiation pattern and/or the detector beam pattern is given by a single spatial mode of an antenna, for which

the area A and main lobe solid angle Ω are related by $A\Omega \sim \lambda^2$. One generally finds that the far-field pattern of a radio telescope beam is approximately Gaussian with an angular full width half maximum of $\vartheta_B \sim 1.22\lambda/D$, where λ is the observing wavelength and D is the telescope diameter. Observations at millimeter and submillimeter wavelengths often have better spatial resolution than comparable single-dish observations at lower frequencies because it is not practical to build the very large telescopes needed at long wavelengths.

To calculate the power received by the telescope through a perfectly transparent atmosphere we must convolve the source brightness temperature distribution $T_b(\Psi)$ with the telescope beam pattern $P(\Psi)$, that is

$$P_A = \frac{k\int\int_{4\pi} T_b(\Omega)P(\Psi - \Omega)d\Psi}{\int\int_{4\pi} P(\Omega)d\Omega} \quad . \tag{2.19}$$

If we define an equivalent antenna temperature T_A by $T_A = P_A/k$ and assume that T_b is constant over the beam, then $T_A = T_b$ as expected. Suppose, however, that the source is characterized by a circularly symmetric disk of diameter ϑ_S and constant temperature T_b such that $\vartheta_S < \vartheta_B$. The integration in eq. (2.19) then yields

$$T_A = (\frac{\vartheta_S}{\vartheta_B})^2 T_b \quad ,$$

and we see that the measured antenna temperature underestimates the true brightness temperature, an effect known as "beam dilution." Thus, any estimate of the actual source brightness temperature from T_A necessarily involves some assumptions about the source structure and size. In addition, as Figure 1.2 shows, the atmospheric attenuation can be appreciable at millimeter wavelengths and the antenna temperature must be scaled by $e^{-\tau_a A}$, where τ_a is the atmospheric opacity and A is the observing airmass. Furthermore, since the

density required for excitation of the various interstellar molecular lines differ greatly, their source sizes may not be the same even within a given chemically homogeneous cloud.

In addition to the source size problems described above, the actual calibration of the temperature scale introduces a measure of uncertainty as well. Usually, loads or absorbers of known and differing temperatures are placed into the telescope beam and observed along with empty regions of the sky to correct for the detector sensitivity and atmospheric opacity. Observations of extended and compact astronomical objects whose temperatures and sizes are known, such as the Moon and the planets, then serve to establish the beam pattern along with the overall system sensitivity on the sky. Since large amounts of power in the antenna pattern may be present in sidelobes far removed from the main lobe, even observations of very extended sources like the Moon must be corrected slightly. Data reduction procedures differ greatly, but more often than not "beam averaged" values of the corrected antenna temperature T_A^* are reported in which the source is assumed to be extended, but which have been corrected for all other telescope and atmospheric losses. For compact sources, the estimated values of T_A^* will obviously depend strongly on the size of the telescope used, and it is essential to correct for these differences when using data from different observatories to construct abundance and temperature estimates. No uniform calibration procedure has been established, however, so such corrections are often difficult or impossible to apply, and in any case the raw calibration of radio astronomical data is probably not accurate to better than $\pm$ 15% at best.

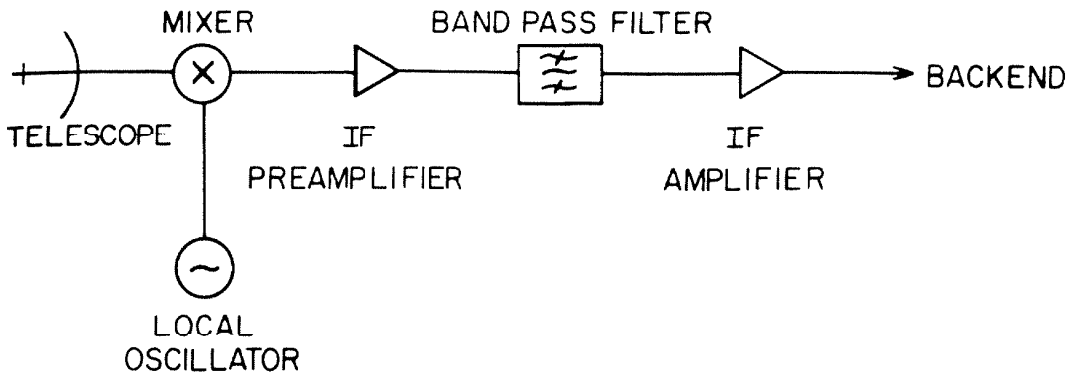

Figure 2.6: Typical components of an astronomical heterodyne receiver/spectrometer.

B. Near Millimeter Wave Astronomical Receivers

Unlike laboratory studies, in astronomy neither the radiation source nor the emitting or absorbing material is under the observer's control. Incoherent direct detection of near millimeter-wave radiation from the interstellar medium is possible, but suffers from low sensitivity and poor spectral resolution. High sensitivity and microwave resolution ($1{:}10^6$) may be obtained, however, by using coherent (heterodyne) techniques. Figure 2.6 shows the block diagram of a "typical" heterodyne receiver, first conceived by E.F. Armstrong. The most important component of a heterodyne receiver, and the one which ultimately determines the receiver performance, is the mixer. Mixers have the property that their output signal (say current) contains a term which is proportional to the input power because of non-linearities in their I-V characteristics. Thus, mixers may be considered to respond to the square of the electric fields present at the device. The key to the operation of heterodyne receivers is to inject monochromatic local oscillator radiation of frequency ω_{LO} onto the mixer in addition to the signal radiation from the telescope. In general, the local oscillator is offset slightly from the desired line frequency, the difference ω_{sky} - ω_{LO}

being known as the "intermediate frequency," or IF. The output of the mixer is therefore

$$I_{out} = a[\, E_{sky}\cos\omega_{sky}t + E_{LO}\cos\omega_{LO}t\,]^2 \quad , \tag{2.20a}$$

$$\text{or} \qquad I_{out} = \frac{a}{2}[\, E_{sky}^2 + E_{LO}^2\,] + \frac{a}{2}[\, E_{sky}^2\cos 2\omega_{sky}t + E_{LO}^2\cos 2\omega_{LO}t\,] \tag{2.20b}$$

$$+ aE_{sky}E_{LO}[\, \cos(\omega_{sky} - \omega_{LO})t + \cos(\omega_{sky} + \omega_{LO})t\,]$$

using standard trigonometric identities. In practice, the DC terms are shunted to ground, while the 2ω and $\omega_{sky} + \omega_{LO}$ terms are rejected either by filtering through the IF amplifiers or because the mixer itself does not respond to these frequencies.

The ac coupled output is therefore $I_{out} \propto E_{sky}\cos(\omega_{sky} - \omega_{LO})t = E_{sky}\cos\omega_{IF}t$, so the mixer acts as a down converter. After amplification, the IF signal is passed to some sort of "back end" spectrometer where it is detected in a set of channels of the required resolution and finally displayed. Since the frequency of the incoming signal radiation cannot be swept, for a given LO frequency the range detected by the receiver is equal to the bandwidth $\Delta\nu$ of the mixer/back end system. Because frequencies in the IF band may be generated by either $\omega_{sky} - \omega_{LO}$ or $\omega_{LO} - \omega_{sky}$, two sidebands of sky frequency $\omega_{sky} = \omega_{LO} \pm \omega_{IF}$ can be detected by heterodyne receivers. Double sideband (DSB) operation occurs when both signal sidebands are converted by the mixer; whereas if a Fabry-Perot cavity or diplexer is used to reject one of the sidebands (e.g. Erickson 1977), or if the mixer itself has a very narrow bandwidth, then the receiver is said to be operating in a single sideband (SSB) mode.

Astronomical receiver performance, like line intensity, is expressed in degrees Kelvin. In this case, the receiver noise temperature is related to the total receiver noise power P_r by Nyquist's theorem, which states that $P_r = kT_r\Delta\nu$.

Let T_N be the noise temperature of the total receiver/telescope system, and let T_A^* be the equivalent Rayleigh-Jeans temperature of a signal from the telescope. The signal-to-noise achievable in a time Δt and bandwidth $\Delta\nu$ is then

$$S/N = \frac{T_A^*}{T_N}\sqrt{\Delta\nu\Delta t} \quad , \tag{2.21}$$

which is known as the Dicke radiometer equation. This equation may be modified by factors of two depending on the subtraction techniques used, but the basic form remains the same. Thus, receiver research centers on the development of mixers that combine low noise performance with large instantaneous bandwidth. However, quantum mechanics sets a lower limit of $h\nu/k$ (SSB) for T_r. This limit, arising from the uncertainty principle, applies to receivers measuring both the phase and amplitude of the photon field. Mixer noise temperatures in the near millimeter-wave region are currently at least one order of magnitude above the quantum limit. The three most widely used mixers in this region are Schottky diodes, InSb hot-electron bolometers, and SIS (superconductor-insulator-superconductor) tunnel junctions. The latter two mixers have been used extensively at Caltech. For a full discussion of the physics of these mixers, the interested reader is referred to the recent review by Phillips and Woody (1982).

The Submillimeter InSb Receiver

When mounted in a waveguide such that its dimensions are small compared to the wavelengths involved, InSb acts as a very sensitive mixer for frequencies up to at least 600 GHz via the hot-electron bolometer effect. This effect arises at cryogenic ($\lesssim 4°K$) temperatures in highly purified InSb because there are still free conduction electrons available whose interactions with the lattice are weak. Current flows in the bulk material significantly increase the electron gas temperature T_e, thereby changing the mobility ($\alpha\ T_e^{3/2}$) and resistance of the

InSb chip - hence the name hot-electron bolometer. The major advantages of this mixer are its simplicity, modest local oscillator requirements (a few μW), and low noise temperature (about 150°K at 115 GHz to ~350°K at 600 GHz). The small instantaneous bandwidth of 1-2 MHz in InSb means the local oscillator must be swept to record spectra, and is the major disadvantage of this mixer. Broad band devices with noise temperatures in the 1000-2000 degree range are therefore competitive with InSb in certain applications. For observations which do not require large bandwidth, however, InSb currently provides the best performance for studies above 300 GHz. Moreover, recent experiments in this laboratory by E. Brown (1985) on cyclotron resonance or Putley mode detectors have shown that the application of modest magnetic fields can enhance the InSb receiver performance by factors of 2-4 at frequencies above 500 GHz, through cyclotron resonance absorption by the free electrons. The large direct responsivity and speed of InSb make it particularly suitable for laboratory absorption experiments in the near millimeter-wave region. Small bandwidths pose no problem here because the radiation source must be swept regardless of the detector, and because phase sensitive detection is almost always used.

The InSb receiver used for the detection of H_2D^+, NH_3, and HCl at 372.4, 572.5, and 625.9 GHz is the same one used by Phillips and collaborators (Phillips and Huggins 1981; Phillips and Keene, 1982) in extensive studies of the neutral atomic carbon emission near 492 GHz. Local oscillator power was provided by a Schottky diode harmonic generator driven by a millimeter-wave klystron. Lower klystron harmonics were rejected by coaxial waveguide filters placed at the end of the multiplier's output waveguide. Receiver temperatures were measured using 290°K and 78°K loads, and ranged from 200° to 600°K during the observations, which were performed from the Kuiper Airborne Observatory on a number of flight series between November 1982 and November 1984 due to the high atmospheric opacity encountered by ground-based observatories at these

wavelengths. IF filtering produced a single-channel instrument of 1.0 MHz resolution, with spectra taken by stepping the local oscillator frequency under computer control, typically in 1 km/s^{-1} intervals. Planets were rarely available to check beam patterns and pointing during the observations, so continuum emission from the Moon served as the primary calibration source. Corrections for atmospheric opacity were not required. The measured beam efficiency varied between 40-50%, while the efficiency for more compact sources is estimated to be about 30%. The diffraction-limited beam pattern of the 0.91m telescope had a FWHM of approximately 2' at 600 GHz. Spectra were taken using symmetrical position switching about the source, and have had low order baselines removed when necessary.

The OVRO 1.3mm SIS Receiver

SIS junctions, unlike InSb bolometers, are "quantum mixers" in that the individual photon energy $h\nu$ can have significant effects on mixer properties. Mixing in SIS junctions relies on the sharp non-linearity of the quasi-particle tunneling current between two superconductors separated by a thin insulating oxide barrier (Phillips and Woody 1982). Recently developed SIS mixers have large usable instantaneous bandwidths (>500 MHz), have very low local oscillator requirements (10^{-8} W at 115 GHz), are low noise devices (from 70°K SSB at 115 GHz to 800°K SSB at 500 GHz, Wengler *et al.* 1985), and, unlike classical mixers, can exhibit conversion gain. These devices may provide the best opportunity for quantum noise-limited performance in the millimeter and submillimeter regions. The higher frequency performance of SIS receivers is likely to degrade above $4\Delta/h$ (2Δ = the superconducting energy gap), which occurs near 1500-2000 GHz for some superconducting alloys (Wengler *et al.* 1985), but this effect has yet to be investigated thoroughly. The low local oscillator power requirements insure that multiplied klystrons or Gunn oscillators will suffice up to at least 500-700 GHz.

The Orion spectral line survey was performed with the #1 10.4m telescope of the OVRO millimeter-wave interferometer and an SIS receiver constructed and described in detail by Sutton (1983). The junctions, consisting of a thermally recyclable Pb alloy (In and Au are the minor constituents), were fabricated by R.E. Miller of AT&T Bell Laboratories, Murray Hill. Receiver temperatures varied from 300° to 700°K SSB throughout the spectral scan. A 512 MHz AOS similar to that described by Masson (1982) was used as the back end spectrometer. Pointing errors and beam patterns were determined by observations of circumstellar CO emission or continuum emission from Saturn, and gave a telescope beam FWHM of 0.5'. Zenith opacities ranged from τ_a = 0.2 - 0.6 on usable nights. Symmetrical position switching by 30' in azimuth was used to record the spectra, which were divided by calibrated scans of hot vs. sky loads to correct for telescope losses and atmospheric attenuation. A fuller description of the data reduction procedures and the Orion spectrum is presented in Appendix A.

2.5. Laboratory Instrumentation

A. The Near Millimeter Wave Laboratory Spectrometer

As noted in Section 2.3, near millimeter-wave laboratory spectroscopy is almost always carried out in absorption because both the sample and the radiation source are under the experimenter's control. Although designed to achieve the same goals, most millimeter and submillimeter-wave spectrometers are "home built" and often differ substantially in configuration. Nonetheless, all frequency-agile microwave absorption spectrometers contain three basic elements; namely, a highly monochromatic, tunable source of radiation, an absorption cell in which the species of interest is contained or produced, and a detector which monitors microwave power level after the radiation has passed

through the cell. Electric and magnetic resonance techniques, such as electron spin resonance or laser magnetic resonance, utilize a fixed frequency source and tune the energy levels by applying variable fields onto the sample, but are less accurate than swept frequency methods and can only be applied to species whose transition frequencies tune rapidly with field strength. A block diagram of spectrometer at Duke University used in the absorption experiments on HOC^+, CN, HCO, $^{13}CH_3OH$, and $HCOOCH_3$ is shown in Figure 2.7. The Jet Propulsion Laboratory (JPL) spectrometer used in the absorption experiments on OH, NH_3, HDO, SO_2, and CH_3OH is similar in general design.

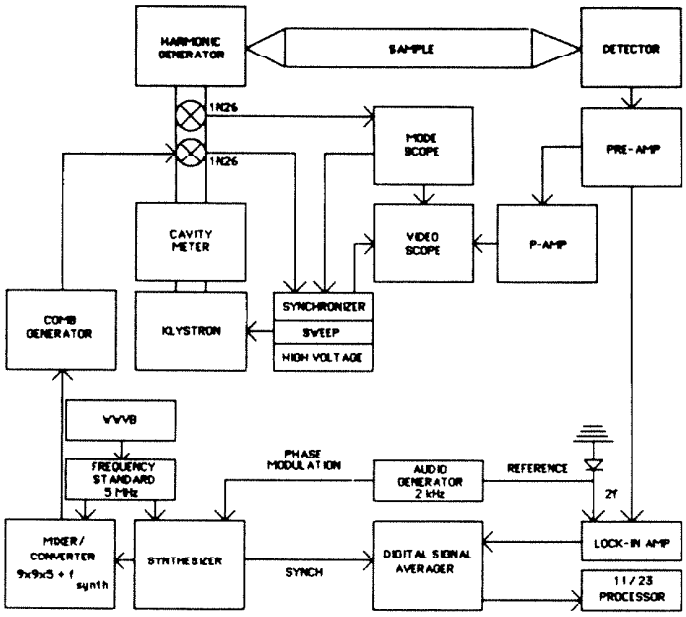

Figure 2.7: The Duke University Near Millimeter Wave Absorption Spectrometer.

Near millimeter-wave radiation between 100 and 500 GHz used in these experiments was produced by the harmonic generation of reflex klystrons operating in the 50 GHz range at Duke, while klystrons in the 70-120 GHz region were used at JPL. In both cases, the klystrons were phase-locked to tunable lower frequency sources that were referenced against a highly stable ($1:10^9$) 5 or 10 MHz oscillator to insure accurate frequency measurements. An ion

implanted Si point contact diode mounted in a crossed rectangular waveguide structure served as the the multiplying device at Duke (King and Gordy 1954), the point contact being made by a sharpened 2 mil tungsten wire mounted on a 30 mil diameter post. The JPL multipliers were similar in construction, but utilized GaAs Schottky barrier diodes as the non-linear element. To optimize harmonic production efficiency the diodes could be biased to the most non-linear portion of their I-V curves. The output power of these devices drops rapidly with frequency, and experiments above 500 - 600 GHz often suffered from a lack of sensitivity. In fact, the submillimeter and FIR region of the spectrum is quite notorious for its lack of tunable, monochromatic sources so abundant at both higher and lower frequencies, having long been referred to as the "gap in the electromagnetic spectrum." After considerable work, a new laser sideband source has been developed at JPL which promises to revolutionize spectroscopy at submillimeter and FIR wavelengths. The new source produces several μW of tunable radiation at frequencies between 300-3000 GHz, more than enough to drive sensitive astronomical receivers and to perform high resolution laboratory experiments in this relatively unexplored spectral region. A more detailed description of the JPL laser sideband source and its initial applications is presented in Appendix B.

Since the output multiplier waveguides had cutoffs near 75 and 145 GHz, only second and higher harmonics left the housing. Several step-down waveguide filters and dichroic plates could be placed between the multiplier and the absorption cell to eliminate unwanted lower frequency harmonics. In both cases, optically focused millimeter or submillimeter radiation traversed the free space absorption cell and was then detected by an InSb detector operated at 1.6°K. At 300 GHz the noise equivalent power of each InSb detector was ~1 x 10^{-12} W/$\sqrt{\text{Hz}}$, while the intrinsic detector voltage responsivities were about 5000 V/W. The output of the InSb detectors were fed into wideband, low-noise

preamplifiers, the output of which then traveled to either a video or lock-in amplifier for signal detection.

B. Sample Cells and Modulation Techniques

The sample cells used to study the rotational spectra of stable molecules such as SO_2 or CH_3OH are often nothing more than a glass or metal pipe to which windows have been attached in order to evacuate the cell and to allow radiation to interact with the sample. In order to study the more reactive species so prevalent in the interstellar medium, considerably more complex sample cells must be constructed. An ideal microwave absorption cell would produce copious amounts of transient species, provide a means for molecular modulation of absorption signals, be noise-free, and perfectly transparent to radiation. With so many variables present, the design of a cell which will even yield marginally observable signals from transient species in the millimeter-wave region is a considerable task, some would say a black art. The difficulties encountered in generating radiation at higher frequencies and in accurately predicting transition frequencies to reduce frequency searches only exacerbate the problem further. The high signal-to-noise obtained in this work on the highly reactive HOC^+, CN, OH, and HCO molecules indicates, however, that such problems are not insurmountable.

i. *HOC^+*

Figure 2.8 shows a diagram of the apparatus used for the study of several molecular ions, including HOC^+. A five-foot section of 1.5" ID commercial glass pipe is connected to concentric reducers that flare to 4". Inside each reducer cylindrical electrodes 3" in length are mounted in teflon rings which provide a vacuum seal against the glass. In order to maximize the transmission of microwave radiation through the cell, the ID of the electrodes is matched to

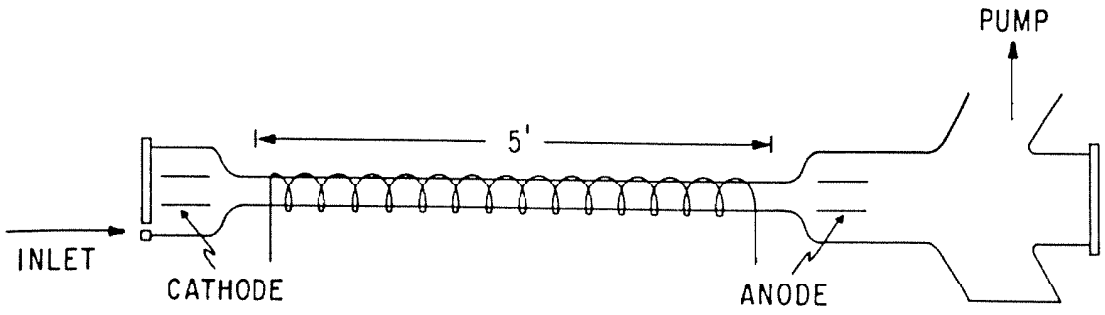

Figure 2.8: The anomalous glow discharge apparatus used for the production of molecular ions.

that of the glass. The back of the polished stainless steel cathode is blocked by a teflon slab, with gas entering the cell through a capillary "pigtail" inserted into the cathode. This arrangement limits the discharge to the inside surface of the cathode and is essential for optimum performance of the new cell, which increases ion abundances roughly two orders of magnitude in excess of previously reported methods. The operation of this novel glow discharge cell, about which a solenoid of #18 wire is wrapped to provide longitudinal magnetic fields of up to 300 Gauss, is described in detail in Appendix B. The solenoid and glass pipe may be immersed in liquid nitrogen to rotationally cool the ions.

HOC^+ was produced in a discharge operating in the anomalous glow mode at a total pressure of 10 mTorr. The potential drop across the tube was 5 kV, at a discharge current of 10 mA. As in the initial work on HOC^+ by Gudeman and Woods (1982), Ar was the chief constituent with H_2 and CO present only in trace amounts. The magnetic field enhancement allowed HOC^+ to be detected in single 100 second sweeps with a time constant of 1 sec. Evidence is presented in Appendix B that the longitudinal magnetic field increases ion abundances by restricting fast electrons accelerated across the large cathode drop of the discharge along the entire length of the small diameter glass pipe.

Source modulation proved to be the most convenient scheme for lock-in detection of HOC^+ since neither Stark nor Zeeman modulation techniques are possible with $^1\Sigma$ ions produced in discharges. A 2.6 kHz sinusoidal signal was introduced onto the slow sweep of the lock-in synchronizer, producing a small FM modulation of the klystron. Recovery of the signal is achieved by a lock-in amplifier tuned to 5.2 kHz in order to avoid pickup occurring at the modulation frequency, thereby producing a second derivative of the true line shape along with any variations in the baseline. A great deal of effort was therefore expended to eliminate any standing waves in the baseline by altering the position of various spectrometer elements, such as feedhorns and the detector.

ii. *CN, OH, and HCO*

Discharge-based methods have also been used to study the rotational spectra of the CN, OH, and HCO radicals. Although CN is a contaminant of almost any discharge containing carbon and nitrogen, its extreme reactivity precluded the laboratory observation of its pure rotational spectrum for many years. Dixon and Woods (1977) eventually detected the $N = 0 \rightarrow 1$ transition of CN in its $v = 0$ and $v = 1$ vibrational states in a glow discharge of cyanogen and nitrogen, but only after radio astronomical molecular line searches by Penzias, Wilson, and Jefferts (1974) first provided accurate frequencies of this transition. In the present study, CN was first observed in the plasma of an HCN laser by D.D. Skatrud (Skatrud *et al.* 1983). CN, which may be a chemical precursor of the lasing HCN, was observed under typical laser operating conditions: an equimolar mixture of N_2 and CH_4 at a total pressure of 60 mTorr and a discharge current of 200 mA.

Figure 2.9 presents schematics of the high sensitivity discharge absorption cells used for the spectroscopic studies of CN, OH, and HCO. For the CN and OH work, hollow stainless steel electrodes were placed at both ends of a five-foot

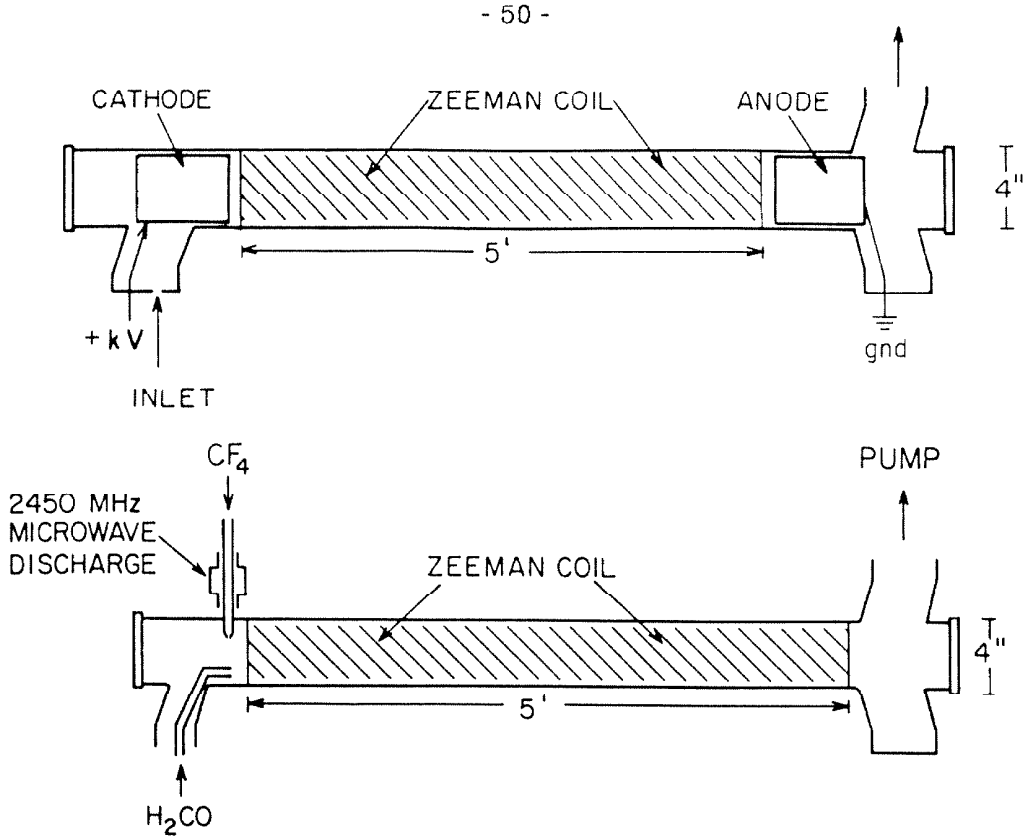

Figure 2.9: Diagrams of the glow and microwave discharge cells used to produce CN, OH, *and* HCO.

section of 4" diameter glass pipe about which a solenoid of #18 magnet wire was wound. The electrodes were thermally isolated from the glass by thin teflon rings. The strongest CN signals were obtained with an 8:1 mixture of N_2:CH_4 at a total pressure of 50 mTorr, and were followed up to the $\nu = 3$ vibrational state. A fast-flow environment was maintained by a 4" diffusion pump, which was nearly fully throttled at maximum signal strength. The potential drop across the tube was 850 V, with a maximum current of 185 mA limited by the power supply. For convenience, all measurements were taken at room temperature. Similarly, OH was produced by a DC discharge through pure water vapor at total pressures of 80 - 100 mTorr and currents in the 50 - 100 mA range.

A low pressure discharge of H_2 and CO failed to produce observable signals from HCO. Therefore, as in previous ESR studies the formyl radical was produced by the reaction of atomic fluorine, formed in a microwave discharge from

CF_4, with formaldehyde (Bowater, Brown, and Carrington 1972). Gas phase formaldehyde was obtained by heating solid paraformaldehyde to 90°C. The same solenoid section and pumping tee used in the CN work were retained for convenience, with the electrodes removed. An Evenson microwave discharge cavity powered by a 100 watt microwave diathermy unit mounted on a small arm at the head of the cell adjacent to the solenoid generated the atomic fluorine, while formaldehyde entered the cell through a thin glass pipe whose tip was placed just at the end of the microwave discharge tube to insure efficient mixing. Produced under a wide range of conditions, maximum HCO absorption signals were obtained with an equimolar mixture of H_2CO and CF_4 at a total pressure of 30 mTorr. Unlike CN, maximum HCO production occurred with the diffusion pump fully open.

The unpaired electrons in $X^2\Sigma$ CN and X^2A' HCO allowed Zeeman modulation to be used, which eliminated most of the annoying baseline problems associated with source modulation. Sinusoidal Zeeman field modulation at 2.6 kHz was applied along the entire length of the cells, with lock-in detection at 5.2 kHz. Sweeps of 10 sec duration were collected with a lock-in time constant of 0.1 sec, and were recorded by a digital signal averager. To check for possible frequency shifts induced by the Zeeman modulation, several lines were remeasured with source modulation and no statistically significant shifts were detected. Baseline problems were not encountered even for arbitrarily long integrations principally because of the much reduced magnetic field modulation of the index of refraction of a plasma at submillimeter wavelengths. Strong lines were recorded in one minute, while partially forbidden CN $\nu = 3$ lines required 40 to 60 minutes of integration to achieve adequate signal-to-noise. Figures 2.10a and 2.10b show typical data.

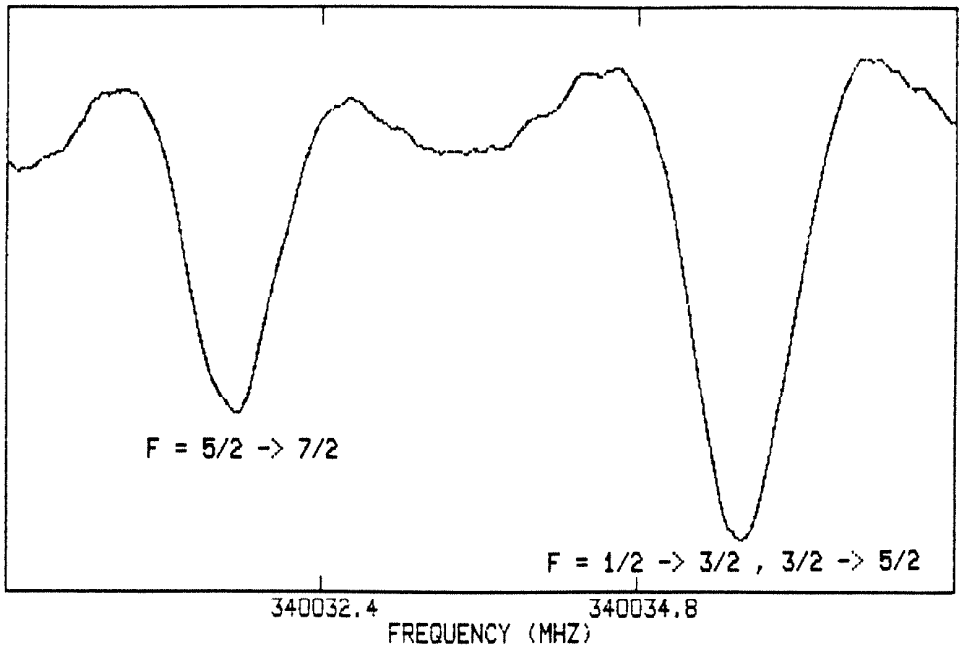

Figure 2.10a: Hyperfine components of the $N = 2 \rightarrow 3$, $J = 3/2 \rightarrow 5/2$ transition of CN *in its ground vibrational state.*

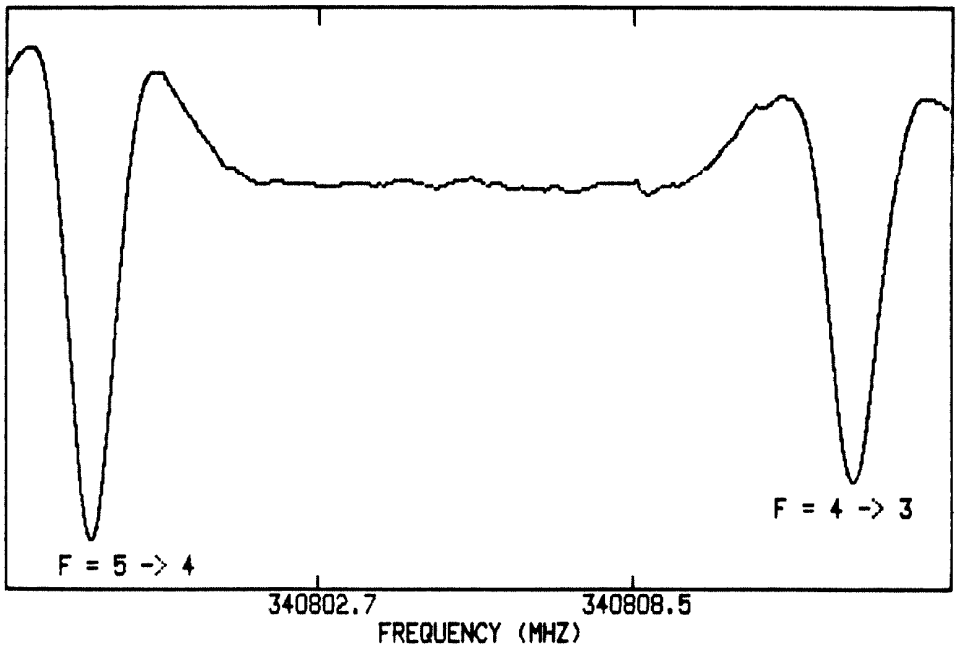

Figure 2.10b: The $J = 7/2 \rightarrow 9/2$ component of the $N = 3_{13} \rightarrow 4_{14}$ a-type rotational transition of ground state HCO.

The Millimeter Observing Song

Drunk last night,
Drunk the night before,
Gonna get drunk tonight like we never got drunk before,
Cause when we're drunk, we're productive as can be,
We're the millimeter observers, as you see,
And the millimeter runs are the best observing runs,
At Palomar or Kitt Peak they act like monks and nuns.
So pour for us, pour for us,
Our quantity of data is glorious,
When the high dish comes, there'll be even more for us,
While we sunbathe on the beach at Waikiki.

- Lyrics by Erich N. Grossman.

3. RESULTS

As noted in Chapter 1, the main body of work in this thesis is concerned with a systematic spectral line survey of the Orion molecular cloud in the 1.3 mm region. The complicated nature of this source is such that a brief description of its physical structure is warranted before beginning any detailed discussion of the spectral line survey.

3.1. An Overview of the Structure of OMC-1

Visible manifestations of the interstellar gas in the vicinity of OMC-1 may be seen with the naked eye, and this region has therefore been studied in one way or another since the dawn of man. Detailed astronomical observations of the great nebula in Orion began in 1610 when Fabri de Peiresc examined it with an early version of the telescope. The young O and B stars of the Trapezium cluster, which excite the well-known HII region M42 visible in optical photographs of the Orion region, are indicative of a recent epoch of massive star formation. When viewed at infrared (IR) and millimeter wavelengths, a large complex of molecular clouds responsible for the numerous young stars in Orion and Monoceros is seen to extend over a region of nearly 30 square degrees (Kutner *et al.* 1977). The Orion-Monoceros complex lies only 500 pc from the Sun (Genzel *et al.* 1981), and because of its proximity has now become the prototypical region of massive star formation. The complex has been observed at nearly every conceivable wavelength from meter radio waves to gamma rays, and the results of these studies are so extensive that books and symposia have been devoted to Orion (e.g. Glassgold, Huggins, and Shucking 1982).

The brightest infrared region of the molecular cloud complex, detected in 1967 by Kleinmann and Low (1967), lies approximately 1' NW of the Trapezium cluster and contains extremely young and massive embedded stars which are

not yet visible due to the cocoons of gas and dust which surround them. It is with this region, Orion-KL or OMC-1, that we shall be concerned. The brightest source at 2 μm is the Becklin-Neugebauer object (BN), also discovered in in 1967 (Becklin and Neugebauer 1967), but observations at other IR wavelengths reveal the presence of the numerous sources shown in Figure 3.1a. Studies of the color temperatures and dust opacities of these sources (Wynn-Williams *et al.* 1984), and of the 3.8 μm polarization vectors (Werner, Dinerstein, and Capps 1983), have shown that only BN, IRc 2, and IRc 9 are self-luminous. Of these, IRc 2 is intrinsically the brightest, providing most of the luminosity ($L = 10^5\ L_\odot$) in this region. The stellar luminosities must be inferred from far-infrared continuum measurements because dust surrounding the embedded stars absorbs and is heated by the visible and UV stellar flux, which is then re-radiated at longer wavelengths. BN appears brighter at 2 μm only because IRc 2 is buried behind a large column of obscuring material along our line of sight. The remaining infrared sources appear to be manifestations of the complex spatial structure of the surrounding molecular cloud. Other indications of the pivotal nature of IRc 2 to the structure of OMC-1 are provided by the many molecular line observations of this source.

In addition to the relatively cool and quiescent gas of the Orion-Monoceros complex visible in observations of OMC-1 as a strip or "ridge" of material running SW to NE, there are also other more turbulent components of the gas which have been associated with outflow from IRc 2. First discovered in Orion as high-velocity wings on H_2S and CO lines ($\Delta v_{CO} \gtrsim 100$ km s^{-1}; Wilson, Jefferts, and Penzias 1970; Thaddeus *et al.* 1972; Zuckerman, Kuiper, and Rodriguez-Kuiper 1976), such molecular outflows now appear to be a common evolutionary phase of young stars, but little is known about the engine that drives the mass loss. The ridge or "spike" clouds are perhaps most easily visible in the H_2CO $J_{K_pK_o} = 2_{12} \rightarrow 2_{11}$ transition shown in Figure 3.1c (Bastien *et al.* 1981), and lie on either

Figure 3.1: (Opposite, adapted from Watson 1982) Infrared and radio emission line maps of OMC-1. (a) Map of the 20 μm continuum emission from warm dust, 2" resolution (Downes et al. 1981). (b) H_2O maser distribution (Genzel et al. 1981). (c) The two quiescent "ridge" clouds as represented by the H_2CO $J_{K_pK_o}=2_{12}\rightarrow 2_{11}$ transition at 14.5 GHz (Bastien et al. 1981). (d) Owens Valley interferometer map (7" resolution) of the 2.6 mm continuum emission from the hot core (Masson et al. 1985). (e) Hat Creek interferometer map (6" resolution) of the SO $J_K=2_2\rightarrow 1_1$ line at 86 GHz arising from the low-velocity (LV) 18 km s^{-1} outflow (Plambeck et al. 1982). (f) Hat Creek interferometer map (2" resolution) of the SiO J=2→1 outflow (87 GHz), illustrating the bipolar nature of the red-shifted (broken contours) and blue-shifted (solid contours) high-velocity (HV) plateau source (Wright et al. 1983). (g) H_2 2 μm shock-excited emission (Beckwith et al. 1978). (h) Artist's conception of the low- and high-velocity outflow and the region of shocked material (adapted from Plambeck et al. 1982).

---

side of the infrared sources. The sharp velocity gradient across the ridge has been interpreted as rotation of the overall cloud structure about Orion-KL with a period of approximately 5 x 10^5 years (Lizst *et al.* 1974, Kutner *et al.* 1977). Intense H_2O maser emission, located on the inner periphery of the quiescent clouds, has been detected (Figure 3.1b). Measurements of the proper motions of the H_2O masers with the VLA (Genzel *et al.* 1981) demonstrate unambiguously that the turbulent gas in Orion-KL is indeed contained in an outflow, and that this outflow or "plateau" source is highly anisotropic in nature. In addition to the high-velocity plateau emission seen in CO, H_2O, and a number of other species, there also appears to be a lower velocity (18 km s^{-1}) outflow. The low-velocity emission is centered on IRc 2, as both the low-velocity H_2O maser centroids and the Hat Creek interferometric SO map in Figure 3.1e show (Plambeck *et al.* 1982). The high-velocity ($|\Delta v| \gtrsim 30$ km s^{-1}) plateau is bipolar, oriented roughly orthogonal to the low-velocity SO "disk," and centered somewhat north

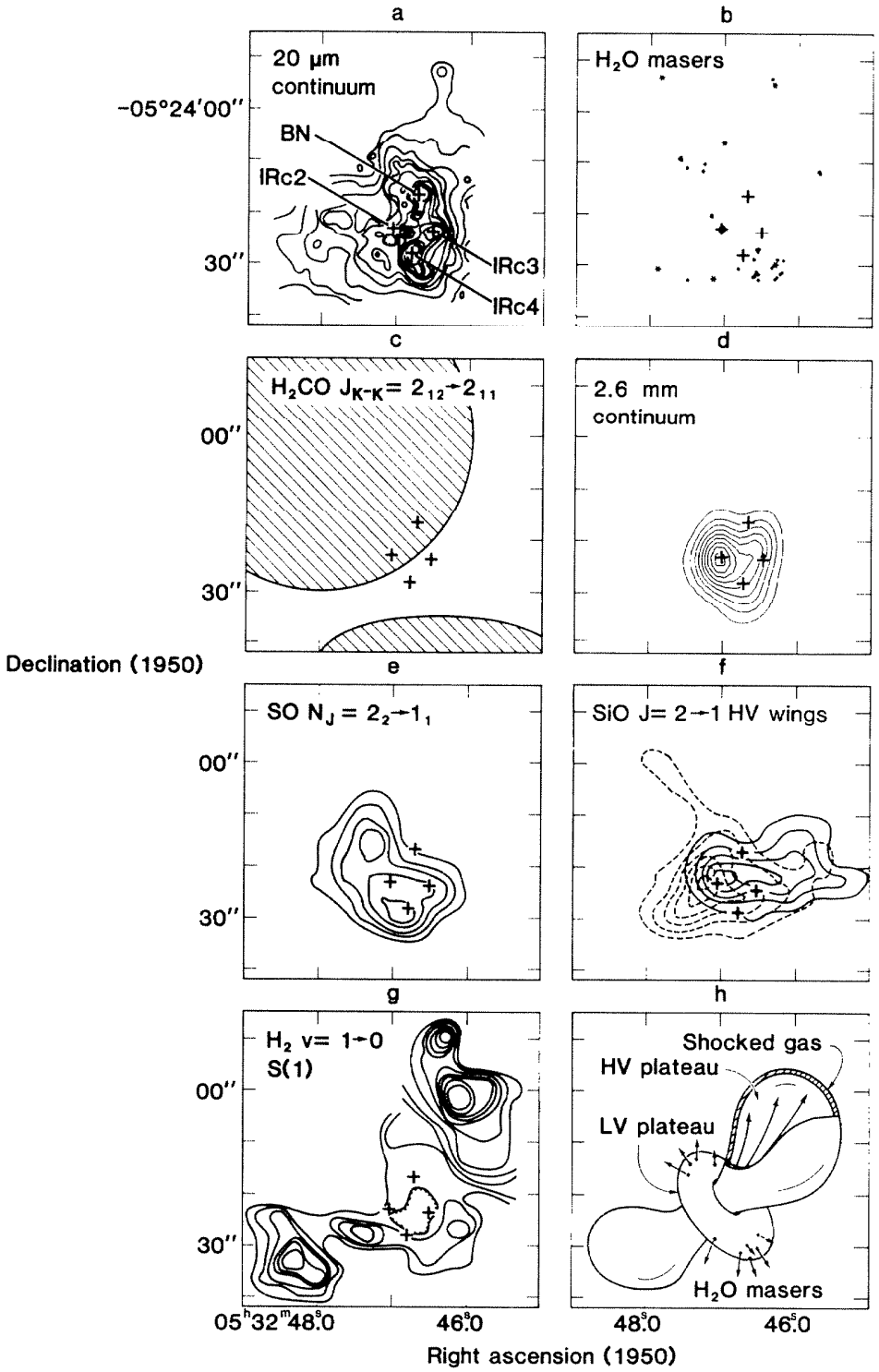

Figure 3.1: The structure of OMC-1

of IRc 2, as is illustrated by the SiO emission mapped in Figure 3.1f (Wright *et al.* 1983). Immediately outside this SiO bipolar outflow is an extensive region of very hot (T~2000 K) shock-excited H_2 vibrational emission that is adjacent to a somewhat cooler (T~750 K) region of material first detected via high-J (up to J=34 → 33) CO emission (Gautier *et al.* 1976, Watson *et al.* 1980). Finally, lying along our line of sight toward IRc 2 are clumps of very dense, warm material known as the "hot core," first detected in the inversion lines of NH_3 (Morris, Palmer, and Zuckerman 1980; Genzel *et al.* 1982) and recently mapped via its 2.6 mm continuum emission presented in Figure 3.1d by Masson *et al.* (1985).

Most of the models constructed to explain the the wide variety of emission features in Orion have centered on mass outflow from IRc 2 which accelerates and alters the composition of the surrounding gas. Anisotropies in the density structure of the originally collapsing gas which produced IRc 2 are thought to be responsible for the observed anisotropy of the outflow. The higher density in the NE-SW direction outlined by the H_2CO emission slows down the flow in this direction and creates the low-velocity plateau source, while the lower density and/or faster density gradient orthogonal to this axis has allowed the flow to expand more rapidly. The low-velocity H_2O masers arise where the outflow strikes the ambient molecular cloud material. Similarly, vibrationally excited H_2 emission and the high-J CO features occur where the high-velocity wind has driven shocks into the quiescent cloud. H_2 probes a thin shell of the hottest material within the shock while the CO emission emanates from the cooler post-shock regions. The hot core is identified as a large remnant of material left over from the collapse of IRc 2 which, because of it density and mass, has not yet been dispersed by the outflow. Figure 3.1h presents a schematic illustration of this outflow model. A more complete description of the Orion-KL sources and the restrictions implied from the line survey results on the physical models of Orion are discussed below.

3.2. Statistics of the Spectral Line Survey

The compressed view of the OVRO 1.3mm spectral line survey shown in Figure 1.4 and repeated here for convenience (Figure 3.2) illustrates the large amount of data obtained on the spectrum of Orion-KL. As this figure shows, emission between 208 and 263 GHz has been studied at a resolution of 1 MHz. The spectrum between 208 and 215 GHz is not so well calibrated as the other regions, and only the interval from 215 to 263 GHz has actually been used in the abundance determinations that follow. In addition to the 1.3mm work, submillimeter transitions of CI, HCl, H_2D^+, and NH_3 have been observed to assess the relative importance of light molecular hydride emission in the interstellar medium. We include the atomic CI species because of its extreme usefulness in examining the chemical and physical processes operating in molecular clouds. A total of 33 species and 16 isotopic variants, including the parent isotopic species and ranging in complexity from atomic CI to the nine-atom species CH_3OCH_3 and C_2H_5CN, have been detected and are presented in Table 3.1. Some are quite familiar and stable, but others, like CN, CCH, and HCO^+ are very reactive and most difficult to study in the laboratory. Also summarized in Table 3.1 are other parameters of the line search such as frequency coverage and sensitivity. The complete spectrum and a description of the individual emission lines may be found in Appendix A.

The average noise level in the OVRO scan is approximately 0.2 - 0.3 K per resolution element which, as Figure 3.2 indicates, places the spectral line survey near the confusion limit. Some 787 resolvable emission features have been detected in the 215-263 GHz interval, while the total line search plus the submillimeter studies contain over 825 lines. In comparison, the lower frequency surveys of Johansson *et al.* (1984) performed at the Onsala Space Observatory and that of Cummins, Linke, and Thaddeus (1985) at Bell Laboratories report the

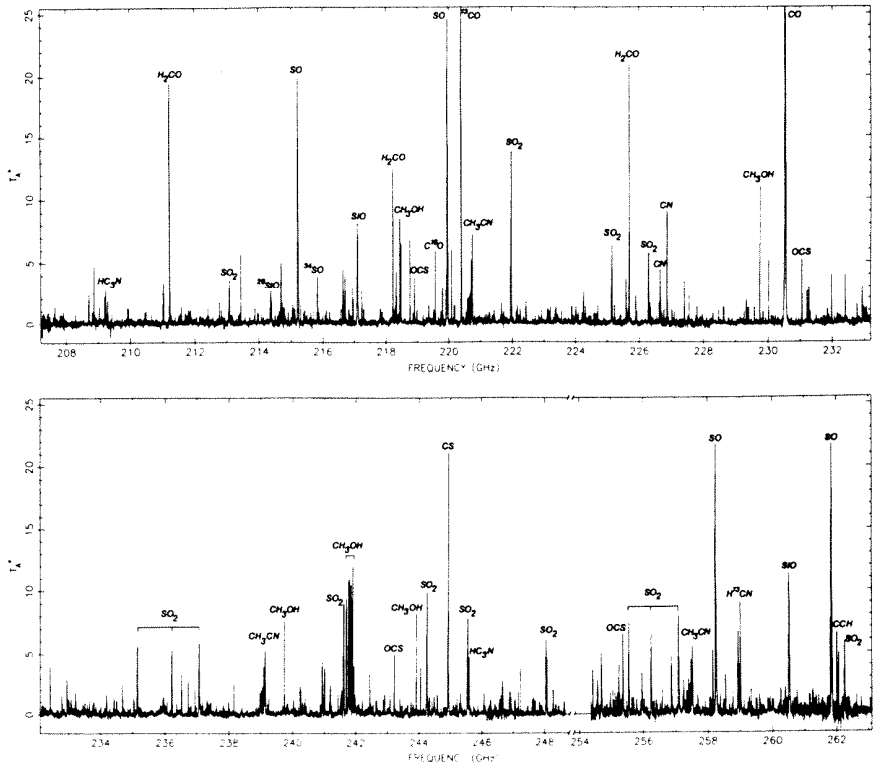

Figure 3.2: The compressed 1.3mm OVRO spectral line survey of OMC-1.

Table 3.1
Detected Species and Line Survey Parameters

Cl	C_2H	HDO	H_2CCO
CO	C_3H_2	H_2S	CH_3OH
CN	HCN	NH_3	CH_3CN
NO	HNC	HNCO	CH_3CCH
CS	H_2D^+	H_2CO	C_2H_3CN
SiO	HCO^+	H_2CS	C_2H_5CN
SO	HCS^+	HC_3N	$HCOOCH_3$
HCl	SO_2	HCOOH	CH_3OCH_3
	OCS		

Source: OMC-1
Sensitivity: $\lesssim$0.2-0.3 K
Lines Identified: $\gtrsim$825
Isotopes Detected:

Coverage: 208 - 263 GHz
Resolution: 1 MHz
Unidentified Lines: 33
H,D
^{12}C,^{13}C
^{14}N,^{15}N
^{16}O,^{17}O,^{18}O
^{28}Si,^{29}Si,^{30}Si
^{32}S,^{33}S,^{34}S
^{35}Cl

detection of 170 and 45 lines from Orion and IRc+10216 between 73 and 91 GHz, and 457 lines from Sgr B2 in the 70 to 145 GHz range, respectively. The Onsala survey of Orion was conducted with a similar beam size as the OVRO survey, but the line density is roughly a factor of two lower. The increased density and strength of the rotational line emission in the OVRO survey as compared with the lower frequency work is due primarily to the higher strengths and excitation requirements of rotational transitions at near millimeter wavelengths and the small telescope beam size with which the OVRO survey was conducted, making it particularly sensitive to emission from the active core of Orion-KL. By combining an extensive set of laboratory measurements with existing spectral line catalogues, over 95% of the emission lines have been identified and assigned to known interstellar species. Indeed, only 33 unidentified lines remain in the entire data set. With the exception of C_3H_2 (Thaddeus 1985) and possibly PN, no "new" molecules have been identified in the 1.3mm spectrum, but the submillimeter work on HCl and H_2D^+ represents the first detection of these species in the interstellar medium. The H_2D^+ ion was detected only in NGC 2264, but because of its crucial role in interstellar chemistry and the the similarity of NGC 2264 to the extended Orion molecular cloud it will also be discussed here. Upper limits for a number of other species, including several molecules like CO^+ and CH_3NH_2 that were previously claimed to have been identified in OMC-1, are presented as well.

Of the over 800 resolvable lines, roughly 40% have detectable emission from the hot core, 20% from the plateau, and another 40% from the ridge gas. Although their absolute numbers are small, the strong and large line width emission lines from the plateau source are responsible for most of the integrated molecular flux from Orion-KL, with over 70% of the measured flux concentrated in CO, CS, SO, and SO_2. Further, nearly three-quarters of the detected emission features may be assigned to the six terrestrially stable SO_2, CH_3CN, CH_3OH,

$HCOOCH_3$, CH_3OCH_3, and C_2H_5CN rotors. Thus, a small number of species dominate the millimeter wavelength spectrum of Orion.

The interpretation of the laboratory spectra taken as part of the investigation of the millimeter and submillimeter emission from OMC-1, while informative and interesting in its own right - particularly for those species that are charged or which possess intrinsic electronic angular momentum - does not bear directly on the main topic of this thesis. A detailed presentation of the laboratory spectra and spectral constants is therefore deferred to Appendix B. The importance of the laboratory work to the quality of the line search data is difficult to overemphasize, however, for without it hundreds of lines from *known* interstellar species would have remained unidentified.

3.3 Physical Properties of the Orion-KL Kinematic Components

As Figure 3.1 shows, the various subsources in OMC-1 are observed simultaneously by the 30" beam of the OVRO survey. Thus, in the absence of mapping information each of the emission components must be identified by its line profile alone. A convincing demonstration of the potential line confusion in the Orion-KL region and of the various spectral line signatures which delineate the kinematic components therein is provided by the emission from the J=5→4 a-type band of methanol near 242 GHz shown in Figure 3.3. Within this small spectral window the emission from six different molecules, HDO, SO_2, HNCO, CH_3OH, C_2H_5CN, and CH_3OCH_3, is visible and occupies the entire baseline. This spectrum is a good example of the significant contribution of molecular lines to broad-band emission studies of this region (cf. Sutton *et al.* 1984); before this work it was generally assumed that the broad-band millimeter-wave flux was produced entirely by continuous emission from dust (e.g., Elias *et al.* 1978). The narrow emission lines from CH_3OH and CH_3OCH_3 emanate from the quiescent ridge gas,

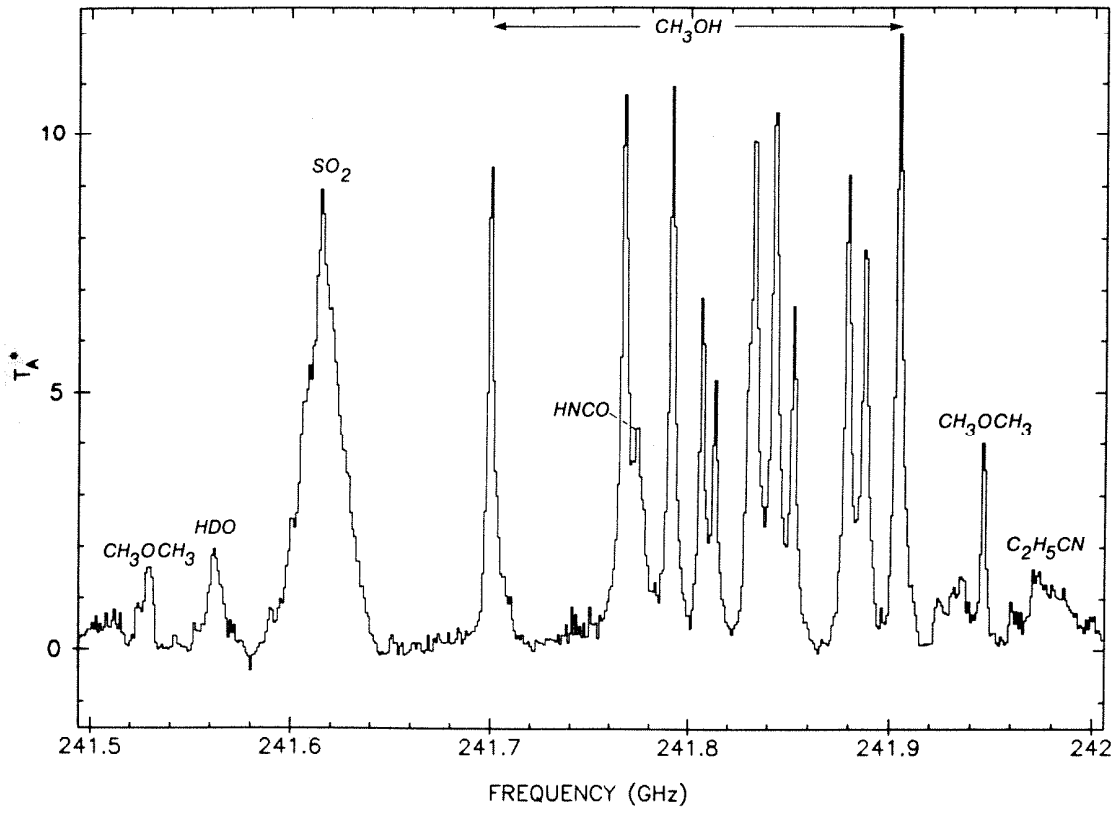

Figure 3.3: An illustration of the high line density and varying spectral signatures of Orion-KL.

while the broad SO_2 profile clearly demonstrates the turbulent and supersonic nature of the plateau, or outflow, source. Emission from HDO and C_2H_5CN arises mainly from the hot core, and shows that the line widths in this source are intermediate between those of the ridge and plateau components. Although not demonstrated by Figure 3.3, in addition to possessing different line widths each source in Orion also appears at a characteristic radial velocity, or v_{LSR}. By separating the various emission components seen in the OVRO survey and comparing them to previous single dish studies, especially that of Johansson *et al.* (1984), and with interferometric maps of several key species it has been possible to construct a detailed description of the physical conditions of the emission regions in Orion.

3.3a. Ridge Emission

Emission from the quiescent clouds near Orion-KL mapped in Figure 3.1c appears to be composed of both an extended and a more compact component, although the distinction between these regions is often ill defined. The extended ridge emission is characterized by a velocity of v_{LSR}~9 km s^{-1} and line widths of Δv~3-4 km s^{-1} at the center of OMC-1, but elsewhere in OMC-1 the emission exhibits a shift from 8 km s^{-1} in the SW to 10 km s^{-1} in the NE. Extended ridge emission is seen here in Cl, CO, CN, CS, SO, HCl, C_2H, C_3H_2, HCO^+, HCS^+, H_2D^+(in NGC 2264), NH_3, HNC, HCN, HC_3N, and CH_3CCH, as summarized in Table 3.2. The rotational temperature of the moderate dipole moment CH_3CCH symmetric top, which should have a thermalized or nearly thermalized population distribution, is about T_{ROT}= 55 ± 9 K. Further supporting a thermal, or kinetic, interpretation of the CH_3CCH rotational temperature is the optically thick ^{12}CO (fitted) brightness temperature of 60 K. The kinetic temperature of the extended ridge clouds near OMC-1 would therefore appear to be approximately 55-60 K. A comparison of the OVRO emission strengths of high dipole moment species such as CS, HCO^+, or HCN with those of Johansson *et al.* (1984) demonstrates that the excitation temperatures for these molecules are substantially subthermal, however, on the order of 15-20 K. Examination of the critical densities required to reach thermal equilibrium for the numerous molecules detected suggests that the density must be about 10^5 cm^{-3}, or slightly less. Emission away from the center of Orion-KL is strongly subthermal relative to CO for all detected species, and the density here must be $\lesssim 10^4$ cm^{-3}. The strengths of the $C^{17}O$ and $C^{18}O$ J = 2 → 1 lines imply an H_2 column density of approximately 3 x 10^{23} cm^{-2}.

Spatially confined ridge emission is, for the most part, still rather narrow (Δv~3-5 km s^{-1}) but lies at slightly lower radial velocities of v_{LSR}~7-8 km s^{-1}. As its name implies, this source is fairly compact and it is also characterized by the

Table 3.2 Extended Ridge Emission	
$v_{LSR} \sim 9.0$ km s^{-1}	$\Delta v \sim 4.0$ km s^{-1}
$T_{ROT} \sim 55$ - 60 K	$n \sim 10^5$ cm^{-3}
ϑ_{source} = extended	$N_{H_2} \sim 3 \times 10^{23}$ cm^{-2}
Molecules Detected	
CI, CN, CO, CS, SO, C_2H, C_3H_2, CH_3CCH HCl, H_2D^+, HCO^+, HCS^+, NH_3, HCN, HNC, HC_3N	

high abundances of the complicated oxygen-rich molecules which are found there, namely HDO, OCS, H_2CO, HCOOH, CH_3OH, $HCOOCH_3$, CH_3OCH_3, and perhaps SO (see Table 3.3). The small nature of this source is illustrated by a comparison of the beam averaged OVRO T_A^* values for the J=5→4 band of CH_3OH with those of Boland *et al.* (1983) taken with the 3.8m UKIRT telescope: Boland *et al.* report a maximum brightness temperature of 4.0 K in the $J_K=5_{\pm4}\rightarrow4_{\pm4}$ components for which we report an antenna temperature of 11.8 K, implying a source size of $\lesssim$30". A source of this size is also inferred from interferometric studies of the 25 GHz CH_3OH masers (Matsakis *et al.* 1980) and of the 6 cm H_2CO emission mapped at the VLA by Johnston *et al.* (1983), which are also coincident with the HDO and CH_3OCH_3 emission mapped by Olofsson (1984). These maps show that the spatially compact ridge is located on the edge of the SW 8 km s^{-1} cloud in the vicinity of IRc 5.

The spatially confined ridge source also appears to be a good deal warmer than the spatially extended material. For example, rotation diagrams of H_2CS, H_2CCO, CH_3OH, and $HCOOCH_3$ among others yield values of T_{ROT} between 90 - 140 K. Since it is observed in so many states, emission from CH_3OH serves as the best cloud temperature "thermometer" and although its v_{LSR} is roughly constant there is also clear line width and temperature gradient as a function of

Table 3.3
Compact Ridge Emission

v_{LSR} ~ 7-8 km s^{-1}	Δv ~ 3-5 km s^{-1}
T_{ROT} ~80 - 140 K	$n \gtrsim 10^6$ cm^{-3}
$\vartheta_{source} \lesssim 30''$	

Molecules Detected

PN(?),HDO, OCS, H_2CO, H_2CS, HCOOH,CH_3CHO(?)
CH_3CN, H_2CCO, CH_3OH, $HCOOCH_3$, CH_3OCH_3

excitation energy. The lowest energy lines are characterized by line widths of 3.3 km s^{-1} and a rotational temperature of 120-140 K, while the highest energy lines, including those from the first torsionally excited state, have line widths of about 6.5-9.5 km s^{-1} and a rotational temperature in excess of 200 K. Spontaneous emission rates of the torsionally excited lines require central densities of $\gtrsim 10^7$ cm^{-3} for purely collisional population of the upper transition states. The geometrical location, radial velocity, temperature gradient, and chemical composition of the compact ridge source is suggestive of a linkage between it and the plateau source, in which outflow from IRc 2 interacts with the 8 km s^{-1} cloud thereby compressing, heating, and altering the chemical composition of the ambient molecular cloud material (cf. Section 3.3b, Johansson *et al.* 1984; Irvine and Hjalmarson 1984).

3.3b. Plateau Emission

Emission from the plateau source is detected here in CO, CS, SiO, SO, SO_2, OCS, H_2S, HDO, H_2CO, HCN, and HC_3N, as Table 3.4 shows. It is characterized by the v_{LSR} of 7-8 km s^{-1} also found for the compact ridge source but is spatially distinct and has substantially greater line widths of at least $|\Delta v| \gtrsim 20$-25 km s^{-1} for the high-velocity outflow, and $|\Delta v| \sim 18$ km s^{-1} for the lower-velocity material. Interferometer maps of SO, SiO, and CO show that the source size is less than

Table 3.4
Plateau Emission

v_{LSR} ~ 7-8 km s^{-1}	$\Delta v \gtrsim$ 20-25 km s^{-1}
T_{ROT} ~95 - 150 K	$n \gtrsim 10^6$ cm^{-3}
$\vartheta_{source} \lesssim 17''$	$N_{H_2} \lesssim 5 \times 10^{22}$ cm^{-2}

Molecules Detected

CO, CS, SiO, SO, SO_2
OCS, H_2S, HDO, H_2CO, HCN, HC_3N

$\vartheta_{plateau} \lesssim 17''$ for both components (Plambeck *et al.* 1982; Wright *et al.* 1983; Masson *et al.* 1984). The thermalized emission from high dipole moment species such as SO_2 implies that the densities in the plateau exceed 10^6 cm^{-3}, consistent with the estimated source mass of 10-20 $M_\odot$ and the source size noted above. Higher density clumps of material are also evident through the presence of very fragile molecular species such as H_2CO. A rotation diagram analysis of SO_2 produces an excitation temperature on the order of 95 K, but as with the compact ridge material a range of excitation is evident. For example, the highest excitation lines of SO_2 are best fit by a T_{ROT} of at least 150-175 K. From the derived column density of SO_2 and the intensity ratios of various SO_2 transitions to the J=2→1 line of ^{13}CO, the plateau is estimated to have an H_2 column density of $\lesssim 5 \times 10^{22}$ cm^{-2} for an assumed CO fractional abundance of $f(CO/H_2) \sim 1.2 \times 10^{-4}$. This value is in good agreement with the column density given by the 2.6mm dust continuum maps (Masson *et al.* 1985) but stands in sharp contrast to the value of $\sim 10^{24}$ inferred by Plambeck *et al.* (1982), and places important constraints on the nature of the outflow.

Whereas Plambeck *et al.* (1982) conclude that the low velocity plateau is composed of a rather massive, organized disk or "doughnut" of gas and dust which channels the higher velocity outflow, the low column density derived

above is more supportive of the "clumpy cavity" model by Wynn-Williams *et al.* (1984) in which outflowing winds from IRc 2 have only partially evacuated an irregular cavity which surrounds it. Easily destroyed molecules such as H_2CO are confined to small, dense clumps of matter embedded in the outflow, while species such as SO trace out a relatively thin shell of material on the outer boundaries of the cavity where the outflow is decelerated by the dense molecular cloud. The high velocity plateau is interpreted as expanding more forcefully along the most rapid density gradients within the cavity.

3.3c. Hot Core Emission

As noted in Section 3.1, the hot core is a particularly warm, compact, and dense region of material located immediately adjacent to IRc 2. In either a cavity or a disk model the hot core is simply a very large, dense clump (or an ensemble of smaller clumps) left over from the formation of IRc 2 that has not yet been significantly disrupted by the outflow. The v_{LSR} and Δv (FWHM) of the hot core are not so well defined as those of the plateau or ridge sources, but lie predominantly in the 3-5 and 10-15 km s^{-1} range, respectively.

Table 3.5
Hot Core Emission

$v_{LSR} \sim$ 3-5 km s^{-1}	$\Delta v \gtrsim$ 5-10 km s^{-1}
$T_{ROT} \sim$150-300 K	$n \gtrsim 10^8$ cm^{-3}
$\vartheta_{source} \lesssim$12"	$N_{H_2} \sim 1 \times 10^{24}$ cm^{-2}

Molecules Detected

CO, HDO, H_2CO, H_2S, HNCO
HCN, HC_3N, CH_3CN, C_2H_3CN, C_2H_5CN

Molecules detected in this predominantly nitrogen-rich source include CO, HDO, H_2CO, H_2S, HNCO, HCN, HC_3N, CH_3CN, C_2H_3CN, and C_2H_5CN (see Table 3.5). Because of its close proximity to IRc 2, a considerable range of excitation

temperatures are present in the hot core. Scoville and Kwan (1976) have shown that the temperature of the gas and dust surrounding an embedded stellar source should fall off roughly as $r^{1/2}$. Thus, the species requiring highest excitation should be closest to IRc 2 and indeed, the energetic high-J ground state and vibrationally excited lines of HC_3N and CH_3CN have excitation temperatures on the order of 285-350 K, have quite small source sizes ($\vartheta \lesssim$ 3-5''), and are centered on IRc 2. Lower rotational temperatures of ~110-200 K and more extended source sizes are derived from the ground state lines of NH_3, C_2H_3CN, and C_2H_5CN (Hermsen *et al.* 1985). The equalization of the ground and excited vibrational state excitation temperatures via purely collisional means would require densities in excess of 10^{10} cm^{-3}, but radiative pumping is likely to be important throughout this source and could produce excitation temperatures similar to those observed over a radius of some 5'' (Goldsmith *et al.* 1983). Correcting the measured ^{13}CO antenna temperature with the source size derived by Masson *et al.* (1984) from an interferometric study of CO results in an estimated hot core H_2 column density of $\sim 10^{24}$ cm^{-2}, in agreement with the recent continuum maps by Masson *et al.* (1985) shown in Figure 3.1d and the ammonia hot core emission mapped at the VLA (Genzel *et. al.* 1982).

3.4. Molecular Abundance Determinations

As the previous sections indicate, emission from the individual molecules in Orion is not restricted to a single region, but may arise from a complicated blend of several or all of the subsources. Figure 3.4 presents a good example of the often complex nature of the emission from Orion, the J=24 → 23 transition of HC_3N, in which all three of the distinct kinematic components are visible. Any estimates of the chemical composition of the differing regions must therefore attempt to deconvolve the overall emission into its constituent parts, and are subject to several sources of error which are summarized below (after Irvine *et*

al. 1985).

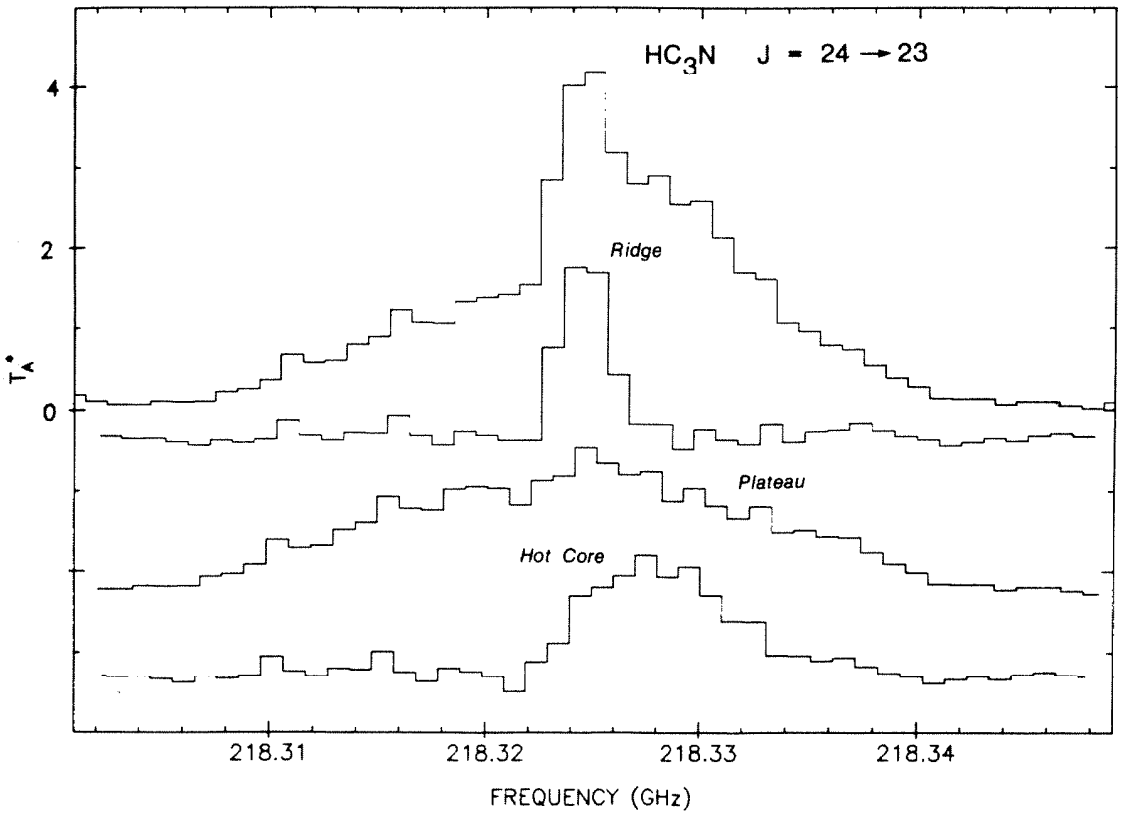

Figure 3.4: The HC_3N J=24→23 line and the different kinematic components which produce its complex line profile.

The initial errors encountered in any astronomical study are those discussed in the Instrumentation sections of Chapter 2, namely, the calibration of raw spectral data to produce the corrected antenna temperatures T_A^* and the conversion of these values into line brightness temperatures T_b via estimates of the source size. All values reported here are left as beam averaged quantities; no corrections have been made for emission thought to arise from compact sources. The brightness temperatures of lines from the hot core and plateau regions will therefore be systematically underestimated. When several emission features are present, non-linear least-squares fits of unconstrained Gaussian components to the emission profile such as those shown in Figure 3.3 have been used to separate their relative contributions. Molecules whose emission is

confined to one particular source such as CH_3CCH, SO_2, and C_2H_5CN were analyzed first to parameterize the emission from the various kinematic components and to construct the initial guesses used in the Gaussian fits. In addition, constrained fits, which fixed the velocities and line widths of the Gaussian components at values derived from the single component emission, were also performed on a number of test species, and no statistically significant differences were found between the excitation temperatures and column densities derived from the unconstrained and constrained fits. Although potentially biased by the initial guesses utilized, the resulting strengths and velocities were quite consistent and should be good to within the calibration errors quoted in Chapter 2.

Once the individual values of T_A^* have been established, it is then necessary to convert them into a single-state column density through the application of eqs. (2.10) and (2.11), which obviously requires information about the line optical depths and excitation temperatures. Further assumptions must next be made about the general population distribution if total column densities are to be obtained from the observations of a single transition. Wherever possible we have analyzed many transitions, whose optical depths were checked by observations of isotopically substituted species, simultaneously with the rotation diagram method outlined in Chapter 2 to bypass the use of single transitions in the determination of molecular column densities and to increase the statistical redundancy. Errors in the derived column density stem mainly from uncertainties in the estimated source sizes, which do not enter into the determination of excitation temperatures since they depend only on the *relative* transition strengths and because the spectral line survey has been uniformly calibrated. The formal errors associated with the LTE procedure were typically on the order of 20-30%, but as Figure 2.5b illustrated the population distributions of molecules in Orion can also be far from equilibrium. For the most part,

however, the large data base obtained has allowed us to insure that only the most accurately calibrated lines of known optical depth were used in the fitting procedures, the result of which is a highly consistent set of chemical and physical parameters for the Orion-KL region.

In some cases, only one or two lines were detectable (e.g., HCO^+, HCN, etc.) whose parent isotopic transitions were most likely optically thick. For such species, isotopically substituted lines whose optical depths are small, as judged by comparing their intensities with those of the lower J transitions detected at Onsala (Johansson *et al.* 1984), have been used in conjunction with the rotational temperatures derived from molecules found to have similar excitation requirements and velocity profiles to estimate the total column densities and to reduce the effects of clumping or other excitation gradients which may selectively excite various species relative to each other.

The large line widths associated with the plateau emission have allowed the results derived from the Gaussian fits noted above to be verified for this source using a different method, first applied by Kuiper, Zuckerman, and Rodriguez-Kuiper (1981). At velocities greater than about 20-25 km s^{-1} from the line center emission from the ridge and hot core components is negligible, and these velocities may safely be used to estimate molecular abundances in the plateau region. By dividing the lines of various species into the plateau emission from ^{13}CO the relative abundances of CO to the species under study were calculated assuming thermal population distributions characterized by the excitation temperature derived from an extensive LTE analysis of SO_2. ^{13}CO is utilized in place of ^{12}CO to insure that the CO emission is optically thin. The ^{13}CO abundance derived by Masson *et al.* (1984) is then used to construct column densities, which agree with those determined from the Gaussian fits to better than a factor of two. A comprehensive listing of of the calculated beam averaged column

densities, excitation temperatures, and velocity characteristics of the 32 species detected in this work are presented in Table 3.6.

Nearly all of the theoretical chemical models of interstellar molecular clouds calculate the absolute fractional abundance f(X) of a species X relative to the most abundant interstellar molecule, H_2, defined by $f(X) = N(X)/N(H_2)$; and for a direct comparison of the observational and theoretical results it is necessary to convert the column densities N(X) listed in Table 3.6 into absolute fractional abundances f(X), which requires a number of additional assumptions. First of all, for a meaningful comparison of the abundances of various species it must be assumed that they sample similar regions of space; that is, the source or subsources should be chemically and physically uniform. Fortunately, in Orion the major subsources are clearly recognizable through their distinct spectral signatures and spatial locations, but small-scale variations in their density and size can still induce considerable error. Secondly, the abundance relative to hydrogen of some trace molecule, usually CO, must be known accurately since H_2 is in general unobservable in molecular clouds. Any errors in the abundance of this "standard" will be systematically transferred to all other species. CO is typically chosen because it is the most ubiquitous and abundant trace molecule and because its abundance is not expected to vary strongly with density and temperature. The CO/H_2 abundance is not easily observable directly, but is usually inferred from observations of the CO and H_2 abundances as a function of the visual extinction by dust, A_v. Provided the gas-to-dust ratio and the extinction properties of dust are known, the CO/H_2 ratio may be estimated. This procedure assumes that CO is a valid tracer of H_2; any gradients in the CO/H_2 abundance ratio are ignored. The absolute fractional abundances of other trace species X are obtained from the ratio of the column densities of X

Table 3.6
Molecular Column Densities and Gaussian Decompositions
for the Emission from OMC-1

Species	T_{ROT} (K)	N (mol cm^{-2})	v_{LSR} (km s^{-1})	Δv (km s^{-1})	Notes
Extended Ridge: $N_{H_2} = 3 \times 10^{23}$ cm^{-2}					
CI	(20)	$\gtrsim 7.5\ 10^{17}$	9.5±1.0	5.0±0.0	a
CO	60	$1.5\ 10^{19}$	8.7±0.3	4.3±0.3	b
CN	(60)	$1.5\ 10^{16}$	8.8±0.4	4.4±1.0	c
NO	(60)	$\lesssim 1.5\ 10^{16}$	~9.0±0.0	~4.0±0.0	c
C_2H	(60)	$3\text{-}5.0\ 10^{15}$	8.8±0.8	~4.0±0.0	c
CH_3CCH	55±9	$1.1\ 10^{15}$	9.3±0.6	3.8±0.6	b
HCl	(60)	$\sim 3.0\ 10^{15}$	9.0±1.0	4.2±0.8	c
NH_3	(60)	$1.5\ 10^{17}$	9.0±1.0	7.0±1.0	c,d
CS	(20)	$7.5\ 10^{14}$	8.9±0.2	4.4±0.6	e
HCO^+	(20)	$1.5\ 10^{15}$	8.7±0.2	3.6±0.5	e
HCS^+	(60)	$1.6\ 10^{13}$	~9.0±0.0	~4.0±0.0	c
HCN	(20)	$1.5\ 10^{15}$	9.0±0.2	3.5±0.3	e,f
DCN	(20)	$1.6\ 10^{13}$	|	|	e,f
HNC	(20)	$1.6\ 10^{14}$	8.3±0.1	3.3±0.1	e,f
DNC	(20)	$2.3\ 10^{12}$	|	|	e,f
HC_3N	(20)	$1.2\ 10^{14}$	8.9+0.4	3.3+0.7	e
C_3H_2	(20)	$7.0\ 10^{12}$	~9.0±0.0	~7.0±0.0	g
HNCO	35±3	$\lesssim 1.0\ 10^{14}$	8.4±0.3	~4.3±0.4	h
HDCO	41±7	$1.2\ 10^{14}$	8.8±0.3	~4.0±0.0	b
SiO	(20)	$<1.0\ 10^{14}$	-	-	i
SO	(20)	$\lesssim 2.8\ 10^{14}$	8.4±0.8	3.4±0.6	e,i,j
SO_2	(60)	$<1.0\ 10^{15}$	7.7±0.8	4.2±0.9	c,i,j
HCO	(60)	$<1.0\ 10^{13}$	-	-	c
C_3N	(20)	$<5.0\ 10^{12}$	-	-	
C_4H	(20)	$<2.5\ 10^{12}$	-	-	
HC_5N	(20)	$\lesssim 7.0\ 10^{12}$	-	-	k
Compact Ridge:					
PN	(90)	$\lesssim 3.0\ 10^{12}$	8.0±0.0	3.8±0.0	c
PO	(90)	$<2.0\ 10^{14}$	-	-	c
OCS	(75)	$1.0\ 10^{15}$	7.8±0.5	3.7±0.3	l
HDO	(90)	$1.9\ 10^{14}$	7.0±0.8	2.0±0.7	c
CH_3CN	100±15	$2.0\ 10^{14}$	8.4±0.1	4.0±1.2	
CH_3OH	139±39	$1.4\ 10^{16}$	8.1±0.5	3.3±0.7	m
	230±84	$3.6\ 10^{16}$	7.2±1.0	9.6±3.0	l
H_2CO	100±17	$1.5\ 10^{16}$	8.6±0.2	3.8±0.2	
H_2CS	100±21	$7.3\ 10^{14}$	7.6±0.4	4.1±0.4	
H_2CCO	123±29	$5.2\ 10^{14}$	8.2±0.9	4.0±1.9	
CH_3OCH_3	73±8	$3.0\ 10^{15}$	7.9±0.6	3.6±1.2	
$HCOOCH_3$	89±13	$3.3\ 10^{15}$	7.9±0.6	3.9±1.1	
HCOOH	(90)	$1.0\ 10^{14}$	8.0±0.8	3.9±1.0	c
CH_3CHO	(90)	$\lesssim 5.0\ 10^{13}$	8.3±0.6	3.9±1.0	c
CH_3NH_2	(90)	$<3.0\ 10^{14}$	-	-	c,i
C_2H_5OH	(90)	$<1.5\ 10^{14}$	-	-	c,i
NH_2CHO	(90)	$<3.0\ 10^{13}$	-	-	c,i
NH_2CN	(90)	$<3.0\ 10^{13}$	-	-	c,i

Table 3.6 - continued

Species	T_{ROT} (K)	N (mol cm^{-2})	v_{LSR} (km s^{-1})	Δv (km s^{-1})	Notes
Plateau:	$N_{H_2} \lesssim 5 \times 10^{22}$ cm^{-2}				
CO	(100)	$6.0\ 10^{18}$	7.7±0.0	49.6±0.0	b
CS	(100)	$1.2\ 10^{15}$	7.1±0.3	23.2±6.5	c
OCS	(100)	$2.8\ 10^{15}$	5.3±0.1	19.0±3.7	c,n
SiO	(100)	$1.9\ 10^{15}$	7.0±1.3	34.0±1.1	c
SO	(100)	$2.8\ 10^{16}$	7.6±0.8	28.0±2.5	c
SO_2	97±9	$5.0\ 10^{16}$	7.7±1.0	25.2±2.1	b,o
HCN	(100)	$2.5\ 10^{16}$	8.6±1.4	27.0±1.7	c,f
HC_3N	(100)	$5.5\ 10^{14}$	7.7±1.3	28.5±6.6	c
H_2S	(100)	$5.0\ 10^{15}$	7.2±0.0	22.7±0.0	c
HDO	(100)	$9.0\ 10^{14}$	-	-	p
H_2CO	(100)	$1.6\ 10^{15}$	8.9±2.5	42.2±2.2	c
Hot Core:	$N_{H_2} \sim 1 \times 10^{24}$				
CO	(200)	$1.2\ 10^{20}$	-	-	b,q
SO	(150)	$\lesssim 1.3\ 10^{15}$	6.7±1.1	10.9±1.7	c,i
SO_2	(150)	$\lesssim 2.0\ 10^{15}$	2.6±1.4	6.9±4.4	c,i,j
HDO	(150)	$3.0\ 10^{15}$	5.7±0.6	9.1±2.3	c
H_2CO	(150)	$2.0\ 10^{15}$	6.9±0.7	12.7±1.4	c
HNCO	120±37	$5.0\ 10^{14}$	6.6±0.5	9.1±1.6	
HCN	(250)	$2.5\ 10^{16}$	5.8±0.2	12.6±0.7	f,r
DCN	(250)	$1.4\ 10^{14}$	6.0±0.1	11.7±0.2	r
HC_3N	300±75	$1.8\ 10^{14}$	3.8±1.8	10.0±2.9	
CH_3CN	285±55	$2.0\ 10^{15}$	5.0±1.7	10.3±3.0	
C_2H_3CN	160±35	$2.8\ 10^{14}$	5.0±1.4	8.6±3.4	
C_2H_5CN	150±25	$2.8\ 10^{15}$	5.0±1.2	11.4±3.6	

a- Taken from Phillips and Huggins (1981).
b- CO brightness temperatures and LTE diagrams give T_{KIN} of source.
c- T_{ROT} assumed equal to T_{KIN}.
d- From the values of $\tau_p(J_K=1_0 \rightarrow 0_0)$ estimated by Keene *et al.* (1982).
e- Subthermal T_{ROT} as judged by OVRO and Onsala data.
f- Δv and v_{LSR} from average of fits to isotopic lines.
g- Identified by Thaddeus (1985), large Δv from line blend.
h- From a Gaussian decomposition of the lowest K_p lines.
i- Upper limits only.
j- N estimated from a Gaussian decomposition of velocity line shape.
k- Limit from Johansson *et al.* (1984).
l- T_{ROT} from Goldsmith and Linke (1981).
m- Gaussian decomposition into a "cool" and "warm" compact ridge component.
n- v_{LSR} implies hot core also?
o- Gives T_{KIN} and n_{H_2} for plateau.
p- T_{ROT} assumed from Olofsson (1984).
q- From a Gaussian decomposition of ^{13}CO and Masson et al. (1984).
r- HCN temperature estimated from the HC_3N and CH_3CN fits.

Table 3.7
Molecular Fractional Abundances in the OMC-1 Subsources

Species	f(X) (N(X)/N(H_2))	Species	f(X) (N(X)/N(H_2))	Species	f(X) (N(X)/N(H_2))
Extended Ridge:					
CI	$\gtrsim 2.5\ 10^{-6}$	HCl	$\sim 1.0\ 10^{-8}$	NH_3	$5.0\ 10^{-7}$
NO	$\lesssim 5.0\ 10^{-8}$	HDCO	$4.0\ 10^{-10}$	SiO	$<3.3\ 10^{-10}$
CO	$5.0\ 10^{-5}$	HCO^+	$5.0\ 10^{-9}$	HCO	$<1.0\ 10^{-10}$
CS	$2.5\ 10^{-9}$	HCS^+	$5.3\ 10^{-11}$	SO	$\lesssim 9.3\ 10^{-9}$
CN	$5.0\ 10^{-8}$	HC_3N	$4.2\ 10^{-10}$	SO_2	$\lesssim 3.3\ 10^{-9}$
HNC	$5.3\ 10^{-10}$	DNC	$7.7\ 10^{-12}$	HNCO	$3.3\ 10^{-10}$
HCN	$5.0\ 10^{-9}$	DCN	$5.3\ 10^{-11}$	C_3N	$<1.7\ 10^{-11}$
C_2H	$\sim 1.5\ 10^{-8}$	CH_3CCH	$3.7\ 10^{-9}$	C_4H	$<0.8\ 10^{-11}$
C_3H_2	$2.3\ 10^{-11}$	HC_5N	$\lesssim 2.3\ 10^{-11}$		
Compact Ridge:					
PN	$\lesssim 1.0\ 10^{-11}$	PO	$<6.7\ 10^{-10}$	OCS	$3.3\ 10^{-9}$
HDO	$6.3\ 10^{-10}$	CH_3CN	$6.7\ 10^{-10}$	H_2CS	$2.4\ 10^{-9}$
H_2CO	$5.0\ 10^{-8}$	H_2CCO	$1.7\ 10^{-9}$	CH_3CHO	$\lesssim 1.7\ 10^{-10}$
CH_3OH	$1.7\ 10^{-7}$	CH_3OCH_3	$1.0\ 10^{-8}$	C_2H_5OH	$<5.0\ 10^{-10}$
HCOOH	$3.3\ 10^{-10}$	$HCOOCH_3$	$1.1\ 10^{-8}$	CH_3COOH	$<5.0\ 10^{-9}$
CH_3NH_2	$<1.0\ 10^{-9}$	NH_2CN	$<1.0\ 10^{-10}$	NH_2CHO	$<1.0\ 10^{-10}$
Plateau:					
CO	$1.2\ 10^{-4}$	SiO	$3.8\ 10^{-8}$	HDO	$1.8\ 10^{-8}$
CS	$2.5\ 10^{-8}$	OCS	$5.6\ 10^{-8}$	H_2S	$1.0\ 10^{-7}$
SO	$5.5\ 10^{-7}$	SO_2	$1.0\ 10^{-6}$	H_2CO	$3.2\ 10^{-8}$
HCN	$5.0\ 10^{-7}$	HC_3N	$1.1\ 10^{-8}$		
Hot Core:					
CO	$1.2\ 10^{-4}$	SO	$\gtrsim 8.1\ 10^{-9}$	SO_2	$1.2\ 10^{-8}$
HDO	$1.9\ 10^{-8}$	H_2CO	$1.2\ 10^{-8}$	HNCO	$3.1\ 10^{-9}$
HCN	$2.5\ 10^{-7}$	DCN	$8.8\ 10^{-10}$	CH_3CN	$1.2\ 10^{-8}$
HC_3N	$1.1\ 10^{-9}$	C_2H_3CN	$1.7\ 10^{-9}$	C_2H_5CN	$1.7\ 10^{-8}$

and CO, or

$$f(X) = \frac{N(X)}{N(H_2)} = \frac{N(X)}{N(CO)} \frac{N(CO)}{A_v} \frac{A_v}{N(H_2)} \quad . \tag{3.1}$$

As Irvine *et al.* (1985) note, since CO is very easily excited this procedure may well underestimate molecular fractional abundances, particularly for those species whose excitation requirements are severe. The uncertainties are somewhat smaller in Orion because the gas there is relatively warm and in Orion-KL it

has been possible to obtain direct estimates of the CO/H_2 ratio (cf. Watson 1982; Scoville *et al.* 1983); the absolute fractional abundances listed in Table 3.7 have been calculated using these canonical values of the CO/H_2 abundance in the various kinematic components ($f(CO)_{spike} \sim 5 \times 10^{-5}$, $f(CO)_{pl.,hc.} \sim 1.2 \times 10^{-4}$).

The net effect of the numerous assumptions required to obtain abundances relative to H_2 from the observations of interstellar molecular rotational emission lines are such that the individual values presented in Table 3.7 are probably not accurate to better than a factor of 5-10. However, since the bulk of the data has been acquired in a uniformly calibrated spectral scan the *relative* abundance values should be considerably more accurate. For example, consider the plateau abundances obtained from the ratios of high-velocity line emission. Provided the source sizes do not vary greatly from molecule to molecule, the beam averaged T_A^* values for optically thin lines should be equally in error for all species and any calibration mistakes, like the uncertainty in the CO/H_2 ratio, will be canceled out in a comparison of the relative abundances.

Even with the caveats of the preceding discussion it should be clear from Tables 3.6 and 3.7 that the Orion molecular cloud is not chemically homogeneous, but is instead composed of a number of sources whose chemical compositions vary considerably. Indeed, while the reactive carbon-rich species CI, CN, and C_2H are quite abundant in the extended molecular material, they have not been detected, and are much rarer, in the other sources. The hot core and condensed ridge sources appear to share some similar physical properties, but one is highly nitrogen-rich while the other is dominated by heavy oxygen-containing species. Plateau emission has very strong signatures from silicon and sulfur molecular species which are not evident elsewhere, but also contains appreciable quantities of simple and more complex molecules such as HDO and H_2CO found in both the ridge and hot core sources. The unification of these seemingly

disparate emission regions and a more thorough discussion of the effects of mass outflow on the chemical composition of molecular clouds is presented in Chapter 4, along with a comparison of the observational results with the most recent theoretical models of interstellar chemistry.

3.5. Isotopic Ratios

As matter cycles between stars and the clouds from which they form, the isotopic composition of the interstellar gas is affected by the nuclear processing of matter in stellar interiors. Thus, a comparison of interstellar and terrestrial isotopic ratios can trace evolutionary changes in the composition of the interstellar medium, and knowledge of the isotopic ratios in molecular clouds are therefore important because they provide invaluable clues to the understanding of the interplay of matter in our galaxy. The observations of lighter elements such as D and Li which were produced entirely in the Big Bang (they are, in fact, destroyed by stars) can also, in principle, place important constraints on cosmological models of the structure of the universe.

Within the observational errors the estimated ^{15}N, ^{29}Si, and ^{30}Si abundances appear to be similar to their terrestrial values, in agreement with extensive galactic surveys of HCN, HNN^+, and SiO (Wannier *et al.* 1981; Linke *et al.* 1983; Penzias 1981). However, the $^{18}O/^{17}O$ and $^{32}S/^{34}S$ ratios are lower than those found in the solar system by roughly 30-40%. The J=2 → 1 $C^{18}O$ and $C^{17}O$ lines produce a $^{18}O/^{17}O$ isotopic ratio of 3.5 (terrestrial ratio=5.5), while the many ^{34}SO and $^{34}SO_2$ transitions available are consistent with a $^{32}S/^{34}S$ ratio of 14-16, compared to the terrestrial value of 23. Similar results have been found for the oxygen isotopes by Penzias (1981), and for the sulfur species by Schloerb *et al.* (1983) and Johansson *et al.* (1984).

The $^{12}C/^{13}C$ and H/D ratios are lower still in a relative sense, but isotopic fractionation makes a detailed interpretation of the observed ratios rather uncertain, particularly for deuterium. Isotopic fractionation is an unavoidable consequence of the ion-molecule scheme used to model low temperature interstellar chemistry because of the rapid isotopic exchange reactions

$$^{13}C^+ + {}^{12}CO \rightleftarrows {}^{12}C^+ + {}^{13}CO + 35K \qquad (3.2)$$

$$H_3^+ + HD \rightleftarrows H_2D^+ + H_2 + 298K\ , \qquad (3.3)$$

and can enhance or deplete the isotopic ratios in different species. The equilibria of reactions (3.2) and (3.3), and thereby the isotopic fractionation, can vary considerably at the low temperatures characterizing the interstellar medium because their small exothermicities, induced by differences in the zero-point energies of the isotopically substituted species, are well matched to the kinetic temperatures of typical molecular clouds. Fractionation is most apparent in the H/D ratio which may be raised by factors of 10000 in the coldest clouds, as is discussed more fully in the interpretation of the H_2D^+ spectra presented in Chapter 4. Large-scale time dependent computer models have also predicted that the $^{13}C/^{12}C$ ratio can become significantly fractionated via eq. (3.2), with ^{13}C abundances enhanced in CO to values near 20-30 and depleted by similar amounts in molecules formed from C^+ such as HCN or CH_3OH when the cloud temperature is below 50 K. Like H_2, CO can "self-shield" itself against photodissociation to some extent, and differential photodissociation of the ^{13}CO and ^{12}CO molecules causes the $^{12}C/^{13}C$ ratio to vary as a function of depth into the cloud (Glassgold, Huggins, and Langer 1985). In contrast to the theoretical expectations, all of the isotopically substituted species detected in the OVRO and Onsala surveys are consistent with a $^{12}C/^{13}C$ ratio of 40 throughout OMC-1. Numerically, it is found that $^{12}CO/^{13}CO$ is about 40 in the high-velocity plateau

gas where optical depths are low, while HCN, HNC, OCS, H_2CO, and CH_3OH all produce values in range of 30-40 (Johansson *et al.* 1984; Blake *et al.* 1984). As Johansson *et al.* note, these low values agree with the optically determined $^{12}CO/^{13}CO$ ratio of 55 ± 11 (Wannier *et al.* 1982) and may indicate an evolutionary decrease of the galactic $^{12}C/^{13}C$ content, but the uncertainties are still considerable and values nearer to the terrestrial ratio of 89 have also been derived in Orion (Scoville *et al.* 1983).

3.6. The Integrated Emission Line Flux at 1.3mm

Measurements of the millimeter and far-infrared broad-band emission from molecular clouds have been used to establish, among other things, the luminosities of stellar clusters embedded in, the radiative energy loss from, and most importantly for chemistry, the total H_2 column density of a number of objects. To date these studies have assumed that the detected emission arises solely from the dust grains associated with the gas, the potential contribution of integrated molecular line emission has been ignored. If molecular lines account for a substantial fraction of the broad-band millimeter and submillimeter emission from interstellar clouds, then it is essential to separate their contribution from the true continuum flux if dust is to be used as a tracer for the total luminosity and column density of molecular cloud complexes. The great frequency range covered by the OVRO line search has made it possible, for the first time, to experimentally address the relative importance of molecular lines to the total radiative output of dense molecular clouds since the data reduction procedure used to create the single sideband spectrum depicted in Figure 3.2 also allowed the total integrated flux from molecular line emission to be calculated. A detailed discussion of the measured Orion broad-band fluxes has been presented by Sutton *et al.* (1984), and only the highlights will be outlined here.

In order to estimate the spectral index of the integrated molecular line flux the line survey was separated into a lower band from 215-247 GHz and an upper section between 247 and 263 GHz. Baseline offsets in the raw spectral line data were used to measure simultaneously the true continuum flux, thereby minimizing uncertainties from beam size, pointing errors, and so forth. Flux calibration was provided by observations of Saturn, and the uncertainties are estimated to be ± 20% from supporting measurements of Venus and Jupiter. The integrated spectral line fluxes in the lower and upper bands were 25 and 51 Jansky (1 Jy = 10^{-26} W m^{-2} Hz^{-1}), and the total broad-band intensity including true continuum emission was approximately 86 Jy at 1.3mm (230 GHz).

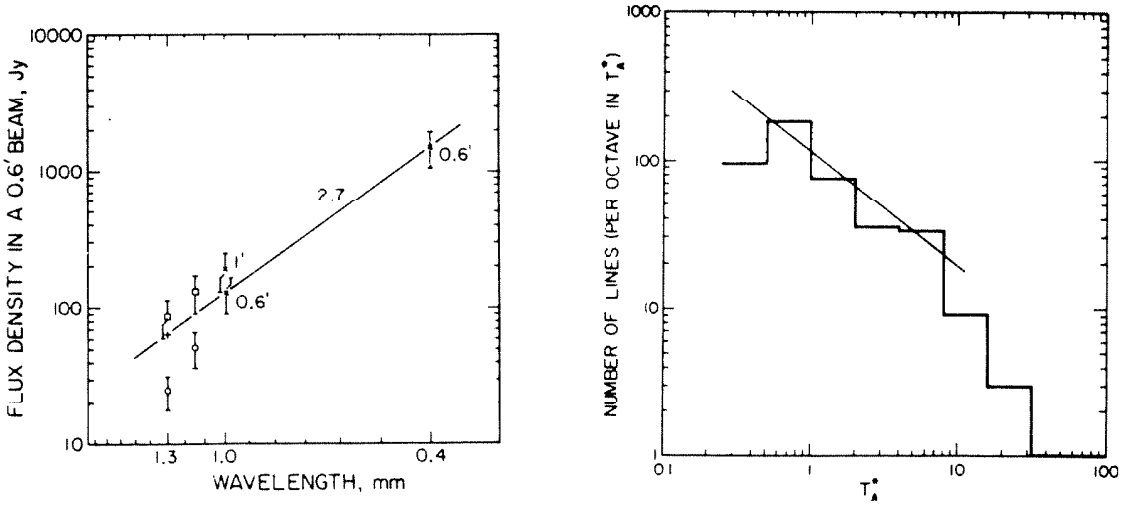

Figures 3.5a and 3.5b: a) Broad-band and spectral line flux densities in a 0.6' beam centered on BN. Open circles and boxes represent the line and total broad-band fluxes measured simultaneously at 1.3 an 1.15mm. Crosses indicate the broad-band fluxes of Keene, Hildebrand, and Whitcomb (1982) and Elias et al. (1978), the latter for both a 1' beam and corrected for a 0.6' beam. b) Distribution of the peak beam averaged antenna temperatures for lines in the 215-247 GHz interval.

A comparison of the OVRO values to those found in the published literature is presented in Figure 3.5a. Keene, Hildebrand, and Whitcomb (1982) have mapped the 400μm broad-band emission from OMC-1 with a 0.6' beam using the IRTF, while the 1mm broad-band flux has been measured, and subsequently

recalibrated, in a 1' beam by Westbrook *et al.* (1976) and Elias *et al.* (1978). Assuming that the 400μm and 1mm emission have identical spatial distributions produces corrected broad-band fluxes of 1500 (± 30%) and 128 Jy in a 0.6' beam, resulting in a spectral index of 2.7. Using this spectral index yields a predicted flux of 63 Jy within a 0.6' beam at 1.3 mm, which, within errors, agrees with the measured line plus continuum flux of 86 (± 20%) Jy. Thus, the integrated spectral line flux contributes some 30-40% of the total broad-band flux at 1.3mm. No lines whose strengths were less than ~0.2-0.3 K were used in this calculation, however, and it must therefore be considered a lower bound only.

In general, an *a priori* extrapolation of the line flux and density to noise levels below that of the line survey is not possible because, although many of the weaker lines will be due to highly excited or isotopically substituted states of known molecules, there will also be a number of new species whose rotational spectra and abundance are completely unknown. A statistical approach in which the line strength distribution shown in Figure 3.5b is extended to lower intensities has therefore been used. The rapid roll-off of lines above 20 K is due to optical depth saturation, and there also seems to be a serious undercounting of lines in the 0.25-0.5 K bin because of the finite 0.2-0.3 K noise level. Most of these "missing" lines are likely to originate in the large line width plateau source since they would be most easily overlooked in the nearly confusion-limited Orion spectrum. The fitted slope of -0.8 indicates that the true line flux contribution is nearer to 45% of the measured total if an average line width is assumed, whereas if all of the weaker lines are from the plateau, then at least 60% of the broad-band flux arises from molecules. In either case, integrated rotational line emission clearly accounts for a large, if not dominant, fraction of the measured broad-band flux.

The less well-determined spectral index of the observed line emission is similar to the value of 2.7 derived from the shorter wavelength measurements. What index is expected for the integrated emission from molecules? For a diatomic or linear molecule whose population distribution is fully thermalized, the expected millimeter-wave flux at frequencies below the rotational envelope maximum increases as ν^3 for optically thick lines and as fast as ν^5 for optically thin emission. Symmetric tops and asymmetric rotors have an even faster variation in their integrated flux since the number of states available for a given J grows as J^2, not J. At frequencies near the envelope maximum or for subthermal excitation the expected distribution will flatten out considerably. As Table 1.2 shows, the various rotational envelope maxima lie between 100 and 1000 GHz and since the integrated line emission is composed of a complex mixture of light, heavy, linear, and asymmetric molecules, nearly any desired spectral index can be obtained through a judicious combination of species and excitation. The somewhat low value of 2.7 suggests, however, that most of the molecular flux arises from lines which are optically thick.

Well, back in the old days, I wanted a brain, so I went to the advisor and asked him to give me one. He said he couldn't give me a brain, but that he'd do something even better and give me a large truckload of data instead, and then I wouldn't need a brain.

- The scarecrow, in *The Advisor of Ours*,
by Mike J. Wengler and Erich N. Grossman.

4. CHEMISTRY IN OMC-1

The remarkable chemical diversity of the differing kinematic components of OMC-1 derived in Chapter 3 demonstrates that both the chemical and physical composition of molecular clouds may be substantially altered by the process of star formation. In order to more fully address the mechanisms responsible for the production of interstellar molecules and the potential impact of star formation on the chemistry of molecular clouds, a more detailed analysis of the abundances in Chapter 3 is presented. The composition of the extended Orion component will be examined first as it should be most directly comparable to the observational results on other quiescent clouds, and since it should reflect the composition of OMC-1 prior to the onset of star formation.

4.1. The Extended Ridge

Early work on simple interstellar species such as CO, HCN, and H_2CO (Wootten *et al.* 1978, 1980a, 1980b) had suggested that their abundances declined rapidly as the densities of the regions studied increased, which was interpreted as the depletion of molecules onto grain mantles. The motivation behind this conclusion is that for sticking coefficients on the order of unity, grain-molecule adsorption times are about $t_{stick} \sim 2.5 \times 10^9/n_{H_2}$ years, where n_{H_2} is the cloud H_2 density per cm^{-3}. Even for a moderate density region with $n_{H_2} = 10^4$ cm^{-3} the adsorption time of $t_{stick} \sim 2.5 \times 10^5$ yr is significantly shorter than the inferred cloud lifetimes ($\sim 10^7$ yr), and the density-dependent adsorption of gas-phase species onto grain mantles would therefore be expected to be a serious problem in maintaining the high observed abundances of molecular species in the dense cores of molecular clouds. The depletion of atoms and molecules onto grain surfaces has recently been *directly* measured via 4.6 μm observations of the CO $\nu = 0 \rightarrow 1$ band by Hall (1984), who finds there is a marked decrease in $N(CO)/A_v$

Table 4.1
Molecular Abundances in Quiescent Clouds

	Abundance relative to H_2				
				Leung *et al.*	
Species	OMC−1[a]	Sgr B2[b]	TMC−1[c]	Model 1[d]	Model 2[e]
C	$2.5\ 10^{-8}$	-	-	$6.8\ 10^{-8}$	$5.4\ 10^{-11}$
CO	$5.0\ 10^{-5}$	$6.0\ 10^{-5}$	$5.8\ 10^{-5}$	$1.2\ 10^{-4}$	$1.5\ 10^{-4}$
CN	$2.5\ 10^{-8}$	$3.4\ 10^{-10}$	$3.0\ 10^{-8}$	$8.9\ 10^{-9}$	$9.7\ 10^{-11}$
CS	$2.5\ 10^{-9}$	$3.0\ 10^{-9}$	$2.0\ 10^{-9}$	$5.5\ 10^{-8}$	$2.9\ 10^{-8}$
SO	$\lesssim 9.0\ 10^{-9}$	$1.5\ 10^{-10}$	$5.0\ 10^{-9}$	$8.7\ 10^{-10}$	
SO_2	$<3.0\ 10^{-9}$	$2.0\ 10^{-9}$	-	$3.9\ 10^{-9}$	$9.3\ 10^{-8}$
C_2H	$1.3\ 10^{-8}$	-	$6.4\ 10^{-9}$	$7.8\ 10^{-6}$	$9.0\ 10^{-10}$
HCN	$5.0\ 10^{-9}$	$\sim 3.0\ 10^{-9}$	$1.2\ 10^{-8}$	$1.2\ 10^{-6}$	$2.3\ 10^{-9}$
HNC	$5.3\ 10^{-10}$	$\sim 3.0\ 10^{-9}$	$8.0\ 10^{-9}$	$1.2\ 10^{-6}$	$2.4\ 10^{-9}$
HCO^+	$5.0\ 10^{-9}$	$2.3\ 10^{-9}$	$8.0\ 10^{-9}$	$1.0\ 10^{-9}$	$2.5\ 10^{-9}$
HCS^+	$5.3\ 10^{-11}$	$3.0\ 10^{-11}$	$5.0\ 10^{-10}$	$7.5\ 10^{-13}$	$1.9\ 10^{-12}$
H_2D^+	$\sim 1.0\ 10^{-10}$	-	$<3.0\ 10^{-8}$	-	$\sim 1.1\ 10^{-10}$
HC_3N	$4.2\ 10^{-10}$	$3.8\ 10^{-10}$	$6.0\ 10^{-9}$	$5.1\ 10^{-8}$	$4.4\ 10^{-13}$
HC_5N	$\lesssim 2.3\ 10^{-11}$	-	$1.0\ 10^{-8}$	$5.4\ 10^{-9}$	$5.1\ 10^{-17}$
CH_3CN	$6.7\ 10^{-10}$	$2.0\ 10^{-10}$	$5.0\ 10^{-10}$	$1.0\ 10^{-7}$	$1.3\ 10^{-11}$
H_2CO	$5.0\ 10^{-8}$	$3.0\ 10^{-9}$	$1.2\ 10^{-8}$	$8.7\ 10^{-7}$	$9.6\ 10^{-8}$
CH_3OH	$1.7\ 10^{-7}$	$2.0\ 10^{-8}$	-	$1.8\ 10^{-9}$	$1.2\ 10^{-10}$

[a]- Derived from this work and Johansson *et al.* (1984). [b]- Derived from Cummins, Linke, and Thaddeus (1985). [c]- From the data compilation in Leung, Herbst, and Huebner (1984). [d]- Model results for $n_{H_2}=10^5$ cm^{-3}, t=2.15 10^5 yr. [e]- Model results for $n_{H_2}=10^5$ cm^{-3}, $t \gtrsim 10^7$ yr.

for $T_{ROT}(CO)<20$ K compared to clouds for which $T_{ROT}>20$ K.

However, as the more accurately calibrated data from the spectral line surveys conducted at Onsala, OVRO, and Bell Laboratories have supplanted the earlier exploratory work in the near millimeter wave region, it has become clear that the abundances of simple species in various clouds of quiescent gas are, in fact, rather uniform, as will be shown below. For example, Table 4.1 presents a listing of the abundances of a number of species in the Orion, Taurus, and Sagittarius molecular clouds derived from the OVRO, Onsala, and Bell Labs spectral line surveys outlined above, along with predictions from the extensive time-dependent chemical model of Leung, Herbst, and Huebner (1984). The two theoretical predictions apply to those abundances found under steady-state

conditions ($t>10^7$ years) and for an earlier time at which Leung, Herbst, and Heubner find that complex molecules are most abundant($t\sim2\ 10^5$ years). Also included in Table 4.1 are the abundances of more complex molecules such as CH_3CN and CH_3OH appearing in Orion at the velocity of the ambient material, but which seem to be more spatially confined. As this Table shows, the abundances of nearly all of the simpler species are within factors of a few, and certainly within a factor of ten, of each other in the differing molecular clouds; and the abundances, for the most part, also seem to be reasonably well predicted by the purely gas phase ion-molecule networks of the type pioneered by Herbst and Klemperer (1973) and Prasad and Huntress (1980) that do not predict strong chemical variations from source to source. Gas phase ion-molecule chemistry would therefore appear to account for much or most of the chemical processing in dense interstellar clouds, as is bolstered by the submillimeter observations of H_2D^+ and HCl. These molecules are discussed separately below due to the unique insights they offer regarding the chemistry of the interstellar medium.

It should be noted that most of the thousands of reaction rates used in such models have not been measured experimentally, and that considerable work remains before any definite conclusions about the dominance of gas phase chemistry can be reached. It would appear, however, that the abundances of most species are *not* strongly correlated with density, implying that some mechanism must exist to remove adsorbed molecules from grain surfaces deep within quiescent molecular clouds without significantly altering the composition of the gas. Several types of desorption mechanisms have been suggested ranging from grain mantle chemical explosions (d'Henecourt *et al.* 1982) to impulsive spot heating by X-rays and cosmic rays (Leger, Jura, and Omont 1985), but little is actually known which could differentiate between the various hypotheses.

Although the abundances in Table 4.1 are well predicted and rather similar for the various sources, there are also quite clearly a few sizable differences between the clouds and major failings in the chemical models, mostly related to the so-called "carbon problem" in dense molecular clouds (Phillips and Huggins 1981; Herbst 1983). For example, one sees that many carbon-rich species, particularly the higher cyanopolyacetylenes and the C_3N and C_4H radicals, have substantially greater abundances in TMC-1 than in either OMC-1 or Sgr B2. Moreover, the abundances of even simpler carbon-rich species such as CI, CN, HCS^+, or C_2H are sometimes vastly underestimated by models of evolved clouds under steady-state conditions, and only somewhat better followed at intermediate time scales because of reactions of the type

$$C + O_2 \rightarrow CO + O \qquad (4.1)$$

$$CN + O \rightarrow CO + N . \qquad (4.2)$$

Significant quantities of OI and O_2 are present in chemical models of dense interstellar clouds since the cosmic ratio of C/O = 0.4 leaves a considerable gas phase reservoir of oxygen even after reactions such as (4.1) and (4.2) convert reactive carbon-containing species like CI and CN into CO. In quiescent clouds such as the extended Orion ridge, the neutral-neutral reactions are not as fast as their ion-molecule counterparts, and it is for this reason that the predicted abundances of the carbon species noted above peak early in the cloud's evolution. Complicating this matter further in OMC-1 (and other clouds as well) is the presence of oxygen-rich species such as CH_3OH or $HCOOCH_3$ at similar velocities and positions to the carbon-rich molecules, but whose abundances are also underestimated by the models. How can a cloud simultaneously be both carbon and oxygen-rich? More will be said about this question in the section on the compact ridge source.

The species which illustrates the carbon problem in dense molecular clouds most dramatically is the neutral CI atom, first observed by Phillips *et al.* (1980). More extensive observations (Phillips and Huggins 1981; Keene *et al.* 1985, Frerking *et al.* 1985) have shown that CI is widespread throughout molecular clouds and not simply restricted to the outer edges of these objects, in contrast to the predictions of early models. The inferred CI/CO ratio of 0.01-0.5 is nearly three orders of magnitude greater than even the most optimistic steady-state predictions for the shielded cores of molecular clouds in which, as the preceding discussion shows, the conversion of CI→CO is expected to be essentially complete for cloud ages greater than approximately 10^6 years. While it is difficult to accurately determine the ages of individual molecular clouds, observations of the distribution of these objects on a galactic scale suggests that their lifetimes are $\lesssim 10^6$ years (Cohen *et al.* 1980). For large complexes like Orion the ages of stellar associations formed from the molecular gas may be used to establish lower bounds for the cloud lifetime, and are generally about 10^7 years (Kutner *et al.* 1977). Thus, it would appear that the physical age of most molecular clouds is on the order of 10^7-10^8 years.

A number of new theories have been introduced since the observations of Phillips and Huggins (1981) which attempt to explain the large observed CI abundances by delaying the onset of *chemical* maturity in molecular clouds via a wide variety of processes. Keene *et al.* (1985) have recently summarized these models and have embarked on a series of of observations designed to test their validity and observational consequences. Whether they utilize a delayed dynamical collapse of diffuse clouds into a set of denser fragments (Tarafdar *et al.* 1985), the convective transport of material deep within the cloud core to its unshielded outer edges (Boland and de Jong 1982), frequent mild shocking of the molecular cloud gas (Williams and Hartquist 1984), or the internal production of CI from CO via photodissociation by internal UV or X-ray sources (Prasad

and Tarafdar 1983; Krolik and Kallman 1983), all such models assume that the available CI is in fact rapidly converted into CO and that some process must be found to "recycle" CO into the more reactive atomic species.

An alternative suggestion is concerned with the possibility that the *gas phase* C/O ratio in molecular clouds may vary considerably from its cosmic value of 0.4 (Langer *et al.* 1984). Obviously, if the gas phase C/O ratio is greater than unity in the cores of dense molecular clouds, then substantial amounts of CI and other carbon-rich species may remain long after all of the available gas phase oxygen has been locked away in CO. The major difficulty with this approach is that it now becomes difficult to reproduce the observed abundances of the oxygen-containing molecules such as CH_3OH, but it does have a number of supporting observations and theoretical predictions. In addition to the high abundances of CI, CN, and C_2H, Prasad and Huntress (1982) also conclude from their theoretical study of sulfur in dense molecular clouds that the observed chemistry of this family is inconsistent with an undepleted gas phase oxygen concentration. Specifically, they use the observed SO abundance and the HCS^+/CS ratio to conclude that $f(O) \lesssim 6 \times 10^{-7}$, well below its predicted (undepleted) value of $4\text{-}5 \times 10^{-5}$. Further, both Herbst (1983) and Leung, Herbst, and Heubner (1984) require a large CI content in the cores of dense clouds in order to reproduce the observed hydrocarbon abundances in many sources, particularly in the dark, truly quiescent clouds like TMC-1 and L183 which do not appear to contain detectable amounts of oxygen-rich molecules like CH_3OH or CH_3OCH_3.

That some selective depletion mechanism is required to increase the C/O gas phase ratio to values greater than unity is clear. Observations of species containing second-row elements may again provide important clues into the nature of the depletion mechanism. While the first-row elements appear to be

depleted by no more than factors of 10-100 the observations of several Si or S-containing species are most consistent with depletions in the range of 1000 (Prasad and Huntress 1982), supporting the intuitively appealing hypothesis that the more refractory elements and molecular species should be the most strongly depleted. Could such a mechanism explain a high gas phase C/O ratio? Early in this lifetimes of molecular clouds most species, with the exception of H_2, are primarily neutral and atomic. Consider a scenario in which CI, NI, and OI collide with grains and stick to them with equal probabilities. Once residing on the grain surface, the chemically active H/H_2 mantle thought to cover most grains (Allen and Robinson 1977; Tielens and Hagen 1982) will proceed to hydrogenate these species until the fully hydrogenated end products, CH_4, NH_3, and H_2O, are formed. Of these, CH_4 will most easily evaporate from the cold grain surfaces due to its non-polar nature. Indeed, the sublimation temperatures of pure ammonia or water mantles are well above 150 K, and such ices will remain frozen onto grain surfaces in all but the warmest regions of molecular clouds Observational support for the existence of a substantial molecular grain mantle stems mainly from the study of several infrared features near 3.0, 3.1, 4.6, and 6.0 μm, observed in absorption against deeply embedded sources, which have been identified as the stretching bands of a "dirty ice" layer composed mainly of H_2O and NH_3, with smaller concentrations of CO, H_2CO, etc. The 3.8 μm bands are best fit by a $4(\pm1):1$ mixture of H_2O:NH_3 and indicate that the fractional abundance of H_2O and NH_3 on the grain mantles exceeds 10^{-5} (Knacke *et al.* 1982, Whittet *et al.* 1983). In addition, searches for gas phase H_2O, which is predicted to be quite abundant by the standard ion-molecule chemical models, have failed to detect H_2O in quiescent clouds, but have shown instead that water emission may be a good tracer of the sometimes violent activity associated with star formation.

Thus, it would appear that there are mechanisms available which could significantly enhance the gas phase C/O ratio in quiescent molecular clouds leading to the high carbon abundance detected there. A major step forward in the verification of this hypothesis would be the identification of CH_4 in the cores of quiescent molecular clouds as it is predicted to be a major reservoir of carbon in a carbon-rich gas (Watt 1985). Unfortunately, it possesses no permanent dipole moment and any study of CH_4 must rely on its infrared absorption spectrum towards bright sources around which the expected depletion is small unless the star is very deeply embedded.

In spite of the above difficulties, it is concluded, for the most part, that the time-dependent ion-molecule reaction networks described in Chapter 4 and Section 4.1 can account both qualitatively and quantitatively for the chemical composition now well characterized in a number of sources, although the initial cloud composition and its subsequent chemical evolution may be selectively influenced by grain depletion processes.

4.1a. Observations of H_2D^+

As outlined in Chapter 2, the H_3^+ ion plays a crucial role in the initiation of interstellar ion-molecule chemistry because it rapidly "protonates" the abundant neutral C, N, and O species to unleash the diverse reaction networks noted above. Observations of H_3^+ would therefore be a most powerful means of verifying the accuracy and general importance of ion-molecule theoretical models of interstellar chemistry. Due to its simple and fundamental nature, the H_3^+ formation and destruction pathways are now well understood. H_3^+ is formed by the reaction of H_2 with H_2^+, which is produced by the cosmic ray ionization of H_2:

$$H_2 \xrightarrow{\zeta} H_2^+ + e^- \qquad (4.3)$$

$$H_2 + H_2^+ \rightarrow H_3^+ + H \quad (4.4)$$

Most positively charged ions in the interstellar medium are destroyed by recombination reactions with electrons, but theoretical calculations have long predicted that the reaction of ground-state H_3^+ with electrons is slow (Carney and Porter 1976; Michels and Hobbs 1984). Experimental verification of this prediction has recently been provided by Smith and Adams (1984), who show that $k(H_3^+ - e^-) \lesssim 10^{-8}$. Thus, the destruction of H_3^+ is governed primarily by its reaction with trace neutral constituents like CO, N_2, H_2O, etc:

$$H_3^+ + CO, N_2, H_2O, \cdots \rightarrow HCO^+, HNN^+, H_3O^+, \cdots + H_2 \quad (4.5)$$

In steady-state the balancing of eqs. (4.2)-(4.5) yields a predicted H_3^+ fractional abundance of

$$f(H_3^+) = \frac{n(H_3^+)}{n(H_2)} \cong \frac{\zeta}{k_{CO} f_{CO} n_{H_2}} \quad (4.6)$$

if it is assumed that $n(CO) >> n(N_2)$, $n(H_2O)$, etc., where f_{CO} is the CO fractional abundance and n_{H_2} is the molecular hydrogen number density. Relation (4.6) demonstrates that the fractional abundances of ions (and thereby the cloud fractional ionization), unlike neutral species, are expected to show a considerable variation with gas density even in the absence of depletion onto grains. Inserting canonical values of 1×10^{-17} s^{-1} and 8×10^{-5} for ζ and f_{CO} produces an estimated H_3^+ fractional abundance of $f(H_3^+) \sim 6 \times 10^{-5}/n_{H_2}$, making it one of the more abundant ions in dense interstellar clouds.

The D_{3h} symmetry of H_3^+ is such, however, that it has no permanent electric dipole moment. Thus, there are no strongly allowed rotational transitions with which its abundance may be measured. Some weakly allowed far-infrared $\Delta k = 3$ transitions are induced by centrifugal distortion effects, but their strengths are

insufficient to permit the detection of H_3^+. High resolution absorption spectroscopy of the stronger infrared vibrational transitions towards embedded stellar sources may eventually allow some direct observations to be made, but a general survey of the H_3^+ abundance in cold, dense clouds will most likely never be possible. However, the observations of strong emission from DCN (Jefferts, Penzias, and Wilson 1973), subsequently detected in a number of other species such as HDO, DCO^+, and HDCO (Turner *et al.* 1975; Hollis *et al.* 1976), indicated that the D/H ratio in certain molecules could be substantially enhanced from its cosmic value of $\sim 10^{-5}$. As Watson (1976) first realized, this strong deuterium enhancement, or fractionation, is primarily a result of the reaction between H_3^+ and HD to produce H_2D^+:

$$H_3^+ + HD \rightleftharpoons H_2D^+ + H_2 + 298\ K\ . \qquad (4.7)$$

At the low temperatures which characterize most molecular clouds the backward channel in reaction (4.7) is sufficiently endothermic that the reaction is driven quite strongly to the right, with its equilibrium constant approaching and exceeding values of 10000 in the coldest regions. The high resulting H_2D^+ abundance is then transferred to other species by reactions such as those listed in eq. (4.5). Unlike most deuterated versions of highly symmetric neutral species, H_2D^+ possesses a substantial permanent dipole moment ($\mu_{H_2D^+} \sim 0.6$ D) because of the large separation of the center of charge and mass in this ion (Dalgarno *et al.* 1973). The detection of H_2D^+ would be of tremendous importance because it would verify not only the predictions of ion-molecule chemistry, but the fractionation process initiated by eq. (4.7) as well.

Early searches for potential H_2D^+ transitions (Angerhofer, Churchwell, and Porter 1978, Phillips *et al.* 1978) were hampered by the lack of accurate transition frequencies and poor instrumental sensitivity. Recent improvements in the

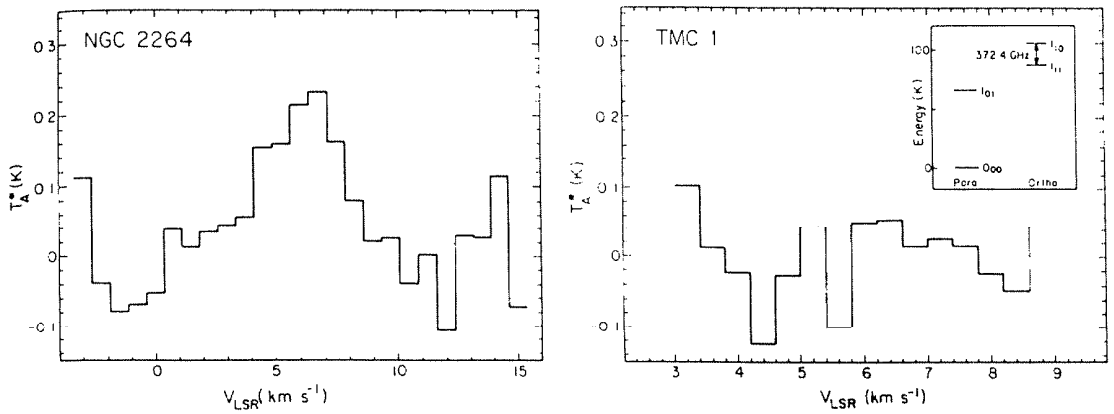

Figure 4.1a) The H_2D^+ spectrum toward the molecular cloud NGC 2264. The velocity scale has been established using a rest frequency of 372.4213 GHz. Individual channels are spaced by 0.75 km s^{-1}. b) A spectrum taken in the vicinity of the H_2D^+ line, toward TMC-1. Channels are spaced by 0.4 km s^{-1}. The inset contains an energy level diagram of the lowest H_2D^+ rotational states.

theoretically calculated structures of H_3^+ and H_2D^+ (Carney 1980) along with the detection of their infrared spectra (Oka 1980a; Amano 1984) have resulted in the laboratory detection of the $1_{11} \rightarrow 1_{10}$ H_2D^+ transition at 372.4213 GHz (Bogey *et al.* 1984; Warner *et al.* 1984) with the magnetic field enhanced glow discharge technique described in Appendix B, thereby providing the accurate rest frequency necessary to begin a careful search for interstellar H_2D^+.

Due to the limited observing time available on the airborne KAO platform, OMC-1 could not be studied. Observations concentrated instead on the NGC 2264 and TMC-1 clouds because of their strong emission from the related DCO^+ ion. The co-added spectra are presented in Figure 4.1a and in Figure 4.1b, which also contains an energy level diagram of the lowest rotational states of H_2D^+. A line at the expected position of the H_2D^+ $1_{11} \rightarrow 1_{10}$ transition is present in NGC 2264 with an estimated strength of $T_A^*(H_2D^+)$~230 mK, while for TMC-1

only an upper limit (2σ) of 120 mK has been obtained. Although the detection of a single line can never be considered as a definitive identification of an interstellar molecule, the catalogues of Poynter and Pickett (1984) and Lovas (1984) have been consulted and a number of laboratory experiments have also been performed on complicated rotors like CH_3OH whose spectra are difficult to predict accurately; in neither case have features been found at or near the measured H_2D^+ frequency. It will hereafter be assumed that the line in NGC 2264 is due solely to H_2D^+.

A detailed calculation of the H_2D^+ abundance from the spectra in Figures 4.1a and 4.1b is complicated by a number of factors, several of which are poorly understood at present. Most significantly, the excitation of the 1_{10} level in interstellar clouds may be dramatically affected by the presence of the two equivalent hydrogen nuclei in H_2D^+, which produce radiatively non-interacting rotational ladders of ortho and para states, just as for H_2CO (cf. Figure 4.1b). The 1_{11} lower transition level, the ground state of ortho-H_2D^+, is not radiatively connected to any para state, including the true rotational ground state 0_{00}, and radiative effects are therefore unable to influence the H_2D^+ ortho/para ratio in dense molecular clouds. Collisions with H_2, on the other hand, can potentially affect the relative populations in the different symmetry states. For stable molecules like H_2CO or NH_3, it has been found that nearly all collisional transitions obey "selection rules" which follow those for radiative transitions (Oka 1980b). Such weak (non-reactive) collisions do not alter the ortho/para balance but serve mainly to produce thermal or quasi-thermal populations within a given symmetry state. Collisions between H_2 and ions like H_2D^+ or CH_3^+ are often weak, but there are also strong, or reactive, collisional encounters in which equivalent hydrogen nuclei may be exchanged. Strong collisions typically produce a fully thermalized population distribution across the symmetry states, and can therefore be quite efficient at interconverting the ortho and para

species. The simplest example of this process is the reaction of H_2 with H^+

$$\widetilde{H}\widetilde{\widetilde{H}}\,(J=1) \;+\; H^+ \;\rightarrow\; \widetilde{H}H\,(J=0) \;+\; \widetilde{\widetilde{H}}^+ \qquad (4.8)$$

which has an estimated rate constant of 4×10^{-10} cm^3 s^{-1} (Dalgarno, Black, and Weisheit 1973). Reaction (4.8) is capable of thermalizing the H_2 rotational population distribution in dense molecular clouds, but as Flower and Watt (1984) show the expected conversion timescale is on the order of 10^7 years. It is therefore possible that the H_2 distribution in molecular clouds is intermediate between the statistical and thermalized limits. The 1_{10} H_2D^+ level lies approximately 100 K above the ground state, and if the population distribution of H_2D^+ is fully thermalized in dense clouds, then it will be quite difficult to observe the $1_{10} \rightarrow 1_{11}$ transition in cold objects like TMC-1 where deuterium fractionation is most appreciable. If, however, the 1_{11} level is truly metastable, the excitation energy of the 1_{10} state is only 18 K and the $1_{10} \rightarrow 1_{11}$ transition should be observable in even the coldest regions.

The exothermicity of reaction (4.7) is insufficient, by itself, to populate rotational states of H_2D^+ with $K_p \gtrsim 2$. Rapid far-infrared spontaneous decay routes in the $K_p = 0,1$ ladders depopulate all levels above their lowest states (0_{00} and 1_{11}) for densities below 10^8 cm^{-3}. It will therefore be assumed, after Herbst (1982), that the entire H_2D^+ rotational state population distribution is contained in the 0_{00}, 1_{10}, and 1_{11} levels. The problem of estimating the the H_2D^+ partition function is then reduced to a calculation of the relative populations of the 1_{11} and 0_{00} states. Since no detailed experimental results exist for the interconversion of the symmetry species in H_2D^+, upper and lower limits for the H_2D^+ abundance will be calculated assuming 1) that the 1_{11}(ortho) and 0_{00}(para) level populations are related by a "normal," or statistical, ratio of 3:1, and 2) that this ratio is instead characterized by a thermal equilibrium distribution in which the symmetry nature of the individual rotational states enters into the level

degeneracies only. The statistical assumption places the maximum population into the observed ortho states; that is, it produces a minimum overall rotational partition function to yield a lower limit to the H_2D^+ fractional abundance. A thermal assumption "shorts out" the 1_{11} state to the true ground state, thereby minimizing the ortho state population and creating an upper limit to the total H_2D^+ fractional abundance. It will further be assumed that the line in NGC 2264 is optically thin with an excitation temperature equal to the cloud kinetic temperature. Table 4.2 presents the results of these calculations for the two objects observed. It should be noted that, given the emission strength in NGC 2264, a statistical population distribution ought to have produced an easily detectable feature in TMC-1, but with a thermalized distribution the expected emission strength is well below the derived upper limits. Like H_2, some intermediate situation is most probable.

Table 4.2
Deduced H_2D^+ and H_3^+ Abundances Toward NGC 2264 and TMC-1

THERMAL	$N(H_2D^+)$ cm^{-2}	$N(H_2D^+)/N(H_2)$	$N(H_3^+)/N(H_2)$
NGC 2264	3.1×10^{13}	1.1×10^{-10}	2.3×10^{-9}
TMC-1	$<6.0\times10^{14}$	$<3.0\times 10^{-8}$	$<5.6\times 10^{-8}$
STATISTICAL	$N(H_2D^+)$ cm^{-2}	$N(H_2D^+)/N(H_2)$	$N(H_3^+)/N(H_2)$
NGC 2264	9.3×10^{12}	3.1×10^{-11}	6.7×10^{-10}
TMC-1	$<1.3\times10^{12}$	$<6.9\times 10^{-11}$	$<1.3\times 10^{-10}$

The H_3^+ abundances derived from the inferred H_2D^+ limits are also listed in Table 4.2, and have been calculated following the procedure of Herbst (1982), who along with Smith, Adams, and Alge (1982) has analyzed the temperature dependence of the deuterium fractionation process is detail. The upper limits derived for TMC-1 are meaningful only if the population distribution is statistical, which is not supported by these observations. However, the results for NGC 2264 are considerably less uncertain and are quite informative. The estimated

H_3^+ fractional abundance lies in the range $f(H_3^+) \sim 0.7 - 2.3 \times 10^{-9}$, compared with the predicted values of $0.3 - 1.5 \times 10^{-9}$ (Leung, Herbst, and Huebner 1984; Prasad and Huntress 1980; Graedel, Langer, and Frerking 1982). Within the admittedly large observational errors, the derived H_3^+ abundance is in remarkably good agreement with the theoretical ion-molecule chemical predictions. The marginally higher observed abundance could be indicative of a slightly smaller CO content than the calculated value of 1.5×10^{-4} or a larger cosmic ray ionization rate than the canonical value of 1×10^{-17} s^{-1} (O'Donnell and Watson 1974; Payne, Salpeter, and Terzian 1985), but otherwise the excellent agreement between theory and observation is another powerful illustration of the essential correctness and predictive potential of ion-molecule models of interstellar chemistry.

4.1b. The Chemistry of Chlorine in Dense Interstellar Clouds

The rich chemistry of the C,N, and O families observed in interstellar clouds has found no counterpart in the heavier elements of the periodic table. While this may be due in part to depletion effects, the dominance of H_2 and the lower fractional abundances of the heavier elements combine to make the rotational spectra of metal hydrides, which lie exclusively in the relatively unexplored submillimeter and FIR regions, the most promising means of tracing metal abundances in the dense interstellar gas.

Following such reasoning, HCl was chosen as the initial target in a continuing study of interstellar "metal" hydrides because chlorine is rather abundant ($f(Cl) \sim 3 \times 10^{-7}$), because the HCl rotational spectrum is accurately characterized (De Lucia, Helminger, and Gordy 1971), and because early models of chlorine chemistry had suggested that all of the available chlorine should be in the form of HCl (Jura 1974; Dalgarno *et al.* 1974). The large chlorine quadrupole moment splits the ground state HCl $J = 1 \rightarrow 0$ transition into the three

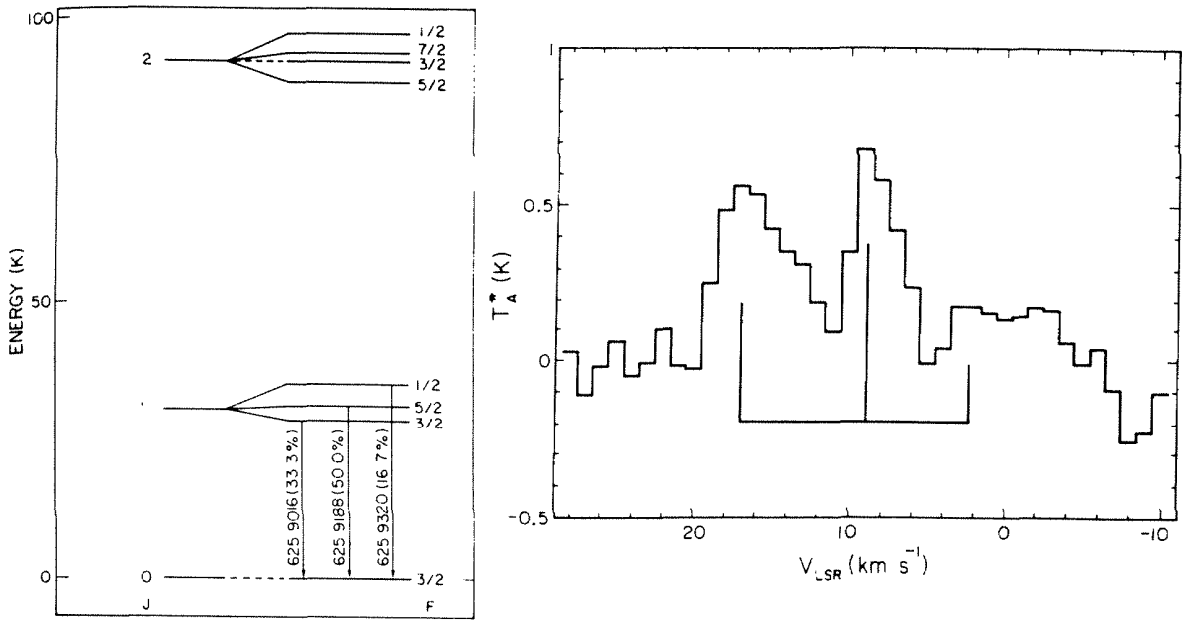

Figure 4.2a) Energy-level diagram for the lowest three rotational levels of HCl, with the hyperfine splittings exaggerated for clarity. Arrows mark the observed transitions along with their laboratory rest frequencies and intrinsic line strengths. b) Observed HCl J= 1→0 spectra toward OMC-1. The measurements were spaced by 1 km s^{-1} but have been smoothed to an effective resolution of 2 km s^{-1}. The velocity scale has been established using a main hyperfine component frequency of 625.9188 GHz. Vertical lines mark the expected hyperfine component positions and LTE strengths assuming a v_{LSR} of 9 km s^{-1}.

resolvable hyperfine components shown in the energy level diagram presented in Figure 4.2a, and places the identification of the emission detected towards OMC-1 shown in Figure 4.2b on a secure footing. A detailed analysis of the strength of the ground state emission (Blake, Keene, and Phillips 1985) leads to an estimated HCl fractional abundance of f(HCl)~0.5-5.0 x 10^{-8}, which is somewhat below that expected for an undepleted chlorine abundance fully associated into hydrogen chloride. In order to determine whether depletion mechanisms alone are responsible for this decrease, or whether chemical processes also limit the HCl abundance, we have carried out a series of laboratory experiments and theoretical model calculations, described below, on the ion-molecule chemistry of interstellar chlorine. These studies show that HCl is a major, but not the sole, reservoir of gaseous chlorine in dense interstellar clouds, with neutral

atomic chlorine remaining as the other significant species. It is also found that, although higher than in diffuse clouds, the chlorine depletion is not severe in dense molecular clouds.

Chemical Data

Many of the reactions of importance to interstellar chlorine chemistry have not been previously measured in the laboratory. A number of these reactions, particularly those involving CCl^+, have therefore been measured at JPL using the ion cyclotron resonance techniques discussed in Thorne, Anicich, and Huntress (1983). Table 4.3 summarizes the laboratory work performed on the ion molecule reactions of chlorine. The CCl^+ and H_2CCl^+ ions were generated by electron impact on chloroform and dichloromethane, while H_2Cl^+ was produced via the reaction of H_3^+ and HCl. The rapid proton transfer reactions from H_2Cl^+, and the reactions leading to and involving CCl^+ and H_2CCl^+ were neglected in earliest models (Dalgarno *et al.* 1974), but are quite important to the ion-molecule chemistry of chlorine. These reactions are the key result of the laboratory study.

The theoretical calculation used to model interstellar chlorine chemistry requires the rate coefficients of more reactions than can be currently measured, particularly those involving the reactive atomic species Cl and Ol. Thermodynamic data and chemical intuition have therefore been used in place of laboratory measurements to predict the allowed reaction pathways and most probable products of processes involving these reactants. Heats of formation for the Cl^+ and HCl^+ ions have been calculated from the ionization potentials (IP) and ΔH_f° of the corresponding neutrals, while that of H_2Cl^+ has been calculated using the measured proton affinity of HCl.

Table 4.3
Laboratory Rate Constants for Ion-Molecule Reactions Involving Chlorine

Reactions			Rate Constant $k(10^{-9}\ cm^3\ s^{-1})$
Reactions of H_2Cl^+			
$H_2Cl^+ + CO$	→	$HCO^+ + HCl$	0.42
$H_2Cl^+ + H_2O$	→	$H_3O^+ + HCl$	2.00
Reactions of CCl^+			
$CCl^+ + H_2$	→	No Reaction	≲0.01
$CCl^+ + N_2$	→	No Reaction	≲0.03
$CCl^+ + O_2$	→	No Reaction	≲0.03
$CCl^+ + CO$	→	No Reaction	≲0.03
$CCl^+ + CO_2$	→	No Reaction	≲0.03
$CCl^+ + H_2O$	→	No Reaction	≲0.03
$CCl^+ + NH_3$	→	$HCNH^+ + HCl$	1.25
$CCl^+ + NH_3$	→	$H_3CN^+ + Cl$	0.05
$CCl^+ + CH_4$	→	No Reaction	≲0.03
$CCl^+ + HCN$	→	No Reaction	≲0.03
$CCl^+ + H_2CO$	→	$H_2CCl^+ + CO$	0.53
Reactions of H_2CCl^+			
$H_2CCl^+ + H_2$	→	No reaction	≲0.01
$H_2CCl^+ + CO$	→	No reaction	≲0.01
Miscellaneous			
$HCl + H_3^+$	→	$H_2Cl^+ + H_2$	3.50
$HCl + HCO^+$	→	$H_2Cl^+ + CO$	0.30
$HCl + CH_3^+$	→	$H_2CCl^+ + H_2$	0.19

No accepted values of ΔH_f° exist for CCl^+ or H_2CCl^+. We have obtained an upper limit of $\Delta H_f^\circ(CCl^+) \lesssim 340$ kcal/mole by examining charge transfer reactions between CCl^+ and a number of low IP neutrals such as NO, CH_3NH_2, and Cl_2. No charge transfer was detected between any of these species implying an upper limit of 9.26 eV for IP(CCl), determined from NO. The low IP's of CCl and H_2CCl are consistent with the observed stability and low reactivity of the CCl^+ and H_2CCl^+ ions, which are explained in part by the fact that these ions are isoelectronic with the familiar and stable interstellar species CS and H_2CS.

Table 4.4
Chemical Equations used in the Chlorine Model

	Reactions			Rate Constant $k(10^{-9}\ cm^3\ s^{-1})$
	$Cl + C.Rays$	$\rightarrow$	$Cl^+ + e^-$	$1.0\ 10^{-8}$ [b]
*	$Cl + H^+$	$\rightarrow$	$Cl^+ + H$	1.0[b]
*	$Cl + H_3^+$	$\rightarrow$	$HCl^+ + H_2$	1.0[b]
	$HCl + H^+$	$\rightarrow$	$HCl^+ + H$	4.0[b]
	$HCl + He^+$	$\rightarrow$	$Cl^+ + H + He$	3.3[c]
	$HCl + H_3^+$	$\rightarrow$	$H_2Cl^+ + H_2$	3.5[a]
	$HCl + HCO^+$	$\rightarrow$	$H_2Cl^+ + CO$	0.0004[f]
*	$HCl + C^+$	$\rightarrow$	$CCl^+ + H$	1.0[d]
	$HCl + CH_3^+$	$\rightarrow$	$H_2CCl^+ + H_2$	0.13[a,f]
*	$Cl^+ + H_2$	$\rightarrow$	$HCl^+ + H$	1.0[e]
	$HCl^+ + e^-$	$\rightarrow$	$Cl + H$	300.[b]
*	$HCl^+ + H_2$	$\rightarrow$	$H_2Cl^+ + H$	1.30[e]
	$H_2Cl^+ + e^-$	$\rightarrow$	$Cl + H_2$	150.[b]
	$H_2Cl^+ + e^-$	$\rightarrow$	$HCl + H$	150.[b]
*	$H_2Cl^+ + C$	$\rightarrow$	$CCl^+ + H_2$	0.5[b]
*	$H_2Cl^+ + C$	$\rightarrow$	$HCl + CH^+$	0.5[b]
	$H_2Cl^+ + S$	$\rightarrow$	$HCl + HS^+$	1.0[b]
*	$H_2Cl^+ + CO$	$\rightarrow$	$HCl + HCO^+$	0.73[a,f]
	$H_2Cl^+ + H_2O$	$\rightarrow$	$HCl + H_3O^+$	0.73[a]
	$CCl^+ + e^-$	$\rightarrow$	$Cl + C$	300.[b]
	$CCl^+ + C$	$\rightarrow$	$Cl + C_2^+$	1.0[b]
	$CCl^+ + N$	$\rightarrow$	$Cl + CN^+$	1.0[b]
*	$CCl^+ + O$	$\rightarrow$	$Cl + CO^+$	1.0[b]
	$CCl^+ + NH_3$	$\rightarrow$	$HCl + HCNH^+$	1.30[a]
	$CCl^+ + H_2CO$	$\rightarrow$	$H_2CCl^+ + CO$	0.53[a]
	$H_2CCl^+ + e^-$	$\rightarrow$	$Cl + CH_2$	300.[b]
	$H_2CCl^+ + C$	$\rightarrow$	$HCl + C_2H^+$	1.0[b]
*	$H_2CCl^+ + O$	$\rightarrow$	$HCl + HCO^+$	1.0[b]
	$H_2CCl^+ + H_2O$	$\rightarrow$	$HCl + H_3CO^+$	1.90[b]

* Most significant reactions.

[a]- Measured in this work.

[b]- Guessed reaction and estimated rate constant.

[c]- Bush, Y.A., McFarland, M., Albritton, D.L., and Schmeltekopf, A.L. (1973).

[d]- Anicich, V.G., Huntress, W.T., and Futrell, J.H. (1976); Watson, W.D., Anicich, V.G., and Huntress, W.T. (1976).

[e]- Smith, D. and Adams, N.G. (1981).

[f]- Smith, D. and Adams, N.G. (1985).

The Model

The procedure used to examine the interstellar chemistry of chlorine is essentially identical to that described by Thorne *et al.* (1984) in their study of interstellar phosphorus. The low fractional abundance of chlorine insures that, like phosphorus, its chemistry acts only as a small perturbation on the overall composition and chemistry of molecular clouds. Because of the low chlorine fractional abundance and the currently limited understanding of chlorine ion-molecule chemistry, a simple kinetic model has been constructed in place of a large-scale theoretical calculation. This model employs the results of previous laboratory, astronomical, and theoretical modeling efforts to effectively decouple the interstellar chlorine chemistry from those processes occurring among the more abundant first-row elements. The Runge-Kutta procedure used to examine interstellar phosphorus (Thorne *et al.* 1984) has been implemented on a VAX/11-780 computer to solve the set of kinetic equations listed in Table 4.4. Exothermic reactions included in the model which have not been measured experimentally are assigned rate coefficients of 1×10^{-9} cm^3s^{-1}. These would represent upper limits and therefore introduce the maximum effect of the predicted channels. Abundances for currently unobservable species are set to the values obtained by comprehensive chemical models of molecular clouds (Prasad and Huntress 1980; Graedel, Langer, and Frerking 1982; Leung, Herbst, and Huebner 1984), while those for the density dependent variables (ions) listed in Table 4.5 are calculated from equations incorporating the major production and destruction channels found from such theoretical models of oxygen-rich dense clouds ($10^3 < n < 10^6$ cm^{-3}.)

The model results for a cloud of "typical" composition with a density of 10^5 molecules cm^{-3} are presented in Table 4.6, and are quite similar to that found for phosphorus (Thorne *et al.* 1984). A significant amount of atomic material

Table 4.5
Constants and Density-Dependent Variables in the Chlorine Model

Constants		Density-Dependent Variables
γ	$= 1\ 10^{-17}\ s^{-1}$	$f_{H^+} \sim 5 \times 10^{-10}/n(f_O + f_{H_2O})$
f_{Cl}	$= 1\ 10^{-7}$	$f_{He^+} \sim 2.5\ 10^{-10}/nf_{CO}$
f_O	$= 5\ 10^{-5}$	$f_{O^+} \sim 2\ 10^{-11}/nf_{H_2O}$
f_C	$= 5\ 10^{-6}$	$f_{CH_3^+} \sim 5\ 10^{-11}/nf_O$
f_N	$= 2\ 10^{-6}$	$f_{H_3^+} + f_{HCO^+} \sim 3\ 10^{-12}/nf_e$
f_{CO}	$= 5\ 10^{-5}$	
f_{H_2O}	$= 2\ 10^{-6}$	
f_{NH_3}	$= 1\ 10^{-7}$	
f_{H_2CO}	$= 1\ 10^{-8}$	
f_e	$= 1\ 10^{-8}$	

remains and two neutral species, Cl and HCl, dominate the interstellar chlorine chemistry comprising about 99.9 % of the gas phase chlorine abundance. H_2Cl^+ and CCl^+ follow the neutral species in abundance, but are lower by at least a factor of 1000. The dominant production and loss channels for each species are marked by asterisks in Table 4.4 and are illustrated in Figure 4.3 which summarizes the important chlorine chemistry in dense clouds as judged by this reduced set of reactions. Again, none of the interstellar non-chlorine species are significantly affected by this chemistry because of the low fractional abundance of chlorine.

The prediction that HCl is a major component of the gas phase chlorine abundance in dense clouds is in agreement with astronomical observations, and shows that the species comprising interstellar chlorine differ significantly in diffuse and dense clouds. Several modifications to early chlorine models, which produced too much HCl and too little Cl^+, have been suggested to explain the lack of HCl in diffuse clouds. In these objects neutral atomic chlorine is ionized by the ambient UV field, and the resulting Cl^+ then produces the ionic precursor to hydrogen chloride, H_2Cl^+, via H-atom abstraction reactions with H_2:

Table 4.6
Chlorine Model Results

Species	Fractional Abundance (for $f_{\Sigma Cl} = 10^{-7}$)
Cl	3.8×10^{-8}
HCl	6.2×10^{-8}
Cl^+	1.2×10^{-17}
HCl^+	3.9×10^{-17}
H_2Cl^+	3.3×10^{-12}
CCl^+	2.4×10^{-13}
H_2CCl^+	1.3×10^{-15}

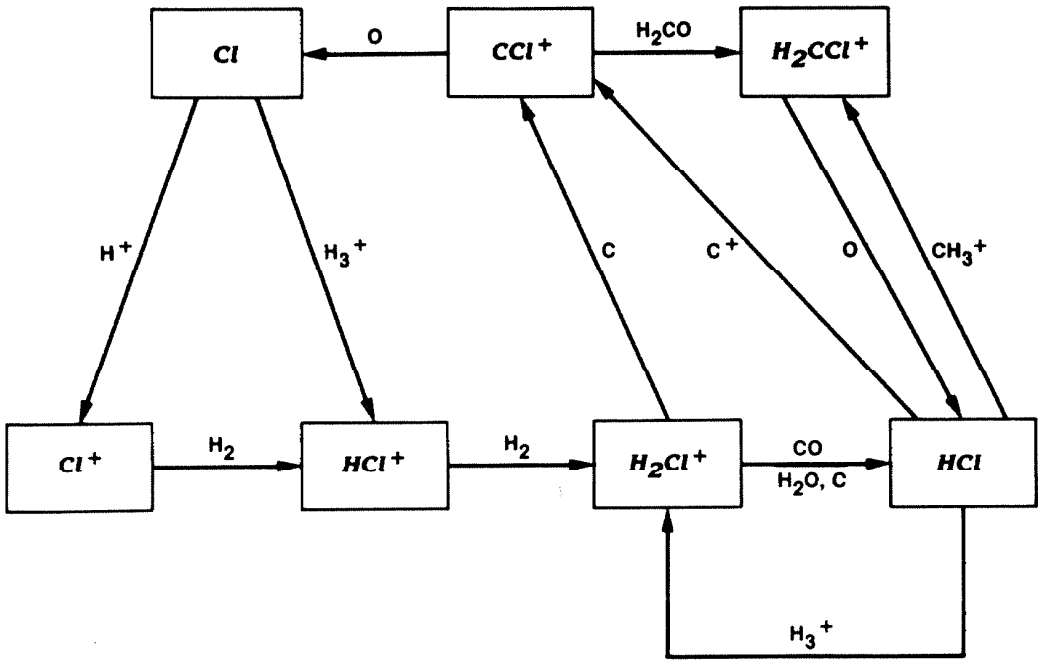

Figure 4.3: Summary of the reactions found to be important in the dense cloud model. The arrows indicate reaction pathways, with the species written next to the arrow indicating the other reactant involved in the bimolecular reaction.

$$Cl^+ + H_2 \rightarrow HCl^+ + H \qquad (4.9)$$

$$HCl^+ + H_2 \rightarrow H_2Cl^+ + H\,. \qquad (4.10)$$

The high electron abundance in diffuse clouds rapidly neutralizes H_2Cl^+, which does not react with H_2, producing Cl and HCl:

$$H_2Cl^+ + e^- \rightarrow Cl + H_2 \qquad (4.11a)$$

$$H_2Cl^+ + e^- \rightarrow HCl + H \qquad (4.11b)$$

The major loss channels for HCl are photodissociation and reaction with C^+. By including the C^+ channel, neglected in earlier models, increasing the HCl photodissociation rates, as has been suggested by recent ***ab initio*** calculations (van Dishoeck, van Hemert, and Dalgarno 1982), and using a small ($\lesssim$10 %) branching ratio into channel (3b), van Dishoeck (1984) has been able to drive the predicted HCl abundance to below the derived observational upper limits while simultaneously increasing the Cl^+ abundance to near that observed if a slow temperature dependent rate constant is used for reaction (4.9). Experimental measurements by Smith and Adams (1981), at temperatures as low as 80 K, indicate that both reactions (4.9) and (4.10) are reasonably temperature insensitive, but that reaction (4.9) is only mildly exothermic ($\Delta H \sim 5$ kcal/mole). A modest activation barrier cannot therefore be excluded at very low temperatures.

In dense clouds any atomic chlorine will remain predominantly neutral so the formation of hydrogen chloride is initiated mainly by the reaction of Cl and H_3^+:

$$Cl + H_3^+ \rightarrow HCl^+ + H_2 \qquad (4.12)$$

followed by reactions (4.10) and (4.11). A slow reaction between Cl^+ and H_2

would therefore not limit the production of HCl in dense clouds. The proton affinity of HCl, which is slightly below that of CO, implies that H_2Cl^+ will react rapidly with abundant interstellar neutral species such as CO and H_2O to produce HCl:

$$H_2Cl^+ + CO \rightarrow HCl + HCO^+ \qquad (4.13)$$

$$H_2Cl^+ + H_2O \rightarrow HCl + H_3O^+ \; . \qquad (4.14)$$

Even though the difference between the proton affinities of HCl and CO is very small ($\lesssim$ 3 kcal/mole), reaction (4.13) proceeds rapidly at 300 K (Table 1). Smith and Adams (1985) have also shown (4.13) to proceed rapidly at lower temperatures, but that the reverse reaction is very slow. For the low predicted electron abundance ($f(e^-) \sim 10^{-8}$) and high molecular content ($f(CO) \sim 10^{-4}$) of dense interstellar clouds, reactions (4.13) and (4.14) proceed at significantly faster rates than the electron recombination processes listed in (4.11a & b), and the impact of any reduction of the branching ratio into channel (4.11b) is small. Thus, the removal of H_2Cl^+ by electrons in dense, dark clouds is orders of magnitude less efficient than in diffuse clouds, and the production rates of chlorine-bearing molecules are correspondingly higher. One might therefore naively expect that chlorine would be fully associated into HCl in dense clouds as the major impediments to its production in diffuse clouds are no longer of importance. For the most part this is true, but several processes also act to limit the HCl fraction to about 50 % of the available chlorine abundance.

The largest HCl loss channels involve reactions of H_2Cl^+ with C, and HCl with C^+, both of which produce CCl^+. CCl^+ is isoelectronic with CS and quite stable. The IP of CCl is low and the CCl^+ ion is therefore relatively unreactive. Reaction with O, charge transfer to neutrals, and electron recombination are the most likely loss processes for CCl^+ in dense clouds. The net effect of these reactions,

as shown in Figure 4.3, is to regenerate Cl and to establish a reaction pathway which cycles the chlorine rapidly between Cl and HCl. All other species in this pathway have abundances which are quite small with respect to the neutral end-points. The steady-state abundance ratio of Cl to HCl is fairly insensitive to order of magnitude variations in the chemical composition of the model molecular cloud, being most sensitive to the abundance of C^+ and the rate constant used for the reaction of H_2Cl^+ with CO. The backward channel in reaction (4.13) is not important because proton transfer between HCl and H_3^+ occurs at a much faster rate, but the reaction of H_2Cl^+ and CO contributes substantially to the predicted HCl abundance. Even so, alteration of the C^+ abundance by factors of 10 and complete elimination of the proton transfer reaction between H_2Cl^+ and CO only changes the estimated fractional abundance of HCl by at most a factor of two, with the higher and lower C^+ abundances producing less or more HCl. Order of magnitude variations in other important reactants such as C, O, and e- produce even smaller changes in the predicted HCl abundance, on the order of 15 % or less. Under all of these conditions, the predicted fraction of gas phase chlorine present as HCl varies between 25 - 65 % in dense clouds. This produces an estimated fractional abundance of X(HCl) ~ 2.5 - 6.5 x 10^{-8} for a depletion factor of three, in good agreement with the observational estimates of 0.5 - 5.0 x 10^{-8}.

The prediction that Cl is also a major repository of chlorine in dense clouds, and that Cl and HCl by themselves constitute the overwhelming fraction of chlorine in such objects, may be tested by observing the fine structure transition of atomic chlorine at 11.3 μm in absorption towards such objects as BN or IRc 2 in Orion, or IRc+10216. The frequency of this transition is known to better than 0.3 km s^{-1} from infrared LMR work (Dagenais, Johns, and Mc Kellar 1976), and calculations indicate that for the suggested Cl abundance the optical depth of the fine structure transition should be near unity, making its detection

feasible with high resolution instruments.

Finally, the chlorine depletion in dense interstellar clouds may be estimated by combining the calculated model HCl fractional abundances with limits inferred from astronomical observations of the $J = 1 \rightarrow 0$ transition. For a cosmic chlorine abundance of 3×10^{-7} the models suggest that the chlorine depletion in Orion lies between 3 - 30. The large uncertainty arises mainly from difficulties associated with the astronomical observations and their interpretation. Jura and York (1978) find from optical studies that chlorine in diffuse clouds is depleted by no more than a factor of three, although more recent work by Tarafdar, Prasad, and Huntress (1983) and Harris, Gry, and Bromage (1984) argues that elemental depletion in clouds increases strongly with either the H_2 column density or number density and that chlorine may be depleted by a factor of five or more. In any case, the estimated chlorine depletion in dense clouds appears to be at most a factor of ten above that in diffuse clouds, which implies that, compared with other more refractory second-row elements like Si and P, gas phase chlorine species may well remain abundant even in the cores of dense molecular clouds.

4.2. The Plateau Source

In contrast to the relatively well-understood composition of the extended Orion molecular cloud, the abundances of various species in the plateau source have been interpreted as resulting from a wide variety of processes, all related to outflow driven by IRc 2. The basic difference in the chemistry of the ridge and the plateau sources is that the passage of shock waves in the latter, and the concomitant temperature increase, make the high-activation neutral-neutral reactions more important. Some molecules have their abundances markedly enhanced or reduced, while others remain nearly unchanged relative to the ambient cloud. A pictorial representation of the differing chemistry in the plateau and ridge sources is presented in Figure 4.4, which depicts the $^{13}CO/SO$ abundance ratio as a function of radial velocity and which also illustrates the method used in Chapter 3 to determine the plateau fractional abundances. As one can see, the SO abundance relative to CO increases sharply away from velocities characterizing the quiescent ridge clouds, but is roughly constant in the region with $\delta v \gtrsim 20$-25 km s^{-1} (δv = velocity offset from line center).

By performing such analyses on the many species found to exhibit high-velocity emission, the overall plateau chemical composition shown graphically in Figure 4.5 has been established, from which a number of general conclusions may be drawn. Emission from the reactive CI, CN, and C_2H species so prominent in the ambient gas is now undetectable, while the abundances of several oxygen-rich species like SiO, SO, and SO_2 are considerably enhanced. Unlike the chemistry discussed in Section 4.1, the plateau composition is most consistent with a region in which the gas phase C/O ratio is normal or high, as would be expected for an outflow from young, oxygen-rich stars or for rapid desorption from grains. Further support for this hypothesis are the observations of OI and CO in the high velocity shocked material surrounding the plateau source.

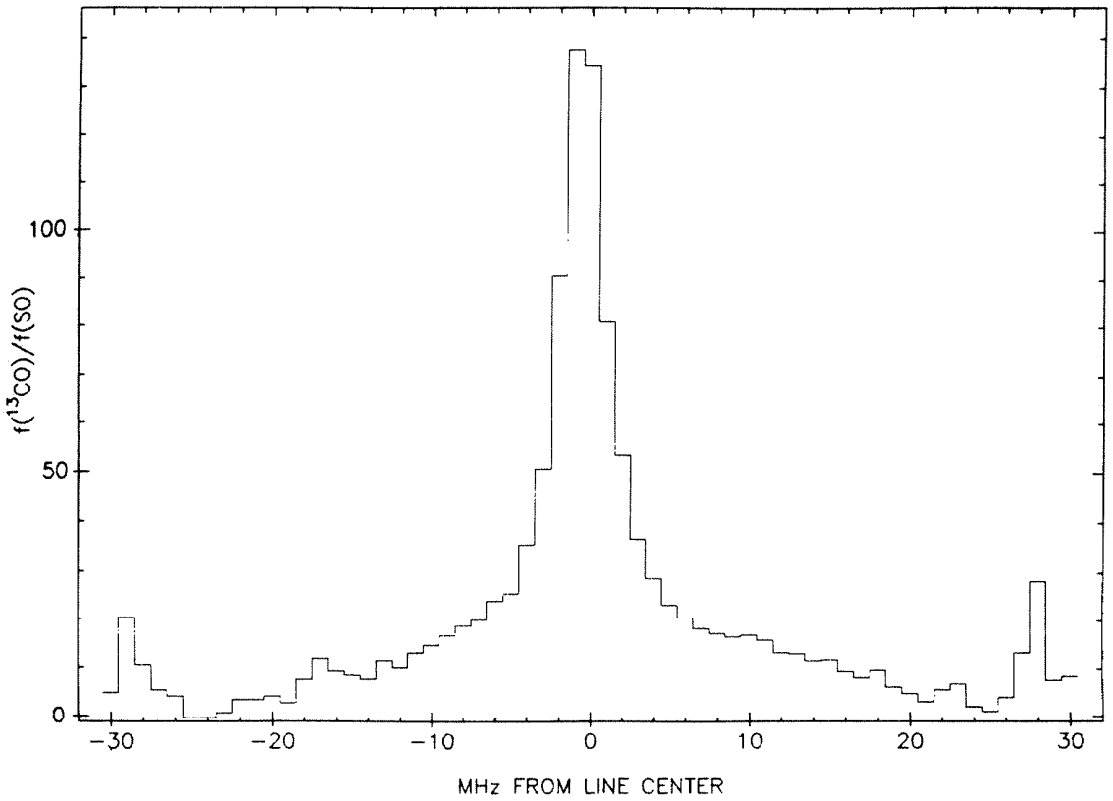

Figure 4.4: The CO/SO abundance as a function of offset frequency (velocity), illustrating the potentially large enhancements in sulfur compound relative abundances observed in the plateau.

Werner *et al.* (1984) conclude that if the [OI] 63.2 μm emission arises in the warm, post-shocked gas, the abundance of OI is $f(OI) \gtrsim 2 \times 10^{-4}$. For CO, Watson *et al.* (1985) find that $CO/H_2 = 0.8 - 1.5 \times 10^{-4}$ in the warm, post-shock gas. An even higher CO fractional abundance ($CO/H_2 \sim 5.5 \times 10^{-4}$) has been derived by Scoville *et al.* (1983), who infer from high resolution 4.6 μm infrared observations toward BN that all of the available carbon in the gas phase is in the form of CO. The estimated OI abundance is particularly high, and leads to a number of enhancements in other species.

Most dramatically enhanced are the silicon and sulfur species SiO, SO, SO_2, and H_2S whose relative abundances are greater than those in the quiescent gas by factors exceeding 100 (c.f. Figures 4.4 and 4.5). HDO, HCN, and HC_3N are enhanced by similar, though slightly smaller, amounts, while species such as CS,

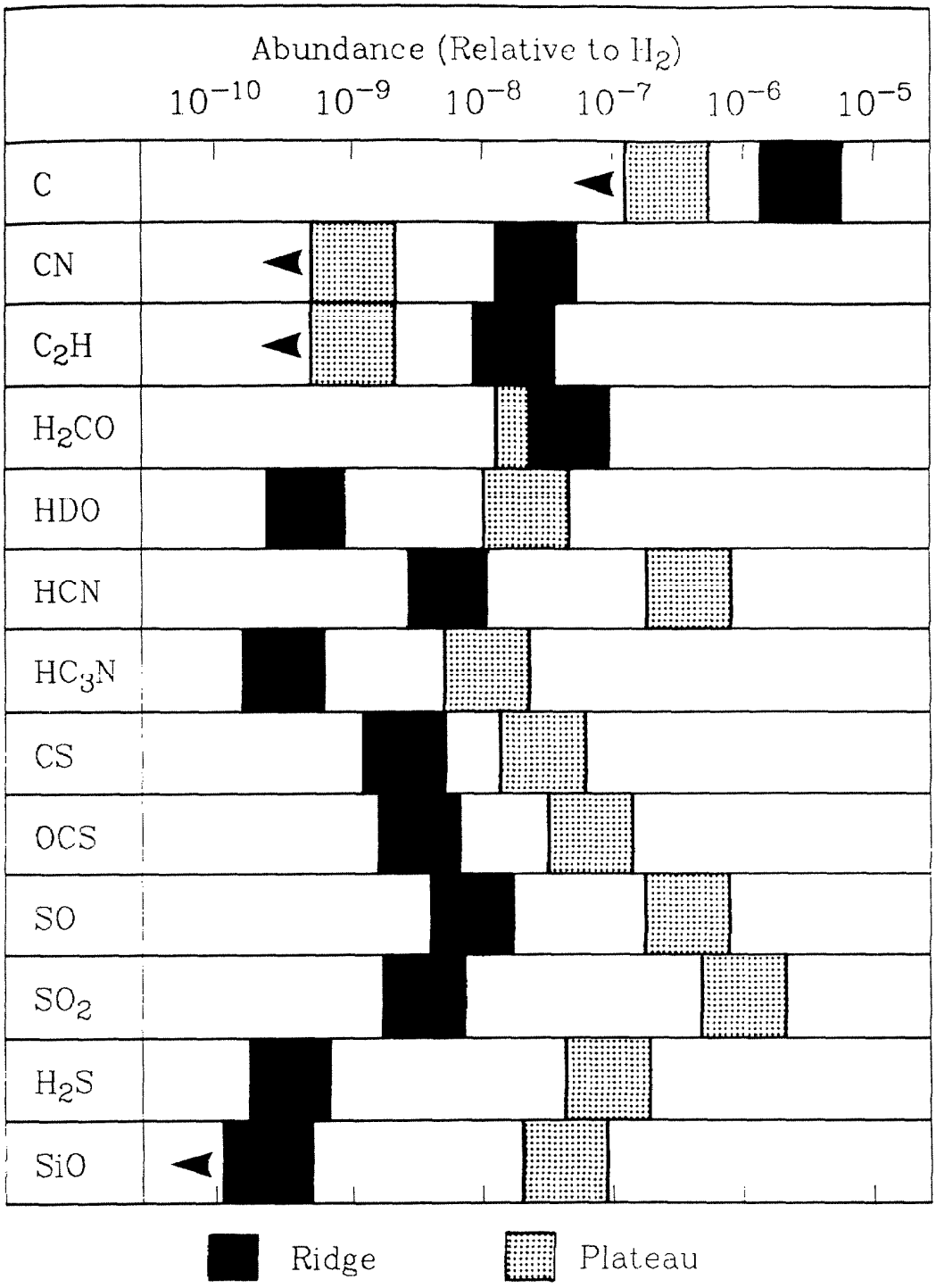

Figure 4.5: A comparison of the Orion ridge and plateau fractional abundances.

OCS, and H_2CO are only slightly enhanced. The low CS enhancement is further indication of a high gas-phase oxygen abundance in the plateau because, unlike SiO, OCS, or H_2S, it reacts rapidly with OI:

$$CS + O \rightarrow CO + S \qquad (4.15)$$

forming CO. The high sulfur abundances in the plateau have been interpreted by a number of authors as evidence for a shock-induced chemistry (Iglesias and Silk 1978; Hartquist, Oppenheimer, and Dalgarno 1980; Dalgarno 1982). That shocks exist in Orion is clear from the observations of vibrationally excited H_2 and far-infrared high-J CO emission. The apparent absence of hot gas in the "low-velocity" (18 km s^{-1}) outflow may simply be due to sensitivity and observational effects, since the high density in this source will rapidly cool the post-shocked region resulting in a very thin shock front with little column density. The chemical modifications arising from a propagating shock front last much longer (Iglesias and Silk 1978), but it is not clear from the observed chemistry that shocks have affected the bulk of the material in the 18 km s^{-1} outflow. Some species must clearly be formed very close to IRc 2 in a presumably less turbulent, high-temperature outflow more characteristic of circumstellar shells, as is illustrated by the SiO masers which lie only 70 AU from IRc 2 (Wright and Plambeck 1983). Further, the high fractional abundances of fragile species like HDO and H_2CO, which could not survive the passage of a strong shock front nor which would be created in significant amounts in the post-shock medium, illustrate that a significant fraction of the outflow material is contained in high-density clumps whose composition is not greatly altered from their initial states (Wootten, Loren, and Bally 1984). The plateau HDO content is a particularly good indication of density inhomogeneities, for although the expected shock-induced H_2O abundance is extremely high ($f(H_2O) \sim 2 \times 10^{-4}$), the degree of deuterium fractionation in the high temperature post-shocked gas is negligible, and

the resulting HDO abundance of $f(HDO) \lesssim 10^{-9}$ is well below the observed value.

Table 4.7
Theoretical Predictions of the Shocked and Quiescent Cloud Models

Species	Abundance relative to H_2 Hartquist *et al.*	Prasad and Huntress	Observed
	Shocked	Quiescent	
CS	4.7×10^{-8}	3.9×10^{-8}	2.5×10^{-8}
OCS	1.6×10^{-7}	2.4×10^{-8}	5.6×10^{-8}
SO	3.7×10^{-8}	5.5×10^{-7}	5.5×10^{-7}
SO_2	3.7×10^{-11}	8.8×10^{-7}	1.0×10^{-6}
H_2S	4.0×10^{-7}	2.3×10^{-9}	1.0×10^{-7}
SiO	2.5×10^{-8}	-	3.8×10^{-8}
HCN	2.0×10^{-8}	2.3×10^{-9}	4.5×10^{-7}
H_2O	2.0×10^{-4}	2.0×10^{-6}	$\lesssim 2.0 \times 10^{-5}$
H_2CO	$<1.0\ 10^{-11}$	$2.0\ 10^{-9}$	$2.0\ 10^{-8}$

Typical carbon star circumstellar abundances
$f(H_2S) = 5.3\ 10^{-7}$ $f(SiO) = \lesssim 6.0\ 10^{-7}$ $f(HCN) = 1.1\ 10^{-5}$

Prasad and Huntress (1982) have shown, moreover, that if one simply assumes a smaller depletion of the heavier elements, then "standard" ion-molecule and neutral-neutral reaction networks can account for much of the observed sulfur chemistry. A comparison of the shock-induced chemical models with the results from Prasad and Huntress, which assume a gas phase oxygen content of $f(O) \sim 5.5 \times 10^{-5}$ and a sulfur depletion of 10 ($f(\Sigma S) \sim 1.7 \times 10^{-6}$), is presented in Table 4.7. The model of Hartquist, Oppenheimer, and Dalgarno (1980) has been used for the oxygen and sulfur high-temperature shock chemistry, while the results of Iglesias and Silk (1978) have been used for the remaining species. For the simpler CS, SO, and OCS molecules the models are nearly identical, but major differences arise in the predicted abundances of HCN, H_2O, H_2S, and SO_2. In the quiescent cloud model all reactions which initiate the formation of H_2S, unlike those for H_2O, are quite endothermic and its predicted abundance is therefore rather low. The high kinetic temperatures associated with the post-shocked gas easily overcome such endothermicity barriers,

however, and the great thermodynamic stability of H_2S leads to the large predicted hydrogen sulfide abundance in the shock models. Similarly, the endothermic reaction

$$H_2 + CN \rightarrow HCN + H \qquad (4.16)$$

is quite rapid in the hot, shocked regions and is primarily responsible for the decreased CN and increased HCN abundances, but is negligible in the time dependent cloud models. Conversely, the shock models produce too little SO_2 because of the high OI abundance and the

$$SO_2 + O \rightarrow SO + O_2 \qquad (4.17)$$

reaction, while the standard cloud models reproduce the observed SO/SO_2 ratio extremely well. The (highly uncertain) observed H_2O abundance of $\sim 2 \times 10^{-5}$ (Phillips, Kwan, and Huggins 1980) lies between the upper and lower limits defined by the shock and cloud chemistry models, and the resulting fractionation ratio of $f(H_2O)/f(HDO) \sim 1000$ (compared to the extended cloud value of ~ 100) suggests that the outflow material is strongly clumped.

Also listed in Table 4.7 are the abundances found in circumstellar shells for the HCN, H_2S, and SiO species not well predicted by the cloud model. As these values show, a combination of high-temperature chemistry in the initial outflow close to the star with lower temperature ion-molecule and neutral-neutral processing of the dense gas in the outer outflow can mimic the large enhancements found in most shock models. It should also be noted that the SO_2 abundance in the shock models could be substantially increased by the inclusion of a stellar outflow chemistry. Little is actually known about the composition of circumstellar shells around oxygen-rich stars, and a general spectral line survey of such objects may yield a great deal of useful information on the contribution of circumstellar chemistry to the observed composition of the plateau source.

Perhaps, then, the most plausible scenario is one in which outflow from IRc 2 produces species like the SiO and OH or H_2O, which are manifest as masers immediately surrounding the star, while simultaneously accelerating the gas, raising its temperature and disrupting some of the smaller dust grains to liberate the more refractory elements such as silicon and sulfur. As the outflow expands into the partially evacuated cavity enveloping IRc 2, chemical reactions in the gas and in the shock fronts created where the outflow strikes the dense cavity walls produce the high observed abundances of SO, SO_2, HCN, H_2O, etc. Embedded in the outflow are dense clumps of gas and dust containing molecules such as HDO, H_2CO, and HC_3N. The temperature in these clumps is sufficient to release most molecules from the grain surfaces on which they condensed but not to destroy them, thereby offsetting the destruction of such species in the shocked regions of the less dense material. In any case, the similar predictions of the various models make it difficult to distinguish between them, meaning that any unbiased survey of shock activity in molecular clouds will not be easily undertaken.

4.3. The Hot Core

The crucial nature of gas-grain interactions to the chemistry of dense molecular clouds is perhaps most easily recognized here in the hot core region of Orion. Radiative heating from the luminous IRc 2 source passively induces temperatures of $\gtrsim$200-300 K, more than sufficient to release even the most tightly bound grain mantle constituents such as H_2O and NH_3. The high density and temperature of the hot core leads to a low fractional ionization of the gas (cf. eq. (4.6)) and therefore "shuts down" the ion-molecule reaction networks while increasing the importance of neutral-neutral processes. Any initial mixture of gas phase and grain produced species will therefore be driven rapidly toward kinetic equilibrium with the abundances of the most reactive species

markedly reduced. As the discussion in Section 4.1 should make clear, the evaporation of grain mantles will return the gas phase C/O ratio to near its cosmic value, thereby producing an oxygen-rich environment.

The observed hot core chemical composition summarized graphically in Figure 4.6 is, in general, consistent with the hypothesis that grain mantle evaporation and kinetic equilibrium dominate chemistry in the hot core. Just as in the plateau source the abundances of reactive carbon-rich species like CI, CS, CN, and C_2H are dramatically suppressed while the CO abundance is enhanced relative to the quiescent ridge clouds, indicating a high gas-phase oxygen content. However, the oxygen-rich species SiO, SO, and SO_2, which dominate the plateau chemistry, are not clearly detectable, but nitrogen-containing compounds such as HCN and NH_3 are very abundant. Where is the remaining oxygen? An analysis of the expected grain mantle composition provides some clues. Tielens and Hagen (1982) have calculated the molecular composition of adsorbed grain mantles under a wide variety of conditions. Their results, presented in Table 4.8 along with some observed hot core abundances, show that the final mantle composition depends sensitively on the nature of the accreting species. The two predicted abundance columns in Table 4.8 correspond to a set of cosmic elemental abundances and a set of depleted abundances as observed toward ζ Oph, and have been normalized using the 3.1 μm ice band absorption spectra of Knacke *et al.* (1982). The predicted abundances demonstrate that, as expected, the grain mantle is oxygen-rich.

If, as Tielens and Hagen assume, most of the carbon and nitrogen adsorbed onto the grain mantle is molecular in form, then the unobservable species CO_2 would contain the bulk of both the carbon and oxygen in the hot core. However, if a significant atomic population initially resides on the grains, then H_2O, NH_3, and CH_4 are the dominant mantle constituents. The H_2O hot core abundance

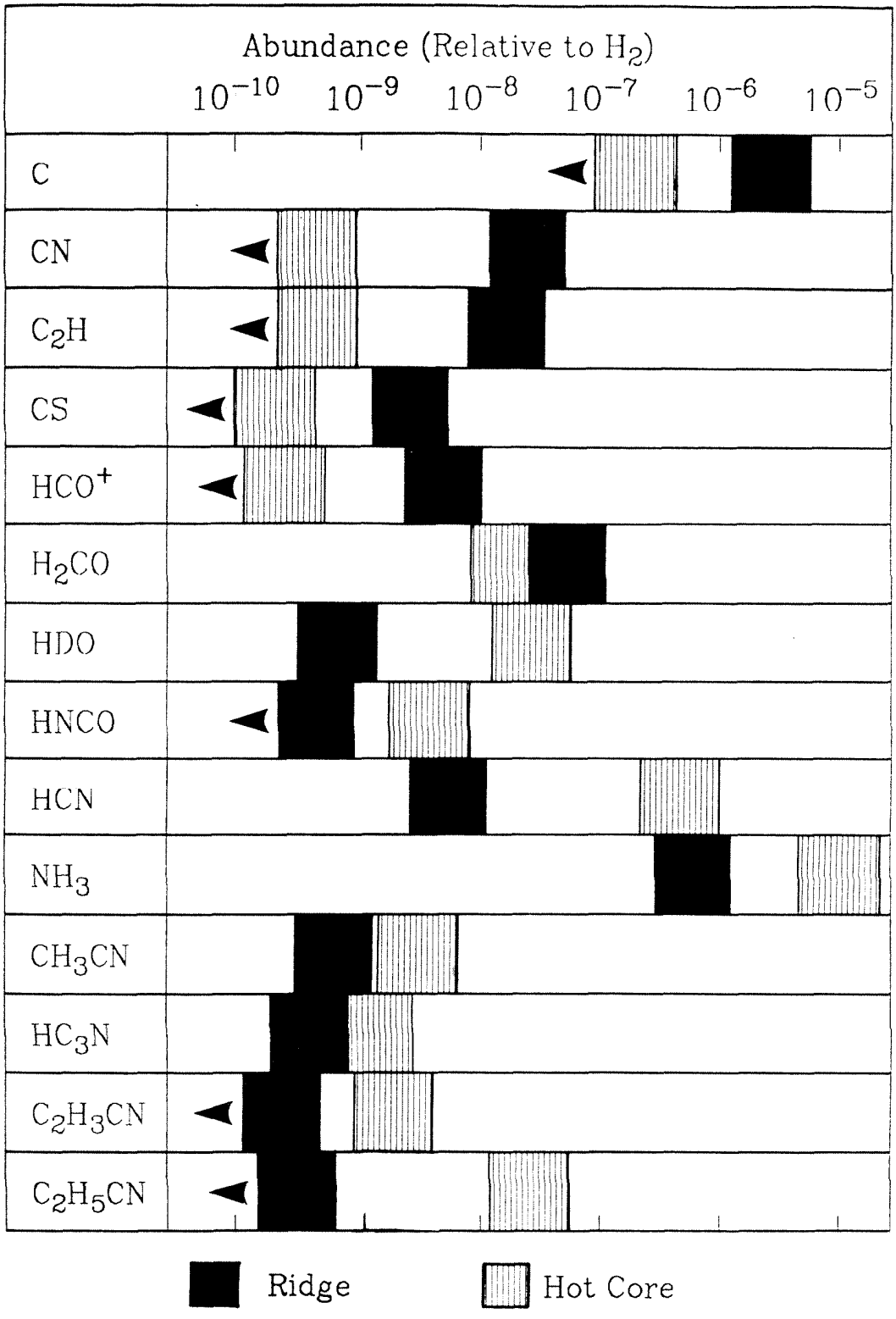

Figure 4.6: A comparison of the Orion ridge and hot core fractional abundances.

Table 4.8
Predicted Grain Mantle Compositions
and Some Observed Hot Core Abundances

Species	"Cosmic"	ζ Oph	Observed
N_2	1.1×10^{-5}	3.7×10^{-6}	-
O_2	1.4×10^{-7}	5.0×10^{-7}	$<1.0 \times 10^{-4}$[a]
CO	5.6×10^{-6}	1.7×10^{-7}	1.2×10^{-4}
H_2O	8.3×10^{-6}	4.0×10^{-5}	$\gtrsim 5.0 \times 10^{-6}$
CO_2	1.1×10^{-4}	3.6×10^{-6}	$<1.0 \times 10^{-5}$[b]
H_2CO	1.5×10^{-5}	1.7×10^{-5}	1.2×10^{-8}
NH_3	1.0×10^{-5}	4.8×10^{-7}	1.0×10^{-5}
CH_4	1.6×10^{-5}	2.7×10^{-9}	1.0×10^{-5}
H_2O_2	8.2×10^{-8}	1.4×10^{-6}	$<4.5 \times 10^{-10}$

[a]- From the $^{18}O^{18}O$ N = 2 → 0, J = 1 → 1 line at 233946 MHz.
[b]- Inferred from the related $HOCO^+$ ion.

must be estimated from the detected HDO species, and uncertainties in the residual fractionation introduce large errors into its estimated concentration. A lower bound of $f(H_2O) > 3 \times 10^{-6}$ is provided by the large fractionation observed in the HCN/DCN ratio in the hot core, while the deuterium fractionation observed in the plateau source gives an H_2O fractional abundance of $f(H_2O) \gtrsim 5 \times 10^{-5}$ or higher (Olofsson 1984). The large inferred values of $f(H_2O)$ and $f(NH_3)$ are more consistent with an initially atomic grain mantle composition, as is the low observed enhancement of the H_2CO abundance in the hot core and the quiescent cloud chemistry discussed earlier. In either case, the dominant oxygen carrier (CO_2 or H_2O) is relatively chemically inert and only observable with great difficulty. The OI abundance may also be appreciable, but the spectral and spatial resolution of present far-IR instruments is insufficient to separate the hot core from the strong foreground emission arising in the photodissociation region between M42 and OMC-1. Thus, nitrogen-containing species like HCN, HC_3N, and NH_3, that are so readily observable at millimeter wavelengths because of their simple rotational spectra and large dipole moments, dominate the spectral appearance of the hot core. Oxygen-rich sulfur species such as SO or SO_2 are not observed in the hot core because its passively achieved temperature,

while high enough to liberate the grain mantles, is insufficient to disrupt the highly refractory grain cores which are thought to contain most of the heavier elements like Si or S.

The abundances of several hot core species, particularly H_2O and NH_3, are well-matched by models incorporating complete evaporation of grain mantles, and are indicative of the high efficiency of hydrogenation of grain surfaces (Sweitzer 1978). For example, in their analysis of the 3.1 μm water ice bands observed toward TMC-1, Jones and Williams (1984) conclude that the conversion of $O \rightarrow H_2O$ on grain surfaces has an efficiency of greater than 70%. One might therefore expect fully hydrogenated, or saturated, species to dominate the hot core chemistry, and, as Figure 4.6 shows, they do. The abundances of HCN, NH_3, CH_3CN, C_2H_5CN, and HDO are all markedly higher in the hot core than in the quiescent clouds. The C_2H_3CN and C_2H_5CN molecules are most naturally explained by a grain surface production mechanism as gas phase reactions like

$$HC_3NH^+ + H_2 \rightarrow C_2H_3CN^+ + H \qquad (4.18a)$$

$$C_2H_3CN^+ + H_2 \rightarrow C_2H_4CN^+ + H \qquad \text{etc.} \qquad (4.18b)$$

are highly endothermic and proceed quite slowly (Herbst, Adams, and Smith 1983), while the hydrogenation of cyanoacetylene on grain surfaces should be fairly efficient. The fact that C_2H_3CN and C_2H_5CN are observed only in the hot core is further indication that they originate on grain surfaces, as only the hot core has temperatures that are sufficient to release them from the grain mantles. The observed ratios of $f(HC_3N/C_2H_3CN)$ and $f(HC_3N/C_2H_5CN)$ in the ridge and hot core sources suggest that the hydrogenation process prefers to completely saturate any cyanoacetylene deposited on the grain surface, and that the conversion efficiency is on the order of 25-75%.

From the abundances of chemically stable molecules such as HCN, H_2CO, and CH_3CN which are found in both the ridge and hot core components, limits may be placed on the degree of carbon and oxygen depletion in the cool, quiescent gas. The observed ratios suggest that the depletion of most simple carbon-rich species is not greater than a factor of ten in the ridge clouds near Orion-KL. The oxygen depletion is more difficult to assess because of the difficulty or impossibility of observing H_2O and CO_2, but it would appear to be much greater than the carbon depletion from observed abundances of HDO. These conclusions confirm the necessity for some mechanism which could remove molecules selectively from grain surfaces, but do not in any way constrain the possible alternatives.

4.4. The Compact Ridge Source

Yet another example of the chemical selectivity in OMC-1 is provided by the compact ridge source in which most of the large,oxygen-rich molecules found in Orion have their maximum abundance. The high HDO content of this source and the presence of other species such as SO and OCS strongly suggest that the compact ridge has been created by an interaction between outflowing material from the plateau and the quiescent 8 km s^{-1} cloud (cf. Section 3.3a). Such an interaction would naturally release the large gas-phase oxygen abundance required in the compact ridge. Carbon-rich species such as HCN or HC_3N are also undoubtedly present, but their extended emission "masks" any contribution from the more compact source. Since the oxygen-rich species do not appear to have an extended counterpart, they stand out more clearly to produce the spectral signature of the compact ridge source.

As an illustration of the unique chemistry of the compact ridge, Table 4.9 presents a comparison of the abundances found in this region with those

Table 4.9
Molecular Abundances in the Orion Compact Ridge and Sgr B2

Species	OMC-1	Sgr B2	Leung *et al.*	Steady State
CH_3CN	$6.7\ 10^{-10}$	$2.0\ 10^{-10}$	$8.1\ 10^{-10}$	$1.0\ 10^{-9}$
HCOOH	$3.3\ 10^{-10}$	$1.0\ 10^{-10}$	$4.6\ 10^{-9}$	$4.0\ 10^{-9}$
CH_3CHO	$\lesssim 1.7\ 10^{-10}$	$2.0\ 10^{-10}$	$2.1\ 10^{-10}$	$1.0\ 10^{-11}$
C_2H_5OH	$<5.0\ 10^{-10}$	$7.5\ 10^{-10}$	$4.1\ 10^{-11}$	$1.0\ 10^{-10}$
H_2CO	$5.0\ 10^{-8}$	$3.0\ 10^{-9}$	$1.5\ 10^{-8}$	$1.0\ 10^{-7}$
CH_3OH	$1.7\ 10^{-7}$	$3.1\ 10^{-8}$	$1.8\ 10^{-9}$	$2.0\ 10^{-7}$
$HCOOCH_3$	$1.1\ 10^{-8}$	$3.4\ 10^{-10}$	$1.0\ 10^{-11}$	$7.0\ 10^{-9}$
CH_3OCH_3	$1.0\ 10^{-8}$	$5.0\ 10^{-10}$	$1.9\ 10^{-11}$	$1.3\ 10^{-8}$

observed in another source of oxygen-rich molecules, Sgr B2 (Cummins, Linke, and Thaddeus 1985), and with the theoretical predictions of Leung, Herbst, and Huebner (1984). This comparison shows that the enhancements observed in the abundances of complex molecules in the compact ridge are not uniform but are, in fact, rather selective. Apparently simple species such as HCOOH and CH_3CHO have similar abundances in the two clouds and are well predicted theoretically, but other species like CH_3OH or $HCOOCH_3$ are significantly enhanced relative to other regions in Orion, Sgr B2, and the model predictions. Further, neither C_2H_5OH nor CH_3COOH has been detected in OMC-1, while their structural isomers CH_3OCH_3 and $HCOOCH_3$ are quite abundant. Thus, the mechanism which drives the oxygen chemistry in the compact ridge must be fundamentally different from those processes operating in the plateau or hot core regions, particularly in its ability to produce complex molecular species.

The very nature of the large molecules found in the compact ridge provides the key to an understanding of both the enhancement process and its chemical selectivity. As Herbst and Klemperer (1973), Huntress and Mitchell (1979), and Leung, Herbst, and Huebner (1984) have shown in their pioneering calculations, the most efficient formation routes to complex interstellar species are via

radiative association reactions of the type

$$A^+ + B \rightarrow AB^+ + h\nu \ . \qquad (4.19)$$

Radiative association reactions involving purely neutral reactants are considerably slower than the ion-molecule radiative association process depicted in eq. (4.19) because the neutral-neutral intermediate complex has a much shorter lifetime in which to stabilize itself radiatively. In addition, the spontaneous emission rates of even quite simple molecular ions appear to be significantly greater than their neutral counterparts, and such ions are therefore more easily stabilized radiatively (Herbst 1985). The rates of ion-molecule radiative association reactions are particularly sensitive to temperature with a temperature dependence of $T^{-(r_{A^+} + r_B)/2}$, provided the rotational state quantization may be ignored, where r_{A^+} and r_B are the rotational degrees of freedom of the reacting fragments. Regions with high temperatures or a small fractional ionization, such as the plateau and hot core components, do not therefore favor the production of large, complex molecules by radiative association reaction pathways. The lower temperature and intermediate density of the compact ridge is such, however, that radiative association reactions should still proceed rapidly. Combined with the increased oxygen content available from material introduced by the interaction with the outflow source, such reactions may be able to account for the high abundances and the remarkable degree of chemical selectivity found in the compact ridge.

Table 4.10 presents a listing of some of the most important radiative association reactions found in the model of Leung, Herbst, and Huebner (1984) for a kinetic temperature of 10 K. Uncertainties in the reaction rates are difficult to estimate, but a recent measurement of the $CH_3^+ + H_2$ reaction yielded a value of roughly five times the predicted rate constant (Barlow, Dunn, and Schauer

Table 4.10
Some Important Radiative Association Reaction Rates

Reaction	Rate ($cm^3\ s^{-1}$)
$CH_3^+ + HCN \rightarrow CH_3CNH^+$	$4.9\ 10^{-8}$
$CH_3^+ + H_2O \rightarrow CH_3OH_2^+$	$3.6\ 10^{-10}$
$C_2H_5^+ + H_2O \rightarrow C_2H_5OH_2^+$	$4.7\ 10^{-10}$
$HCO^+ + H_2O \rightarrow H_2COOH^+$	$6.7\ 10^{-12}$
$HCO^+ + CH_4 \rightarrow CH_3CHOH^+$	$1.5\ 10^{-12}$

1984), and the rates listed in Table 4.10 should provide useful lower bounds (Herbst 1985). The CH_3^+ ion is a particularly suitable partner in radiative association reactions as is evidenced by its rapid predicted reactions with HCN and H_2O, the products of which ultimately produce CH_3CN and CH_3OH. Because of the high HCN and H_2O abundances in the outflow and the prominence of CH_3^+ in the ion-molecule models of interstellar chemistry (Prasad and Huntress 1980; Leung, Herbst, and Huebner 1984), these reactions should substantially increase the abundances of both CH_3CN and CH_3OH. From the estimated reaction rates and the observed plateau fractional abundances a simple algebraic calculation predicts that $f(CH_3CN) \sim 10^{-9}$ and $f(CH_3OH) \sim 10^{-7}$ with enhancement timescales of $\gtrsim$100 years, substantially less than the inferred outflow age of 1000 years and in good agreement with the observed abundances. In contrast, the reaction rates leading to the formation of HCOOH, CH_3CHO, and C_2H_5OH are considerably slower (the $C_2H_5^+$ ion is substantially less abundant than CH_3^+), and even though HCO^+, H_2O, and CH_4 are quite abundant the expected enhancement time is $\gtrsim$1000 years. Thus, one expects CH_3CN and CH_3OH to have enhanced abundances while HCOOH, CH_3CHO, and C_2H_5OH should not be greatly affected, as is observed.

What of the other species observed in the condensed ridge? Except for H_2CO, most of these species are characterized by a CH_3O-R structure and are

intimately related chemically, as Figure 4.7 shows. The initial production of $CH_3OH_2^+$ from the radiative association of CH_3^+ and H_2 eventually leads to a number of other species. Except for this reaction and the interaction of $CH_3OH_2^+$ with H_2CO, all of the channels presented in Figure 4.7 are well understood. Reactions of the abundant CH_3OH and H_2CO neutral molecules with $CH_3OH_2^+$ selectively produces the ionic precursors to CH_3OCH_3 and $HCOOCH_3$, whose structures are shown in Figure 4.7. The creation of $C_2H_5OH_2^+$ or $CH_3COOH_2^+$ ions from the dimerization of methanol or the reaction of $CH_3OH_2^+$ with H_2CO would clearly require a great deal of structural rearrangement, and their probabilities are correspondingly low. Reactions with the abundant C^+ ion, such as that which produces H_2CO from CH_3OH, are not shown in Figure 4.7 but are the dominant loss channels of CH_3OCH_3 and $HCOOCH_3$, and lead back to CH_3OH. Thus, the H_2CO, CH_3OH, CH_3OCH_3, and $HCOOCH_3$ species are connected to each other chemically and will be similarly enhanced, while neither C_2H_5OH nor CH_3COOH will be produced.

A steady-state analysis of the reaction network outlined in Figure 4.7 is presented in Table 4.9 which quantitatively reflects the hypothesized enhancement process. If, as we have assumed, the recombination reactions of the precursor ions with electrons and the reactions of C^+ with the neutral species proceed at the same rates k_e and k_{C^+} (Huntress 1977), then the steady-state model leads to a number of very simple relationships between the abundances of the R-OCH_3 family. Specifically, we find that

$$\frac{[H_2CO]}{[CH_3OH]} = R \qquad (4.20a)$$

$$\frac{[HCOOCH_3]}{[CH_3OCH_3]} = \frac{[H_2CO]}{[CH_3OH]} \qquad (4.20b)$$

and

$$\frac{[CH_3OH]}{[CH_3OCH_3]} = \frac{k_e[e]}{k_{CH_3OH_2^+}[CH_3OH]} , \qquad (4.20c)$$

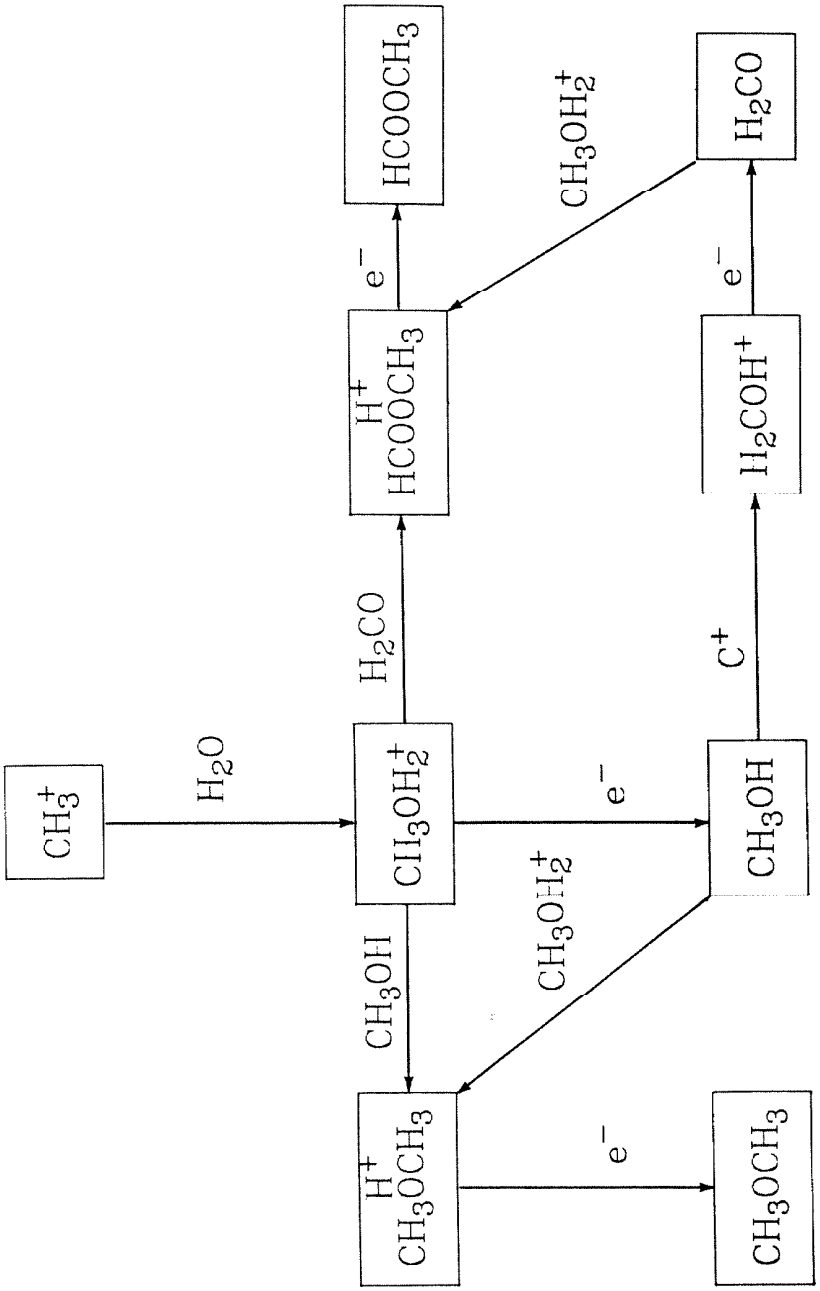

Figure 4.7: An illustration of the compact ridge oxygen-based chemistry.

where R is the branching ratio of the electron recombination reaction

$$H_2COH^+ + e^- \xrightarrow{R} H_2CO + H \qquad (4.21a)$$

$$H_2COH^+ + e^- \xrightarrow{1-R} H_2CO + H_2 \qquad (4.21b)$$

and k_e and $k_{CH_3OH_2^+}$ are the rate constants of the reactions of $CH_3OH_2^+$ with electrons and CH_3OH:

$$CH_3OH_2^+ + e^- \xrightarrow{k_e} CH_3OH + H \qquad (4.22)$$

$$CH_3OH_2^+ + CH_3OH \xrightarrow{k_{CH_3OH_2^+}} CH_3OCH_4^+ + H_2 \; . \qquad (4.23)$$

As Table 4.9 shows, the predicted abundances generally reproduce the observed abundances to within factors of 2-5. In particular, this simple model correctly predicts the ratio of CH_3OH to its heavier analogues $HCOOCH_3$ and CH_3OCH_3. The observed H_2CO/CH_3OH ratio implies that $R \lesssim 0.3$, where the upper limit arises because H_2CO also produced by the reaction of CH_3 with OI:

$$CH_3 + O \rightarrow H_2CO + H \; . \qquad (4.24)$$

This reaction has not been included in the steady-state model, but the high OI abundance in the plateau gas should make it a major source of formaldehyde. The greatest discrepancy between the observed and calculated abundances occurs for HCOOH, which the model predicts to be nearly as abundant as either $HCOOCH_3$ or CH_3OCH_3. Presumably this results from an overoptimistic value of the rate constant for the radiative association reaction that forms the ionic precursor to HCOOH (Table 4.10), since the abundances of the HCO^+ and H_2O reactants are known to be high.

The abundances of CH_3OH, CH_3OCH_3, and $HCOOCH_3$ in Sgr B2, while lower than those detected in Orion, are still considerably higher than predicted by the

model of Leung, Herbst, and Huebner (1984), and may indicate that similar processes operate in other giant molecular clouds in which embedded sources and molecular outflows are regularly observed. Orion may be somewhat special in that it contains a strong shock which produces considerable quantities of H_2O, but milder versions of the Orion outflow should also maintain a high gas-phase oxygen abundance in the cores of molecular clouds. The separation and selectivity of the chemistry in the various regions of OMC-1 is suggestive of a model of the chemistry and structure of molecular clouds in which the cooler and spatially extended halos of these objects contain most of the carbon-rich species while the active cloud cores liberate the more refractory elements depleted onto grains to produce the oxygen-rich molecules also widely observed in dense molecular clouds. Such species appear to be coincident in many clouds because of the weaker velocity structure of most objects and because of the limited spatial resolution that has been used to study them. A general interferometric survey of varying structure of dense molecular clouds would provide a most useful means of examining the generality of the chemical and physical processes at work in OMC-1.

Never aspire to too high a position,
you'll only regret it in the end.

- T.G. Phillips

5. SUMMARY

By combining a dedicated millimeter-wave spectral line survey with frequency selective submillimeter observations of important molecular hydrides, it has been possible to investigate the chemical composition of the Orion molecular cloud in considerable detail. Specifically, over 800 individual features from 33 distinct species have been identified, dramatically illustrating the usefulness of molecular rotational line emission in determining the chemical and physical nature of the interstellar medium. The emission from Orion is clearly resolvable into at least four distinct subsources whose chemical compositions differ markedly from each other:

(1) The cool and extended quiescent ridge gas is characterized by fairly simple carbon-rich species such as Cl, CN, C_2H, and HC_3N whose abundances are similar to that found in other well-studied objects like TMC-1 and Sgr B2. Its chemical composition is reasonably well predicted by purely gas phase ion-molecule reaction networks, although the relative constancy of the observed abundances in various objects and the low inferred gas phase oxygen content may be indicative of selective grain adsorption and desorption mechanisms.

(2) Abundances in the high-velocity plateau source are dominated, as expected, by outflow from IRc 2. Shock-induced chemistry clearly plays a role in the production of the highly enhanced abundances of the silicon and sulfur molecules SiO, SO, SO_2, and H_2S observed predominantly in this source, but the relative contributions of a more organized and quiescent high temperature circumstellar outflow or cloud embedded chemistry may

also be substantial. The significant fractional abundances of fragile species such as HDO and H_2CO, which could not survive the passage of a strong shock front, imply that the density structure of the outflow is quite inhomogeneous; and that even if shocks are prevalent, they do not process all of the material involved in the outflow from IRc 2.

(3) The hot core is interpreted as a particularly large and dense clump of gas left over from the formation of IRc 2 that has not yet been dispersed by the supersonic outflow. Its close proximity to IRc 2 accounts for its high density and temperature, which are sufficient to shut down the ion-molecule reaction networks and release all of the material adsorbed onto grain mantles. At such high temperatures neutral-neutral reactions become important and drive the chemistry toward kinetic equilibrium. Most of the oxygen in this source is tied up in the currently unobservable OI, H_2O, or CO_2 species, and easily detected nitrogen-rich compounds like NH_3 or CH_3CN therefore dominate its spectral appearance. Significant processing of the atoms and molecules adsorbed onto the grain mantles may have occurred, as is evidenced by the prevalence of fully hydrogenated species such as H_2O, HCN, NH_3, CH_3CN, and C_2H_5CN in the hot core as compared with the rest of the Orion molecular cloud.

(4) Finally, the production of complex oxygen-rich species such as CH_3OH in the compact ridge, which is formed by the interaction of the plateau source with the ambient molecular cloud, is accomplished via radiation association reactions between smaller molecular ions in the quiescent cloud material and highly abundant neutral species such as HCN and H_2O supplied by the outflow from IRc 2. The reaction between CH_3^+ and H_2O is particularly important as it leads to enhanced abundances of H_2CO, CH_3OH, CH_3OCH_3, and $HCOOCH_3$. A highly selective chemical composition is maintained in the

compact ridge by the greatly different rates of the ion-molecule radiative association reactions which initiate the formation sequences of the complex molecules. Other species similar to those found in the extended ridge cloud are also present, but the observed contrast is highest for the large oxygen-rich species because they are produced only in the compact ridge, thereby providing it with its unique spectral signature.

Similar mechanisms may also operate in other giant molecular clouds containing embedded sources, but due to its proximity and brightness Orion is likely to remain the testing ground upon which much of our knowledge of interstellar chemistry is based.

Somewhat surprisingly, of the over 800 emission lines detected in the Orion spectral line survey at least 96% of them may be attributed to well-known interstellar molecules. In fact, the number of species identified in Orion has actually decreased as the results of this survey have supplanted earlier exploratory work in the near millimeter wave region. More sensitive observations at these frequencies may eventually reveal a number of new species, but their identification will become extremely difficult because of the crowded nature of the millimeter-wave spectrum of Orion. Of the remaining unidentified lines, it is probably safe to say that at least some of them are due to the states of currently identified molecules whose spectra have not been fully characterized above 200 GHz.

Indeed, it has become clear during the course of this research that a great deal more laboratory work will be necessary before a full examination of the chemical composition of the interstellar medium may be attempted. Even for the intermediate frequencies at which the present survey was conducted only a dedicated combination of laboratory spectroscopy and theoretical predictions has allowed the majority of transitions from *known* molecules to be assigned.

Line searches in the higher frequency submillimeter region, in which the fundamental transitions of new species such as the potentially important molecular hydrides may be found, will become increasingly hampered by the limited amount of laboratory data, but may now be efficiently conducted because of the availability of accurate large aperture telescopes and sensitive high frequency receivers such as those which have made this thesis possible.

REFERENCES

Allen, M. and Robinson, G.W. 1977, *Ap. J.*, **212**, 396.

Amano, T. 1984, 39th Symposium on Molecular Spectroscopy, Columbus, paper TE3.

Angerhofer, P., Churchwell, E., and Porter, R.N. 1978, *Ap. Lett.*, **19**, 137.

Anicich, V.G., Huntress, W.T., and Futrell, J.H. 1976, *Chem. Phys. Lett.*, **40**, 233.

Barlow, S.E., Dunn, G.H., and Schauer, M. 1984, *Phys. Rev. Lett.*, **52**, 902.

Bastien, P., Bieging, J., Henkel, C., Martin, R.N., Pauls, T., Walmsley, C.M., and Ziurys, L.M. 1981, *Astr. Ap.*, **98**, L4.

Becklin, E.E. and Neugebauer, G. 1967, *Ap. J.*, **147**, 799.

Beckwith, S., Persson, S.E., Nuegebauer, G., and Becklin, E.E. 1978, *Ap. J.*, **223**, 464.

Blake, G.A., Sutton, E.C., Masson, C.R., Phillips, T.G., Herbst, E., Plummer, G.M., and De Lucia, F.C. 1984, *Ap. J.*, **286**, 586.

Blake, G.A., Keene, J., and Phillips, T.G. 1985, *Ap. J.*, **295**, in press.

Blake, G.A., Sutton, E.C., Masson, C.R., and Phillips, T.G. 1986, *Ap. J. Suppl.*, in press.

Bogey, M., Demuynck, C., Denis, M., Destombes, J.L., and Lemoine, B. 1984, *Astr. Ap.*, **137**, L15.

Boland, W., and de Jong, T. 1982, *Ap. J.*, **261**, 110.

Boland, W., de Graauw, T., Lidholm, S., and Lee, T.J. 1983, *Ap. J.*, **271**, 183.

Bowater, I.C., Brown, J.M., and Carrington, A. 1972, *Proc. R. Soc. Lond. A*, **333**, 265.

Brown, E.R. 1985, Ph.D. Thesis, California Institute of Technology.

Buhl, D. and Snyder, L.E. 1970, *Nature*, **228**, 1230.

Bush, Y.A., McFarland, M., Albritton, D.L., and Schmeltekopf, A.L. 1973, *J. Chem. Phys.*, **58**, 3504.

Cameron, R.M., Bader, M., and Mobley, R.E. 1971, *Appl. Opt.*, **10**, 2011.

Carney, G.D. and Porter, R.N. 1976, J. Chem. Phys., **69**, 3547.

Carney, G.D. 1980, *Chem. Phys.*, **54**, 103.

Cheung, A.C., Rank, D.M., Townes, C.H., Thornton, D.D., and Welch, W.J. 1968, *Phys. Rev. Lett.*, **21**, 1701.

Cheung, A.C., Rank, D.M., Townes, C.H., Thornton, D.D., and Welch, W.J. 1969, *Nature*, **221**, 626.

Cohen, R.S., Cong, H., Dame, T.M., and Thaddeus, P. 1980, Ap. J.(Letters), **239**, L53.

Cummins, S.E., Linke, R.A., and Thaddeus, P. 1985, submitted to *Ap. J.*

Dagenais, M., Johns, J.W.C., and Mc Kellar, A.R.W. 1976, *Can. J. Phys.*, **54**, 1438.

Dalgarno, A., Black, J.H., and Weisheit, J.C. 1973, *Ap. Lett.*, **14**, 77.

Dalgarno, A., Herbst, E., Novick, S., and Klemperer, W. 1973, Ap. J.(Letters), **183**, L131.

Dalgarno, A., de Jong, T., Oppenheimer, M., and Black, J.H. 1974, *Ap. J.(Letters)*, **192**, L37.

Dalgarno, A. 1982, *Phil. Trans. R. Soc. Lond. A*, **303**, 513.

d'Hendecourt, L.B., Allamandola, L.J., Baas, F., and Greenberg, J.M. 1982, *Astr. Ap.*, **109**, L12.

de Jong, T., Chu, S.I., and Dalgarno, A. 1975, *Ap. J.*, **199**, 69.

De Lucia, F.C., Helminger, P., and Gordy, W. 1971, *Phys. Rev. A*, **3**, 1849.

Dixon, T.A. and Woods, R.C. 1977, J. Chem. Phys., **67**, 3956.

Douglas, A.E. and Herzberg, G. 1941, *Ap. J.*, **94**, 381.

Downes, D., Genzel, R., Becklin, E.E., and Wynn-Williams, C.G. 1981, *Ap. J.*, **244**, 869.

Dunham, T. Jr. and Adams, W.S. 1937, *Publ. Am. Astr. Soc.*, **9**, 15.

Elias, J.H., Ennis, D.J., Gezari, D.Y., Hauser, M.G., Houck, J.R., Lo, K.Y., Matthews, K., Nadeau, D., Neugebauer, G., Werner, M.W., and Westbrook, W.E. 1978, *Ap. J.*, **220**, 25.

Erickson, N.R. 1977, *IEEE Trans. MTT*, **MTT-25**, 865.

Falgarone, E. and Puget, J.L. 1985, *Astr. Ap.*, **142**, 157.

Flower, D.R. and Watt, G.D. 1984, *Mon. Not. R. Astro. Soc.*, **209**, 25.

Frerking, M.A., Keene, J., Blake, G.A., Phillips, T.G., and Beichman, C.A. 1985, submitted to *Ap. J.*

Gautier, T.N. III, Fink, U., Treffers, R.R., and Larson, H.P. 1976, Ap. J.(Letters), **207**, L129.

Genzel, R., Reid, M.J., Moran, J.M., and Downes, D. 1981, *Ap. J.*, **244**, 884.

Genzel, R., Downes, D., Ho, P.T.P., and Bieging, J. 1982, *Ap. J.(Letters)*, **259**, L103.

Gillespie, C.M. Jr. 1981, *Proc. SPIE*, **265**, 1.

Glassgold, A.E., Huggins, P.J., and Shucking, E.L. 1982, *Proceedings of the Symposium on the Orion Nebula to Honor Henry Draper*, *Ann. N.Y. Acad. Sci.*, **395**.

Glassgold, A.E., Huggins, P.J., and Langer, W.D. 1985, *Ap. J.*, **290**, 615.

Goldsmith, P.F. and Linke, R.A. 1981, *Ap. J.*, **245**, 482.

Goldsmith, P.F., Krotkov, P.F., Krotkov, R., Snell, R.L., Brown, R.D., and Godfrey, P. 1983, *Ap. J.*, **274**, 183.

Graedel, T. E., Langer, W. D., and Frerking, M. A. 1982, *Ap. J. Suppl.* **48**, 321.

Gudeman, C.S. and Woods, R.C. 1982, *Phys. Rev. Lett.*, **48**, 1344.

Guélin, M., Langer, W.D., and Wilson, R.W. 1982, *Astr. Ap.*, **107**, 107.

Hall, D.N.B. 1984, *Galactic and Extragalactic Infrared Spectroscopy*, ed. Kessler, M.F. and Phillips, J.P., (D. Reidel), 267.

Harris, A.W., Gry, G., and Bromage, G.E. 1984, *Ap. J.*, **284**, 157.

Hartquist, T.W., Oppenheimer, M., and Dalgarno, A. 1980, *Ap. J.*, **236**, 182.

Herbst, E. and Klemperer, W. 1973, *Ap. J.*, **185**, 505.

Herbst, E. 1982, *Astr. Ap.*, **111**, 76.

Herbst, E. 1983, Ap. J. Suppl., **53**, 41.

Herbst, E., Adams, N.G., and Smith, D. 1983, *Ap. J.*, **269**, 329.

Herbst, E. 1985, *Ap. J.*, **291**, 226.

Hermsen, W., Wilson, T.L., Walmsley, C.M., and Batrla, W. 1985, *Astr. Ap.*, in press.

Hill, J. and Silk, J. 1975, Ap. J.(Letters), **202**, L97.

Hollenbach, D.J., Werner, M.W., and Salpeter, E.E. 1971, *Ap. J.*, **163**, 165.

Hollis, J. M., Snyder, L. E., Lovas, F. J., and Buhl, D. 1976, Ap. J.(Letters), **209**, L83.

Huntress, W.T. Jr. 1977, *Ap. J. Suppl.*, **33**, 495.

Huntress, W.T. Jr., and Mitchell, G.F. 1979, *Ap. J.*, **231**, 456.

Iglesias, E.R. and Silk, J. 1978, *Ap. J.*, **226**, 851.

Irvine, W.M. and Hjalmarson, A. 1984, *Origins of Life* (Dordrecht: Reidel), 15.

Irvine, W.M., Schloerb, F.P., Hjalmarson, A., and Herbst, E. 1985, preprint.

Jefferts, K.B., Penzias, A.A., and Wilson, R.W. 1973, *Ap. J.(Letters)*, **179**, L57.

Johansson, L.E.B., Andersson, C., Ellder, J., Friberg, P., Hjalmarson, A., Hoglund, B., Irvine, W.M., Olofsson, H., and Rydbeck, G. 1984, *Astr. Ap.*, **130**, 227.

Johnston, K.J., Palmer, P., Wilson, T.L., and Bieging, J.H. 1983, Ap. J.(Letters), **271**, L89.

Jones, A.P. and Williams, D.A. 1984, M. Not. Roy. Astr. Soc., **209**, 955.

Jura, M. 1974, *Ap. J.(Letters)*, **190**, L33.

Jura, M. and York, D.G. 1978, *Ap. J.*, **219**, 861.

Keene, J., Hildebrand, R.H., and Whitcomb, S.E. 1981, *Ap. J.(Letters)*, **252**, L11.

Keene, J., Blake, G.A., and Phillips, T.G. 1983, Ap. J.(Letters), **271**, L27.

Keene, J., Blake, G.A., Phillips, T.G., Huggins, P.J., and Beichman C.A. 1985, *Ap. J.*, in press.

King, W.C. and Gordy, W. 1954, *Phys. Rev.*, **93**, 407.

Kleinmann, D.W., and Low, F.J. 1967, Ap. J.(Letters), **149**, L1.

Klemperer, W. 1970, *Nature*, **227**, 1230.

Knacke, R.F., McCorkle, S., Puetter, R.C., Erickson, E.F., and Kratschmer, W. 1982, *Ap. J.*, **260**, 141.

Krolik, J.H., and Kallman, T.R. 1983, *Ap. J.*, **267**, 610.

Kuiper, T.B.H., Zuckerman, B., and Rodriguez-Kuiper, E.N. 1981, *Ap. J.*, **251**, 88.

Kutner, M.L., Tucker, K.D., Chin, G., and Thaddeus, P. 1977, *Ap. J.*, **215**, 521.

Langer, W.D., Graedel, T.E., Frerking, M.A., and Armentrout, P.B. 1984, *Ap. J.*, **277**, 581.

Lee, T.J. 1972, *Nature*, **237**, 99.

Leger, A., Jura, M., and Omont, A. 1985, *Astr. Ap.*, **144**, 147.

Leung, C.M. and Liszt, H.S. 1976, *Ap. J.*, **208**, 732.

Leung, C.M., Herbst, E., and Huebner, W.F. 1984, *Ap. J. Suppl.*, **56**, 231.

Linke, R.A., Frerking, M.A., and Thaddeus, P. 1978, Ap. J.(Letters), **234**, L139.

Linke, R.A., Guélin, M., and Langer, W.D. 1983, Ap. J.(Letters), **271**, L85.

Liszt, H.S., Wilson, R.W., Penzias, A.A., Jefferts, K.B., Wannier, P.G., and Solomon, P.M. 1974, *Ap. J.*, **190**, 557.

Lovas, F.J. 1984, private communication.

Masson, C.R. 1982, *Astr. Ap.*, **114**, 270.

Masson, C.R., Berge, G.L., Claussen, M.J., Heiligman, G.M., Leighton, R.L., Lo, K.Y., Moffet, A.T., Phillips, T.G., Sargent, A.I., Scott, S.L., Wannier, P.G., and Woody, D.P. 1984, Ap. J.(Letters), **283**, L37.

Masson, C.R., Claussen, M.J., Lo. K.Y., Moffett, A.T., Phillips, T.G., Sargent, A.I., Scott, S.L., and Scoville, N.Z. 1985, *Ap. J.(Letters)*, **297**, in press.

Matsakis, D.N., Cheung, A.C., Wright, M.C.H., Askne, J.I.H., Townes, C.H., and Welch, W.J. 1980, *Ap. J.*, **236**, 481.

McKellar, A. 1941, *Publ. Dom. Astr. Obs.*, **7**, 251.

Michels, H.H. and Hobbs, R.H. 1984, Ap. J.(Letters), **286**, L27.

Morris, M., Palmer, P., and Zuckerman, B. 1980, *Ap. J.*, **237**, 1.

O'Donnell, E.J. and Watson, W.D. 1974, *Ap. J.*, **191**, 89.

Oka, T. 1980a, *Phys. Rev. Letters*, **45**, 531.

Oka, T. 1980b, *Advances in Atomic and Molecular Physics*, **9**, 127.

Olofsson, H. 1984, *Astr. Ap.*, **134**, 36.

Payne, H.E., Salpeter, E.E., and Terzian, Y. 1985, preprint.

Penzias, A.A., Wilson, R.W., and Jefferts, K.B. 1974, *Phys. Rev. Lett.*, **32**, 701.

Penzias, A.A. 1981, *Ap. J.*, **249**, 518.

Phillips, T.G., Solomon, P.M., Huggins, P.J., and Blair, G. 1978, unpublished.

Phillips, T.G., Huggins, P.J., Kuiper, T.B.H., and Miller, R.E. 1980, Ap. J.(Letters), **238**, L103.

Phillips, T.G., Kwan, J., and Huggins, P.J. 1980, *Interstellar Molecules*, ed. B. Andrews (Reidel:Dordrecht), 21.

Phillips, T.G., and Huggins, P.J. 1981, *Ap. J.*, **251**, 533.

Phillips, T.G and Keene, J. 1982, *Workshop on the Scientific Importance of Submillimeter Observations*, **ESA SP-189**, 45.

Phillips, T.G. and Woody, D.P. 1982, *Ann. Rev. Astr. Ap.*, ed. Burbridge, G., Layzer, D., and Phillips, J.G. (Annual Reviews, Inc.), 285.

Plambeck, R.L., Wright, M.C.H., Welch, W.J., Bieging, J.H., Baud, B., Ho, P.T.P., and Vogel, S.N. 1982, *Ap. J.*, **259**, 617.

Poynter, R.L. and Pickett, H.M. 1984, *Submillimeter, Millimeter, and Microwave Spectral Line Catalogue*, JPL Publication 80-23, Revision 2.

Prasad, S.S. and Huntress, W.T., Jr. 1980, *Ap. J. Suppl.*, **43**, 1.

Prasad, S.S. and Huntress, W.T. Jr. 1982, *Ap J.*, **260**, 590.

Prasad, S.S. and Tarafdar, S.P. 1983, *Ap. J.*, **267**, 603.

Sanders, D.B., Solomon, P.M., and Scoville, N.Z. 1984, *Ap. J.*, **276**, 182.

Schloerb, F.P., Friberg, P., Hjalmarson, A., Hoglund, B., and Irvine, W.M. 1983, *Ap. J.*, **264**, 161.

Schmeltekopf, A.L., Fehsenfeld, F.C., and Ferguson, E.E. 1967, *Ap. J.(Letters)*, **148**, L155.

Scoville, N.Z. and Solomon, P.M. 1974, Ap. J.(Letters), **187**, L67.

Scoville, N.Z. and Kwan, J. 1976, *Ap. J.*, **206**, 718.

Scoville, N.Z., Kleinmann, S.G., Hall, D.N.B., and Ridgeway, S.T. 1983, *Ap. J.*, **275**, 201.

Shklovskii, I.S. 1949, *Astr. Zhurnal*, **XXVI**, 10.

Skatrud, D.D., De Lucia, F.C., Blake, G.A., and Sastry, K.V.L.N. 1983, J. Mol. Spec., **99**, 35.

Smith, D. and Adams, N.G. 1981, *Mon. Not. R. Astr. Soc.*, **197**, 377.

Smith, D., Adams, N.G., and Alge, E. 1982, *Ap. J.*, **263**, 123.

Smith, D. and Adams, N.G. 1984, Ap. J.(Letters), **284**, L13.

Smith, D. and Adams, N.G. 1985, private communication.

Snyder, L.E., Hollis, J.M., Zuckerman, B., and Palmer, P. 1969, *Phys. Rev. Lett.*, **22**, 679.

Snyder, L.E., Hollis, J.M., Lovas, F.J., and Ulich, B.L. 1976, *Ap. J.*, **209**, 67.

Sobolev, V.V. 1963, *A Treatise on Radiative Transfer* (Princeton:Van Nostrand).

Spitzer, L. Jr. 1978, *Physical Processes in the Interstellar Medium* (John Wiley & Sons).

Stecher, T.P. and Williams, D.A. 1967, Ap. J.(Letters), **149**, L29.

Sutton, E.C. 1983, *IEEE Trans. MTT*, **MTT-31**, 589.

Sutton, E.C., Blake, G.A., Masson, C.R., and Phillips, T.G. 1984, *Ap. J.(Letters)*, **283**, L41.

Sutton, E.C., Blake, G.A., Masson, C.R., and Phillips, T.G. 1985, *Ap. J. Suppl.*, **58**, 341.

Sweitzer, J.S. 1978, *Ap. J.*, **225**, 116.

Swings, P. and Rosenfield, L. 1937, *Ap. J.*, **86**, 483.

Tarafdar, S.P., Prasad, S.S., and Huntress, W.T., Jr. 1983, *Ap. J.*, **267**, 156.

Tarafdar, S.P., Prasad, S.S., Huntress, W.T., Villere, K.R., and Black, D.C. 1985, *Ap. J.*, **289**, 220.

Thaddeus, P., Kutner, M.L., Penzias, A.A., Wilson, R.W., and Jefferts, K.B. 1972, Ap. J.(Letters), **176**, L73.

Thaddeus, P. 1982, in *Proceedings of the Symposium on the Orion Nebula to Honor Henry Draper*, ed. Glassgold, A.E., Huggins, P.J., and Shucking, E.L., *Ann. N.Y. Acad. Sci.*, **395**, 9.

Thaddeus, P. 1985, private communication.

Thorne, L.R., Anicich, V.G., and Huntress, W.T. 1983, *Chem. Phys. Lett.*, **98**, 162.

Thorne, L.R., Anicich, V.G., Prasad, S.S., and Huntress, W.T., Jr. 1984, *Ap. J.*, **280**, 139.

Tielens, A.G.G.M. and Hagen, W. 1982, *Astr. Ap.*, **114**, 245.

Townes, C.H. 1954, *Washington Conf. on Radio Astr., J. Geophys. Res.*, **59**, 198.

Turner, B.E., Zuckerman, B., Fourikis, N., Morris, M., and Palmer, P. 1975, Ap. J.(Letters), **198**, L125.

van Dishoeck, E.F., van Hemert, M.C., and Dalgarno, A. 1982, *J. Chem. Phys.*, **77**, 3693.

van Dishoeck, E.F. 1984, Ph.D. Thesis, University of Leiden.

Wahlgren, U., Liu, B., Pearson, D.K., and Schaefer, H.F. 1973, *Nature*, **264**, 4.

Wannier, P.G., Linke, R.A., and Penzias, A.A. 1981, *Ap. J.*, **247**, 522.

Wannier, P.G., Penzias, A.A., and Jenkins, E.B. 1982, *Ap. J.*, **254**, 100.

Warner, H. E., Connor, W. T., Petrmickl, R. H., and Woods, R. C. 1984, *J. Chem. Phys.*, **81**, 2514.

Watson, D.M., Storey, J.W.V., Townes, C.H., Haller, E.E., and Hansen, W.L. 1980, Ap. J.(Letters), **239**, L129.

Watson, D.M. 1982, Ph.D. Thesis, University of California, Berkeley.

Watson, D.M., Genzel, R., Townes, C.H., and Storey, J.W.V. 1985, *Ap. J.*, **298**, in press.

Watson, W. 1973, *Ap. J.(Letters)*, **183**, L17.

Watson, W.D. 1976, *Rev. Mod. Phys.*, **48**, 513.

Watson, W.D., Anicich, V.G., and Huntress, W.T. 1976, *Ap. J.(Letters)*, **205**, L165.

Watt, G.D. 1985, *Mon. Not. R. Astr. Soc.*, **212**, 93.

Weinreb, S., Barret, A.H., Meeks, M.L., and Henry, J.C. 1963, *Nature*, **200**, 829.

Wengler, M.J., Woody, D.P., Miller, R.E., and Phillips, T.G. 1985, *Int. J. Infra. Mill. Waves*, **6**, no. 8, 697.

Werner, M.W., Dinerstein, H.L., and Capps, R.W. 1983, Ap. J.(Letters), **265**, L13.

Werner, M.W., Crawford, M.K., Genzel, R., Hollenbach, D.J., Townes, C.H., and Watson, D.M. 1984, Ap. J.(Letters), **282**, L81.

Westbrook, W.E., Werner, M.W., Elias, J.H., Gezari, D.Y., Hauser, M.G., Lo, K.Y., and Neugebauer, G. 1976, *Ap. J.*, **209**, 94.

Whittet, D.C.B., Bode, M.F., Longmore, A.J., Baines, D.W.T., and Evans, A. 1983, *Nature*, **303**, 218.

Williams, D.A., and Hartquist, T.W. 1984, *Mon. Not. R. Astr. Soc.*, **210**, 141.

Wilson, R.W., Jefferts, K.B., and Penzias, A.A. 1970, Ap. J.(Letters), **161**, L43.

Winnewisser, G., Churchwell, E., and Walmsley, C.M. 1979, *Modern Aspects of Microwave Spectroscopy*, ed. Chantry, G.W. (Academic Press), 313.

Woods, R.C., Dixon, T.A., Saykally, R.J., and Szanto, P.G. 1975, *Phys. Rev. Lett.*, **35**, 1269.

Wootten, A., Evans, N.J., Snell, R., and Vanden Bout, P. 1978, Ap. J.(Letters), **225**, L143.

Wootten, A., Bozyan, E.P., Garrett, D.B., Loren, R.B., and Snell, R.L. 1980a, *Ap. J.*, **239**, 844.

Wootten, A., Snell, R., and Evans, N.J. 1980b, *Ap. J.*, **240**, 532.

Wootten, A., Loren, R.B., and Snell, R.L. 1982, *Ap. J.*, **255**, 160.

Wootten, A., Loren, R.B., and Bally, J. 1984, *Ap. J.*, **277**, 189.

Wright, M.C.H., Plambeck, R.L., Vogel, S.N., Ho, P.T.P., and Welch, W.J. 1983, Ap. J.(Letters), **267**, L41.

Wright, M.C.H. and Plambeck, R.L. 1983, Ap. J.(Letters), **267**, L115.

Wynn-Williams, C.G., Genzel, R., Becklin, E.E., and Downes, D. 1984, *Ap. J.*, **281**, 172.

Zuckerman, B. 1973, *Ap. J.*, **183**, 863.

Zuckerman, B., Kuiper, T.B.H., and Rodriguez-Kuiper, E.N. 1976, Ap. J.(Letters), **209**, L137.

APPENDIX A - THE ROTATIONAL EMISSION LINE SPECTRUM OF OMC-1 BETWEEN 215 AND 263 GHz*

A1.1 Observations

The Orion spectral line survey observations were carried out with the 1.3 mm spectroscopy system of the Owens Valley Radio Observatory, and were centered on a nominal source position of $\alpha(1950) = 05^h32^m47^s$, $\delta(1950) = -05°24'21''$. The 10.4 m telescope beam size was approximately 0.5' averaged over the 215 to 247 GHz range and slightly under 0.5' throughout the 250 - 265 GHz region. A superconducting tunnel junction (SIS) receiver (Sutton 1983), operated in the double sideband mode with an IF center frequency of 1388 MHz, served as the front end and provided a noise temperature between 300 - 700 K (SSB) throughout the observing band, while a 512 channel AOS similar to that described by Masson (1982) was used as the back end. The fixed AOS channel width of 1.03 MHz yielded a resolution of 1.3 km s^{-1} at 230 GHz, and 1.2 km s^{-1} at 250 GHz.

The raw double sideband spectra reported here were recorded during a series of observing sessions in the winters of 1982-1983 and 1983-1984, and were processed into a single sideband spectrum with the "cleaning" procedure described in section A1.2a. Some 111 double sideband spectra from a total of 28 nights were used in the final data set. Due to insufficient observing time, gaps near 249, 252, and 254 GHz exist in the spectrum. The double sideband spectra have been calibrated for telescopic and atmospheric losses using standard "chopper wheel" techniques. We estimate an uncertainty of approximately ± 15% for the corrected double sideband data. The line brightness temperatures of the various Orion emission regions cannot be properly estimated using a single beam efficiency correction, however, because of their differing size. We have

*Condensed from Sutton *et al.* (1985) and Blake *et al.* (1986).

therefore established the final antenna temperature scale using the extended source efficiency of η~0.85, derived from maps of the Moon. No corrections have been made for the beam dilution of spatially compact sources, such as the plateau and hot core components.

The procedure used to separate the receiver sidebands (Section A1.2a) improves the accuracy of the overall calibration. Since each line is observed in several spectra, the detected line strengths are used to correct the relative calibration. In general the relative calibration is much better ($\lesssim$5%) over small ~1 GHz intervals in the spectrum and deteriorates to the original ±15% uncertainty over intervals greater than about 5 GHz.

A1.2. Analysis

A1.2a. Reduction to SSB Information

Each double sideband (DSB) spectrum, considered by itself, has an unavoidable confusion as to the sideband in which each feature falls and hence its frequency. However, by observing a large set of frequencies spaced closely enough that each individual line is observed several times, it is possible to deconvolve the set of double sideband spectra into one "cleaned" single sideband spectrum. For example, if a line is seen in one spectrum, its assignment as a lower sideband feature can be determined by whether it appears (e.g., in the upper sideband) in other appropriate spectra.

This type of analysis was automated using an algorithm similar to that used for "cleaning" aperture synthesis maps. First the strongest feature in the entire spectrum was found, based on the naive assumption that the observed DSB temperatures were due to equal contributions from the two sidebands. A small fraction (~0.3) of the strength of this feature was then subtracted from all the DSB spectra in which it should have appeared. This procedure, applied on a

channel by channel basis, was repeated iteratively until the noise level in the data was reached. It was necessary to treat the ^{12}CO line at 230538 MHz in a special way because of its great strength and breadth, and, as a result, the image sidebands of the ^{12}CO observations (approximately 227497-227543 MHz and 233453-233497 MHz) have somewhat worse signal-to-noise since the data folded into the ^{12}CO line have been ignored.

In order for this procedure to work it is necessary to know precisely the gains of the individual spectra. Relative gains were determined by comparing the observed strengths of the strongest lines in all of the spectra in which they appear. Incorrect gain settings would leave false peaks (ghosts) in the image sidebands. A few false peaks as strong as about 0.5 K remain in the spectrum, mostly between 215 and 247 GHz, implying a dynamic range of about 15-20 dB for this "cleaning" procedure.

If the double sideband data are taken by stepping the local oscillator by the full width of the back end, then each line will appear at most twice, once each in the upper and lower receiver sidebands. The data between 215 and 249 GHz were collected in this manner, namely, by stepping the local oscillator in 500 MHz increments, although a number of additional scans were also recorded at intermediate local oscillator frequencies in the 215-247 GHz interval. The disadvantage of this procedure is that large regions of the spectrum (at the two ends) were represented by only a single observation. Hence it was difficult to insure good separation of the data from the two sidebands. Also, even in the center region lines were often observed only twice, which at times was insufficient when both instances were coincident with the lines in the opposite sidebands.

It quickly became obvious in the data analysis that a more densely spaced set of observations would be advantageous, particularly where the density of

lines was expected to be high. Since this was expected to be especially true for the higher frequency band above 250 GHz, spectra in this region were spaced 250 MHz apart instead of the previous 500 MHz. Integration times were shortened to about 500 seconds per spectrum instead of 1000 seconds, maintaining a uniform 0.2 - 0.3 K RMS noise level per resolution element. The resulting single sideband spectrum was indeed less troubled by false ghosts due to improper sideband separation, despite the generally more intense and crowded spectrum.

As with any deconvolution procedure the results are not unique. However, we have several reasons to trust the results obtained here. The convolving function is particularly simple, corresponding to a set of delta functions. Each sky frequency will appear in precisely defined places in a small number of spectra. The deconvolution is similarly straightforward, assuming that all of the gains are well known. Ambiguities arise primarily from the treatment of the ends of the spectrum. The algorithm converges to the same result with moderate variations in parameters such as the loop gain (the amount subtracted per iteration), and the vast majority of the resulting features can be identified with transitions of molecules known to exist in the interstellar medium. A few unidentified lines are present and the strongest of these have been individually examined to confirm their presence in the original DSB data. In general, the single sideband spectrum is thought to be trustworthy down to about 0.3 K.

A1.2b. Line Assignments

The millimeter wave spectral line catalogues of F.J. Lovas (1984) and the Jet Propulsion Laboratory (Poynter and Pickett 1984) have served as the primary sources of reference for our initial line assignments. The difficulties associated with predicting the spectra of the heavier and more complex internal rotors such as CH_3OH and $HCOOCH_3$ did require some additional laboratory

spectroscopy as well, however. Many measurements in this frequency range have been kindly provided by F.C. De Lucia, E. Herbst, and Grant M. Plummer of Duke University and K.V.L.N. Sastry of the University of New Brunswick, particularly for $HCOOCH_3$ (Plummer *et al.* 1984, 1985) and CH_3NH_2 (Sastry *et al.* 1985). A number of laboratory measurements were also performed on CH_3OH at JPL to investigate the possibility that high J methanol transitions were responsible for some of the unidentified lines in our survey (Blake and Pickett 1985).

The combination of supporting laboratory spectroscopy with the existing spectral line catalogues has permitted the identification of nearly all the lines detected in Orion. Only 16 unidentified lines remain in the upper frequency scan, and a total of 33 are left in the entire survey of over 780 detected transitions. We suspect that many of the presently unidentified lines may be due to the excited torsional states or isotopic variants of abundant internal rotors such as CH_3OCH_3, $HCOOCH_3$, or CH_3OH whose rotational spectra are not predictable at present (Blake *et al.* 1984). We would like especially to emphasize that without this supporting laboratory work, ***hundreds*** of lines from known interstellar species would have remained unidentified in our surveys.

A2.1. Results

The reduced single-sideband spectrum is presented in Figure A1. A total of 787 resolvable molecular lines, which we ascribe to 28 distinct species, have been detected and labeled in Figure A1. Table A1 presents a list of the detected lines in order of frequency together with the molecules to which the emission is assigned and the laboratory rest frequencies of the associated rotational transitions. Unidentified lines have been assigned rest frequencies based on a v_{LSR} of 8 km s^{-1}. Further data on the exact line frequencies, transition quantum numbers, and emission strengths are contained below.

Table A1

Transitions: 215 - 263 GHz

Frequency (MHz)	Species	Frequency (MHz)	Species	Frequency (MHz)	Species	Frequency (MHz)	Species
215041	C_2H_5CN	218452	C_2H_3CN	220815	$HCOOCH_3$	222248	CH_3OCH_3
215059	C_2H_5CN	218476	H_2CO	220889	$HCOOCH_3$	222255	CH_3OCH_3
215088	C_2H_5CN	218574	C_2H_3CN	220926	$HCOOCH_3$	222259	unidentified
215109	C_2H_5CN	218585	C_2H_3CN	220978	$HCOOCH_3$	222314	CH_2CO
215119	C_2H_5CN	218615	C_2H_3CN	221048	$HCOOCH_3$	222422	$HCOOCH_3$
215127	C_2H_5CN	218760	H_2CO	221066	$HCOOCH_3$	222427	CH_3OCH_3
215173	C_2H_5CN	218861	$HC_3N(\nu_7=1)$	221124	C_2H_3CN	222435	CH_3OCH_3
215221	SO	218903	OCS	221141	$HCOOCH_3$	222439	$HCOOCH_3$
215302	$CH_3OH(\nu_t=1)$	218981	HNCO	221158	$HCOOCH_3$	222707	C_2H_5CN
215401	C_2H_5CN	219174	$HC_3N(\nu_7=1)$	221199	$CH_3CN(\nu_8=1)$	222723	unidentified
215428	C_2H_5CN	219276	SO_2	221252	$CH_3CN(\nu_8=1)$	222918	C_2H_5CN
215620	C_2H_5CN	219355	$^{34}SO_2$	221261	$HCOOCH_3$	223038	$HCOOCH_3$
215840	^{34}SO	219401	C_2H_3CN	221266	$HCOOCH_3$	223119	$HCOOCH_3$
215886	unidentified	219464	C_2H_5CN	221281	$HCOOCH_3$	223125	$HCOOCH_3$
215966	C_2H_5CN	219506	C_2H_5CN	221300	$CH_3CN(\nu_8=1)$	223135	$HCOOCH_3$
216000	$^{34}SO_2$	219547	HNCO	221312	$CH_3CN(\nu_8=1)$	223163	$HCOOCH_3$
216077	C_2H_3CN	219560	$C^{18}O$	221338	$CH_3CN(\nu_8=1)$	223202	CH_3OCH_3
216110	$HCOOCH_3$	219657	HNCO	221350	$CH_3CN(\nu_8=1)$	223385	C_2H_5CN
216116	$HCOOCH_3$	219734	HNCO	221368	$CH_3CN(\nu_8=1)$	223434	SO_2
216211	$HCOOCH_3$	219737	HNCO	221381	$CH_3CN(\nu_8=1)$	223554	C_2H_5CN
216217	$HCOOCH_3$	219798	HNCO	221387	$CH_3CN(\nu_8=1)$	223650	CH_3CHO
216569	H_2CO	219909	$H_2{}^{13}CO$	221394	$CH_3CN(\nu_8=1)$	223661	CH_3CHO
216643	SO_2	219949	SO	221404	$CH_3CN(\nu_8=1)$	223884	SO_2
216710	H_2S	220038	HCOOH	221425	$CH_3CN(\nu_8=1), HCOOCH_3$	223916	HCOOH
216830	$HCOOCH_3$	220079	CH_3OH	221433	$HCOOCH_3$	223934	C_2H_5CN
216839	$HCOOCH_3$	220167	$HCOOCH_3$	221446	$HCOOCH_3$	224002	C_2H_5CN
216937	C_2H_3CN	220178	CH_2CO	221626	$CH_3CN(\nu_8=1)$	224018	C_2H_5CN
216946	CH_3OH	220190	$HCOOCH_3$	221650	$HCOOCH_3$	224023	$HCOOCH_3$
216966	$HCOOCH_3$	220399	^{13}CO	221660	$HCOOCH_3$	224028	C_2H_5CN
217105	SiO	220476	CH_3CN	221671	$HCOOCH_3$	224046	C_2H_5CN
217239	DCN	220539	CH_3CN	221675	$HCOOCH_3$	224086	C_2H_5CN
217300	unidentified	220561	C_2H_3CN	221736	$^{34}SO_2$	224132	C_2H_5CN
217817	SiS ?	220585	HNCO	221768	C_2H_3CN	224186	C_2H_5CN
217823	unidentified	220594	CH_3CN	221965	SO_2	224207	C_2H_5CN
217830	^{33}SO	220621	$CH_3{}^{13}CN$	222099	CH_3CCH	224265	SO_2
217887	unidentified	220634	$CH_3{}^{13}CN$	222129	CH_3CCH	224313	$HCOOCH_3$
218199	$O^{13}CS$	220641	CH_3CN	222150	CH_3CCH	224327	$CH_2CO, HCOOCH_3$
218222	H_2CO	220661	C_2H_5CN	222154	C_2H_3CN	224420	C_2H_5CN
218281	$HCOOCH_3$	220679	CH_3CN	222163	CH_3CCH	224459	C_2H_5CN
218298	$HCOOCH_3$	220709	CH_3CN	222167	CH_3CCH	224469	C_2H_5CN
218325	HC_3N	220730	CH_3CN	222177	unidentified	224493	unidentified
218390	C_2H_5CN	220743	CH_3CN	222198	CH_2CO	224583	$HCOOCH_3$
218422	C_2H_3CN	220747	CH_3CN	222229	CH_2CO	224609	$HCOOCH_3$
218440	CH_3OH	220812	$HCOOCH_3$	222239	CH_3OCH_3	224640	C_2H_5CN

Table A1 - continued

Frequency (MHz)	Species	Frequency (MHz)	Species	Frequency (MHz)	Species	Frequency (MHz)	Species
224699	unidentified	227815	unidentified	231952	C_2H_3CN	234502	$HCOOCH_3$
224714	$C^{17}O$	227898	C_2H_3CN	231967	$HCOOCH_3$	234509	$HCOOCH_3$
224895	unidentified	227907	C_2H_3CN	231988	CH_3OCH_3	234683	CH_3OH
225154	SO_2	227919	C_2H_3CN	231990	C_2H_5CN	234698	CH_3OH
225236	C_2H_5CN	227963	C_2H_3CN	232163	unidentified	234739	$HCOOCH_3$
225413	$OC^{34}S$	227977	$HC_3N(\nu_7=1)$	232216	$^{13}CH_3CN$	234936	PN ?
225513	HCOOH	228091	C_2H_3CN	232230	$^{13}CH_3CN$	235030	$HCOOCH_3$
225599	CH_3OCH_3	228105	C_2H_3CN	232234	$^{13}CH_3CN$	235047	$HCOOCH_3$
225609	$HCOOCH_3$	228303	$HC_3N(\nu_7=1)$	232419	CH_3OH	235051	$HCOOCH_3$
225619	$HCOOCH_3$	228483	C_2H_5CN	232784	CH_3OH	235152	SO_2
225625	unidentified	228544	HCOOH	232790	C_2H_5CN	235261	unidentified
225698	H_2CO	228629	$HCOOCH_3$	232945	CH_3OH	235564	C_2H_3CN
225897	HDO	228651	$HCOOCH_3$	232965	C_2H_5CN	235845	$HCOOCH_3$
225929	$HCOCCH_3$	228798	C_2H_5CN	232976	C_2H_5CN	235866	$HCOOCH_3$
226257	C_2H_3CN	228911	DNC	233000	C_2H_5CN	235881	$^{13}CH_3OH$
226300	SO_2	228979	CH_3OCH_3	233041	C_2H_5CN	235887	$HCOOCH_3$
226333	CN	228983	CH_3OCH_3	233069	C_2H_5CN	235928	$^{34}SO_2$
226342	CN	229087	C_2H_3CN	233089	C_2H_5CN	235932	$HCOOCH_3$
226347	CH_3QCH_3	229265	C_2H_5CN	233145	C_2H_5CN	235938	$^{13}CH_3OH$
226360	CN	229348	SO_2	233207	C_2H_5CN	235952	$^{34}SO_2$
226384	unidentified	229405	$HCOOCH_3$	233227	$HCOOCH_3$	235960	$^{13}CH_3OH$
226436	unidentified	229420	$HCOOCH_3$	233310	$HCOOCH_3$	235971	$^{13}CH_3OH$
226552	CH_3CHO	228475	$HCOOCH_3$	233395	$HCOOCH_3$	235997	$^{13}CH_3OH$
226593	CH_3CHO	229505	$HCOOCH_3$	233443	C_2H_5CN	236006	$^{13}CH_3OH$
226617	CN	229590	unidentified	233498	C_2H_5CN	236008	$^{13}CH_3OH$
226634	CN, $HCOOCH_3$	229648	C_2H_3CN	233507	$HCOOCH_3$	236017	$^{13}CH_3OH$
226660	CN	229759	CH_3OH	233524	$C_2H_5CN, HCOOCH_3$	236041	$^{13}CH_3OH$
226664	CN	229858	$^{34}SO_2$	233628	$HCOOCH_3$	236050	$^{13}CH_3OH$
226679	CN	229864	CH_3OH	233650	$HCOOCH_3$	236062	$^{13}CH_3OH$
226713	$HCOOCH_3$	229939	CH_3OH	233655	$HCOOCH_3$, C_2H_5CN	236217	SO_2
226719	$HCOOCH_3$	230027	CH_3OH	233671	$HCOOCH_3$	236356	$HCOOCH_3$
226773	$HCOOCH_3$	230233	unidentified	233754	$HCOOCH_3$	236366	$HCOOCH_3$
226779	$HCOOCH_3$	230318	$O^{13}CS$	233778	$HCOOCH_3$	236513	HC_3N
226857	$HCOOCH_3$	230369	CH_3OH	233796	CH_3OH	236717	HCOOH
226862	$HCOOCH_3$	230468	CH_3OCH_3	233845	$HCOOCH_3$	236726	H_2CS
226875	CN	230538	CO	233854	$HCOOCH_3$	236744	$HCOOCH_3$
226887	CN	230738	C_2H_3CN	233867	$HCOOCH_3$	236760	$HCOOCH_3$
226892	CN	231061	OCS	234011	$HCOOCH_3$, $^{13}CH_3OH$	236801	$HCOOCH_3$
226905	CN	231199	$HCOOCH_3$	234112	$HCOOCH_3$	236810	$HCOOCH_3$
227020	$HCOOCH_3$	231221	^{13}CS	234125	$HCOOCH_3$	236936	CH_3OH
227028	$HCOOCH_3$	231239	$HCOOCH_3$	234135	$HCOOCH_3$	236977	unidentified
227032	$^{34}SO_2$	231281	CH_3OH	234187	SO_2	237049	CH_3OCH_3
227095	unidentified	231312	C_2H_5CN	234291	unidentified	237069	SO_2
227419	HC_3N	231506	HCOOH	234329	$HCOOCH_3$	237093	$HC_3N(\nu_7=1)$
227562	$HCOOCH_3$	231654	C_2H_5CN	234422	SO_2, C_2H_5CN	237131	unidentified
227781	C_2H_5CN	231901	H30α	234486	$HCOOCH_3$	237170	C_2H_3CN

Table A1 - continued

Frequency (MHz)	Species	Frequency (MHz)	Species	Frequency (MHz)	Species	Frequency (MHz)	Species
237267	$HCOOCH_3$	239746	CH_3OH	241562	HDO	243747	unidentified
237273	$OC^{34}S$	239777	$CH_3CN(\nu_8=1)$	241616	SO_2	243916	CH_3OH
237298	$HCOOCH_3$	239792	$CH_3CN(\nu_8=1)$	241700	CH_3OH	244048	H_2CS
237308	$HCOOCH_3$	239809	$CH_3CN(\nu_8=1)$	241767	CH_3OH	244254	SO_2
237315	$HCOOCH_3$	239816	C_2H_3CN	241774	HNCO	244331	CH_3OH
237345	$HCOOCH_3$	239825	$CH_3CN(\nu_8=1)$	241791	CH_3OH	244338	$CH_3OH(\nu_t=1)$
237350	$HCOOCH_3$	239830	$CH_3CN(\nu_8=1)$	241807	CH_3OH	244482	$^{34}SO_2$
237405	C_2H_5CN, C_2H_3CN	239836	$CH_3CN(\nu_8=1)$	241813	CH_3OH	244580	$HCOOCH_3$
237432	$HC_3N(\nu_7=1)$	239850	$CH_3CN(\nu_8=1)$	241831	CH_3OH	244594	$HCOOCH_3$
237456	C_2H_3CN	239872	$CH_3CN(\nu_8=1)$	241843	CH_3OH	244712	CH_2CO
237484	C_2H_3CN	240021	$HCOOCH_3$	241852	CH_3OH	244857	C_2H_3CN
237591	C_2H_3CN	240035	$HCOOCH_3$	241879	CH_3OH	244936	CS
237621	CH_3OCH_3	240090	$CH_3CN(\nu_8=1)$	241888	CH_3OH	245179	$^{34}SO_2$
237712	C_2H_3CN	240186	CH_2CO	241904	CH_3OH	245223	CH_3OH
237808	$HCOOCH_3$	240242	CH_3OH	241923	C_2H_5CN	245302	$^{34}SO_2$
237830	$HCOOCH_3$	240266	H_2CS	241933	C_2H_5CN	245339	SO_2
237852	C_2H_5CN	240319	C_2H_5CN	241947	CH_3OCH_3	245563	SO_2
237983	$^{13}CH_3OH$	240331	H_2CS	241959	C_2H_5CN	245606	HC_3N
238017	unidentified	240381	H_2CS	241970	C_2H_5CN	245651	$HCOOCH_3$
238156	$HCOOCH_3$	240393	H_2CS	241986	$^{34}SO_2$	245752	$HCOOCH_3$
238190	$HCOOCH_3$	240429	C_2H_5CN	241997	C_2H_5CN	245772	$HCOOCH_3$
238727	C_2H_3CN	240548	H_2CS	242048	C_2H_5CN	245883	$HCOOCH_3$
238766	CH_3CN	240861	C_2H_5CN	242077	unidentified	245885	$HCOOCH_3$
238796	C_2H_3CN	240876	HNCO	242102	C_2H_5CN	245904	$HCOOCH_3$
238844	CH_3CN	240943	SO_2	242167	C_2H_5CN	246055	$HCOOCH_3$
238913	CH_3CN	240961	$CH_3OH(\nu_t=1)$	242209	C_2H_5CN	246061	$HCOOCH_3$
238927	$HCOOCH_3$	240978	CH_3OCH_3	242376	CH_2CO	246075	CH_3OH
238972	CH_3CN	240984	CH_3OCH_3	242399	CH_2CO	246106	HCOOH
238993	SO_2	240990	CH_3OCH_3	242425	CH_2CO	246269	C_2H_5CN
239001	$CH_3{}^{13}CN$	241016	$C^{34}S$	242446	CH_3OH	246285	$HCOOCH_3$
239015	$CH_3{}^{13}CN$	241146	HCOOH	242470	C_2H_5CN	246295	$HCOOCH_3$
239023	CH_3CN	241159	$CH_3OH(\nu_t=1)$	242490	CH_3OH	246308	$HCOOCH_3$
239064	CH_3CN	241167	$CH_3OH(\nu_t=1)$	242536	CH_2CO	246422	C_2H_5CN
239097	CH_3CN	241179	$CH_3OH(\nu_t=1)$	242547	C_2H_5CN	246549	C_2H_5CN
239120	CH_3CN	241184	$CH_3OH(\nu_t=1)$	242640	HNCO	246561	$HC_3N(\nu_7=1)$
239133	CH_3CN	241187	$CH_3OH(\nu_t=1)$	242665	C_2H_5CN	246600	$HCOOCH_3$
239138	CH_3CN	241193	$CH_3OH(\nu_t=1)$	242872	$HCOOCH_3$	246613	$HCOOCH_3$
239179	CH_3CCH	241197	$CH_3OH(\nu_t=1)$	242898	$HCOOCH_3$	246623	$HCOOCH_3$
239211	CH_3CCH	241205	$CH_3OH(\nu_t=1)$	242914	$C^{33}S$	246663	^{34}SO
239234	CH_3CCH	241211	$CH_3OH(\nu_t=1)$	243088	SO_2	246873	CH_3OH
239248	CH_3CCH	241238	$CH_3OH(\nu_t=1)$	243218	OCS	246891	$HCOOCH_3$
239252	CH_3CCH	241268	$CH_3OH(\nu_t=1)$	243398	CH_3OH	246897	C_2H_3CN
239627	$CH_3CN(\nu_8=1)$	241441	$CH_3OH(\nu_t=1)$	243413	CH_3OH	246915	$HCOOCH_3$
239683	C_2H_5CN	241509	$^{34}SO_2$	243523	$SO_2(\nu_2=1)$	246918	C_2H_3CN
239708	C_2H_3CN	241524	CH_3OCH_3	243643	C_2H_5CN	246925	HDCO
239732	unidentified	241530	CH_3OCH_3	243740	unidentified	246952	C_2H_3CN

Table A1 - continued

Frequency (MHz)	Species	Frequency (MHz)	Species	Frequency (MHz)	Species	Frequency (MHz)	Species
247003	C_2H_3CN	248282	CH_3OH	255071	C_2H_5CN	256448	C_2H_3CN
247041	$HCOOCH_3$ E	248365	$^{34}SO_2$	255121	CH_3OH	256523	C_2H_3CN
247044	$HCOOCH_3$ E	248437	C_2H_5CN,SO_2	255173	CH_3OH	256527	C_2H_3CN
247053	$HCOOCH_3$ A	248529	C_2H_3CN	255194	CH_3OH	256585	HDCO
247057	$HCOOCH_3$ A	248617	$HCOOCH_3$ A	255204	CH_3OH	256712	C_2H_3CN
247063	$HCOOCH_3$ E	248634	$HCOOCH_3$ E	255215	CH_3OH	256837	C_2H_3CN
247087	C_2H_3CN	249887	CH_3OH	255221	CH_3OH	256878	^{34}SO
247162	CH_3OH	249924	CH_3OCH_3	255242	CH_3OH	256967	C_2H_5CN (tent.)
247228	CH_3OH	250050	$^{13}CH_3CN$	255256	CH_3OH	257033	CH_3CN
247271	C_2H_3CN	250074	$^{13}CH_3CN$	255324	HC_3N (ν_7=1)	257100	SO_2
247440	$^{34}SO_2$	250088	$^{13}CH_3CN$	255374	OCS	257127	CH_3CN
247469	Unidentified	250092	$^{13}CH_3CN$	255479	$HC^{18}O^+$	257211	CH_3CN
247611	CH_3OH	250246	$HCOOCH_3$ E	255553	SO_2	257227	$HCOOCH_3$ E
247630	Unidentified	250258	$HCOOCH_3$ A	255602	NS,SO_2?	257240	C_2H_5CN
247636	Unidentified	250291	CH_3OH	255651	Unidentified	257253	$HCOOCH_3$ A
247657	$HCOOCH_3$ E	250358	$^{34}SO_2$	255689	HC_3N (ν_7=1)	257255	^{29}SiO
247665	$HCOOCH_3$ A	250440	C_2H_5CN,NO	255776	$HCOOCH_3$ E	257285	CH_3CN
247683	$HCOOCH_3$ E	250483	NO(tent.)	255789	$HCOOCH_3$ A	257311	C_2H_5CN
247697	$HCOOCH_3$ A	250507	CH_3OH	255907	C_2H_5CN	257349	CH_3CN
247704	$HCOOCH_3$ E	250635	CH_3OH	255958	SO_2	257380	$CH_3{}^{13}CN$
247708	$HCOOCH_3$ A	252803	CH_3OH	256027	HCS^+	257403	CH_3OH,CH_3CN
247799	C_2H_3CN	252896	C_2H_5CN	256229	CH_3OH	257420	SO_2 (tent.)
247840	CH_3OH	253206	^{34}SO	256247	SO_2	257448	CH_3CN
247875	Unidentified	253221	CH_3OH	256293	CH_3CCH	257483	CH_3CN
247902	$HCOOCH_3$ E	254423	CH_3OH	256317	CH_3CCH	257508	CH_3CN
247907	$HCOOCH_3$ A	254574	SO	256332	CH_3CCH	257522	CH_3CN
247911	Unidentified	254700	HC_3N	256337	CH_3CCH	257527	CH_3CN
247922	$HCOOCH_3$ E	254960	CH_3OH	256396	C_2H_5CN,C_2H_3CN	257584	C_2H_5CN
247927	$HCOOCH_3$ A	254976	C_2H_5CN	256409	C_2H_3CN	257646	C_2H_5CN
248057	SO_2	255050	HDO	256426	C_2H_3CN	257690	$HCOOCH_3$ E

Table A1 - continued

Frequency (MHz)	Species	Frequency (MHz)	Species	Frequency (MHz)	Species	Frequency (MHz)	Species
257699	$HCOOCH_3$ A	259114	$HCOOCH_3$ E	260156	C_2H_5CN	261844	SO
257749	HDCO	259128	$HCOOCH_3$ A	260192	CH_2CO	261898	CH_3OCH_3
257912	Unidentified	259138	$HCOOCH_3$ E	260222	C_2H_5CN	261956	CH_3OCH_3
257975	HCOOH	259233	C_2H_5CN	260229	C_2H_5CN	261959	CH_3OCH_3
258054	CH_3CN (ν_8=1)	259274	CH_3OH	260244	$HCOOCH_3$ E	261978	CCH (tent.)
258081	$HCOOCH_3$ E	259285	Unidentified	260256	$HCOOCH_3$ A,$H^{13}CO^+$	262005	CCH
258090	$HCOOCH_3$ A	259311	Unidentified	260327	$^{34}SO_2$	262067	CCH
258121	$HCOOCH_3$ A	259343	$HCOOCH_3$ A,E	260383	CH_3OH,$HCOOCH_3$ E	262079	CCH
258157	$HC^{15}N$	259486	CH_3OCH_3	260393	$HCOOCH_3$ A	262103	HCOOH
258256	SO	259490	CH_3OCH_3	260404	$HCOOCH_3$ E	262184	C_2H_5CN
258296	CH_3CN (ν_8=1)	259494	CH_3OCH_3	260415	$HCOOCH_3$ A	262209	CCH
258320	CH_3CN (ν_8=1)	259500	$HCOOCH_3$ E	260440	Unidentified	262224	CH_3OH
258360	C_2H_3CN	259522	$HCOOCH_3$ A	260518	SiO	262257	SO_2
258380	SO_2	259600	SO_2	260666	C_2H_5CN	262308	CH_3OCH_3
258447	$HCOOCH_3$ E	259617	$^{34}SO_2$	260679	C_2H_5CN	262312	CH_3OCH_3
258483	$HCOOCH_3$ A	259629	$HCOOCH_3$ E	260726	Unidentified	262316	CH_3OCH_3
258491	$HCOOCH_3$ E	259647	$HCOOCH_3$ A	260758	CH_3OCH_3	262325	$HCOOCH_3$ E
258496	$HCOOCH_3$ A	259653	$HCOOCH_3$ E	260761	CH_3OCH_3	262341	$HCOOCH_3$ A
258499	$HCOOCH_3$ E	259690	Unidentified	261062	CH_3OH (tent.)	262394	CH_3OCH_3
258503	$HCOOCH_3$ E	259733	Unidentified	261149	$HCOOCH_3$ E	262548	CH_2CO
258508	$HCOOCH_3$ A	259843	C_2H_5CN	261165	$HCOOCH_3$ A	262625	CH_3OCH_3
258549	CH_3OCH_3,CH_3CN (ν_8=1)	259847	C_2H_5CN	261248	CH_3OCH_3	262629	CH_3OCH_3
258552	CH_3CN (ν_8=1)	259863	C_2H_5CN	261250	CH_3OCH_3	262770	$HNCO,CH_3OCH_3$
258667	SO_2	259870	C_2H_5CN	261263	$HN^{13}C$	262774	CH_3OCH_3
258746	$HCOOCH_3$ E	259907	C_2H_5CN	261434	$HCOOCH_3$ E	262890	CH_3OCH_3
258757	$HCOOCH_3$ A	259917	C_2H_5CN	261437	$HCOOCH_3$ A	262895	CH_3OCH_3
258770	$HCOOCH_3$ E	259955	C_2H_5CN	261564	Unidentified	263050	CH_3OCH_3
258780	CH_3OH	259986	Unidentified	261704	CH_3OH	263065	Unidentified
258942	SO_2	260014	C_2H_5CN	261715	$HCOOCH_3$ E	263107	CH_3OCH_3
259011	$H^{13}CN$	260025	C_2H_5CN	261747	$HCOOCH_3$ A	263113	CH_3OCH_3
259035	HDCO	260081	C_2H_5CN	261806	CH_3OH		

A2.2. Discussion of Individual Species

A. CO, CS, SiO, SiS, and SO

Many of the strongest individual lines in the spectrum are from diatomic molecules of the most abundant elements. Carbon monoxide (CO) provides the strongest line in the spectrum, its J = 2 - 1 transition at 230538 MHz. The species CS and SiO are isoelectronic with CO, yet have qualitatively different characteristics because of the very different abundances, chemistry, and dipole moments of these forms.

Emission from CO and its isotopic forms is described in Table A2. The J = 2 - 1 line of the principal isotopic form, $^{12}C^{16}O$, is dominated by plateau emission with a full width to zero intensity of at least 150 MHz (200 km s^{-1}). The high-velocity wings of the line are particularly strong in these observations because of the small 0.5' beam width which emphasizes emission from the compact plateau source. The ^{13}CO line is also extremely strong, but with less pronounced wings. The variation in the $^{12}CO/^{13}CO$ intensity ratio across the line profile indicates that the transition in ^{12}CO is highly optically thick at the line center but becomes optically thin at velocities of $\pm$ 25 km s^{-1} relative to the line center. The intensities of the rarer isotopic forms $C^{18}O$ and $C^{17}O$ are consistent with optically thin emission at the velocity of the ambient molecular cloud (v_{LSR}~8.5 km s^{-1}). Emission from $^{12}C^{16}O$ in the first vibrationally excited state was looked for but not detected.

CS is detected through its intense J = 5 - 4 line at 244936 MHz, which, as expected due to the known concentration of sulphur-containing molecules in the high-velocity outflow, also has a line shape with a strong plateau component. Several rarer isotopic forms are detected in ratios indicating that the parent line is optically thick and the isotopic lines optically thin. The isotopic lines, seen at an average v_{LSR} of 8.4 km s^{-1} with 7.3 km s^{-1} width, are dominated

Table A2

Transitions of CO, CS, and SiS

	ν (MHz)	J	T_a^*(pk) (K)	$\int T_a^* dv$ (K km s^{-1})	notes
CO.....	230538.0	2-1	111.	2242.	
^{13}CO.....	220398.7		37.6	319.	
C^{18}O.....	219560.3		5.7	39.4	
C^{17}O.....	224714.4		1.5	6.7	
CO(ν=1)...	228439.2		nd	...	
CS.....	244935.6	5-4	21.1	291.	
^{13}CS.....	231220.8		2.5	16.0	
C^{34}S.....	241016.2		3.9	33.5	
C^{33}S.....	242913.7		1.5	11.0	
CS(ν=1)...	243160.8		nd	...	
SiS.....	217817.3	12-11	0.5 ?	4.5 ?	a
	235961.1	13-12	...	...	b

notes: a-unusual v_{LSR}, now identified as C_3H_2 (Thaddeus 1985). b-lost under $^{13}CH_3OH$ 235960.

by the spike component, although the C^{34}S line clearly shows broad plateau-type wings.

Silicon sulfide (SiS) has been reported in OMC-1 by Dickinson and Rodriguez-Kuiper (1981) whose detection of the J = 6 - 5 line gave an LSR velocity of 14 km s^{-1}, rather different than the 5-9 km s^{-1} range of most molecular components in Orion. Two transitions of SiS fall within the range of this survey. The J = 13-12 line at 235961 MHz falls in a band of $^{13}CH_3OH$ lines and is inaccessible, but the J = 12-11 line at 217817 MHz is in a clear region. There is no evidence of emission at "normal" velocities near 8 km s^{-1}, but there is an otherwise unidentified line which could be interpreted as SiS at a v_{LSR} of 14 km s^{-1}. Similarly, though, there is an even stronger line on the other side of the expected position which could be SiS at v_{LSR}~2 km s^{-1}. In principle either or both of these velocities could be correct since such velocities are clearly present in Orion. However, it is hard to see why SiS should have a velocity structure so different from all of the other molecules identified. The 14 km s^{-1} feature is perhaps

more likely since it is coincident with the previously reported detection. However, the detection of SiS at all in OMC-1 still seems rather tentative.

Table A3

Transitions of SiO and SO

	ν (MHz)	J/N_J	T_A^*(pk) (K)	$\int T_A^* dv$ (K km s^{-1})	notes
SiO(ν=1)....	215596.0	5-4	nd	...	
^{29}SiO.....	214385.6	5-4	~1.8	45.0	
SiO.....	217104.9	5-4	8.1	278.	
	260518.0	6-5	11.3	374.	
^{29}SiO.....	257255.0	6-5	1.6	41.2	a
SO.....	215220.6	5_5-4_4	20.0	562.	
	219949.4	6_5-5_4	24.7	680.	
	236452.3	1_2-2_1	0.4 ?	...	
	254573.5	8_8-8_0	3.0	74.3	
	258255.8	6_6-5_5	21.8	662.	
	261843.7	7_6-6_5	21.8	647.	
^{34}SO.....	215839.9	6_5-5_4	3.9	93.9	
	246663.4	5_6-4_5	2.9	65.4	
	253206.6	6_6-5_5	3.0	72.5	
	256877.8	7_6-6_5	4.7	115.	
^{33}SO.....	217830.	6_5-5_4	0.9	21.2	b
S^{18}O.....	232265.9	5_6-4_5	0.3 ?	...	
	239128.5	6_6-5_5	...	...	c
	243039.3	7_6-6_5	0.4 ?	...	

notes: a - blend w/C_2H_5CN 257240 and $HCOOCH_3$ 257253. b-blend of hyperfine components. c-lost under CH_3CN 239120 and 239133.

Silicon monoxide (SiO), like CO, CS, and SiS, has the spectrum of a simple $^1\Sigma$ diatomic rotor and is detected through its strong J = 5 - 4 and J = 6 - 5 lines in both the parent ^{28}Si and ^{29}Si isotopes, as Table A3 shows. All of the lines are quite broad ($\Delta v \gtrsim 30$ km s^{-1}), indicating that they originate in the plateau source, and seem to show no indication of measurable spike or hot core emission. The v_{LSR} of the emission peak is near 7 km s^{-1} for all of the lines. Ratios of the two sets of lines to each other and to CO indicate that the SiO emission becomes optically thin at velocities greater than about 25 km s^{-1} from the line center and that the silicon monoxide column density is approximately 2 10^{15} cm^{-2}.

Unlike SiO, sulphur monoxide (SO) possesses a non-zero electronic angular momentum which greatly complicates its rotational spectrum. Six lines of ^{32}SO and four transitions of ^{34}SO have been detected in the 215 - 263 GHz range and are listed in Table A3. We have also detected a single ^{33}SO transition, but there is no clear detection of $S^{18}O$. As is typical of most sulphur-containing species, all of the lines are dominated by plateau emission ($\Delta v \sim 30$ km s^{-1}), but fits of unconstrained Gaussian components to the line shapes strongly suggest that spike and possibly hot core emission also contribute (Friberg 1984). A more detailed discussion of these results and of the fitting procedure will be presented in Chapters 3 and 4. They show that SO is greatly enhanced in the plateau source, with at most 2 - 3% of the integrated flux due to emission from spike material. The great uniformity of our peak antenna temperatures in the strongest components across the 215 - 263 GHz region indicates that emission from SO is highly saturated. Indeed, ratios of the $^{32}SO/^{34}SO$ 6_6 - 5_5 and 7_6 - 6_5 transitions show that only when $\delta v \gtrsim 25$ - 30 km s^{-1} (δv = velocity offset from line center) is the emission optically thin. The beam averaged SO column density is about 3 10^{16} cm^{-2}.

B. CN and CCH

Emission from CN is seen in the N = 2 - 1 spin multiplet centered near 227 GHz. The spin doubling, which is of the order of a few hundred megahertz, is further split by magnetic hyperfine structure (cf. Appendix B). Emission from OMC-1 in this band was previously studied by Wootten *et al.* (1982). The current results are listed in Table A4, where the frequencies are taken from Appendix B (Skatrud *et al.* 1983). The results are consistent with those of Wootten *et al.*, showing central velocities of v_{LSR} = 9 km s^{-1}, widths of 4 km s^{-1}, and a peak antenna temperature in the blended 226875 MHz transition of 9.1 K. The

Table A4

Transitions of CN and CCH

	ν (MHz)	N,J,F	T_A^*(pk) (K)	$\int T_A^* dv$ (K km s^{-1})	notes
CN.....	226287.4	$2, {}^3/_2, {}^1/_2 - 1, {}^3/_2, {}^1/_2$			a
	226298.9	$2, {}^3/_2, {}^1/_2 - 1, {}^3/_2, {}^3/_2$			
	226303.0	$2, {}^3/_2, {}^3/_2 - 1, {}^3/_2, {}^1/_2$	...	...	
	226314.6	$2, {}^3/_2, {}^3/_2 - 1, {}^3/_2, {}^3/_2$			
	226332.5	$2, {}^3/_2, {}^3/_2 - 1, {}^3/_2, {}^5/_2$	0.3	1.1	
	226341.9	$2, {}^3/_2, {}^5/_2 - 1, {}^3/_2, {}^3/_2$	0.3	1.3	
	226359.9	$2, {}^3/_2, {}^5/_2 - 1, {}^3/_2, {}^5/_2$	1.2	4.2	
	226616.5	$2, {}^3/_2, {}^1/_2 - 1, {}^1/_2, {}^3/_2$	0.2	1.1	
	226632.2	$2, {}^3/_2, {}^3/_2 - 1, {}^1/_2, {}^3/_2$	1.4	7.8	
	226659.5	$2, {}^3/_2, {}^5/_2 - 1, {}^1/_2, {}^3/_2$	4.3	15.4	
	226663.7	$2, {}^3/_2, {}^1/_2 - 1, {}^1/_2, {}^1/_2$	1.5	9.4	
	226679.3	$2, {}^3/_2, {}^3/_2 - 1, {}^1/_2, {}^1/_2$	1.9	7.2	
	226874.2	$2, {}^5/_2, {}^5/_2 - 1, {}^3/_2, {}^3/_2$			
	226874.8	$2, {}^5/_2, {}^7/_2 - 1, {}^3/_2, {}^5/_2$	9.1	51.6	
	226875.9	$2, {}^5/_2, {}^3/_2 - 1, {}^3/_2, {}^1/_2$			
	226887.4	$2, {}^5/_2, {}^3/_2 - 1, {}^3/_2, {}^3/_2$	1.4	7.5	
	226892.2	$2, {}^5/_2, {}^5/_2 - 1, {}^3/_2, {}^5/_2$	1.7	6.9	
	226905.4	$2, {}^5/_2, {}^3/_2 - 1, {}^3/_2, {}^5/_2$	0.2	0.5	
CCH.....	261978.3	$3, {}^7/_2, 3 - 2, {}^5/_2, 3$	$\lesssim$0.2	...	
	262004.5	$3, {}^7/_2, 4 - 2, {}^5/_2, 3$	6.7	35.9	b
	262006.7	$3, {}^7/_2, 3 - 2, {}^5/_2, 2$			
	262065.2	$3, {}^5/_2, 3 - 2, {}^3/_2, 2$	4.7	29.4	b
	262067.6	$3, {}^5/_2, 2 - 2, {}^3/_2, 1$			
	262079.1	$3, {}^5/_2, 2 - 2, {}^3/_2, 2$	0.8	1.4	
	262208.8	$3, {}^5/_2, 3 - 2, {}^3/_2, 3$	~0.8	2.1	

notes: a-lost under SO_2 226300. b- hyperfine components not resolved.

relative strengths of the hyperfine components show that the emission is just beginning to saturate in the strongest components (τ_p = 1.4±0.1 at 226875 MHz), indicating a CN column density of around 1.5 10^{16} cm^{-2}.

We have also detected several components of the CCH N = 3 - 2 transition at 262 GHz, previously investigated in detail towards Orion by Ziurys *et al.* (1982). The rotational spectrum of CCH is qualitatively similar to that of the CN radical in that each rotational transition possesses resolvable fine and hyperfine structure which may be used to estimate the optical depths of individual emission lines. Transition frequencies for the $\Delta J = \Delta N$ components listed in

Table A4 have been taken from Sastry *et al.* (1981), while those for the ΔJ and $\Delta F = 0$ transitions are from Ziurys *et al.* The hyperfine splittings of the strongly allowed J = 7/2 - 5/2 and J = 5/2 - 3/2 fine structure lines at 262005 and 262066 MHz are not resolved due to the intrinsic Orion line widths of ~4 km s^{-1}, but other than this our results are in agreement with the previous studies of CCH at lower frequencies. The strongest lines are marginally optically thick ($\tau_{262005} \sim 1.0 \pm 0.5$), corresponding to total column densities of $\sim 3 - 5\ 10^{15}$ cm^{-2} for an assumed rotational temperature of 55 K, derived from the chemically related CH_3CCH symmetric top.

C. NO, NS, PO, and PN

Table A5 describes the emission that we have ascribed to the J = 5/2 - 3/2 transition of another free radical, the nitric oxide (NO) molecule. N-O bonds are now known to be quite difficult to synthesize in the interstellar medium, and emission from NO is expected to be quite weak. For example, Wootten, Loren, and Bally (1984) tentatively detected one of the J = 3/2 - 1/2 lambda doubling components near 150.5 GHz at a level of ~0.2 K in their study of high velocity H_2CO emission towards Orion. The J = 5/2 - 3/2 transitions should be substantially stronger than the ground state lines since the NO transitions will undoubtedly be optically thin and fully thermalized because of the low NO dipole moment ($\mu_{NO} \sim 0.16$ D). Because of the gap near 251 GHz only one of the most strongly allowed lambda doubling components is presently observed, and it is totally blended with the $28_{3,26} - 27_{3,25}$ transition of C_2H_5CN. However, the observed emission is at least a factor of two stronger than the expected contribution from C_2H_5CN, and we probably have detected a weaker $\Delta F = 0$ hyperfine satellite nearby. Using the known rotational temperature and column density of C_2H_5CN

we have subtracted its expected emission strength from the blended lines to yield the T_A^* values given in Table A5. When combined with the upper limits derived from the weaker $\Delta F = 0$ satellites, we estimate the column density of NO to be $\lesssim 1.5\ 10^{16}$ cm^{-2}.

Table A5

Transitions of NO, NS, PO, and PN

	ν (MHz)	N,J,F	T_A^*(pk) (K)	$\int T_A^* dv$ (K km s^{-1})	notes
NO....	250436.8	$^5/_2, ^7/_2 - ^3/_2, ^5/_2$ e			a
	250440.7	$^5/_2, ^5/_2 - ^3/_2, ^3/_2$ e	~0.8	14.4	
	250448.5	$^5/_2, ^3/_2 - ^3/_2, ^1/_2$ e			
	250482.9	$^5/_2, ^5/_2 - ^3/_2, ^5/_2$ e	~0.3	0.7	
NS....	255598.8	$^{11}/_2, ^{13}/_2 - ^9/_2, ^{11}/_2$ c			b
	255602.3	$^{11}/_2, ^{11}/_2 - ^9/_2, ^9/_2$ c	0.4 ?	2.7 ?	
	255604.9	$^{11}/_2, ^9/_2 - ^9/_2, ^7/_2$ c			
PO....	239948.9	$^{11}/_2$,6 $- ^9/_2$,5 e	nd	...	
	239958.1	$^{11}/_2$,5 $- ^9/_2$,4 e	nd	...	
	240141.0	$^{11}/_2$,6 $- ^9/_2$,5 f	nd	...	
	240152.5	$^{11}/_2$,5 $- ^9/_2$,4 f	nd	...	
PN....	234935.7	5-4	0.4	1.5	

notes: a-NO lines blended with C_2H_5CN 250440, total integrated flux from all 3 components listed. b-due to SO_2 255595?

The isoelectronic species NS has not, to our knowledge, been detected in Orion, though a number of investigators have reported its presence in Sgr B2 (Gottlieb *et al.* 1975; Kuiper *et al.* 1975; Cummins, Linke, and Thaddeus 1985). The only ground state $\Pi_{1/2}$ lines in our survey fall near 253.5 GHz, where we currently have no spectra. There is an emission feature at the expected position of the excited state $\Pi_{3/2}$ lines, but a very high-energy SO_2 transition ($51_{7,45}$ - $50_{8,44}$) is also present at this frequency and it will not be possible to deconvolve any NS contribution to the emission strength until limits ground state lines are obtained.

Phosphorus-containing compounds have not been detected in the interstellar medium. Recent laboratory work has shown that two of the most likely

forms in dense molecular clouds are the diatomic PO and PN species (Thorne *et al.* 1984). Transition frequencies for the PO radical have been calculated (Pickett 1984) based on the measurements of Kawaguchi, Saito, and Hirota (1983). Although four lines are predicted to fall in the spectral line survey, as shown in Table A5, there is no good evidence for emission at any of the expected frequencies. An upper limit of roughly 2 10^{14} cm^{-2} can be deduced from these data for an assumed dipole moment of 1 debye.

PN has no electronic angular momentum and hence has a single rotational transition accessible. There is a weak line clearly present at the J = 5 - 4 frequency (Wyse, Manson, and Gordy 1972) which is not currently identified as due to any other molecular species. However, its identification as PN must await the detection of some other transition in another frequency band due to the number of weak lines of well-known species (e.g., CH_3OH, $HCOOCH_3$) whose frequencies are currently unknown. If the line seen is due to PN, its v_{LSR} of 8 km s^{-1} and width of 4 km s^{-1} indicates that it arises in the ridge, or spike, component of OMC-1. The column density of PN would be roughly 3 10^{12} for the rotational temperature of 100 K characteristic of the compact ridge material appearing at a velocity of 8 km s^{-1}.

D. OCS, HCN, HNC, HC_3N, HCO^+ and HCS^+

The linear OCS molecule has a diatomic rotor-like spectrum and is detected in the four successive rotational transitions listed in Table A6 having lower J values of 17-20. The difference in line intensities is somewhat larger than expected, possibly indicating a calibration problem with the lowest and highest frequency lines. Line shapes clearly indicate the contributions from both quiescent and high-velocity emission, but some hot core emission may also be present. The isotopically substituted $OC^{34}S$ form is detected in the J = 19 - 18

Table A6

Transitions of OCS

	ν (MHz)	J	T_a^*(pk) (K)	$\int T_A^* dv$ (K km s^{-1})
OCS.....	218903.4	18-17	3.9	40.0
	231061.0	19-18	5.2	50.1
	243218.0	20-19	4.9	59.3
	255374.5	21-20	6.5	88.8
$OC^{34}S$....	225413.0	19-18	0.7	3.9
	237272.9	20-19	0.5	1.9
$O^{13}CS$....	218199.0	18-17	0.5	2.5
	230317.5	19-18	0.5	1.6
	242435.4	20-19	0.4 ?	...

and J = 20 - 19 lines. The former is convincingly detected but at a level rather stronger than expected on the basis of a $^{32}S/^{34}S$ ratio of 16 (Johansson *et al.* 1984; Chapter 3). This is possibly the result of a coincidence with a currently unidentified line at this frequency. The J = 20 - 19 transition of $OC^{34}S$ is marginally detected at about the level expected from the above ratio. $O^{13}CS$ may have also been detected since there are indications of emission at the J = 18-17, 19-18, and 20-19 frequencies, although this would not be expected for an $OCS/O^{13}CS$ ratio of 40.

The J = 3 - 2 transitions of HCN and HNC have been detected in the ^{13}C, ^{15}N, and D isotopic variants of HCN and only the ^{13}C and D substituted isotopes for HNC. for HNC. The parent isotopic transitions for both species lie above the frequency range searched. As Figure A1 and Table A7 show, emission from the $HC^{15}N$ and $H^{13}CN$ lines is quite strong and is clearly composed of spike, hot core, and plateau components. The DCN line is composed primarily of hot core emission with some additional ridge emission, but is too weak to detect any plateau features. Fits of Gaussian profiles to the data yield average v_{LSR} and Δv parameters of 9.0 and 3.5 km s^{-1} for the spike material, 5.8 and 12.3 km s^{-1} for the hot core, and 8.6 and 27.0 km s^{-1} for the plateau source, and reveal that the HCN abundance is enhanced in both the hot core and plateau sources relative to the

Table A7

Transitions of HCN, HNC, and HC_3N

	ν (MHz)	J		T_A^*(pk) (K)	$\int T_A^* dv$ (K km s^{-1})
DCN.....	217238.5	3-2		2.9	21.8
$HC^{15}N$.....	258157.3	3-2		5.2	75.8
$H^{13}CN$.....	259011.7	3-2		9.0	157.
DNC.....	228910.5	3-2		0.6	2.0
$HN^{13}C$.....	261263.4	3-2		0.9	4.0
$HCNH^+$.....	222323.	3-2		nd	...
HC_3N.....	218324.8	24-23		4.0	62.1
	227419.0	25-24		3.5	41.5
	236512.8	26-25		3.5	53.6
	245606.4	27-26		4.8	81.6
	254699.6	28-27		5.0	106.
$HC_3N(\nu_7)$.....	218860.6	24-23	1e	0.6	7.6
	219173.6	24-23	1f	0.6	9.2
	227977.1	25-24	1e	0.7	8.4
	228303.0	25-24	1f	0.8	10.8
	237093.2	26-25	1e	0.8	7.5
	237432.0	26-25	1f	0.7	9.9
	246208.9	27-26	1e	0.4 ?	...
	246560.7	27-26	1f	1.1	8.0
	255324.3	28-27	1e	1.0	17.7
	255689.1	28-27	1f	1.1	15.6

ambient molecular cloud. HNC shows mostly spike emission, however, with the possibility of some hot core emission at a lower level.

Protonated hydrogen cyanide ($HCNH^+$) has not been detected in dense interstellar clouds, but is of considerable importance chemically as a precursor to both HCN and HNC. Molecular constants have recently been determined by Altman *et al.* (1984), allowing the J = 3-2 transition frequency to be predicted to a precision of about 10 MHz. This is sufficient to show that emission in this transition is not present in our OMC-1 spectrum to a limit of $T_A^*<0.2$ K (3σ). If, as expected, the $HNCH^+$ dipole moment is small ($\mu_{theo.}\lesssim 0.2$-0.3 D), then the upper limits to the $HCNH^+$ column density are not inconsistent with the predictions of standard ion-molecule chemical models.

Like HCN, the ground-state cyanoacetylene (HC_3N) line shape is seen to consist of emission from all three Orion kinematic components. Five successive rotational transitions between 218 and 255 GHz have been detected and are presented in Table A7. Emission from the five sets of vibrationally excited transitions located close to and slightly above the ground state lines is also clearly evident in Figure A1, and shows only the hot core line shape ($v_{LSR} \sim 4.6$ km s^{-1}, $\Delta v \sim 12.1$ km s^{-1}) because of the excitation requirements of these transitions ($E_{lower} \sim 250$ cm^{-1}). Average parameters for Gaussian components fit to the ground-state HC_3N lines are quite similar to the HCN values, and indicate that cyanoacetylene is most abundant in the hot core and plateau sources. No isotopic lines have been detected throughout the 215 - 263 GHz interval.

Cyanodiacetylene (HC_5N) is not detected in any of the twelve pure rotational transitions which fall within our frequency band. This is consistent with the results of Johansson *et al.* (1984) who report a tentative detection of HC_5N with an integrated strength of approximately 0.015 of the nearby HC_3N lines.

The HCO^+ and HCS^+ ionized variations of the familiar HCX linear interstellar molecules have also been detected here and are listed in Table A8. As with the neutral HCN and HNC species discussed above the parent isotopic HCO^+ transition lies above our current frequency range, but is detected through the $H^{13}CO^+$ and $HC^{18}O^+$ isotopic forms. Deuterated versions of both HCO^+ and HNN^+ have been searched for, but are blended with transitions of other more abundant species and have not been detected. The HCS^+ and isotopic HCO^+ emission arises purely from the extended, quiescent molecular cloud material ($v_{LSR} \sim 8$ km s^{-1}, $\Delta v \sim 3.8$ km s^{-1}), as expected. Emission from the higher density and temperature hot core and low-velocity plateau components is not favored because of the greatly reduced fractional ionization in these sources. The $H^{13}CO^+$ line is strongly blended with the $21_{3,18}$ - $20_{3,17}$ A-type transition of

Table A8

Transitions of HCO^+, N_2D^+, and HCS^+

	ν (MHz)	J	T_A^*(pk) (K)	$\int T_A^* dv$ (K km s^{-1})	notes
DCO^+.....	216112.6	3-2	nd	...	a
$HC^{18}O^+$...	255479.4	3 - 2	1.0	3.4	
$H^{13}CO^+$...	260255.5	3 - 2	$\gtrsim$1.0	$\gtrsim$4.1	b
N_2D^+.....	231321.8	3-2	nd	...	
HCS^+.....	213360.8	5-4	0.8	4.3	c
	256027.4	6 - 5	1.2	5.2	

notes: a-lost under $HCOOCH_3$ 216110 and 216116. b-blend w/$HCOOCH_3$ 260256. c-This transition was seen in an incomplete set of measurements extending a few GHz below the nominal band discussed in this appendix. Due to the incomplete nature of this datum its uncertainty is considerably greater than that of the rest of the data.

$HCOOCH_3$ whose contribution is subtracted from the overall emission using the nearby E-type $HCOOCH_3$ component to give the $H^{13}CO^+$ T_A^* listed in Table A8. Column densities of HCO^+ and HCS^+ are estimated to be about 1.5 10^{15} and 1.6 10^{13} cm^{-2}, respectively. A lower bound to the quiescent cloud fractional ionization of f(e-) > 5 10^{-9} is derived from the $HC^{18}O^+$ line.

E. CH_3CN and CH_3CCH

The J = 14 - 13, 13 - 12, and 12 -11 ground-state and first vibrationally excited (ν_8 = 1) bands listed in Tables A9, A10, and A11 bring the total number of methyl cyanide (CH_3CN) lines detected in the complete survey to over 100. As discussed by Loren, Mundy and Erickson (1981) and Loren and Mundy (1984), low K lines in the ground-state bands ($K \lesssim 3$) are mixtures of both spike and hot core components while the higher K ground state lines and all of the vibrationally excited transitions are due exclusively to the hot core. Average Gaussian components for the two sources have radial velocities and line widths of 8.4 and 4.0 km s^{-1} and 5.6 and 10.3 km s^{-1}, respectively. Excitation temperatures and

Table A9

Transitions of ground state CH_3CN

	ν (MHz)	J_K	T_A^*(pk) (K)	$\int T_A^* dv$ (K km s^{-1})	notes
CH_3CN....	220403.9	12_9-11_9	...	...	a
	220475.8	12_8-11_8	0.5	2.9	
	220539.3	12_7-11_7	0.9	5.3	
	220594.4	12_6-11_6	1.9	22.9	
	220641.1	12_5-11_5	2.1	20.1	
	220679.3	12_4-11_4	2.5	19.0	
	220709.0	12_3-11_3	4.9	48.2	
	220730.3	12_2-11_2	4.4	60.3	
	220743.0	12_1-11_1	~4.6	~67.	
	220747.3	12_0-11_0	~5.3	~75.	
	238766.1	13_9-12_9	0.4	2.4	
	238843.9	13_8-12_8	0.6	5.8	
	238912.7	13_7-12_7	0.7	5.4	
	238972.4	13_6-12_6	1.7	15.6	
	239022.9	13_5-12_5	1.7	23.4	
	239064.3	13_4-12_4	2.3	28.0	
	239096.5	13_3-12_3	3.9	46.1	
	239119.5	13_2-12_2	3.7	35.3	
	239133.3	13_1-12_1	~4.0	~40.	
	239137.9	13_0-12_0	~4.5	~45.	
	257033.6	$14_{10}-13_{10}$	0.3	3.6	
	257127.1	14_9-13_9	0.6	3.5	
	257211.0	14_8-13_8	0.6	5.0	
	257285.0	14_7-13_7	1.0	9.6	
	257349.2	14_6-13_6	1.8	22.6	
	257403.6	14_5-13_5	2.8	33.3	b
	257448.1	14_4-13_4	2.5	27.3	
	257482.8	14_3-13_3	4.3	54.1	
	257507.6	14_2-13_2	3.6	28.4	
	257522.4	14_1-13_1	~5.1	~40.	
	257527.4	14_0-13_0	~5.6	~44.	

notes: a-lost under ^{13}CO 220399, b-blend w/CH_3OH 257402.

column densities of the two CH_3CN sources are approximately 100 K and 2 10^{14} cm^{-2} for the ridge gas and 285 K and 2 10^{15} cm^{-2} for the hot core material, as estimated from a Gaussian decomposition of the ground-state line shapes. Many of the strongest lines in the higher frequency ν_8 = 1 band near 258 GHz are buried in the intense 6_6 - 5_5 transition of SO, but the unaffected lines have an average width of 9.8 km s^{-1} and a v_{LSR} of 6.4 km s^{-1}. The strengths of these lines are consistent with an extrapolation of the high-K ground-state lines with T_{ex}=285 K.

Table A10

Transitions of vibrationally excited CH_3CN

	ν (MHz)	J_K		T_A^*(pk) (K)	$\int T_A^* dv$ (K km s^{-1})	notes
$CH_3CN(\nu_8=1)$....	221199.0	12_1-11_1	(1)	0.7	10.9	a
	221252.3	12_5-11_5	(-1)	0.3	1.8	
	221265.1	12_7-11_7	(1)	...	...	b
	221299.6	12_4-11_4	(-1)	0.2	0.8	
	221311.9	12_6-11_6	(1)	0.2	1.9	
	221338.0	12_3-11_3	(-1)	0.3	1.7	
	221350.3	12_5-11_5	(1)	0.2	1.6	
	221367.5	12_2-11_2	(-1)	0.6	6.2	
	221380.6	12_4-11_4	(1)	0.6	4.1	
	221387.3	12_1-11_1	(-1)	0.4	2.5	
	221394.1	12_0-11_0	(1)	0.5	3.0	
	221403.5	12_3-11_3	(1)	0.3	2.4	
	221422.3	12_2-11_2	(1)	0.3	2.4	c
	221626.0	12_1-11_1	(1)	0.4	2.9	
	239627.2	13_1-12_1	(1)	0.4	3.5	
	239684.6	13_5-12_5	(-1)	...	...	d
	239699.3	13_7-12_7	(1)	nd	...	
	239735.7	13_4-12_4	(-1)	...	...	e
	239750.0	13_6-12_6	(1)	...	...	e
	239777.2	13_3-12_3	(-1)	0.3	2.1	
	239791.7	13_5-12_5	(1)	0.2	2.0	
	239808.9	13_2-12_2	(-1)	0.6	6.4	
	239824.8	13_4-12_4	(1)	0.8	8.2	
	239830.0	13_1-12_1	(-1)	0.5	4.6	
	239836.1	13_0-12_0	(1)	0.5	5.0	
	239850.0	13_3-12_3	(1)	0.7	6.2	
	239871.7	13_2-12_2	(1)	0.4	2.3	
	240089.8	13_1-12_1	(1)	0.6	5.8	
	258054.1	14_1-13_1	(1)	1.1	5.0	
	258170.4	14_4-13_4	(-1)	...	...	f
	258187.0	14_6-13_6	(1)	0.3	1.8	
	258215.0	14_5-13_5	(-1)	}		g
	258232.1	14_5-13_5	(1)	}...	...	
	258248.9	14_2-13_2	(-1)	}		
	258267.9	14_4-13_4	(1)	}		g
	258271.1	14_1-13_1	(-1)	}...	...	
	258276.2	14_0-13_0	(1)	}		
	258296.6	14_3-13_3	(1)	1.1	6.6	
	258320.4	14_2-13_2	(1)	0.7	3.3	
	258552.4	14_1-13_1	(1)	0.6	3.5	

a-emission too broad to be entirely CH_3CN, b-lost under $HCOOCH_3$ 221266, c-blend with $HCOOCH_3$ 221425, d-lost under C_2H_5CN 239683, e-lost under CH_3OH 239746, f-lost to $HC^{15}N$ 258157, g-lost to SO 258256.

Table A11

Transitions of $^{13}CH_3CN$ and $CH_3{}^{13}CN$

	ν (MHz)	J_K	T_a^*(pk) (K)	$\int T_a^* dv$ (K km s^{-1})	notes
$^{13}CH_3CN$....	232194.6	13_3-12_3	0.7 ?	5.1 ?	a
	232216.4	13_2-12_2	0.5	4.0	
	232229.5	13_1-12_1	0.5	4.3	
	232233.9	13_0-12_0	0.6	4.7	
	250050.2	14_3-13_3	0.6	3.8	a
	250073.7	14_2-13_2	0.5	3.7	
	250087.8	14_1-13_1	0.3	2.8	
	250092.5	14_0-13_0	0.4	3.6	
$CH_3{}^{13}CN$...	220599.9	12_3-11_3	...	...	b
	220621.1	12_2-11_2	0.5	1.9	
	220633.8	12_1-11_1	0.5	2.2	c
	220638.0	12_0-11_0	...	...	d
	238978.3	13_3-12_3	...	...	e
	239001.2	13_2-12_2	0.3	1.3	
	239015.0	13_1-12_1	0.5	2.5	f
	239019.5	13_0-12_0	...	...	g
	257355.5	14_3-13_3	...	...	h
	257380.1	14_2-13_2	0.3	1.9	
	257394.9	14_1-13_1	...	...	i
	257399.9	14_0-13_0	...	...	i

notes: a-too strong relative to K=0,1, and 2; possible blend with unidentified line, b-lost under CH_3CN 220594, c-blended with CH_3CN 220641, d-lost under CH_3CN 220641, e-lost under CH_3CN 238972, f-blended with CH_3CN 239023, g-lost under CH_3CN 239023 h-lost under CH_3CN 257349, i-lost under CH_3CN 257403.

Isotopically substituted methyl cyanide has been detected in both the $^{13}CH_3CN$ and $CH_3{}^{13}CN$ variants, which are listed in Table A11. The average v_{LSR} of 5.3 km s^{-1} and Δv of 7.2 km s^{-1} are suggestive of hot core emission. For an assumed rotational temperature of $\lesssim$ 285 K the derived column density of $\lesssim$ 1 10^{14} cm^{-2} corresponds to a $^{13}C/^{12}C$ ratio of $\gtrsim$20, consistent with the low values derived from HCN, HNC, and CH_3OH, and with those from the Onsala survey of Orion (Johansson *et al.* 1984).

Methyl isocyanide (CH_3NC) has not been convincingly detected in the interstellar medium. If its abundance were are great as suggested by the HCN/HNC ratio it should be easily detected in Orion. The J=14-13, 13-12, and 12-11 bands lie within the frequency range searched, and while the J=13-12 band is partly

obstructed by lines of the CH_3OH J=5-4 ν_t=1 band, the other transitions are in relatively clear regions. There is no compelling evidence for emission from CH_3NC in the line search and its abundance relative to CH_3CN must be down by a factor of at least 10. This is in good agreement with the limit set by Irvine and Schloerb (1984) in TMC-1 from observations at 1.6 cm. It is also at the low end of the range in the CH_3CN/CH_3NC abundance ratio predicted theoretically by DeFrees, McLean, and Herbst (1985).

Table A12

Transitions of CH_3CCH

	ν (MHz)	J_K	T_a^*(pk) (K)	$\int T_a^* dv$ (K km s^{-1})	notes
CH_3CCH....	222099.2	13_4-12_4	0.2	0.9	
	222128.8	13_3-12_3	0.9	4.0	
	222150.0	13_2-12_2	1.1	6.0	
	222162.7	13_1-12_1	1.5	5.8	
	222167.0	13_0-12_0	1.6	8.6	
	239179.3	14_4-13_4	0.3	1.0	
	239211.2	14_3-13_3	0.9	4.3	
	239234.0	14_2-13_2	0.7	2.7	
	239247.7	14_1-13_1	0.9	4.0	
	239252.3	14_0-13_0	1.2	6.3	
	256292.6	15_3-14_3	0.8	2.1	
	256317.1	15_2-14_2	0.9	3.9	a
	256331.8	15_1-14_1	0.8	2.9	
	256336.6	15_0-14_0	0.9	3.3	

a-too strong, blend?

The J=15-14, 14-13, and 13-12 bands of methyl acetylene (CH_3CCH), another symmetric top whose mass and structure are very similar to CH_3CN, lie near 256, 239, and 222 GHz and are characterized by purely spike emission with a v_{LSR} and line width of 9.3 and 3.8 km s^{-1}, as Table A12 shows. Ratios of the K-ladder components imply a low excitation temperature of $T_{ROT} \sim 55\pm9$ K, which has also been used for other molecules showing extended emission such as CN and CCH. The estimated CH_3CCH column density is 10^{15} cm^{-2}. No isotopic lines of methyl acetylene have been detected.

F. CH_3OH

Methanol (CH_3OH) emission in the 215 - 263 GHz region is dominated by the strong J=5-4 a-type band between 239 and 244 GHz and by the $K = 3^+ - 2^-$ and $3^- - 2^+$ A symmetry Q-branches whose band heads lie near 252 GHz. Weaker P and R-branch transitions lie scattered irregularly throughout the scan. The Q-branch lines are quite strong and occur in a monotonically spaced series which may be simply predicted algebraically. Lines up to J = 22 have been detected in our survey by extrapolating the transitions measured in the laboratory to higher J values. It is therefore highly likely that CH_3OH emission from levels as high as J = 25 or 30 will be readily detectable in Orion, but the large perturbations in the rotational spectrum induced by the intermediate torsional barrier height make predictions for $J \gtrsim 10$ highly uncertain (Herbst *et al.* 1984).

As a step towards identifying the higher J spectrum of CH_3OH in the laboratory we have used the initially unidentified lines in our survey to search for unassigned methanol transitions in the 210 to 265 GHz range. By observing the laboratory spectrum of methanol vapor in the vicinity of the unidentified lines we had also hoped to verify our suspicion that a number of them were in fact due to CH_3OH. And indeed, as a result of these laboratory experiments (Blake and Pickett 1985) 15 of some 40 initially unidentified lines have now been definitively assigned to methanol. Rest frequencies of the newly measured CH_3OH lines are listed in Table A13 along with their associated astronomical emission. Assignment of the transition quantum numbers and excitation energies is not possible at the present time, but must await further spectroscopic and theoretical work.

Table A13

Transitions of CH_3OH

	ν (MHz)	J_K		T_A^*(pk) (K)	$\int T_A^* dv$ (K km s^{-1})	notes
CH_3OH...	216945.6	4_2-5_1	E	3.0	17.8	
	217299.2	unassigned		1.2	8.3	a
	217886.6	unassigned		0.9	6.7	a
	218440.0	4_2-3_1	E	8.4	41.1	
	220078.6	7_1-8_0	E	6.1	35.2	
	220401.0	$10_{-5}-11_{-4}$	E	...	...	b
	222722.9	unassigned		0.6	2.1	a
	224699.4	unassigned		0.7	3.6	a
	227094.6	unassigned		0.9	4.8	a
	227814.5	unassigned		1.4	6.8	a
	229589.1	unassigned		1.3	7.0	a
	229758.7	$8_{-1}-7_0$	E	11.0	56.9	
	229864.2	19_5-20_4	A+	0.4	2.3	
	229939.2	19_5-20_4	A-	0.5	1.9	
	230027.1	$3_{-2}-4_{-1}$	E	5.1	24.2	
	230368.7	22_4-21_5	E	0.2	1.4	
	231281.1	10_2-9_3	A-	3.0	18.6	
	232418.6	10_2-9_3	A+	3.9	27.1	
	232783.5	18_3-17_4	A+	1.4	9.0	
	232945.	unassigned		3.0	20.0	a
	233795.8	18_3-17_4	A-	1.0	4.3	
	234683.2	4_2-5_1	A-	2.6	14.6	
	234698.4	$5_{-4}-6_{-3}$	E	1.2	4.6	
	236936.1	14_1-13_2	A-	2.3	15.8	
	237129.4	unassigned		0.7	4.5	a
	239731.4	unassigned		0.6	1.7	a
	239746.3	5_1-4_1	A+	7.4	42.9	
	240241.5	5_3-6_2	E	2.3	15.1	
	241700.2	5_0-4_0	E	9.3	~62.	
	241767.2	$5_{-1}-4_{-1}$	E	10.4	~85.	
	241791.4	5_0-4_0	A	10.7	61.4	
	241806.5	5_4-4_4	A±	6.5	41.3	
	241813.3	$5_{-4}-4_{-4}$	E	5.0	22.8	
	241829.6	5_4-4_4	E	} 9.6	68.3	
	241833.0	5_3-4_3	A±			
	241842.3	5_2-4_2	A-	} 10.3	84.6	
	241843.6	5_3-4_3	E			
	241852.4	$5_{-3}-4_{-3}$	E	6.6	28.6	
	241879.1	5_1-4_1	E	9.2	54.8	
	241887.7	5_2-4_2	A+	7.8	49.4	
	241904.4	$5_{-2}-4_{-2}$	E	} 11.8	69.8	
	241904.5	5_2-4_2	E			

notes: a-rest frequency from laboratory measurement, b-lost under ^{13}CO 220399.

Table A13 - continued

	ν (MHz)	J_K		T_A^*(pk) (K)	$\int T_A^* dv$ (K km s^{-1})	notes
CH_3OH...	242446.2	$13_{-2}-14_{-1}$	E	3.3	22.5	
	242490.3	$24_{-3}-24_{+2}$	A	0.7	4.0	
	243397.5	18_6-19_5	A+	1.6	5.1	
	243412.6	$23_{-3}-23_{+2}$	A	0.9	4.0	
	243915.8	5_1-4_1	A-	8.1	50.5	
	244330.5	$22_{-3}-22_{+2}$	A	1.1	6.0	
	245223.0	$21_{-3}-21_{+2}$	A	1.3	7.6	
	246074.7	$20_{-3}-20_{+2}$	A	1.6	11.3	
	246873.3	$19_{-3}-19_{+2}$	A	1.8	10.7	
	247162.1	unassigned		1.6	10.2	a
	247228.7	$4_2 - 5_1$	A+	3.9	18.2	
	247611.0	$18_{-3}-18_{+2}$	A	1.1	7.5	
	247840.2	unassigned		1.0	4.9	a
	248242.5	$17_{-3}-17_{+2}$	A	2.2	13.4	
	249887.5	$14_{-3}-14_{+2}$	A	3.6	23.0	
	250291.2	$13_{-3}-13_{+2}$	A	4.2	25.8	
	250507.0	11_0-10_1	A+	5.8	32.7	
	250635.2	$12_{-3}-12_{+2}$	A	5.9	37.6	
	252803.4	$12_{+3}-12_{-2}$	A	4.1	20.2	
	253221.4	$13_{+3}-13_{-2}$	A	3.1	17.6	c
	254423.6	$15_{+3}-15_{-2}$	A	3.0	34.6	d
		11_5-12_4	E			d
	254959.5	unassigned		1.2	5.5	a
	255121.0	unassigned		1.7	3.2	a
	255173.0	unassigned		1.2	4.0	a
	255192.5	unassigned		1.8	8.1	a,e
	255193.5	unassigned				a,e
	255203.8	unassigned		1.3	2.8	a
	255214.9	unassigned		1.1	4.3	a
	255220.9	unassigned		0.9	2.7	a
	255242.0	$16_{+3}-16_{-2}$	A	3.8	23.9	
	255265.7	unassigned		1.4	5.2	a
	256228.9	$17_{+3}-17_{-2}$	A	1.7	14.6	f
	257402.2	$18_{+3}-18_{-2}$	A	2.8	33.3	g
	258780.4	$19_{+3}-19_{-2}$	A	1.8	11.7	
	259273.7	unassigned		1.0	4.7	a
	260381.6	$20_{+3}-20_{-2}$	A	1.8	9.8	
	261061.4	$21_{-4}-20_{-5}$	E	0.5	2.7	
	261704.4	12_6-11_5	E	0.9	4.5	
	261805.7	2_1-1_0	E	7.3	34.4	h
	262224.2	$21_{+3}-21_{-2}$	A	1.3	6.6	

notes: a-rest frequency from laboratory measurement, b-lost under ^{13}CO 220399, c-blend w/^{34}SO 253207, d-unresolved in laboratory, e-doublet in laboratory, f-blend w/SO_2 256247, g-blend w/CH_3CN 257404, h-blend with SO 261844.

Although an extended methanol source clearly exists in Orion, its emission arises predominantly from a compact ($\vartheta_{meth.} \lesssim 30''$) region of warm material at the edge of the 8 km s^{-1} cloud labeled the southern condensation, or compact ridge, by Johansson *et al.* (1984). The warmer component is most visible in the energetic high J lines of the K = $3^{\pm}$ - $2^{\mp}$ Q-branches, but also manifests itself as wings on the stronger low J transitions. A simultaneous excitation analysis of all the CH_3OH lines produces a rotational temperature on the order of 140 K, but shows a trend towards higher excitation temperatures and larger line widths as the energy of the transitions increases. Fits of unconstrained Gaussian components to the methanol line shapes consistently divide the CH_3OH emission into two sources characterized by velocities and line widths of 8.1 and 3.3 km s^{-1} for the "cool" component and 7.2 and 9.6 km s^{-1} for the "warm" component. Excitation temperatures for the two sources are approximately 100 and 230 K, and the total CH_3OH column density is approximately 5 10^{16} cm^{-2}.

We suggest that the trends in excitation temperature noted above are due to the presence of this warmer source, which is perhaps most convincingly observed at a v_{LSR} of 7.0 km s^{-1} in torsionally excited CH_3OH a-type band near 241 GHz (Table A14). These lines are quite strong, indicating the torsionally excited and high-energy ground state lines arise from optically thin and spatially compact material. Two torsionally excited b-type lines are also detected, but laboratory data at present are insufficient to accurately predict the frequencies of other such transitions in this frequency range. The v_{LSR} of the warmer component clearly shows that it is not emission from the hot core, but rather is more likely associated with quiescent molecular cloud material interacting with that from the plateau source in the vicinity of IRc 5 (Johansson *et al.* 1984, Chapter 4).

Isotopically substituted methanol ($^{13}CH_3OH$) has also been detected via its

Table A14

Transitions of ν_t=1 CH_3OH

	ν (MHz)	J_K		T_A^*(pk) (K)	$\int T_A^* dv$ (K km s^{-1})
$CH_3OH(\nu_t=1)$...	215302.2	6_1-7_2	A+	1.3	6.0
	240960.6	5_1-4_1	A+	0.9	4.9
	241159.1	5_4-4_4	E	0.7	5.0
	241166.5	5_3-4_3	E	0.8	4.4
	241178.4	5_4-4_4	A±	1.3	7.9
	241179.9	$5_{-3}-4_{-3}$	E		
	241184.1	$5_{-4}-4_{-4}$	E	1.1	6.2
	241187.4	$5_{-2}-4_{-2}$	E	1.4	8.4
	241192.8	5_2-4_2	A+	1.9	11.4
	241196.4	5_2-4_2	A-	2.1	12.4
	241198.3	5_3-4_3	A±		
	241203.7	5_1-4_1	E	2.8	16.8
	241206.0	5_0-4_0	E		
	241210.7	5_2-4_2	E	1.2	7.3
	241238.2	$5_{-1}-4_{-1}$	E	0.7	4.4
	241267.9	5_0-4_0	A	0.4	3.7
	241441.2	5_1-4_1	A-	1.5	9.3
	244338.0	9_1-8_0	E	1.2	8.4

Table A15

Transitions of $^{13}CH_3OH$

	ν (MHz)	J_K		T_A^*(pk) (K)	$\int T_a^* dv$ (K km s^{-1})	notes
$^{13}CH_3OH$...	234011.6	5_1-4_1	A+	0.8	3.1	a
	235881.2	5_0-4_0	E	0.6	2.5	
	235938.2	$5_{-1}-4_{-1}$	E	0.7	2.8	b
	235960.4	5_0-4_0	A±	0.7	2.9	c
	235971.1	5_4-4_4	A±	0.3	1.0	
	235978.6	$5_{-4}-4_{-4}$	E	0.1 ?	...	
	235994.4	5_4-4_4	E	0.7	3.3	
	235997.2	5_3-4_3	A±			
	236006.1	5_3-4_3	E	0.4	1.4	
	236008.4	5_2-4_2	A-	0.7	2.7	
	236016.6	$5_{-3}-4_{-3}$	E	0.4	1.5	
	236041.4	5_1-4_1	E	0.6	2.3	
	236049.5	5_2-4_2	A+	0.4	1.7	
	236062.0	$5_{-2}-4_{-2}$	E	0.9	3.8	
	236062.9	5_2-4_2	E			
	237983.4	5_1-4_1	A-	0.8	3.5	

notes: a-blend with $HCOOCH_3$ 234012, b-blend with $^{34}SO_2$ 235928, c-blend with $^{34}SO_2$ 235952.

emission in the J=5-4 band near 236 GHz. A detailed analysis of the 15 lines presented in Table A15 (Blake *et al.* 1984) and of the methanol formation mechanisms has shown that the $^{12}CH_3OH$ J=5-4 lines are clearly saturated and that the $^{12}C/^{13}C$ ratio in the quiescent gas is about 40. Several lines previously identified as due to other molecules, most importantly CO^+, have now been assigned to $^{13}CH_3OH$. In addition to the lines listed here, several b-type transitions of $^{13}CH_3OH$ should be strong enough to be detectable, but no adequate frequency predictions are currently available for these lines. A detailed investigation of the b-type interstellar $^{13}CH_3OH$ spectrum will therefore await further laboratory and computational work.

G. H_2CO, H_2CS, CH_2CO, HCOOH, and CH_3CHO

Formaldehyde (H_2CO) is a fairly light asymmetric top with a handful of strong lines in the 200-300 GHz region. The detected transitions are shown in Table A16. Line shapes exhibit both quiescent and high-velocity emission as discussed by Wootten *et al.* (1984). Line strength differences for the few lines observed suggest an excitation temperature of ~100 K and an H_2CO column density of about 1 10^{16} cm^{-2}. Isotopically substituted versions of formaldehyde (HDCO and $H_2{}^{13}CO$) have been detected near 220, 247, 255 and 257 GHz and are also presented in Table A16. The HDCO lines are narrow ($\Delta v \sim 4.0$ km s^{-1}) and seem to arise mainly from extended spike material ($v_{LSR} \sim 8.8$ km s^{-1}), while the range of energies detected imply a (poorly determined and most likely subthermal) excitation temperature of 40 K and a $HDCO/H_2CO$ ratio of ~ 0.01, typical of the strong fractionation visible in a number of other neutral molecules in Orion such as HDO and DCN.

Several lines of H_2CS are detected from the J=7-6 band. The lines are predominantly narrow (v_{LSR}=7.5 km s^{-1}, Δv=4.3 km s^{-1}) but with some evidence

Table A16

Transitions of H_2CO and H_2CS

	ν (MHz)	$J_{K_pK_o}$	T_a^*(pk) (K)	$\int T_a^* dv$ (K km s^{-1})	notes
H_2CO.....	216568.6	$9_{1,8}-9_{1,9}$	1.3	6.1	
	218222.2	$3_{0,3}-2_{0,2}$	12.7	114.4	
	218475.6	$3_{2,2}-2_{2,1}$	6.2	40.9	
	218760.1	$3_{2,1}-2_{2,0}$	6.9	51.0	
	225697.8	$3_{1,2}-2_{1,1}$	21.6	181.5	
	227583.5	$17_{2,15}-17_{2,16}$	nd	...	
$H_2^{13}CO$.....	219908.5	$3_{1,2}-2_{1,1}$	2.7	10.3	
HDCO.....	227668.1	$1_{1,1}-0_{0,0}$	nd	...	
	228866.3	$6_{1,5}-6_{0,6}$	nd	...	
	246924.7	$4_{1,4}-3_{1,3}$	1.8	7.5	
	256585.3	$4_{0,4}-3_{0,3}$	1.8	11.6	
	257748.8	$4_{2,3}-3_{2,2}$	0.6	2.3	
	258071.0	$4_{3,2}-3_{3,1}$	0.3	0.9	
	259034.9	$4_{2,2}-3_{2,1}$	0.6	2.7	a
H_2CS.....	236726.3	$7_{1,7}-6_{1,6}$	2.7	13.2	
	240261.4	$7_{5,3}-6_{5,2}$	0.2 ?	...	
		$7_{5,2}-6_{5,1}$			
	240266.2	$7_{0,7}-6_{0,6}$	1.9	9.1	
	240331.4	$7_{4,4}-6_{4,3}$	0.5	1.9	
		$7_{4,3}-6_{4,2}$			
	240381.3	$7_{2,6}-6_{2,5}$	0.7	3.1	
	240392.3	$7_{3,5}-6_{3,4}$	1.4	6.5	
	240393.0	$7_{3,4}-6_{3,3}$			
	240548.3	$7_{2,5}-6_{2,4}$	0.7	4.1	
	244047.8	$7_{1,6}-6_{1,5}$	3.9	17.1	
$H_2C^{34}S$....	232778.5	$7_{1,7}-6_{1,6}$	nd	...	
	236198.8	$7_{0,7}-6_{0,6}$	...	...	b
	239858.5	$7_{1,6}-6_{1,5}$	nd	...	

notes: a-blend w/$H^{13}CN$ 258157 b-lost under SO_2 236217

of broader wings. The excitation temperature is similar to that of H_2CO and the column density is roughly 10^{15} cm^{-2}. No isotopic forms of H_2CS are seen.

Formic acid (HCOOH) was not detected in Orion in the Onsala line survey (Johansson *et al.* 1984). Its absence was rather surprising, given the great abundance of the more complicated but structurally related methyl formate molecule. It seems to be detected here in small amounts, at a level close to the upper limits derived by Johansson *et al.*. The lines listed in Table A17 give an average velocity and line width of v_{LSR}=8.0 km s^{-1} and Δv=4.6 km s^{-1}. Assuming

Table A17

Transitions of HCOOH

	ν (MHz)	$J_{K_pK_o}$	T_A^*(pk) (K)	$\int T_A^* dv$ (K km s^{-1})	notes
HCOOH....	215407.8	$10_{1,10}-9_{1,9}$	...	...	a
	220038.0	$10_{0,10}-9_{0,9}$	0.3	1.2	
	223915.6	$10_{2,9}-9_{2,8}$	0.3	1.0	
	225237.8	$10_{3,8}-9_{3,7}$	...	...	b
	225512.5	$10_{3,7}-9_{3,6}$	0.4	2.0	
	228544.1	$10_{2,8}-9_{2,7}$	0.4	1.2	
	231505.6	$10_{1,9}-9_{1,8}$	0.8	2.4	
	236717.2	$11_{1,11}-10_{1,10}$	0.4	1.5	
	241146.2	$11_{0,11}-10_{0,10}$	0.2	1.6	
	246106.0	$11_{2,10}-10_{2,9}$	0.6	4.8	c
	257975.0	$12_{1,12}-11_{1,11}$	0.3	0.9	
	262103.5	$12_{0,12}-11_{0,11}$	0.4	1.5	

notes: a-lost under C_2H_5CN 215401, b-lost under C_2H_5CN 225236, c-too strong, possible blend with unidentified line.

that T_{ROT}~90 K as for methyl formate and other chemically similar species in the compact ridge source, the derived column density is approximately 10^{14} cm^{-2}.

Table A18

Transitions of CH_3CHO

	ν (MHz)	$J_{K_pK_o}$		T_A^*(pk) (K)	$\int T_A^* dv$ (K km s^{-1})	notes
CH_3CHO....	216580.6	$11_{1,10}-10_{1,9}$	E	nd	...	
	216630.0	$11_{1,10}-10_{1,9}$	A	...	...	a
	223650.3	$12_{1,12}-11_{1,11}$	E	0.2	0.8	
	223660.8	$12_{1,12}-11_{1,11}$	A	0.3	2.4	
	226551.5	$12_{0,12}-11_{0,11}$	E	0.3	2.1	
	226592.8	$12_{0,12}-11_{0,11}$	A	0.2	1.0	
	235997.0	$12_{1,11}-11_{1,10}$	E	...	...	b
	236049.1	$12_{1,11}-11_{1,10}$	A	...	...	c
	255377.6	$13_{1,12}-12_{1,11}$	A	...	...	d
	260536.8	$14_{1,14}-13_{1,13}$	A	...	...	e
	262996.5	$14_{0,14}-13_{0,13}$	A	$\lesssim$0.2	...	

notes: a-lost under SO_2 216643, b-lost under $^{13}CH_3OH$ 235997, c-lost under $^{13}CH_3OH$ 236050, d-lost under OCS 255375, e-lost under SiO 260518.

Acetaldehyde (CH_3CHO) has been searched for in several transitions, but only upper limits have been obtained. Predicted frequencies for the CH_3CHO E symmetry species are not available above 236 GHz, so only the A symmetry lines

Table A19

Transitions of CH_2CO and HNCO

	ν (MHz)	$J_{K_pK_o}$	T_A^*(pk) (K)	$\int T_A^* dv$ (K km s^{-1})	notes
CH_2CO...	220177.5	$11_{1,11}-10_{1,10}$	1.0	3.7	
	222197.7	$11_{0,11}-10_{0,10}$	0.6	3.7	
	222228.6	$11_{2,10}-10_{2,9}$	0.2	0.6	
	222314.4	$11_{2,9}-10_{2,8}$	0.2	0.6	
	224327.2	$11_{1,10}-10_{1,9}$	...	...	a
	240185.8	$12_{1,12}-11_{1,11}$	0.5	5.0	
	242375.8	$12_{0,12}-11_{0,11}$	0.5	2.7	
	242398.7	$12_{3,10}-11_{3,9}$	0.6	2.9	
	242399.2	$12_{3,9}-11_{3,8}$			
	242424.7	$12_{2,11}-11_{2,10}$	0.2	1.5	
	242536.2	$12_{2,10}-11_{2,9}$	0.4	2.5	
	244712.2	$12_{1,11}-11_{1,10}$	0.8	3.0	
	260192.0	$13_{1,13}-12_{1,12}$	0.6	3.6	
	262548.4	$13_{0,13}-12_{0,12}$	0.5	1.9	
HNCO....	218981.0	$10_{1,10}-9_{1,9}$	1.0	9.8	
	219547.1	$10_{4,7}-9_{4,6}$	0.4	2.3	
		$10_{4,6}-9_{4,5}$			
	219656.8	$10_{3,8}-9_{3,7}$	0.4	1.9	
		$10_{3,7}-9_{3,6}$			
	219733.8	$10_{2,9}-9_{2,8}$	0.6	3.5	
	219737.2	$10_{2,8}-9_{2,7}$	0.8	4.4	
	219798.3	$10_{0,10}-9_{0,9}$	2.9	35.3	
	220584.8	$10_{1,9}-9_{1,8}$	1.3	9.0	
	240875.7	$11_{1,11}-10_{1,10}$	0.9	7.0	
	241619.3	$11_{3,9}-10_{3,8}$	...	...	b
	241619.4	$11_{3,8}-10_{3,7}$			
	241703.8	$11_{2,10}-10_{2,9}$	...	...	c
	241708.3	$11_{2,9}-10_{2,8}$			
	241774.0	$11_{0,11}-10_{0,10}$	3.1	23.8	d
	242639.7	$11_{1,10}-10_{1,9}$	1.1	8.8	
	262769.5	$12_{1,12}-11_{1,11}$	1.3	6.9	e

notes: a-blend with $HCOOCH_3$ 224328, b-lost under SO_2 241616, c-blend with CH_3OH 241700, d-blend with CH_3OH 241767, e-blend with CH_3OCH_3 262770, 262774.

for these transitions are listed in Table A18. As is shown in Table A18, there are weak bumps present at several of the expected frequencies, but not all of them. As discussed by Blake *et al.* (1984), the line at 236049 MHz is due primarily to $^{13}CH_3OH$. The derived column density from the tentatively detected lines is on the order of $\lesssim 5\ 10^{13}$ cm^{-2}, but the presence of acetaldehyde in Orion is still rather uncertain.

Although both ketene (CH_2CO) and isocyanic acid (HNCO) are fairly heavy, because of their nearly linear character they have only a few lines each available in the OVRO survey (see Table A19). The strengths of these lines are consistent with an excitation temperature and column density of 120 K and 5 10^{14} for both CH_2CO and HNCO. While the CH_2CO line shapes are narrow (4.9 km s^{-1}) and appear at a velocity characteristic of the ambient molecular cloud material (v_{LSR}=8.0 km s^{-1}), the somewhat broader HNCO line width of Δv=7.2 km s^{-1} is more suggestive of hot core emission (Goldsmith *et al.* 1982, Johansson *et al.* 1984). The average v_{LSR} of 7.1 km s^{-1} is intermediate between that usually associated with the hot core and ridge Orion component, however. A Gaussian decomposition of the HNCO line shape is marginally consistent with a blend of low temperature material (T_{ROT}~35 K) arising from the ridge gas with a warmer (T_{ROT}~175 K) and more dominant component originating from the hot core.

Table A20

Transitions of HDO and H_2S

	ν (MHz)	$J_{K_pK_o}$	T_a^*(pk) (K)	$\int T_a^* dv$ (K km s^{-1})	notes
HDO....	225896.7	$3_{1,2}-2_{2,1}$	2.3	25.0	
	241561.5	$2_{1,1}-2_{1,2}$	1.9	23.1	
	241973.5	$7_{3,4}-6_{4,3}$	?	...	a
	255050.3	$5_{2,3}-4_{3,2}$	2.1	8.3	
H_2S....	216710.4	$2_{2,0}-2_{1,1}$	3.5	31.3	

notes: a-blend with C_2H_5CN 241970 and $^{34}SO_2$ 241986.

H. HDO and H_2S

Deuterated water (HDO) is detected through three of its low-lying transitions as listed in Table A20. A fourth higher J transition falls in a very crowded region of the spectrum and may be present, although it is difficult to separate its contribution from that of the C_2H_5CN and $^{34}SO_2$ lines with which it is blended.

The HDO lines have predominantly hot core line shapes (v_{LSR}=6.8 km s^{-1}, Δv=11.5 km s^{-1}), but both spike and plateau components are also visible. Assuming a rotational temperature of 150 K (Olofsson 1984), a total column density of 4 10^{15} cm^{-2} is derived.

A single line of H_2S has been detected at 216710 MHz. Its line shape can be decomposed into contributions from the hot core region as well as the broader plateau emission so typical of sulfur-containing species.

I. SO_2

As noted by Sutton *et al.* (1984), emission from SO_2 produces by itself about 28% of the total integrated flux from molecular lines in Orion. The large number and great strength of the SO_2 lines listed in Tables A21 and A22 are primarily responsible for, along with SO, the large integrated flux from spectral line emission noted in Chapter 3. The SO_2 line shape is quite broad, and, like SO, is composed predominantly of plateau emission with less than 2% of the integrated flux originating in the extended molecular cloud. The average $^{32}SO_2$ width is 30.2 km s^{-1}, while that of $^{34}SO_2$ is about 25.2 km s^{-1}. Both species have a peak v_{LSR} of approximately 7.7 km s^{-1}.

Ratios of the $^{32}S/^{34}S$ line profiles indicate that for the strongest lines the SO_2 emission is only marginally saturated and becomes optically thin for velocity offsets greater than approximately 15 km s^{-1}. The strengths of the optically thin line wings and other weaker lines which should be optically thin at all velocities imply an excitation temperature of 100 K and a column density of 5 10^{18}, but hotter gas is evident as well (Schloerb *et al.* 1983). For example, the highest energy lines, including the $14_{0,14}$ - $13_{1,13}$ and $22_{2,24}$ - $22_{2,23}$ vibrationally excited lines tentatively detected at 243523 and 257420 MHz, suggest a rotational temperature of $\gtrsim$ 175 K. The vibrationally excited emission has a poorly

Table A21

Transitions of SO_2

	ν (MHz)	$J_{K_pK_o}$	T_A^*(pk) (K)	$\int T_A^* dv$ (K km s^{-1})	notes
SO_2.....	216643.3	$22_{2,20}-22_{1,21}$	4.6	105.	
	219276.0	$22_{7,15}-23_{6,18}$	0.3 ?	...	
	221965.2	$11_{1,11}-10_{0,10}$	13.9	348.	
	223434.4	$27_{8,20}-28_{7,21}$	0.3 ?	...	
	223883.6	$6_{4,2}-7_{3,5}$	1.4	27.1	
	224264.9	$20_{2,18}-19_{3,17}$	2.6	60.8	
	225153.7	$13_{2,12}-13_{1,13}$	6.3	159.	
	226300.0	$14_{3,11}-14_{2,12}$	5.8	143.	
	229347.7	$11_{5,7}-12_{4,8}$	1.9	40.1	
	234187.1	$28_{3,25}-28_{2,26}$	1.6	36.1	
	234421.7	$16_{6,10}-17_{5,13}$	1.5	36.8	a
	235151.7	$4_{2,2}-3_{1,3}$	5.6	145.	
	236216.7	$16_{1,15}-15_{2,14}$	5.3	131.	
	237068.8	$12_{3,9}-12_{2,10}$	5.9	171.	
	238992.6	$21_{7,15}-22_{6,16}$	0.4	6.8	
	240942.8	$18_{1,17}-18_{0,18}$	4.3	111.	
	241615.8	$5_{2,4}-4_{1,3}$	8.9	225.	
	243087.7	$5_{4,2}-6_{3,3}$	1.4	24.5	
	243245.4	$26_{8,18}-27_{7,21}$	nd	...	
	244254.2	$14_{0,14}-13_{1,13}$	9.9	271.	
	245339.4	$26_{3,23}-25_{4,22}$	1.7	31.0	
	245563.4	$10_{3,7}-10_{2,8}$	7.8	220.	
	248057.4	$15_{2,14}-15_{1,15}$	6.1	154.	
	248436.9	$13_{3,11}-14_{0,14}$	0.6	8.0	b
	255553.3	$4_{3,1}-4_{2,2}$	7.4	168.	
	255595.3	$51_{7,45}-50_{8,42}$	0.4 ?	2.7 ?	c
	255958.1	$3_{3,1}-3_{2,2}$	3.5	86.8	
	256247.0	$5_{3,3}-5_{2,4}$	6.5	158.	
	257100.0	$7_{3,5}-7_{2,6}$	7.9	205.	
	258388.8	$32_{4,28}-32_{3,29}$	1.5	25.1	
	258667.0	$20_{7,13}-21_{6,16}$	0.7	6.8	
	258942.2	$9_{3,7}-9_{2,8}$	6.7	174.	
	259599.5	$30_{4,26}-30_{3,27}$	1.5	19.8	
	262256.9	$11_{3,9}-11_{2,10}$	5.9	141.	
$SO_2(\nu_2=1)$...	243522.6	$14_{0,14}-13_{1,13}$	0.5	3.2	
	257420.5	$24_{2,22}-24_{2,23}$	0.4	1.4	

notes: a-blend with C_2H_5CN 234424, b-blend w/C_2H_5CN 248436, c-blend w/NS 255602?

determined v_{LSR} of 5.0 km s^{-1}, possibly indicative of emission from the hot core. The SO_2 measurements provide our best limits on the total amount of material in the plateau source. Following the procedure of Kuiper, Zuckerman, and Rodriguez-Kuiper (1981), we estimate the plateau has an H_2 column density of 5

Table A22

Transitions of $^{34}SO_2$

	ν (MHz)	$J_{K_pK_o}$	T_a^*(pk) (K)	$\int T_a^* dv$ (K km s^{-1})	notes
$^{34}SO_2$....	215999.8	$14_{3,11}-14_{2,12}$	0.7	12.0	
	219355.1	$11_{1,11}-10_{0,10}$	1.3	24.0	
	221735.7	$13_{2,12}-13_{1,13}$	1.0	17.5	
	227031.9	$12_{3,9}-12_{2,10}$	0.7	14.6	a
	229857.7	$4_{2,2}-3_{1,3}$	1.1	21.0	
	230933.5	$5_{4,2}-6_{3,3}$	nd	...	
	235927.5	$5_{2,4}-4_{1,3}$	0.6	14.8	
	235952.0	$10_{3,7}-10_{2,8}$	0.7	19.1	
	241509.0	$16_{1,15}-15_{2,14}$	0.9	13.8	
	241985.5	$8_{3,5}-8_{2,6}$	1.4	29.2	
	243935.9	$18_{1,17}-18_{0,18}$	0.4 ?	...	
	244481.5	$14_{0,14}-13_{1,13}$	1.4	19.5	
	245178.7	$15_{2,14}-15_{1,15}$	0.8	14.2	
	245302.3	$6_{3,3}-6_{2,4}$	0.9	14.3	
	246686.2	$4_{3,1}-4_{2,2}$	0.3 ?	...	
	247440.4	$5_{3,3}-5_{2,4}$	0.7	5.3	
	248364.8	$7_{3,5}-7_{2,6}$	0.9	14.3	
	250358.4	$9_{3,7}-9_{2,8}$	0.9	23.1	
	259617.2	$13_{3,11}-13_{2,12}$	1.0	8.3	
	260327.0	$13_{3,11}-13_{2,12}$	1.0	6.0	

notes: a-blend with $HCOOCH_3$ 227028.

$\lesssim 10^{22}$ cm^{-2}, in agreement with the recent interferometer continuum maps of Masson *et al.* (1985).

J. $HCOOCH_3$

While SO_2 provides the most flux from any single species, the largest number of transitions in this survey belong to the methyl formate ($HCOOCH_3$) molecule. The heavy nature of this species coupled with the rotational line splittings induced by internal rotation of the methyl group with respect to the HCOO-backbone creates scores of transitions spread rather evenly throughout the millimeter wave region. In support of our Orion survey, Plummer *et al.* (1984, 1985, see Appendix B) have recently investigated the rotational spectrum of the A and E symmetry states of methyl formate to produce a highly accurate map of the $HCOOCH_3$ transition frequencies up to 500 GHz. Most of our detected lines, listed in Table A23, have been measured directly, but for consistency we have used the predicted frequencies here. Over 175 lines have been used to derive an average $HCOOCH_3$ v_{LSR} and Δv of 7.9 and 3.9 km s^{-1} in Orion, and also to establish the rotational temperature and column density of 90 K and 3 10^{15} cm^{-2} listed in Table 3.6.

$HCOOCH_3$ is probably produced chemically from methanol in dense interstellar clouds, and is therefore likely to be present in the warm CH_3OH component noted in subsection F. Emission from the first torsionally excited state of methyl formate should be detectable in this material because of the low energy of the torsional motion in $HCOOCH_3$ ($\sim$ 100 cm^{-1}), but to our knowledge no estimates of the torsionally excited $HCOOCH_3$ rotational constants have been made.

Table A23

Transitions of $HCOOCH_3$

ν (MHz)	$J_{K_pK_o}$		T_a^*(pk) (K)	$\int T_A^* dv$ (K km s^{-1})	notes
215972.0....	$19_{1,18}-18_{2,17}$	A	0.2 ?	...	
216109.7....	$19_{2,18}-18_{2,17}$	E	0.9	4.5	
216115.5....	$19_{2,18}-18_{2,17}$	A	1.1	5.8	
216210.9....	$19_{1,18}-18_{1,17}$	E	0.8	4.3	
216216.5....	$19_{1,18}-18_{1,17}$	A	0.9	4.3	
216360.0....	$19_{2,18}-18_{1,17}$	A	0.2 ?	...	
216830.1....	$18_{2,16}-17_{2,15}$	E	1.2	3.9	
216838.8....	$18_{2,16}-17_{2,15}$	A	1.1	3.8	
216964.8....	$20_{1,20}-19_{1,19}$	E			
216965.9....	$20_{1,20}-19_{1,19}$	A	2.0	12.5	
216966.2....	$20_{0,20}-19_{0,19}$	E			
216967.3....	$20_{0,20}-19_{0,19}$	A			
218281.0....	$17_{3,14}-16_{3,13}$	E	1.0	4.2	
218297.8....	$17_{3,14}-16_{3,13}$	A	1.2	4.3	
220166.6....	$17_{4,13}-16_{4,12}$	E	1.3	5.8	
220190.2....	$17_{4,13}-16_{4,12}$	A	1.3	7.2	
220811.6....	$18_{3,16}-17_{2,15}$	E	0.4	1.0	
220815.2....	$18_{3,16}-17_{2,15}$	A	0.4	2.5	
220889.0....	$18_{17,2}-17_{17,1}$	A	0.4	2.3	
	$18_{17,1}-17_{17,0}$	A			
220926.2....	$18_{16,3}-17_{16,2}$	A	0.5	2.1	
	$18_{16,2}-17_{16,1}$	A			
220977.8....	$18_{15,3}-17_{15,2}$	A	0.5	3.2	
	$18_{15,4}-17_{15,3}$	A			
221047.7....	$18_{14,4}-17_{14,3}$	A	0.5	4.5	
	$18_{14,5}-17_{14,4}$	A			
221050.0....	$18_{14,4}-17_{14,3}$	E			
221066.3....	$18_{14,5}-17_{14,4}$	E	0.3	2.0	
221141.0....	$18_{13,5}-17_{13,4}$	A	0.7	4.0	
	$18_{13,6}-17_{13,4}$	A			
	$18_{13,5}-17_{13,4}$	E			
221158.4....	$18_{13,6}-17_{13,5}$	E	0.2	0.8	
221260.9....	$18_{12,6}-17_{12,5}$	E	0.4	1.0	
221265.6....	$18_{12,6}-17_{12,5}$	A	0.6	2.3	
	$18_{12,7}-17_{12,6}$	A			
221280.8....	$18_{12,7}-17_{12,6}$	E	0.4	1.6	
221424.7....	$18_{11,7}-17_{11,6}$	E	0.8	4.4	a
221433.0....	$18_{11,7}-17_{11,6}$	A	0.9	3.8	
	$18_{11,8}-17_{11,7}$	A			
221445.5....	$18_{11,8}-17_{11,7}$	E	0.6	2.6	
221649.7....	$18_{10,8}-17_{10,7}$	E	0.5	1.9	
221660.4....	$18_{4,15}-17_{4,14}$	E	1.5	6.3	
221661.1....	$18_{10,8}-17_{10,7}$	A			
	$18_{10,9}-17_{10,8}$	A			
221670.5....	$18_{10,9}-17_{10,8}$	E	0.4	1.6	

notes: a-blend with $CH_3CN(\nu_8)$ 221422.

Table A23 - continued

ν (MHz)	$J_{K_pK_o}$		T_a^*(pk) (K)	$\int T_A^* dv$ (K km s^{-1})	notes
221674.6....	$18_{4,15}-17_{4,14}$	A	0.8	4.3	
221979.3....	$18_{9,10}-17_{9,9}$	A	...	...	b
221979.4....	$18_{9,9}-17_{9,8}$	A	...	...	b
222421.6....	$18_{8,10}-17_{8,9}$	E	1.0	5.2	
222438.2....	$18_{8,10}-17_{8,9}$	A			
222440.3....	$18_{8,11}-17_{8,10}$	A	1.2	10.8	c
222441.9....	$18_{8,10}-17_{8,9}$	E			
223038.3....	$19_{2,17}-18_{3,16}$	E	0.3	0.8	
223051.7....	$19_{2,17}-18_{3,16}$	A	0.2 ?	...	
223119.2....	$18_{7,12}-17_{7,11}$	A	1.1	5.5	
223125.1....	$18_{7,12}-17_{7,11}$	E	1.0	5.4	
223134.9....	$18_{7,11}-17_{7,10}$	E	1.0	4.6	
223162.7....	$18_{7,11}-17_{7,10}$	A	0.8	2.7	
224021.4....	$18_{6,13}-17_{6,12}$	E	1.0	7.5	d
224024.1....	$18_{6,13}-17_{6,12}$	A			
224312.9....	$18_{5,14}-17_{5,13}$	E	0.8	2.9	
224328.3....	$18_{5,14}-17_{5,13}$	A	0.8	3.2	e
224583.0....	$18_{6,12}-17_{6,11}$	E	0.8	3.2	
224609.3....	$18_{6,12}-17_{6,11}$	A	0.8	2.8	
225608.7....	$19_{3,17}-18_{3,16}$	E	1.1	5.0	
225618.7....	$19_{3,17}-18_{3,16}$	A	1.3	6.3	
225928.6....	$6_{6,1}-5_{5,0}$	A	0.4	2.2	
	$6_{6,0}-5_{5,1}$	A			
226635.2....	$20_{1,19}-19_{2,18}$	A	...	...	f
226713.1....	$20_{2,19}-19_{2,18}$	E	0.9	2.6	
226718.7....	$20_{2,19}-19_{2,18}$	A	0.5	2.6	
226773.2....	$20_{1,19}-19_{1,18}$	E	0.9	3.7	
226778.7....	$20_{1,19}-19_{1,18}$	A	1.0	3.1	
226856.5....	$20_{2,19}-19_{1,18}$	E	0.5	2.0	
226862.2....	$20_{2,19}-19_{1,18}$	A	0.6	1.8	
227019.6....	$19_{2,17}-18_{2,16}$	E	1.0	4.2	
227028.0....	$19_{2,17}-18_{2,16}$	A	1.2	4.5	g
227561.1....	$21_{0,21}-20_{0,20}$	E			
227561.9....	$21_{1,21}-20_{1,20}$	E	2.1	13.0	
227562.0....	$21_{1,21}-20_{1,20}$	A			
227562.8....	$21_{0,21}-20_{0,20}$	A			
228629.1....	$18_{5,13}-17_{5,12}$	E	1.2	4.0	
228651.3....	$18_{5,13}-17_{5,12}$	A	1.2	5.5	
229404.9....	$18_{3,15}-17_{3,14}$	E	1.2	5.0	
229420.3....	$18_{3,15}-17_{3,14}$	A	1.3	4.4	
229474.6....	$20_{3,17}-19_{4,16}$	E	0.3	0.9	
229504.6....	$20_{3,17}-19_{4,16}$	A	0.3	1.5	
229590.0....	$19_{3,17}-18_{2,16}$	E	...	...	h
229595.0....	$19_{3,17}-18_{2,16}$	A	...	...	h
231199.3....	$21_{9,12}-21_{8,13}$	A	0.3	1.8	

notes: b-lost under SO_2 221965, c-blend with CH_3OCH_3 222435, d-blend with C_2H_5CN 224018, e-blend with CH_2CO 224327, f-blend with CN 226332, g-blend with $^{34}SO_2$ 227032, h-blend with unidentified line.

Table A23 - continued

ν (MHz)	$J_{K_pK_o}$		T_a^*(pk) (K)	$\int T_A^* dv$ (K km s^{-1})	notes
231239.1....	$21_{9,13}-21_{8,14}$	A	0.4	2.8	
231960.2....	$20_{9,11}-20_{8,12}$	E	nd	...	
231966.9....	$20_{9,11}-20_{8,12}$	A	0.4	1.6	
233212.6....	$19_{4,16}-18_{4,15}$	E	...	...	i
233226.7....	$19_{4,16}-18_{4,15}$	A	1.1	4.8	
233310.0....	$19_{15,4}-18_{15,3}$	A	0.4	2.2	
	$19_{15,5}-18_{15,4}$	A			
233394.6....	$19_{14,5}-18_{14,4}$	A	0.4	3.3	
	$19_{14,6}-18_{14,5}$	A			
233505.0....	$19_{13,7}-18_{13,6}$	E	...	...	j
233506.6....	$19_{13,6}-18_{13,5}$	A	0.8	7.0	
	$19_{13,7}-18_{13,6}$	A			
233524.6....	$19_{13,6}-18_{13,5}$	E	0.4	3.0	k
233627.1....	$17_{9,8}-17_{8,9}$	A	0.4	7.1	
233628.4....	$17_{9,9}-17_{8,10}$	A			
233649.9....	$19_{12,7}-18_{12,6}$	E	0.5	3.1	
233655.3....	$19_{12,7}-18_{12,6}$	A	1.1	8.2	l
	$19_{12,8}-18_{12,7}$	A			
233671.0....	$19_{12,8}-18_{12,7}$	E	0.3	2.0	
233754.1....	$18_{4,14}-17_{4,13}$	E	0.8	4.5	
233777.5....	$18_{4,14}-17_{4,13}$	A	0.8	3.0	
233845.3....	$19_{11,8}-18_{11,7}$	E	0.5	3.1	
233854.2....	$19_{11,8}-18_{11,7}$	A	0.7	3.1	
	$19_{11,9}-18_{11,8}$	A			
233867.1....	$19_{11,9}-18_{11,8}$	E	0.4	1.6	
234011.3....	$16_{9,7}-16_{8,8}$	A	...	...	m
234011.8....	$16_{9,8}-16_{8,9}$	A	...	...	m
234112.3....	$19_{10,9}-18_{10,8}$	E	0.3	2.3	
234124.8....	$19_{10,9}-18_{10,8}$	A	0.6	2.9	
	$19_{10,10}-18_{10,9}$	A			
234134.6....	$19_{10,10}-18_{10,9}$	E	0.6	3.0	
234328.8....	$15_{9,6}-15_{8,7}$	A	0.3 ?	...	
234328.9....	$15_{9,7}-15_{8,8}$	A			
234486.4....	$19_{9,10}-18_{9,9}$	E	0.6	3.5	
234502.2....	$19_{9,11}-18_{9,10}$	A	1.1	6.5	
234502.4....	$19_{9,10}-18_{9,9}$	A			
234508.5....	$19_{9,11}-18_{9,10}$	E	0.6	3.7	
234739.0....	$20_{2,18}-19_{3,17}$	A	0.5	0.9	
235029.9....	$19_{8,11}-18_{8,10}$	E	1.2	2.4	
235043.2....	$19_{8,12}-18_{8,11}$	E	0.6	2.5	
235046.5....	$19_{8,12}-18_{8,11}$	A			
235051.4....	$19_{8,11}-18_{8,10}$	A	1.2	5.1	
235844.5....	$19_{7,13}-18_{7,12}$	A	0.5	2.1	
235865.9....	$19_{7,13}-18_{7,12}$	E	0.5	2.1	
235887.2....	$19_{7,12}-18_{7,11}$	E	0.5	2.0	

notes: i-lost under C_2H_5CN 233207, j-blend with C_2H_5CN 233498, k-blend with C_2H_5CN 233524, l-blend with C_2H_5CN 233654, m-blend with $^{13}CH_3OH$ 234012.

Table A23 - continued

ν (MHz)	$J_{K_pK_o}$		T_a^*(pk) (K)	$\int T_A^* dv$ (K km s^{-1})	notes
235932.3....	$19_{7,12}-18_{7,11}$	A	0.5	1.6	n
236355.9....	$20_{3,18}-19_{3,17}$	E	0.9	5.8	
236365.5....	$20_{3,18}-19_{3,17}$	A	0.7	3.9	
236743.7....	$19_{5,15}-18_{5,14}$	E	0.6	2.4	
236759.6....	$19_{5,15}-18_{5,14}$	A	0.6	2.6	
236800.5....	$19_{6,14}-18_{6,13}$	E	0.6	2.7	
236810.3....	$19_{6,14}-18_{6,13}$	A	0.8	2.8	
237266.9....	$21_{1,20}-20_{2,19}$	A	0.4	3.3	
237297.5....	$20_{2,18}-19_{2,17}$	E	0.8	3.5	
237306.0....	$20_{2,18}-19_{2,17}$	A	1.1	8.6	
237309.5....	$21_{2,20}-20_{2,19}$	E			
237315.1....	$21_{2,20}-20_{2,19}$	A	1.1	6.2	
237344.8....	$21_{1,20}-20_{1,19}$	E	0.8	2.6	
237350.4....	$21_{1,20}-20_{1,19}$	A	0.7	2.4	
237393.2....	$21_{2,20}-20_{1,19}$	E	0.1 ?	...	
237398.6....	$21_{2,20}-20_{1,19}$	A	0.2 ?	...	
237807.6....	$19_{6,13}-18_{6,12}$	E	0.5	2.3	
237829.8....	$19_{6,13}-18_{6,12}$	A	0.6	2.3	
238156.2....	$22_{1,22}-21_{1,21}$	E	2.7	21.1	
238156.6....	$22_{0,22}-21_{0,21}$	E			
238156.8....	$22_{1,22}-21_{1,21}$	A			
238157.3....	$22_{0,22}-21_{0,21}$	A			
238190.1....	$7_{6,2}-6_{5,1}$	A	0.2	1.7	
238190.2....	$7_{6,1}-6_{5,2}$	A			
238926.8....	$20_{3,18}-19_{2,17}$	E	0.3	0.9	
238932.5....	$20_{3,18}-19_{2,17}$	A	0.1 ?	...	
240021.4....	$19_{3,16}-18_{3,15}$	E	1.0	5.9	
240034.6....	$19_{3,16}-18_{3,15}$	A	1.1	4.9	
242872.2....	$19_{5,14}-18_{5,13}$	E	1.1	6.5	
242896.0....	$19_{5,14}-18_{5,13}$	A	1.1	6.1	
244580.7....	$20_{4,17}-19_{4,16}$	E	1.3	5.3	
244594.0....	$20_{4,17}-19_{4,16}$	A	1.1	5.4	
245137.9....	$21_{3,18}-20_{4,17}$	E	0.3 ?	...	
245165.8....	$21_{3,18}-20_{4,17}$	A	0.4 ?	...	
245651.1....	$20_{15,5}-19_{15,4}$	A	0.6	3.2	
	$20_{15,6}-19_{15,5}$	A			
245752.2....	$20_{14,6}-19_{14,5}$	A	0.7	2.3	
	$20_{14,7}-19_{14,6}$	A			
245754.3....	$20_{14,6}-19_{14,5}$	E			
245772.1....	$20_{14,7}-19_{14,6}$	E	0.5	1.8	
245883.2....	$20_{13,8}-19_{13,7}$	E	0.2	0.5	
245885.1....	$20_{13,7}-19_{13,6}$	A	0.8	3.3	
	$20_{13,8}-19_{13,7}$	A			
245903.5....	$20_{13,7}-19_{13,6}$	E	0.2	0.9	
246055.1....	$20_{12,9}-19_{12,8}$	E	0.5	1.0	

notes: n-blend with $^{34}SO_2$ 235928.

Table A23 - continued

ν (MHz)	$J_{K_pK_o}$		T_A^*(pk) (K)	$\int T_A^* dv$ (K km s^{-1})	notes
246060.8....	$20_{12,8}-19_{12,7}$	A	0.8	3.0	
	$20_{12,9}-19_{12,8}$	A			
246076.6....	$20_{12,8}-19_{12,7}$	E	...	...	o
246285.4....	$20_{11,9}-19_{11,8}$	E	0.4	1.5	
246295.1....	$20_{11,10}-19_{11,9}$	A	1.3	3.0	
	$20_{11,9}-19_{11,8}$	A			
246308.6....	$20_{11,10}-19_{11,9}$	E	0.4	2.0	
246600.2....	$20_{10,11}-19_{10,10}$	E	0.7	3.3	
246613.3....	$20_{10,11}-19_{10,10}$	A	1.1	4.8	
246613.4....	$20_{10,10}-19_{10,9}$	A			
246623.1....	$20_{10,10}-19_{10,9}$	E	0.8	3.7	
246891.1....	$19_{4,15}-18_{4,14}$	E	1.2	3.4	
246914.6....	$19_{4,15}-18_{4,14}$	A	1.2	5.5	
247040.8....	$20_{9,11}-19_{9,10}$	E	0.6	1.3	
247044.1....	$20_{3,19}-19_{3,18}$	E	1.1	2.6	
247053.5....	$20_{3,19}-19_{3,18}$	A	1.2	2.7	
247057.7....	$20_{9,12}-19_{9,11}$	A	1.2	4.9	
	$20_{9,11}-19_{9,10}$	A			
247063.5....	$20_{9,12}-19_{9,11}$	E	0.5	2.0	
247656.8....	$20_{2,19}-19_{2,18}$	E	1.4	3.7	
247665.3....	$20_{2,19}-19_{2,18}$	A	1.2	2.8	
247682.7....	$20_{8,12}-19_{8,11}$	E	0.2	0.4	
247697.4....	$20_{8,13}-19_{8,12}$	A	0.7	1.8	
247704.3....	$20_{8,13}-19_{8,12}$	E	0.8	4.2	
247708.0....	$20_{8,12}-19_{8,11}$	A	1.1	2.2	
247901.6....	$22_{2,21}-21_{2,20}$	E	0.7	3.2	
247907.1....	$22_{2,21}-21_{2,20}$	A	0.6	1.7	
247922.2....	$22_{1,21}-21_{1,20}$	E	0.6	1.9	
247927.7....	$22_{1,21}-21_{1,20}$	A	0.5	2.0	
248617.4....	$20_{7,14}-19_{7,13}$	A	1.0	2.8	
248633.8....	$20_{7,14}-19_{7,13}$	E	1.0	3.6	
250246.5....	$20_{3,17}-19_{3,16}$	E	1.0	2.6	
250258.3....	$20_{3,17}-19_{3,16}$	A	0.9	2.8	
255776.1....	$21_{4,18}-20_{4,17}$	E	1.0	4.0	
255789.4....	$21_{4,18}-20_{4,17}$	A	1.0	5.5	
257226.5....	$20_{5,15}-19_{5,14}$	E	0.8	3.9	
257252.6....	$20_{5,15}-19_{5,14}$	A	0.9	4.0	p
257690.3....	$22_{3,20}-21_{3,19}$	E	1.4	7.2	
257699.4....	$22_{3,20}-21_{3,19}$	A	0.9	5.5	
258081.0....	$22_{2,20}-21_{2,19}$	E	1.2	5.7	
258089.5....	$22_{2,20}-21_{2,19}$	A	1.1	3.2	
258121.1....	$21_{14,8}-20_{14,7}$	A	1.0	2.7	
	$21_{14,7}-20_{14,6}$	A			
258123.0....	$21_{14,7}-20_{14,6}$	E			
258476.6....	$21_{12,9}-20_{12,8}$	E	0.9	4.1	

notes: o-lost under CH_3OH 246075, p-blend with C_2H_5CN 257227, ^{30}SiO 257255.

Table A23 - continued

ν (MHz)	$J_{K_pK_o}$		T_A^*(pk) (K)	$\int T_A^* dv$ (K km s^{-1})	notes
258482.9....	$21_{12,10}$-$20_{12,9}$	A	1.0	5.9	
258490.8....	$23_{2,22}$-$22_{2,21}$	E	1.0	4.1	
258496.3....	$23_{2,22}$-$22_{2,21}$	A	1.1	7.4	
258499.0....	$21_{12,10}$-$20_{12,9}$	E	0.8	3.5	
258502.7....	$23_{1,22}$-$22_{1,21}$	E	1.0	3.7	
258508.1....	$23_{1,22}$-$22_{1,21}$	A	1.0	3.6	
258746.4....	$21_{11,10}$-$20_{11,9}$	E	0.5	1.4	
258756.6....	$21_{11,10}$-$20_{11,9}$	A	0.7	3.3	
	$21_{11,11}$-$20_{11,10}$	A			
258769.7....	$21_{11,11}$-$20_{11,10}$	E	0.4	1.6	
259114.2....	$21_{10,11}$-$20_{10,10}$	E	0.6	2.0	
259128.2....	$21_{10,11}$-$20_{10,10}$	A	1.1	4.4	
	$21_{10,12}$-$20_{10,11}$	A			
259137.7....	$21_{10,12}$-$20_{10,11}$	E	0.3	1.1	
259341.9....	$24_{1,24}$-$23_{1,23}$	E	2.0	10.8	
259342.0....	$24_{0,24}$-$23_{0,23}$	E			
259342.8....	$24_{1,24}$-$23_{1,23}$	A			
259343.0....	$24_{0,24}$-$23_{0,23}$	A			
259499.9....	$20_{4,16}$-$19_{4,15}$	E	0.8	3.3	
259521.7....	$20_{4,16}$-$19_{4,15}$	A	1.0	3.3	
259629.4....	$21_{9,12}$-$20_{9,11}$	E	0.6	2.5	
259646.6....	$21_{9,13}$-$20_{9,12}$	A	0.8	3.7	
259647.7....	$21_{9,12}$-$20_{9,11}$	A			
259652.9....	$21_{9,13}$-$20_{9,12}$	E	0.5	2.5	
260244.4....	$21_{3,18}$-$20_{3,17}$	E	0.8	3.7	
260255.1....	$21_{3,18}$-$20_{3,17}$	A	2.1	8.5	q
260384.2....	$21_{8,13}$-$20_{8,12}$	E	1.6	12.4	r
260392.7....	$21_{8,14}$-$20_{8,13}$	A	1.0	5.8	
260404.2....	$21_{8,14}$-$20_{8,13}$	E	1.8	14.9	
260415.3....	$21_{8,13}$-$20_{8,12}$	A	0.7	5.4	
261148.8....	$21_{5,17}$-$20_{5,16}$	E	1.4	10.0	
261165.4....	$21_{5,17}$-$20_{5,16}$	A	1.2	5.2	
261433.8....	$21_{7,15}$-$20_{7,14}$	E	0.9	3.8	
261436.8....	$21_{7,15}$-$20_{7,14}$	A	1.3	3.9	
261715.4....	$21_{7,14}$-$20_{7,13}$	E	1.1	2.8	
261746.6....	$21_{7,14}$-$20_{7,13}$	A	1.1	6.6	
262324.7....	$21_{6,16}$-$20_{6,15}$	E	1.2	2.7	
262340.5....	$21_{6,16}$-$20_{6,15}$	A	1.0	3.4	

notes: q- blend with $H^{13}CO^+$ 260255, r-blend with CH_3OH 260382.

K. CH_3OCH_3

Dimethyl ether (CH_3OCH_3) is another abundant internal rotor which has been detected through the 29 rotational transitions listed in Table A24. Unlike $HCOOCH_3$, dimethyl ether has two internal rotors and each rotational transition is therefore split into four components corresponding to the allowed products of the A and E symmetry states of the individual CH_3 rotors. For the most part we resolve these splittings even with our 1 MHz filters. The average velocity and line width of the CH_3OCH_3 emission are 7.9 and 3.6 km s^{-1}, which are very similar to those of both CH_3OH and $HCOOCH_3$. In addition, the derived rotational temperature and column density of 80 K and 3 10^{15} cm^{-2} are the same, within errors, as those of $HCOOCH_3$. These results may indicate that CH_3OH, $HCOOCH_3$, and CH_3OCH_3 are intimately related chemically in the interstellar medium, as is suggested in Chaper 4.

Table A24

Transitions of CH_3OCH_3

	ν (MHz)	$J_{K_pK_o}$		T_a^*(pk) (K)	$\int T_a^* dv$ (K km s^{-1})	notes
CH_3OCH_3....	222238.7	$4_{3,2}-3_{2,1}$	EA	0.2	0.8	
	222247.5	$4_{3,2}-3_{2,1}$	AE,EE	1.3	4.3	
	222254.7	$4_{3,2}-3_{2,1}$	AA	1.0	2.6	
	222426.8	$4_{3,1}-3_{2,2}$	AE	0.3	1.2	a
	222434.0	$4_{3,1}-3_{2,2}$	EE,AA	1.5	4.0	b
	222435.6	$4_{3,1}-3_{2,2}$	EA			
	223200.1	$8_{2,7}-7_{1,6}$	AE,EA			
	223202.3	$8_{2,7}-7_{1,6}$	EE	1.1	9.5	
	223204.5	$8_{2,7}-7_{1,6}$	AA			
	225598.8	$12_{1,12}-11_{0,11}$	EA,AE			
	225599.1	$12_{1,12}-11_{0,11}$	EE	3.6	12.5	
	225599.5	$12_{1,12}-11_{0,11}$	AA			
	226346.0	$14_{1,13}-13_{2,12}$	AA			
	226346.9	$14_{1,13}-13_{2,12}$	EE	1.6	5.7	
	226347.8	$14_{1,13}-13_{2,12}$	AE,EA			
	228978.8	$7_{7,1}-8_{6,2}$	EA	0.2	0.6	
	228983.2	$7_{7,1}-8_{6,2}$	EE			
	228984.8	$7_{7,1}-8_{6,2}$	AE			
		$7_{7,0}-8_{6,3}$	AE			
	228987.7	$7_{7,1}-8_{6,2}$	AA	0.2	0.7	
		$7_{7,0}-8_{6,3}$	AA			
	228989.3	$7_{7,0}-8_{6,3}$	EE			
	228990.9	$7_{7,0}-8_{6,3}$	EA			
	230465.8	$10_{8,3}-11_{7,4}$	EA			
	230467.8	$10_{8,3}-11_{7,4}$	EE			
	230469.8	$10_{8,3}-11_{7,4}$	AA			
		$10_{8,2}-11_{7,5}$	AA			
	230470.2	$10_{8,3}-11_{7,4}$	AE	0.4	2.0	
		$10_{8,2}-11_{7,5}$	AE			
	230472.2	$10_{8,2}-11_{7,5}$	EE			
	230474.6	$10_{8,2}-11_{7,5}$	EA			
	231987.8	$13_{0,13}-12_{1,12}$	AA			c
	231987.9	$13_{0,13}-12_{1,12}$	EE	3.2	8.3	
	231988.0	$13_{0,13}-12_{1,12}$	EA,AE			
	237046.3	$7_{2,5}-6_{1,6}$	AE,EA			d
	237049.0	$7_{2,5}-6_{1,6}$	EE	1.5	7.5	
	237051.7	$7_{2,5}-6_{1,6}$	AA			
	237618.9	$9_{2,8}-8_{1,7}$	EA,AE			
	237621.0	$9_{2,8}-8_{1,7}$	EE	0.9	4.8	
	237623.0	$9_{2,8}-8_{1,7}$	AA			
	240978.2	$5_{3,3}-4_{2,2}$	EA	0.1	0.4	
	240982.9	$5_{3,3}-4_{2,2}$	AE	1.0	4.1	
	240985.2	$5_{3,3}-4_{2,2}$	EE			
	240990.1	$5_{3,3}-4_{2,2}$	AA	0.5	1.0	
	241524.0	$5_{3,2}-4_{2,3}$	AE	0.9	4.2	

notes: a-blend with $HCOOCH_3$ 222422, b-blend with $HCOOCH_3$ 222439, c-blend with C_2H_5CN 231990, d-blend with SO_2 237069.

Table A24 - continued

	ν (MHz)	$J_{K_pK_o}$		T_A^*(pk) (K)	$\int T_A^* dv$ (K km s^{-1})	notes
CH_3OCH_3...	241528.8	$5_{3,2}-4_{2,3}$	EA	1.7	10.2	
	241529.0	$5_{3,2}-4_{2,3}$	EE			
	241531.2	$5_{3,2}-4_{2,3}$	AA			
	241946.2	$13_{1,13}-12_{0,12}$	AE/EA	3.8	2.8	
	241946.5	$13_{1,13}-12_{0,12}$	EE			
	241946.9	$13_{1,13}-12_{0,12}$	AA			
	249924.3	$15_{1,14}$-$14_{2,13}$	EE	1.1	4.4	
	258549.1	$14_{1,14}$-$13_{0,13}$	EE	3.2	10.8	e
	258549.3	$14_{1,14}$-$13_{0,13}$	AA			
	259485.8	$6_{3,4}$-$5_{2,3}$	AE,EA	0.7	3.1	
	259489.9	$6_{3,4}$-$5_{2,3}$	EE	1.3	3.2	
	259493.9	$6_{3,4}$-$5_{2,3}$	AA	0.6	2.4	
	260758.6	$6_{3,3}$-$5_{2,4}$	EE	1.9	8.2	
	260761.7	$6_{3,3}$-$5_{2,4}$	AA	1.5	6.5	
	261247.6	$15_{5,10}$-$15_{4,11}$	EE	1.5	12.3	f
	261250.2	$15_{5,10}$-$15_{4,11}$	AA	0.8	8.2	f
	261897.3	$14_{5,9}$-$14_{4,10}$	EE	0.9	3.1	
	261899.5	$14_{5,9}$-$14_{4,10}$	AA			
	261956.0	$15_{5,11}$-$15_{4,12}$	EE	1.0	1.8	
	261959.3	$15_{5,11}$-$15_{4,12}$	AA	1.1	2.2	
	262308.8	$14_{5,10}$-$14_{4,11}$	AE,EA	0.8	1.3	
	262312.4	$14_{5,10}$-$14_{4,11}$	EE	1.0	5.0	
	262316.4	$14_{5,10}$-$14_{4,11}$	AA	0.9	0.9	
	262393.4	$13_{5,8}$-$13_{4,9}$	EE	1.3	4.2	
	262394.9	$13_{5,8}$-$13_{4,9}$	AA			
	262624.7	$13_{5,9}$-$13_{4,10}$	EE	1.6	2.2	
	262629.5	$13_{5,9}$-$13_{4,10}$	AA	0.6	1.2	
	262768.9	$12_{5,7}$-$12_{4,8}$	EE	1.3	6.9	g
	262769.7	$12_{5,7}$-$12_{4,8}$	AA			
	262774.2	$8_{2,6}$-$7_{1,7}$	EE	0.7	4.2	g
	262889.5	$12_{5,8}$-$12_{4,9}$	EE	0.5	1.2	
	262895.3	$12_{5,8}$-$12_{4,9}$	AA	0.5	2.3	
	263050.0	$11_{5,6}$-$11_{4,7}$	EE	1.1	6.4	
	263050.3	$11_{5,6}$-$11_{4,7}$	AA			
	263107.2	$11_{5,7}$-$11_{4,8}$	EE	0.3	1.0	
	263113.7	$11_{5,7}$-$11_{4,8}$	AA	1.2	4.0	

notes: e-blend with $CH_3CN(\nu_8=1)$ 258552, f-marginally resolved, g-blend with HNCO 262769.

L. C_2H_3CN and C_2H_5CN

Vinyl cyanide (C_2H_3CN) and ethyl cyanide (C_2H_5CN) are hydrogenated versions of the abundant cyanoacetylene (HC_3N) molecule with very dense rotational spectra because of their heavy, asymmetric structure. Like cyanoacetylene they show strong emission from the hot core, but unlike HC_3N do not appear to be present in measurable quantities in either the spike or plateau sources. Because of the high excitation in the hot core, lines up to J = 29 are easily visible in Figure A1 from both C_2H_3CN and C_2H_5CN, and are listed in Tables A25 and A26. The average v_{LSR} and Δv for the vinyl and ethyl cyanide transitions are quite similar, namely 5.0 and 11.4 km s^{-1}. The rotational temperatures are also equivalent, within errors, at 150 K, but ethyl cyanide is an order of magnitude more abundant. The derived column densities are approximately 2 10^{14} cm^{-2} for C_2H_3CN and 2 10^{15} cm^{-2} for C_2H_5CN. The great difficulty of hydrogenating cyanopolyacetylene ions in the gas phase (Herbst, Adams, and Smith 1983) and the presence of vinyl cyanide and ethyl cyanide only in the hot core has lead a number of investigators to conclude that the hydrogenated species are most likely produced on grain surfaces and then released into the gas phase (Watson 1976, Irvine and Hjalmarson 1984).

Table A25

Transitions of C_2H_3CN

ν (MHz)	$J_{K_pK_o}$	T_A^*(pk) (K)	$\int T_A^* dv$ (K km s^{-1})	notes
216936.7....	$23_{2,22}-22_{2,21}$	0.6	1.3	
218398.5....	$23_{7,17}-22_{7,16}$			
	$23_{7,16}-22_{7,15}$	0.4 ?	...	a
218402.4....	$23_{6,18}-22_{6,17}$			
	$23_{6,17}-22_{6,16}$			
218421.7....	$23_{8,16}-22_{8,15}$	0.3	1.5	
	$23_{8,15}-22_{8,14}$			
218451.3....	$23_{5,19}-22_{5,18}$	0.2	1.4	
218452.3....	$23_{5,18}-22_{5,17}$			
218573.6....	$23_{4,20}-22_{4,19}$	0.3	2.3	
218585.0....	$23_{3,21}-22_{3,20}$	0.3	3.8	
218615.1....	$23_{4,19}-22_{4,18}$	0.2	2.4	
219400.6....	$23_{3,20}-22_{3,19}$	0.3	1.9	
220561.3....	$24_{1,24}-23_{1,23}$	0.4	1.7	
221123.8....	$23_{1,22}-22_{1,21}$	0.4	3.5	
221766.0....	$24_{0,24}-23_{0,23}$	0.4	2.1	
222153.5....	$23_{2,21}-22_{2,20}$	0.4	3.1	
226256.8....	$24_{2,23}-23_{2,22}$	0.2	3.0	
227897.5....	$24_{7,18}-23_{7,17}$	0.5	1.5	
	$24_{7,17}-23_{7,16}$			
227906.6....	$24_{6,19}-23_{6,18}$	0.5	1.9	
	$24_{6,18}-23_{6,17}$			
227918.5....	$24_{8,16}-23_{8,15}$	0.5	2.4	
	$24_{8,17}-23_{8,16}$			
227960.1....	$24_{9,16}-23_{9,15}$			
	$24_{9,15}-23_{9,14}$	0.5	6.0	
227966.0....	$24_{5,20}-23_{5,19}$			
227967.5....	$24_{5,19}-23_{5,18}$			
228090.5....	$24_{3,22}-23_{3,21}$	0.4	2.5	
228104.6....	$24_{4,21}-23_{4,20}$	0.5	3.5	
228160.3....	$24_{4,20}-23_{4,19}$	nd	...	
229087.0....	$24_{3,21}-23_{3,20}$	0.3	2.8	
229647.8....	$25_{1,25}-24_{1,24}$	0.2	1.0	
230487.9....	$24_{1,23}-23_{1,22}$	...	...	b
230738.5....	$25_{0,25}-24_{0,24}$	0.4	3.8	
231952.3....	$24_{2,22}-23_{2,21}$	0.3	2.7	
235563.8....	$25_{2,24}-24_{2,23}$	0.3	4.5	
237397.0....	$25_{7,19}-24_{7,18}$	...	...	c
	$25_{7,18}-24_{7,17}$			
237411.9....	$25_{6,20}-24_{6,19}$	...	...	d
	$25_{6,19}-24_{6,18}$			
237415.4....	$25_{8,18}-24_{8,17}$	0.4 ?	...	d
	$25_{8,17}-24_{8,16}$			
237456.3....	$25_{9,17}-24_{9,16}$	0.2	1.4	
	$25_{9,16}-24_{9,15}$			

notes: a-blend with C_2H_5CN 2183990, b-lost under CO 230538, c-blend with $HCOOCH_3$ 237399, d-blend with C_2H_5CN 237405.

Table A25 - continued

ν (MHz)	$J_{K_pK_o}$	T_A^*(pk) (K)	$\int T_A^* dv$ (K km s^{-1})	notes
237482.8....	$25_{5,21}-24_{5,20}$	} 0.3	3.1	
237485.0....	$25_{5,20}-24_{5,19}$			
237591.4....	$25_{3,23}-24_{3,22}$	0.4	4.1	
237638.0....	$25_{4,22}-24_{4,21}$	nd	...	
237711.9....	$25_{4,21}-24_{4,20}$	0.3	2.6	
238726.7....	$26_{1,26}-25_{1,25}$	0.2	1.3	
238796.2....	$25_{3,22}-24_{3,21}$	0.2	1.8	
239708.3....	$26_{0,26}-25_{0,25}$	0.1	0.6	
239816.1....	$25_{1,24}-24_{1,23}$	0.5	3.6	
241737.5....	$25_{2,23}-24_{2,22}$	...	...	e
241857.4....	$26_{2,25}-25_{2,24}$	0.5	4.7	
246896.9....	$26_{7,20}-25_{7,19}$	} 0.5	3.2	
	$26_{7,19}-25_{7,18}$			
246912.2....	$26_{8,19}-25_{8,18}$	} ...	...	f
	$26_{8,18}-25_{8,17}$			
246918.3....	$26_{6,21}-25_{6,20}$	} 0.6	4.1	f
	$26_{6,21}-25_{6,19}$			
246952.1....	$26_{9,18}-25_{9,17}$	} 0.6	1.1	
	$26_{9,17}-25_{9,16}$			
247001.7....	$26_{5,22}-25_{5,21}$	} 0.2	2.9	
247004.9....	$26_{5,21}-25_{5,20}$			
247086.9....	$26_{3,24}-25_{3,23}$	0.2	2.0	
247270.6....	$26_{4,22}-25_{4,21}$	0.3	2.8	
247798.6....	$27_{1,27}-26_{1,26}$	0.3	2.9	
248529.0....	$26_{3,23}-25_{3,22}$	0.4	1.6	
256397.2....	$27_{7,21}-26_{7,20}$	} $\lesssim$0.5	...	g
	$27_{7,20}-26_{7,19}$			g
256409.6....	$27_{8,20}-26_{8,19}$	} 0.7	12.6	g
	$27_{8,19}-26_{8,18}$			g
256425.9....	$27_{6,22}-26_{6,21}$	} 0.7	13.1	
	$27_{6,21}-26_{6,20}$			
256447.8....	$27_{9,19}-26_{9,18}$	} 0.4	6.0	
	$27_{9,18}-26_{9,17}$			
256522.9....	$27_{5,23}-26_{5,22}$	0.8	3.6	
256527.4....	$27_{5,22}-26_{5,21}$	0.5	3.1	
256711.8....	$27_{4,24}-26_{4,23}$	0.3	3.7	
256837.2....	$27_{4,23}-26_{4,22}$	0.3	2.0	
257646.0....	$28_{0,28}-27_{0,27}$	0.5	3.5	
258360.0....	$27_{1,26}-26_{1,25}$	0.6	1.7	

notes: e-lost in wings of CH_3OH 241700 NS 241767, f-blend with $HCOOCH_3$ 246915, g-blend with C_2H_5CN 256394.

Table A26

Transitions of C_2H_5CN

ν (MHz)	$J_{K_pK_o}$	T_A^*(pk) (K)	$\int T_A^* dv$ (K km s^{-1})	notes
215039.7....	$24_{9,16}-23_{9,15}$	1.1	19.7	
	$24_{9,15}-23_{9,14}$			
215041.9....	$24_{10,15}-23_{10,14}$			
	$24_{10,14}-23_{10,13}$			
215058.0....	$24_{3,22}-23_{3,21}$	1.3	20.6	
215058.6....	$24_{8,17}-23_{8,16}$			
	$24_{8,16}-23_{8,15}$			
215059.2....	$24_{11,13}-23_{11,12}$			
	$24_{11,14}-23_{11,13}$			
215088.2....	$24_{12,13}-23_{12,12}$	0.5	6.7	
	$24_{12,12}-23_{12,11}$			
215109.1....	$24_{7,18}-23_{7,17}$	1.1	9.2	
	$24_{7,17}-23_{7,16}$			
215119.2....	$25_{0,25}-24_{0,24}$	1.0	13.6	
215126.7....	$24_{13,12}-23_{13,11}$	0.5	3.5	
	$24_{13,11}-23_{13,10}$			
215173.3....	$24_{14,11}-23_{14,10}$	0.3	3.9	
	$24_{14,10}-23_{14,9}$			
215211.5....	$24_{6,19}-23_{6,18}$	...	...	a
215212.5....	$24_{6,18}-23_{6,17}$	...	...	a
215400.8....	$24_{5,20}-23_{5,19}$	0.8	15.2	
215428.0....	$24_{5,19}-23_{5,18}$	1.0	18.4	
215620.2....	$24_{4,21}-23_{4,20}$	0.6	12.5	
215941.1....	$6_{4,3}-5_{3,2}$	0.3 ?	...	
215943.1....	$6_{4,2}-5_{3,3}$			
215965.6....	$25_{1,25}-24_{0,24}$	0.3	1.7	
216077.2....	$24_{4,20}-23_{4,19}$	0.7	9.6	
216752.5....	$26_{1,25}-25_{2,24}$	0.3 ?	...	
218390.0....	$24_{3,21}-23_{3,20}$	0.8	9.9	b
219463.6....	$22_{2,21}-21_{1,20}$	0.3	3.3	
219505.6....	$24_{2,22}-23_{2,21}$	0.9	11.5	
220660.9....	$25_{2,24}-24_{2,23}$	0.7	5.4	
222707.2....	$26_{0,26}-25_{1,25}$	0.3	2.9	
222918.2....	$25_{1,24}-24_{1,23}$	0.9	10.6	
223385.3....	$26_{1,26}-25_{1,25}$	0.9	18.7	
223553.6....	$26_{0,26}-25_{0,25}$	0.6	7.9	
223933.7....	$25_{3,23}-24_{3,22}$	0.6	8.1	
224002.1....	$25_{10,15}-24_{10,14}$	0.9	10.8	
	$25_{10,16}-24_{10,15}$			
224003.4....	$25_{9,17}-24_{9,16}$			
	$25_{9,16}-24_{9,15}$			
224017.5....	$25_{11,15}-24_{11,14}$	0.6	9.5	c
	$25_{11,14}-24_{11,13}$			
224028.1....	$25_{8,18}-24_{8,17}$	0.8	8.2	
	$25_{8,17}-24_{8,16}$			
224045.8....	$25_{12,13}-24_{12,12}$	0.3	4.4	
	$25_{12,14}-24_{12,13}$			

notes: a-lost under SO 215221, b-blend with C_2H_3CN 218399 and 218402, c-blend with $HCOOCH_3$ 224024,

Table A26 - continued

ν (MHz)	$J_{K_p K_o}$	T_A^*(pk) (K)	$\int T_A^* dv$ (K km s^{-1})	notes
224084.3....	$25_{13,12}-24_{13,11}$	0.8	11.4	
	$25_{13,13}-24_{13,12}$			
224088.2....	$25_{7,19}-24_{7,18}$			
	$25_{7,18}-24_{7,17}$			
224131.5....	$25_{14,12}-24_{14,11}$	0.2	2.7	
	$25_{14,11}-24_{14,10}$			
224186.3....	$25_{15,11}-24_{15,10}$	0.2	1.7	
	$25_{15,10}-24_{15,9}$			
224206.6....	$25_{6,20}-24_{6,19}$	0.7	11.8	
224208.1....	$25_{6,19}-24_{6,18}$			
224231.7....	$26_{1,26}-25_{0,25}$	nd	...	
224419.8....	$25_{5,21}-24_{5,20}$	0.4	4.9	
224458.9....	$25_{5,20}-24_{5,19}$	0.7	7.1	
224469.0....	$25_{19,7}-24_{19,6}$	0.3	1.8	
	$25_{19,6}-24_{19,5}$			
224638.7....	$25_{4,22}-24_{4,21}$	0.6	8.4	
224643.3....	$25_{21,4}-24_{21,3}$			
	$25_{21,5}-24_{21,4}$			
225236.1....	$25_{4,21}-24_{4,20}$	0.8	13.7	
227170.2....	$27_{1,26}-26_{2,25}$	nd	...	
227781.0....	$25_{3,22}-24_{3,21}$	0.5	7.9	
228483.1....	$25_{2,23}-24_{2,22}$	0.9	11.9	
228797.5....	$14_{2,12}-13_{1,13}$	0.3	2.1	
229265.2....	$26_{2,25}-25_{2,24}$	0.7	10.7	
231310.4....	$26_{1,25}-25_{1,24}$	0.9	10.6	
231312.3....	$27_{0,27}-26_{1,26}$			
231313.2....	$24_{2,23}-23_{1,22}$			
231854.2....	$27_{1,27}-26_{1,26}$	1.1	11.6	
231990.4....	$27_{0,27}-26_{0,26}$	1.1	17.7	d
232532.3....	$27_{1,27}-26_{0,26}$	nd	...	
232790.0....	$26_{3,24}-25_{3,23}$	1.1	13.7	
232962.3....	$26_{10,16}-25_{10,15}$	1.2	20.0	
	$26_{10,17}-25_{10,16}$			
232967.6....	$26_{9,18}-25_{9,17}$			
	$26_{9,17}-25_{9,16}$			
232975.5....	$26_{11,15}-25_{11,14}$	0.8	10.7	
	$26_{11,16}-25_{11,15}$			
232998.7....	$26_{8,19}-25_{8,18}$	1.1	16.2	
	$26_{8,18}-25_{8,17}$			
233002.7....	$26_{12,15}-25_{12,14}$			
	$26_{12,14}-25_{12,13}$			
233041.1....	$26_{13,14}-25_{13,13}$	0.4	7.7	
	$26_{13,13}-25_{13,12}$			
233069.3....	$26_{7,20}-25_{7,19}$	1.0	12.7	
	$26_{7,19}-25_{7,18}$			
233088.9....	$26_{14,12}-25_{14,11}$	0.5	6.3	
	$26_{14,13}-25_{14,12}$			

notes: d-blend with CH_3OCH_3 231988.

Table A26 - continued

ν (MHz)	$J_{K_pK_o}$	T_A^*(pk) (K)	$\int T_A^* dv$ (K km s^{-1})	notes
233144.8....	$26_{15,11}-25_{15,10}$	0.4	5.6	
	$26_{15,12}-25_{15,11}$			
233205.0....	$26_{6,21}-25_{6,20}$	1.5	21.2	
233207.3....	$26_{6,20}-25_{6,19}$			
233208.1....	$26_{16,10}-25_{16,9}$			
	$26_{16,11}-25_{16,10}$			
233443.1....	$26_{5,22}-25_{5,21}$	0.7	6.9	
233498.3....	$26_{5,21}-25_{5,20}$	0.8	6.7	e
233523.5....	$26_{20,7}-25_{20,6}$	0.5	6.1	f
	$26_{20,6}-25_{20,5}$			
233654.1....	$26_{4,23}-25_{4,22}$	1.1	8.1	g
234423.9....	$26_{4,22}-25_{4,21}$	...	...	h
237170.4....	$26_{3,23}-25_{3,22}$	0.9	10.5	
237360.9....	$28_{1,27}-27_{2,26}$	nd	...	
237405.2....	$26_{2,24}-25_{2,23}$	0.7	10.2	i
237476.0....	$25_{2,24}-24_{1,23}$	0.2 ?	...	
237851.8....	$27_{2,26}-26_{2,25}$	0.4	6.3	
239682.8....	$27_{1,26}-26_{1,25}$	0.7	8.6	j
239887.3....	$28_{0,28}-27_{1,27}$	0.2 ?	...	
240319.3....	$28_{1,28}-27_{1,27}$	0.8	10.5	
240429.2....	$28_{0,28}-27_{0,27}$	0.6	9.4	
240861.3....	$28_{1,28}-27_{0,27}$	0.2 ?	...	
241625.9....	$27_{3,25}-26_{3,24}$	...	...	k
241922.5....	$27_{10,18}-26_{10,17}$	0.9	5.2	
	$27_{10,17}-26_{10,16}$			
241932.2....	$27_{9,19}-26_{9,18}$	1.3	17.4	
	$27_{9,18}-26_{9,17}$			
241933.2....	$27_{11,16}-26_{11,15}$			
	$27_{11,17}-26_{11,16}$			
241959.1....	$27_{12,15}-26_{12,14}$	0.7	5.5	
	$27_{12,16}-26_{12,15}$			
241970.4....	$27_{8,20}-26_{8,19}$	0.8	6.8	
	$27_{8,19}-26_{8,18}$			
241997.1....	$27_{13,15}-26_{13,14}$	0.5	3.5	
	$27_{13,14}-26_{13,13}$			
242045.3....	$27_{14,13}-26_{14,12}$	0.8	14.3	
	$27_{14,14}-25_{14,13}$			
242052.4....	$27_{7,21}-26_{7,20}$			
	$27_{7,20}-26_{7,19}$			
242102.2....	$27_{15,13}-26_{15,12}$	0.8	14.4	
	$27_{15,12}-26_{15,11}$			
242167.0....	$27_{16,12}-26_{16,11}$	0.2	1.7	
	$27_{16,11}-26_{16,10}$			
242207.0....	$27_{6,22}-26_{6,21}$	1.3	21.9	
242210.4....	$27_{6,21}-26_{6,20}$			
242238.8....	$27_{17,11}-26_{17,10}$	0.2 ?	...	
	$27_{17,10}-26_{17,9}$			

notes: e-blend with $HCOOCH_3$ 233505, f-blend with $HCOOCH_3$ 233525, g-blend with $HCOOCH_3$ 233655, h-blend with SO_2 234422, i-blend with C_2H_3CN 237397, 237412, and 237415, j-blend with CH_3CN (ν_8) 239685, k-lost under SO_2 241616.

Table A26 - continued

ν (MHz)	$J_{K_pK_o}$	T_A^* (K)	$\int T_A^* dv$ (K km s^{-1})	notes
242470.4....	$27_{5,23}-26_{5,22}$	0.9	12.5	
242547.3....	$27_{5,22}-26_{5,21}$	0.7	7.0	
242664.7....	$27_{4,24}-26_{4,23}$	1.0	12.4	
243643.2....	$27_{4,23}-26_{4,22}$	0.9	13.6	
243823.0....	$26_{2,25}-25_{1,24}$	nd	...	
246268.7....	$27_{2,25}-26_{2,24}$	0.9	6.5	
246421.9....	$28_{2,27}-27_{2,26}$	0.6	5.5	
246548.7....	$27_{3,24}-26_{3,23}$	0.6	5.4	
250440.3....	$28_{3,26}-27_{3,25}$	1.7	28.1	l
252896.0....	$28_{4,24}-27_{4,23}$	0.7	9.9	
254976.3....	$29_{2,28}-28_{2,27}$	1.5	14.7	
255906.5....	$28_{3,25}-27_{3,24}$	0.9	6.9	
256395.9....	$29_{1,28}-28_{1,27}$	1.0	12.0	m
256966.9....	$30_{0,30}-29_{1,29}$	0.2	1.2	
257239.7....	$30_{1,30}-29_{1,29}$	0.4	2.4	n
257310.6....	$30_{0,30}-29_{0,29}$	0.8	9.9	
257583.6....	$30_{1,30}-29_{0,29}$	0.3	2.8	
259232.7....	$29_{3,27}-28_{3,26}$	0.7	5.3	
259842.9....	$29_{10,19}-28_{10,18}$ $29_{10,20}-28_{10,19}$	1.0	7.8	
259847.4....	$29_{11,19}-28_{11,18}$ $29_{11,18}-28_{11,17}$	0.9	6.8	
259862.8....	$29_{9,21}-28_{9,20}$ $29_{9,20}-28_{9,19}$	0.9	15.1	
259869.9....	$29_{12,18}-28_{12,17}$ $29_{12,17}-28_{12,16}$	0.6	7.3	
259906.7....	$29_{13,17}-28_{13,16}$ $29_{13,16}-28_{13,15}$	0.5	5.5	
259917.3....	$29_{8,22}-28_{8,21}$ $29_{8,21}-28_{8,20}$	1.0	16.9	
259955.2....	$29_{14,16}-28_{14,15}$ $29_{14,15}-28_{14,14}$	0.4	5.7	
260013.7....	$29_{15,15}-28_{15,14}$ $29_{15,14}-28_{15,13}$	0.5	3.14	
260025.3....	$29_{7,23}-28_{7,22}$	0.8	10.0	
260025.6....	$29_{7,23}-28_{7,22}$			
260081.1....	$29_{16,14}-28_{16,13}$ $29_{16,13}-28_{16,12}$	0.3	3.4	
260156.4....	$29_{17,13}-28_{17,12}$ $29_{17,12}-28_{17,11}$	0.4	4.0	
260221.6....	$29_{6,24}-28_{6,23}$	0.9	14.9	
260229.2....	$29_{6,23}-28_{6,22}$			
260664.8....	$29_{4,26}-28_{4,25}$	0.9	10.8	
260667.1....	$11_{4,7}-10_{3,8}$			
260679.0....	$29_{5,24}-28_{5,23}$	0.8	8.9	
262183.8....	$29_{4,25}-28_{4,24}$	0.7	7.5	

notes: l-blend with NO 250437,440,438, m-blend with C_2H_3CN 256397, n-blend with ^{29}SiO 257255.

M. Recombination Lines

Because of the larger spacing between recombination lines at higher frequencies only two Hα lines fall within our spectral range, in contrast with the four Hα lines observed by Johansson *et al.* (1984). The H30α line at 231901.3 MHz is found to have a peak antenna temperature of 0.7 K, and while the H29α line 256302.5 MHz may also be detected, it lies in a crowded band of CH_3CCH lines making an estimate of its strength rather difficult. The H30α v_{LSR} of 4 km s^{-1} is somewhat redshifted with respect to that of Johansson *et al.*, although the velocity is not well determined by this measurement. Its line width of 23 km s^{-1} is consistent with the lower frequency recombination line data and the intensity is comparable with that expected from non-LTE theory for an electron temperature of 10^4 K and a proton emission measure of 10^7 pc cm^{-6}.

Table A27

Recombination lines

	ν (MHz)	T_A^*(pk) (K)	FWHM (km s^{-1})	$\int T_A^* dv$ (K km s^{-1})	v_{LSR} (km s^{-1})
H30α.....	231901.3	0.7	23.0	15.7	+4.
H29α.....	256302.5	?	...	...	...
H38β.....	222012.2	nd	...	...	...
H37β.....	240021.6	nd	...	...	...
H36β.....	2600333.2	nd	...	...	...
He30α...	231995.8	nd	...	...	...
He29α...	256406.9	nd	...	...	...

The H36β, H37β, and H38β lines at 260033.2, 240021.6, and 220012.2 MHz are not convincingly detected. The location for the H37β line is contaminated by the presence of an $HCOOCH_3$ line. Similarly, the He29α and He30α lines are not seen due to their low strength and competing lines of C_2H_5CN and CH_3OCH_3.

N. Unidentified lines

A total of 33 lines are currently unidentified in the spectrum between 215 and 263 GHz. The frequencies, widths, and peak antenna temperatures of these lines are presented in Table A28. The original double sideband data have been consulted to insure that each of the lines in Table A28 is real, and not the ghost of features from the opposite sideband.

Table A28

Unidentified Transitions

	Frequency (MHz)	T_A^*(pk) (K)	FWHM (km s^{-1})
unidentified....	215886	0.9	3.1
	217823	0.7	7.0[a]
	222177	0.4	3.3
	222259	0.6	4.8
	224493	0.5	6.2
	224895	0.7	3.0
	225625	1.0	4.2
	226384	0.5	3.4
	226436	0.4	4.8
	230233	0.6	5.3
	232163	0.8	10.9
	234291	0.6	6.0
	235261	0.5	7.1
	236977	0.9	6.6
	238017	0.4	11.7
	242076	0.7	3.7
	243740	0.8	5.6
	243747	1.1	6.1
	247469	0.6	3.0
	247630	0.4	3.7
	247636	0.4	4.5
	247875	0.7	2.7
	247911	0.5	1.8
	255651	1.2	21.9
	257912	1.0	4.7
	259285	0.8	11.1
	259311	0.6	4.5
	259690	0.5	3.6
	259733	0.7	3.3
	259986	0.8	6.8
	260440	1.2	3.7
	260726	1.2	7.5
	261564	1.1	8.0
	263065	0.9	1.6

notes: a-identified as C_3H_2 by Thaddeus (1985).

We note that the initially unidentified line at 217823 MHz has now been attributed to a blend of the $6_{06} \rightarrow 5_{15}$ and $6_{16} \rightarrow 5_{05}$ transitions of the C_3H_2 cyclopropenylidene radical by Thaddeus (1985). Presumably, other lines of this reactive species may account for some of the unidentified features in our Orion survey, but no published frequencies are currently available.

O. Other Species

Several other species of interest have transitions in this frequency range but have not been convincingly detected. The J=2-1 transitions of NO^+ measured by Bowman *et al.* (1982) are clearly not present. Similarly, CO^+ is no longer seen in Orion as the emission at 236062 MHz can be attributed to $^{13}CH_3OH$ as discussed by Blake *et al.* (1984). The refractory oxides MgO (Steimle *et al.* 1984) and FeO (Endo *et al.* 1984) are also not detected, although the limits are not terribly severe and the frequency for MgO is not well determined. Also not seen are the J=11-10 transition of $HOCO^+$ and the $3_{1,3}$-$2_{2,0}$ components of NH_2 (Charo *et al.* 1981).

The nitroxyl radical (HNO) was tentatively identified in Sgr B2 and NGC 2024 by Ulich *et al.* (1977) on the basis of a single feature, the ground state $1_{0,1}$-$0_{0,0}$ transition. As far as we know this assignment has not been verified by any observations of other transitions, in part due to the lack of accurate frequency predictions. The frequency of the $3_{0,3}$-$2_{0,2}$ transition, which lies in the lower OVRO line search band, has recently been measured to be 244364.0 MHz by Sastry *et al.* (1984). Although a very weak bump is present in Figure A1 at this frequency, it is unclear if this is a real feature or an artifact of the data reduction. At present it is not possible to claim the detection of HNO in Orion.

Two species identified at lower frequencies, the formyl radical (HCO) and methylamine (CH_3NH_2), have also not been convincingly detected in the 215 to

263 GHz range. HCO occupies an intriguing position in the chemistry of interstellar molecular clouds. It is one of a class of radicals like CH and CH_2 which are thought to be formed primarily by reactions involving C^+ (Ulich *et al.* 1977). As C^+ is created efficiently by photoionization of neutral carbon, HCO and similar radicals might therefore be expected to have detectable abundances in regions with or near to sources of ultraviolet radiation, such as the outer edges of molecular clouds. Thus, HCO may provide a useful probe of the excitation mechanisms and physical conditions prevailing in the transition region between diffuse and dense material in the interstellar medium.

Johansson *et al.* (1984) have tentatively detected the strongest component of the N = 1 - 0 HCO multiplet at a level of 0.05 K in their survey of Orion, and to verify this work we have carefully searched for the fine and hyperfine components of the N = 3 - 2 transition near 260.1 GHz (Blake, Sastry, and De Lucia 1984). Unfortunately, the J,F = 7/2,3 - 5/2,2 and 5/2,2 - 3/2,1 lines are buried beneath two C_2H_5CN transitions and are not observable. The remaining hyperfine components are in a cleaner region of the spectrum, but have antenna temperatures of less than 0.2 K (3σ), which imply an excitation temperature of less than 10 K if the line ascribed to HCO by Johansson *et al.* is correct. Although this value is quite low, a highly subthermal rotational temperature has been derived for HCO (μ_a = 1.36, Landsberg, Merer, and Oka 1977) in NGC 2024 by Snyder *et al.* (1985).

Methylamine (CH_3NH_2) was initially identified in Orion at 86.1 and 88.7 GHz by Kaifu *et al.* (1974) and Kutner *et al.* (1980). However, neither of these transitions was detected by Johansson *et al.* (1984), and it therefore seems desirable to check these results at higher frequencies. The millimeter wave spectrum of methylamine is quite complicated because it contains splittings from both the internal rotation of the CH_3 group and inversion of the NH_2 fragment.

In the absence of any predicted frequencies above 100 GHz, K.V.L.N. Sastry (1985) has kindly provided us with a list of measured frequencies for methylamine in the 200 - 300 GHz region. The strongly allowed J = 5 - 4 transitions are accessible in the this work as they occur near 222 GHz. We find no indication of emission at any of the more than ten low-lying transitions in the 222 GHz region. Our upper limits confirm the negative results of Johansson *et al.* and imply that the identification of CH_3NH_2 in Orion must be regarded as highly speculative.

Finally, the remarkable isomeric selectivity found in Orion by Johansson *et al.* (1984) is further strengthened here. Whereas dimethyl ether and methyl formate are easily detectable and quite abundant for molecules of such complexity, the isomerically related C_2H_5OH and CH_3COOH species have not been identified. As discussed in Chapter 4, this most likely arises because of the intimate chemical relationship between CH_3OCH_3, $HCOOCH_3$, and their highly abundant precursor, CH_3OH.

A2.3. Known Defects in the Spectrum

The spectrum presented in Figure A1 contains a few noticeable defects arising from the procedure used to generate a single sideband spectrum from the original double sideband data. The defects are usually in the form of "ghosts," small residuals left when a strong line is not entirely assigned to the proper sideband. Such ghosts will be found separated by approximately twice the IF frequency (a total of ~2.5 GHz) from the stronger features in the spectrum. Their reality can usually be checked by manual examination of the original double sideband data. All unidentified features in the spectrum stronger than 0.4 K were examined to see if they were ghosts. Those which were found to be real, albeit unidentified, features were listed in Table A28. Those which can be

attributed to ghosts are listed below in Table A29.

Table A29

Known defects

ν (MHz)	T_a^*(pk) (K)
215136	0.4
215696	1.0
223357	0.6
223378	0.9
232857	0.5
234913	0.5
235217	0.6
243465	0.7
243811	0.9
244411	1.0
245094	0.7
245099	0.6
248080	0.8
255283	0.9
261360	1.2

As described in Section A1.2a, the spectrum above 247 GHz is generally freer of artifacts associated with the data reduction than that below 247 GHz, due to changes in the data collection procedure. The only ghosts clearly present in this region of the spectrum are a narrow line at 248080 MHz and broad features at 255283 and 261360 MHz.

Figure Captions

Figure A1: Spectrum of Orion A from 215 to 263 GHz. The antenna temperature scale has been corrected by the extended source efficiency of 0.85, while a v_{LSR} of 8 km s^{-1} has been used to establish the rest frequency scale. Identified lines are individually marked and labeled as to their source.

References for Appendix A

Altman, R.S., Crofton, M.W., and Oka, T. 1984. *J. Chem. Phys.*, **80**, 3911.

Blake, G.A., Sastry, K.V.L.N., and De Lucia, F.C. 1984, *J. Chem. Phys.*, **80**, 95.

Blake, G.A., Sutton, E.C., Masson, C.R., Phillips, T.G., Herbst, E., Plummer, G.M., and De Lucia, F.C. 1984, *Ap. J.*, **286**, 586.

Blake, G.A., Sutton, E.C., Masson, C.R., and Phillips, T.G. 1986, *Ap. J. Suppl.*, in press.

Blake, G.A. and Pickett, H.M 1985, unpublished results.

Bowman, W.C., Herbst, E., and De Lucia, F.C. 1982, *J. Chem. Phys.*, **77**, 4261.

Charo, A., Sastry, K.V.L.N., Herbst, E., and De Lucia, F.C. 1981, *Ap. J.(Letters)*, **244**, L111.

Cummins, S.E., Linke, R.A., and Thaddeus, P. 1985, submitted to *Ap. J.*

DeFrees, D.J., McLean, A.D., and Herbst, E. 1985, *Ap. J.*, **293**, 236.

Dickinson, D.F. and Rodriguez-Kuiper, E.N. 1981, *Ap. J.*, **247**, 112.

Endo, Y., Saito, S., and Hirota, E. 1984, *Ap. J.(Letters)*, **278**, L131.

Friberg, P. 1984, *Astr. Ap.*, **132**, 265.

Goldsmith, P.F., Snell, R.L., Deguchi, S., Krotkov, R., and Linke, R.A. 1982, *Ap. J.*, **260**, 147.

Gottlieb, C.A., Ball, J.A., Gottlieb, E.W., Lada, C.J., and Penfield, H. 1975, *Ap. J.(Letters)*, **200**, L147.

Herbst, E., Adams, N.G., and Smith, D. 1983, *Ap. J.*, **269**, 329.

Herbst, E., Messer, J.K., De Lucia, F.C., and Helminger, P. 1984, *J. Mol. Spec.*, **108**, 42.

Irvine, W.M. and Hjalmarson, A. 1984, in *Origins of Life* (Dordrecht: Reidel), pp. 15-23.

Irvine, W.M. and Schloerb, F.P. 1984, *Ap. J.*, **282**, 516.

Johansson, L.E.B., Andersson, C., Ellder, J., Friberg, P., Hjalmarson, A., Hoglund, B., Irvine, W.M., Olofsson, H., and Rydbeck, G. 1984, *Astr. Ap.*, **130**, 227.

Kaifu, N., Morimoto, M., Nagane, K., Akabane, K., Iguchi, T., and Takagi, K. 1974, *Ap. J.(Letters)*, **191**, L135.

Kawaguchi, K., Saito, S., and Hirota, E. 1983, *J. Chem. Phys.*, **79**, 629.

Kuiper, T.B.H, Zuckerman, B., Kakar, R.K., and Rodriguez-Kuiper, E.N. 1975, *Ap. J.(Letters)*, **200**, L151.

Kuiper, T.B.H., Zuckerman, B., and Rodriguez-Kuiper, E.N. 1981, *Ap. J.*, **251**, 88.

Kutner, M.L., Machnik, D.E., Tucker, K.D., and Dickman, R.L. 1980, *Ap. J.*, **242**, 541.

Landsberg, B.M., Merer, A.J., and Oka 1977, *J. Mol. Spec.* **67**, 459.

Loren, R.B. and Mundy, L.E., and Erickson, N.R. 1981, *Ap. J.*, **250**, 573.

Loren, R.B. and Mundy, L.E. 1984, *Ap. J.*, **286**, 232.

Lovas, F.J. 1984, private communication.

Masson, C.R. 1982, *Astr. Ap.*, **114**, 270.

Masson, C.R., Claussen, M.J., Lo. K.Y., Moffett, A.T., Phillips, T.G., Sargent, A.I., Scott, S.L., and Scoville, N.Z. 1985, *Ap. J.(Letters)*, **297**, in press.

Olofsson, H. 1984, *Astr. Ap.*, **134**, 36.

Pickett, H.M. 1984, private communication.

Plummer, G.M., Herbst, E., De Lucia, F.C., and Blake, G.A. 1984, *Ap. J. Suppl.*, **55**, 633.

Plummer, G.M., Herbst, E., De Lucia, F.C., and Blake, G.A. 1985, in preparation.

Poynter, R.L. and Pickett, H.M. 1984, *Submillimeter, Millimeter, and Microwave Spectral Line Catalogue*, JPL Pub. 80-23, Rev. 2.

Sastry, K.V.L.N., Helminger, P., Charo, A., Herbst, E., and De Lucia, F.C. 1981, *Ap. J.(Letters)*, **251**, L119.

Sastry, K.V.L.N., Helminger, P., Plummer, G.M., Herbst, E., and De Lucia, F.C. 1984, *Ap. J. Suppl.*, **55**, 563.

Sastry, K.V.L.N. *et al.* 1985, in preparation.

Schloerb, F.P., Friberg, P., Hjalmarson, A., Hoglund, B., and Irvine, W.M. 1983, *Ap. J.*, **264**, 161.

Skatrud, D.D., De Lucia, F.C., Blake, G.A., and Sastry, K.V.L.N. 1983, *J. Mol. Spec.*, **99**, 35.

Snyder, L.E., Schenewerk, M.J., and Hollis, J.M. 1985, *Ap. J.*, in press.

Steimle, T.C., Azuma, Y., and Carrick, P.G. 1984, *Ap. J.(Letters)*, **277**, L21.

Sutton, E.C. 1983, *IEEE Trans. MTT*, **MTT-31**, 589.

Sutton, E.C., Blake, G.A., Masson, C.R., and Phillips, T.G. 1984, *Ap. J.(Letters)*, **283**, L41.

Sutton, E.C., Blake, G.A., Masson, C.R., and Phillips, T.G. 1985, *Ap. J. Suppl.*, **58**, 341.

Thorne, L.R., Anicich, V.G., Prasad, S.S., and Huntress, W.T., Jr. 1984, *Ap. J.*, **280**, 139.

Ulich, B.L., Hollis, J.M., and Snyder, L.E. 1977, *Ap. J.(Letters)*, **217**, L105.

Watson, W.D. 1976, *Rev. Mod. Phys.*, **48**, 513.

Wootten, A., Lichten, S.M., Sahai, R., and Wannier, P. 1982, *Ap. J.*, **257**, 151.

Wootten, A., Loren, R.B., and Bally, J. 1984, *Ap. J.*, **277**, 189.

Wyse, F.C., Manson, E.L., and Gordy, W. 1972, *J. Chem. Phys.*, **57**, 1106.

Ziurys, L.M., Saykally, R.J., Plambeck, R.L., and Erickson, N.R. 1982, *Ap. J.*, **254**, 94.

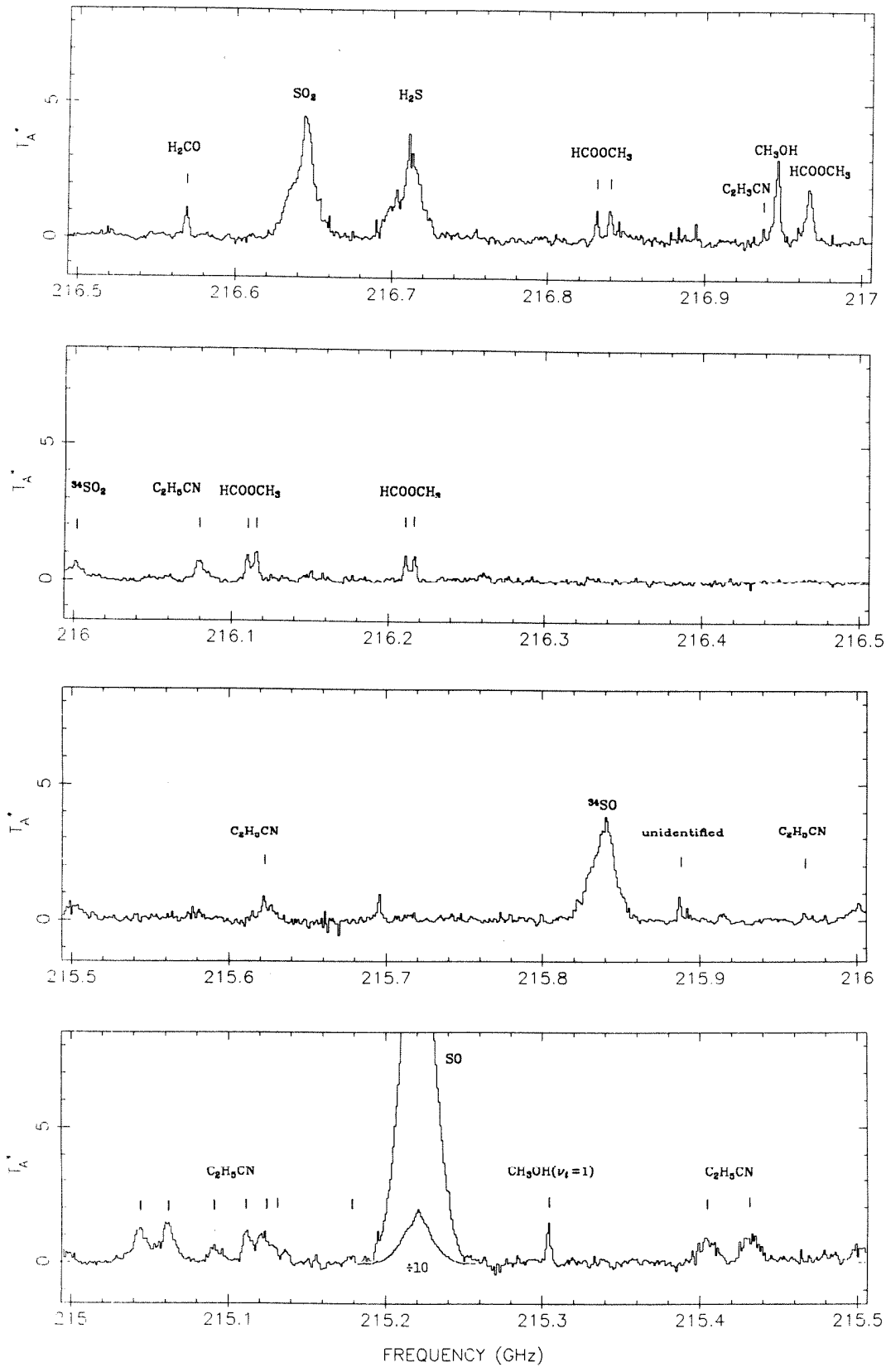
T_A^*
H_2CO
SO_2
H_2S
$HCOOCH_3$
CH_3OH
$HCOOCH_3$
C_2H_3CN
216.5
216.6
216.7
216.8
216.9
217
$^{34}SO_2$
C_2H_5CN
$HCOOCH_3$
$HCOOCH_3$
216
216.1
216.2
216.3
216.4
216.5
C_2H_5CN
^{34}SO
unidentified
C_2H_5CN
215.5
215.6
215.7
215.8
215.9
216
SO
C_2H_5CN
$CH_3OH(\nu_t=1)$
C_2H_5CN
÷10
215
215.1
215.2
215.3
215.4
215.5
FREQUENCY (GHz)

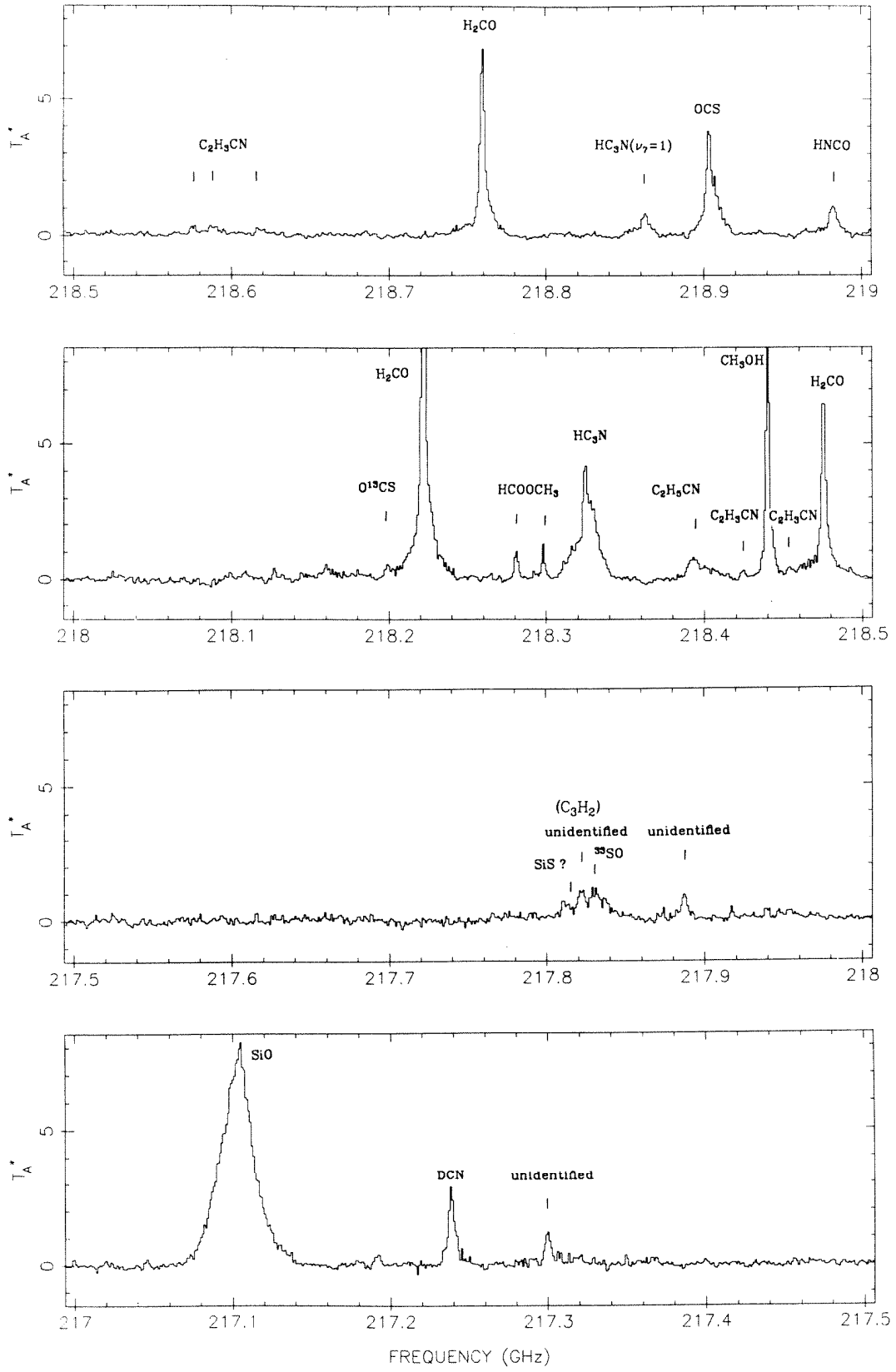
H2CO
C2H3CN
HC3N(ν7=1)
OCS
HNCO
H2CO
CH3OH
H2CO
HC3N
O13CS
HCOOCH3
C2H5CN
C2H3CN
C2H3CN
(C3H2)
unidentified
unidentified
SiS ?
33SO
SiO
DCN
unidentified
TA*
FREQUENCY (GHz)

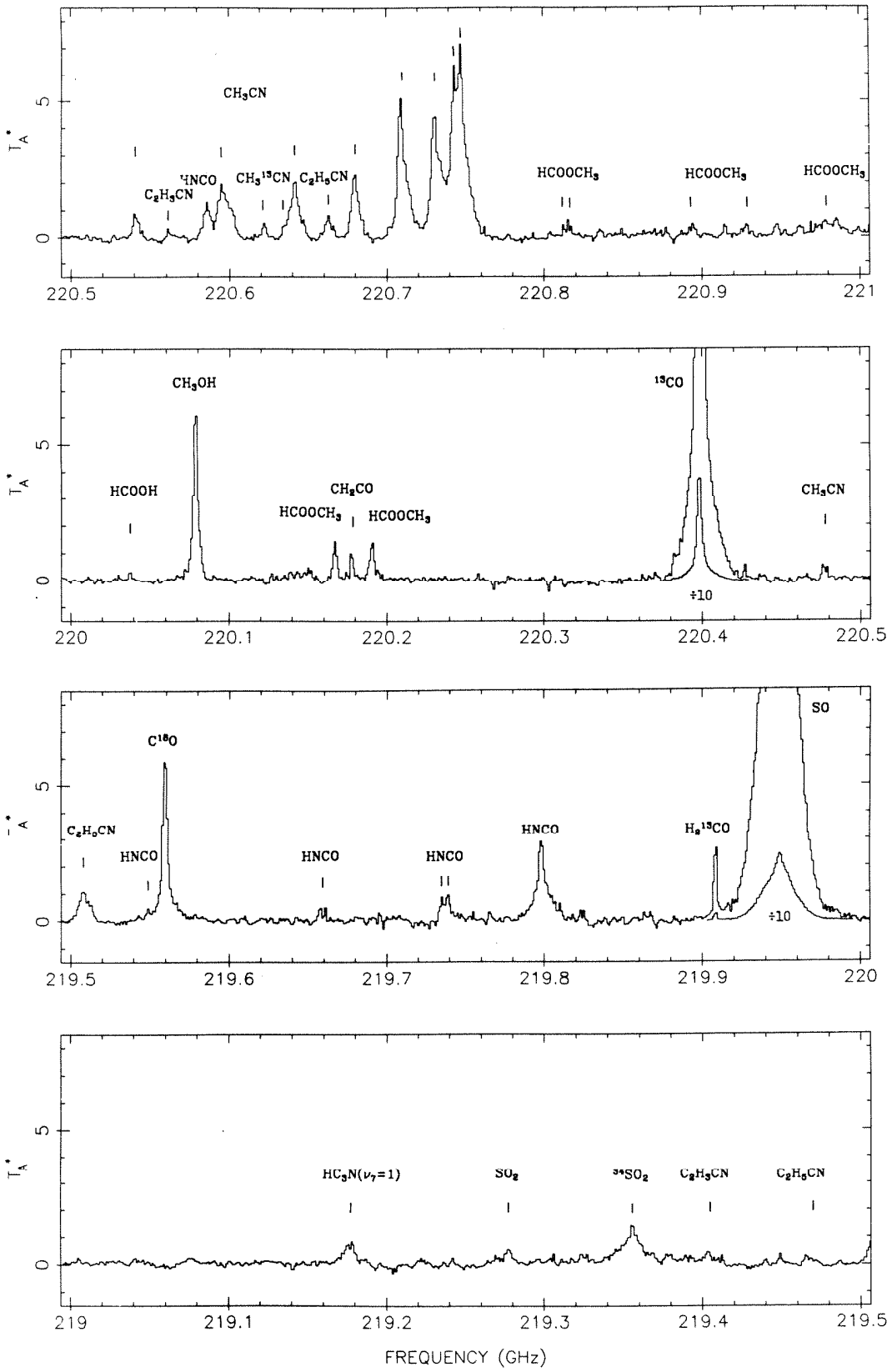
T_A^*
CH_3CN
C_2H_5CN
HNCO
$CH_3{}^{13}CN$
C_2H_5CN
$HCOOCH_3$
$HCOOCH_3$
$HCOOCH_3$
220.5
220.6
220.7
220.8
220.9
221
CH_3OH
HCOOH
CH_2CO
$HCOOCH_3$
$HCOOCH_3$
^{13}CO
CH_3CN
÷10
220
220.1
220.2
220.3
220.4
220.5
SO
$C^{18}O$
C_2H_5CN
HNCO
HNCO
HNCO
HNCO
$H_2{}^{13}CO$
÷10
219.5
219.6
219.7
219.8
219.9
220
$HC_3N(\nu_7=1)$
SO_2
$^{34}SO_2$
C_2H_3CN
C_2H_5CN
219
219.1
219.2
219.3
219.4
219.5
FREQUENCY (GHz)

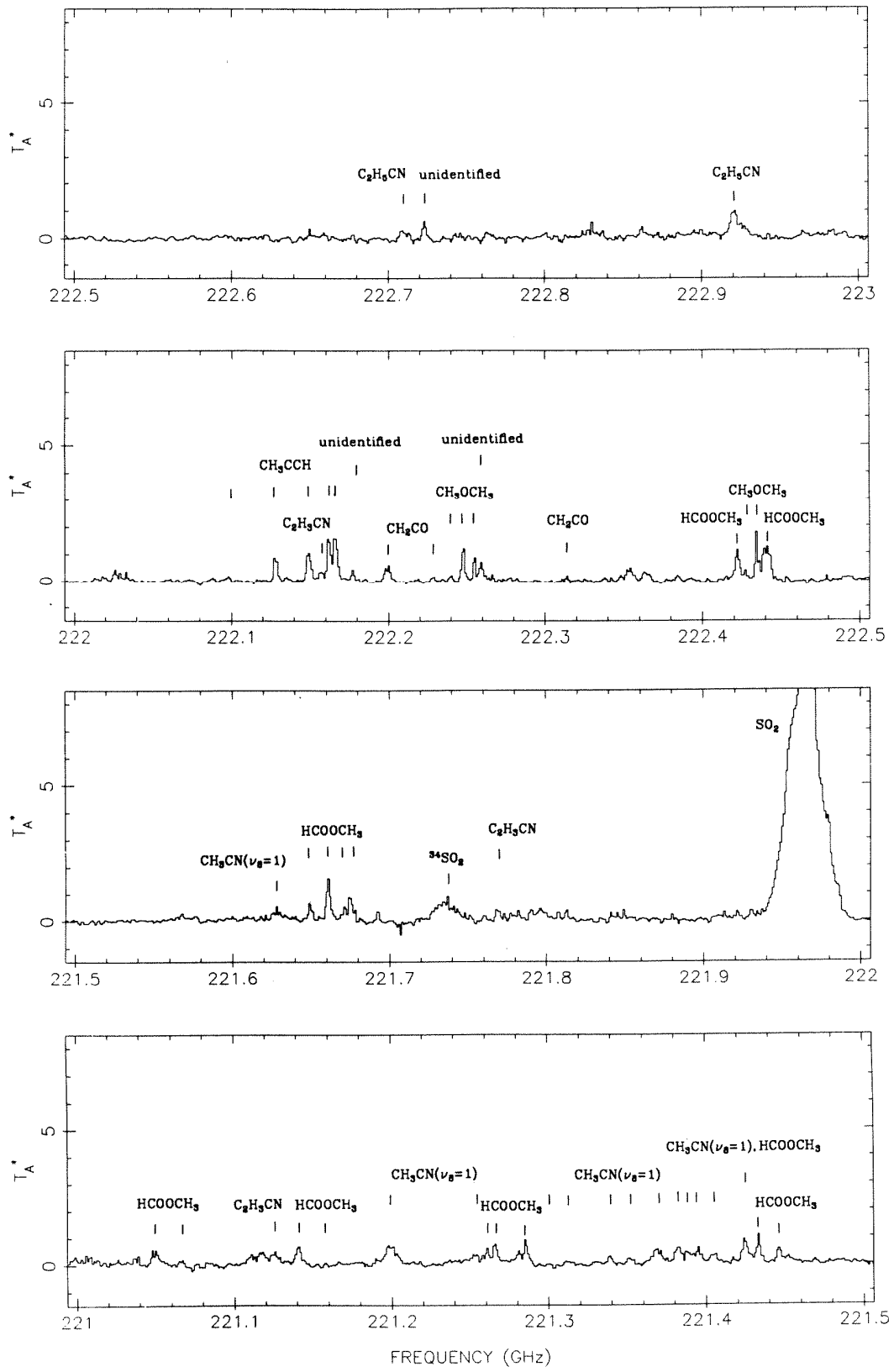
T_A^*
5
0
C_2H_3CN unidentified
C_2H_3CN
222.5
222.6
222.7
222.8
222.9
223
unidentified
unidentified
CH_3CCH
CH_3OCH_3
CH_3OCH_3
C_2H_3CN
CH_2CO
CH_2CO
$HCOOCH_3$
$HCOOCH_3$
222
222.1
222.2
222.3
222.4
222.5
SO_2
$HCOOCH_3$
C_2H_3CN
$CH_3CN(\nu_8=1)$
$^{34}SO_2$
221.5
221.6
221.7
221.8
221.9
222
$CH_3CN(\nu_8=1), HCOOCH_3$
$CH_3CN(\nu_8=1)$
$CH_3CN(\nu_8=1)$
$HCOOCH_3$
C_2H_3CN $HCOOCH_3$
$HCOOCH_3$
$HCOOCH_3$
$HCOOCH_3$
221
221.1
221.2
221.3
221.4
221.5
FREQUENCY (GHz)

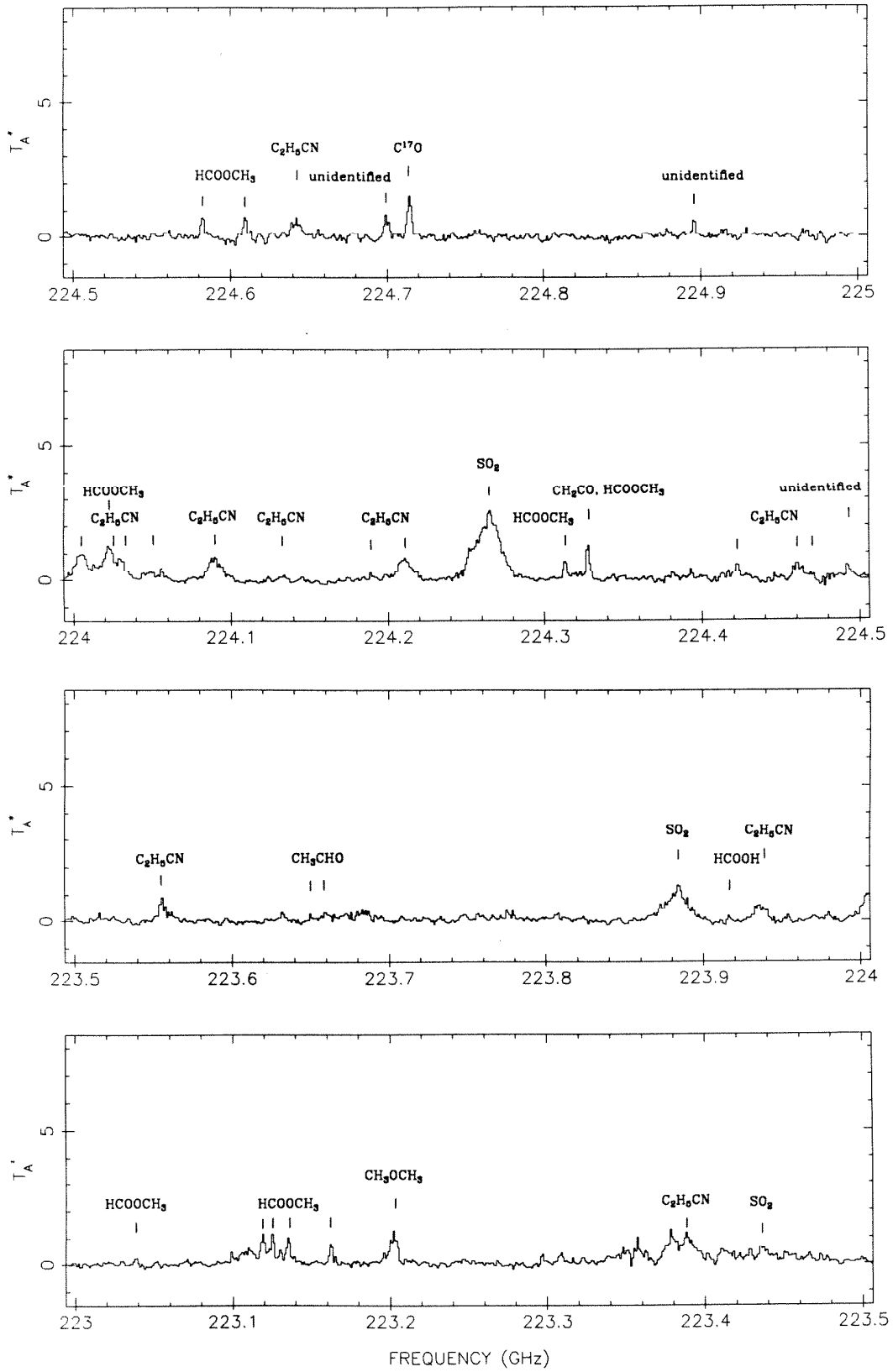
T_A^*
5
0
C_2H_5CN
$C^{17}O$
$HCOOCH_3$
unidentified
unidentified
224.5
224.6
224.7
224.8
224.9
225
SO_2
$HCOOCH_3$
CH_2CO, $HCOOCH_3$
unidentified
C_2H_5CN
C_2H_5CN
C_2H_5CN
C_2H_5CN
$HCOOCH_3$
C_2H_5CN
224
224.1
224.2
224.3
224.4
224.5
SO_2
C_2H_5CN
C_2H_5CN
CH_3CHO
HCOOH
223.5
223.6
223.7
223.8
223.9
224
CH_3OCH_3
$HCOOCH_3$
$HCOOCH_3$
C_2H_5CN
SO_2
223
223.1
223.2
223.3
223.4
223.5
FREQUENCY (GHz)

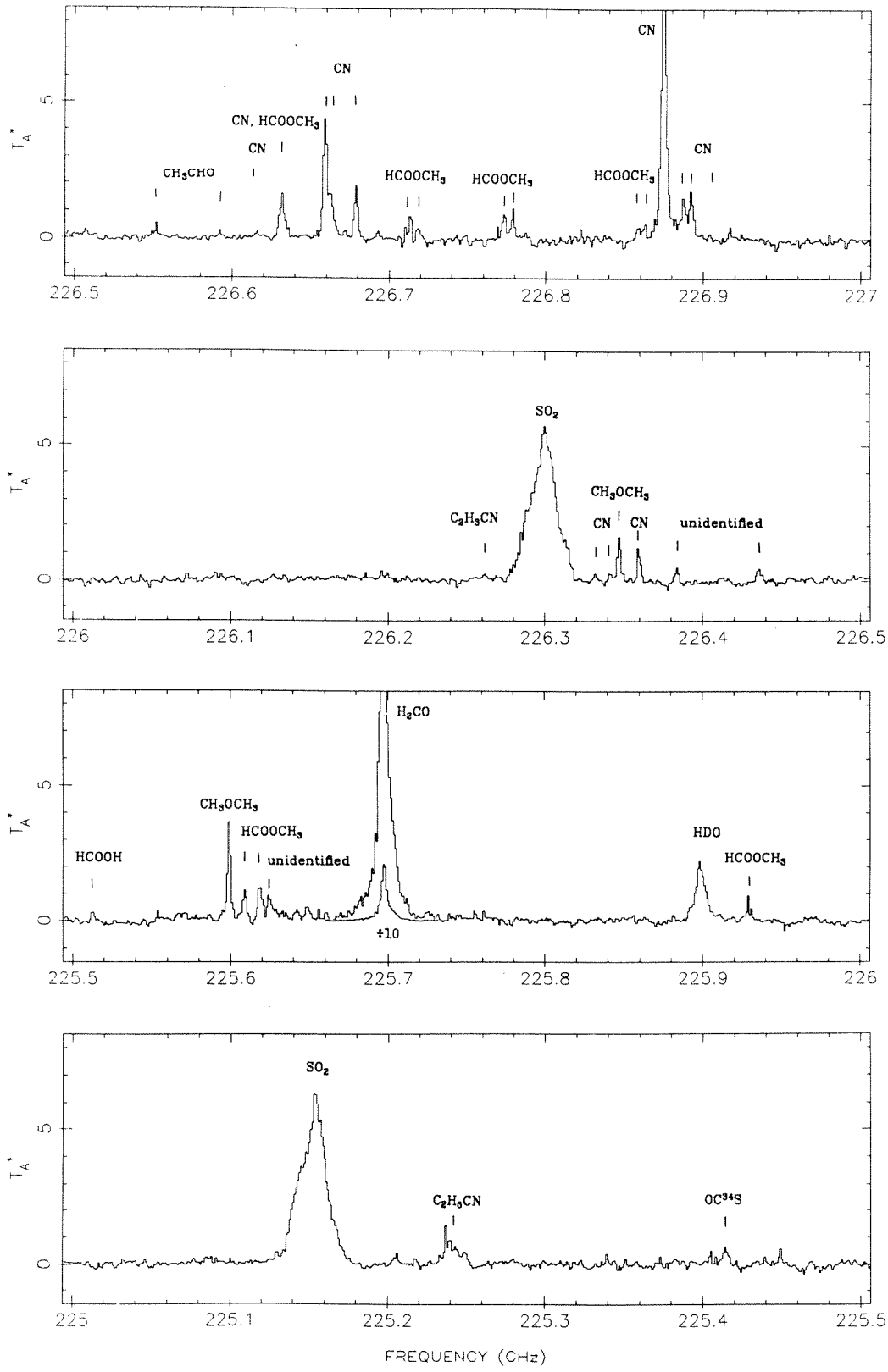
CN
CN
CN, HCOOCH3
CN
CH3CHO
HCOOCH3
HCOOCH3
HCOOCH3
CN
T_A*
5
0
226.5
226.6
226.7
226.8
226.9
227
SO2
CH3OCH3
C2H3CN
CN
CN
unidentified
T_A*
5
0
226
226.1
226.2
226.3
226.4
226.5
H2CO
CH3OCH3
HCOOCH3
unidentified
HCOOH
HDO
HCOOCH3
÷10
T_A*
5
0
225.5
225.6
225.7
225.8
225.9
226
SO2
C2H5CN
OC34S
T_A*
5
0
225
225.1
225.2
225.3
225.4
225.5
FREQUENCY (GHz)

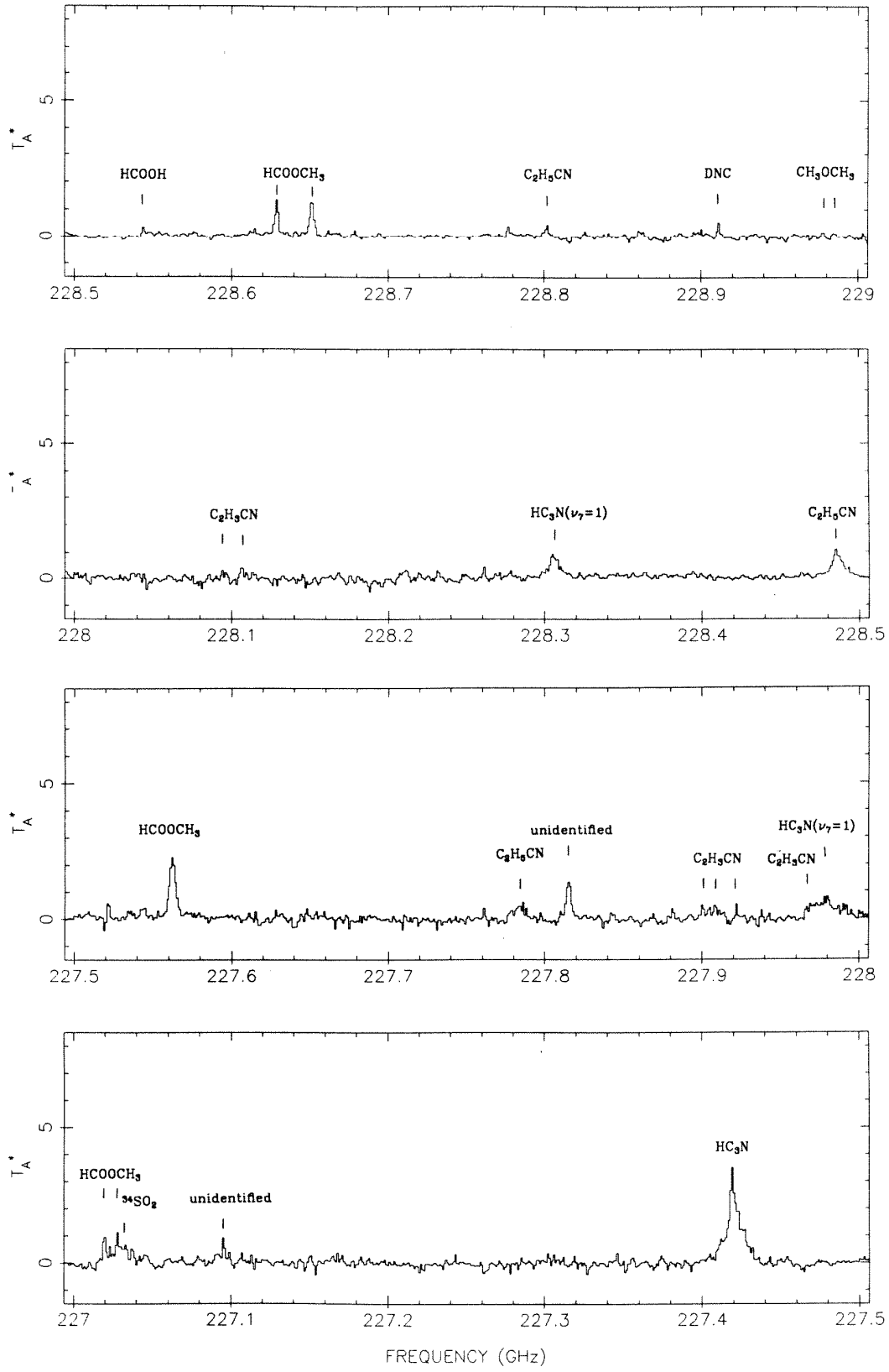
HCOOH
HCOOCH3
C2H5CN
DNC
CH3OCH3
C2H3CN
HC3N(ν7=1)
C2H5CN
HCOOCH3
C2H5CN
unidentified
C2H3CN
C2H3CN
HC3N(ν7=1)
HCOOCH3
34SO2
unidentified
HC3N
TA*
0
5
228.5
228.6
228.7
228.8
228.9
229
228
228.1
228.2
228.3
228.4
228.5
227.5
227.6
227.7
227.8
227.9
228
227
227.1
227.2
227.3
227.4
227.5
FREQUENCY (GHz)

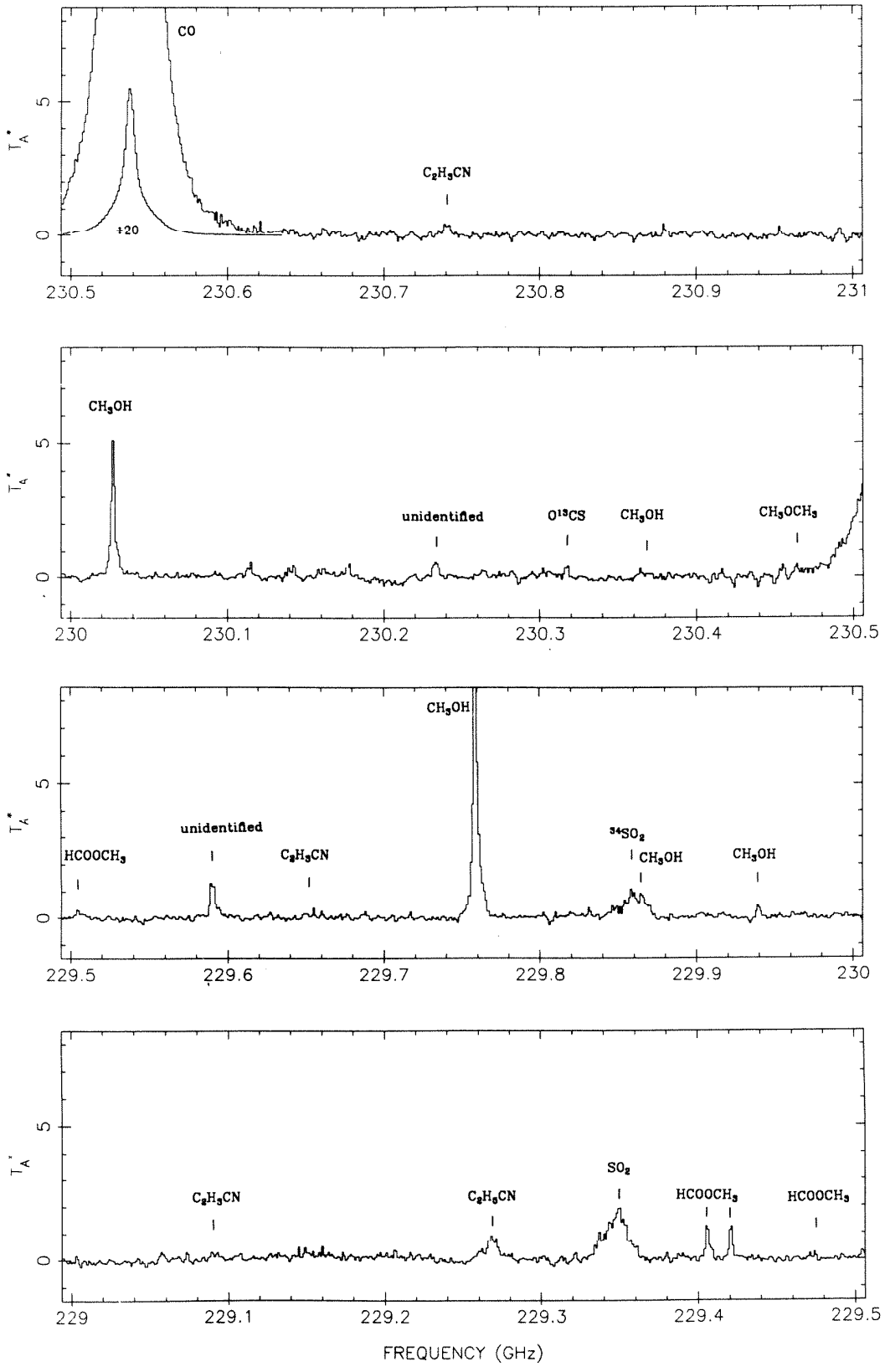
CO
C_2H_3CN
÷20
T_A^*
230.5
230.6
230.7
230.8
230.9
231
CH_3OH
unidentified
$O^{13}CS$
CH_3OH
CH_3OCH_3
230
230.1
230.2
230.3
230.4
230.5
CH_3OH
$HCOOCH_3$
unidentified
C_2H_3CN
$^{34}SO_2$
CH_3OH
CH_3OH
229.5
229.6
229.7
229.8
229.9
230
SO_2
C_2H_3CN
C_2H_3CN
$HCOOCH_3$
$HCOOCH_3$
229
229.1
229.2
229.3
229.4
229.5
FREQUENCY (GHz)

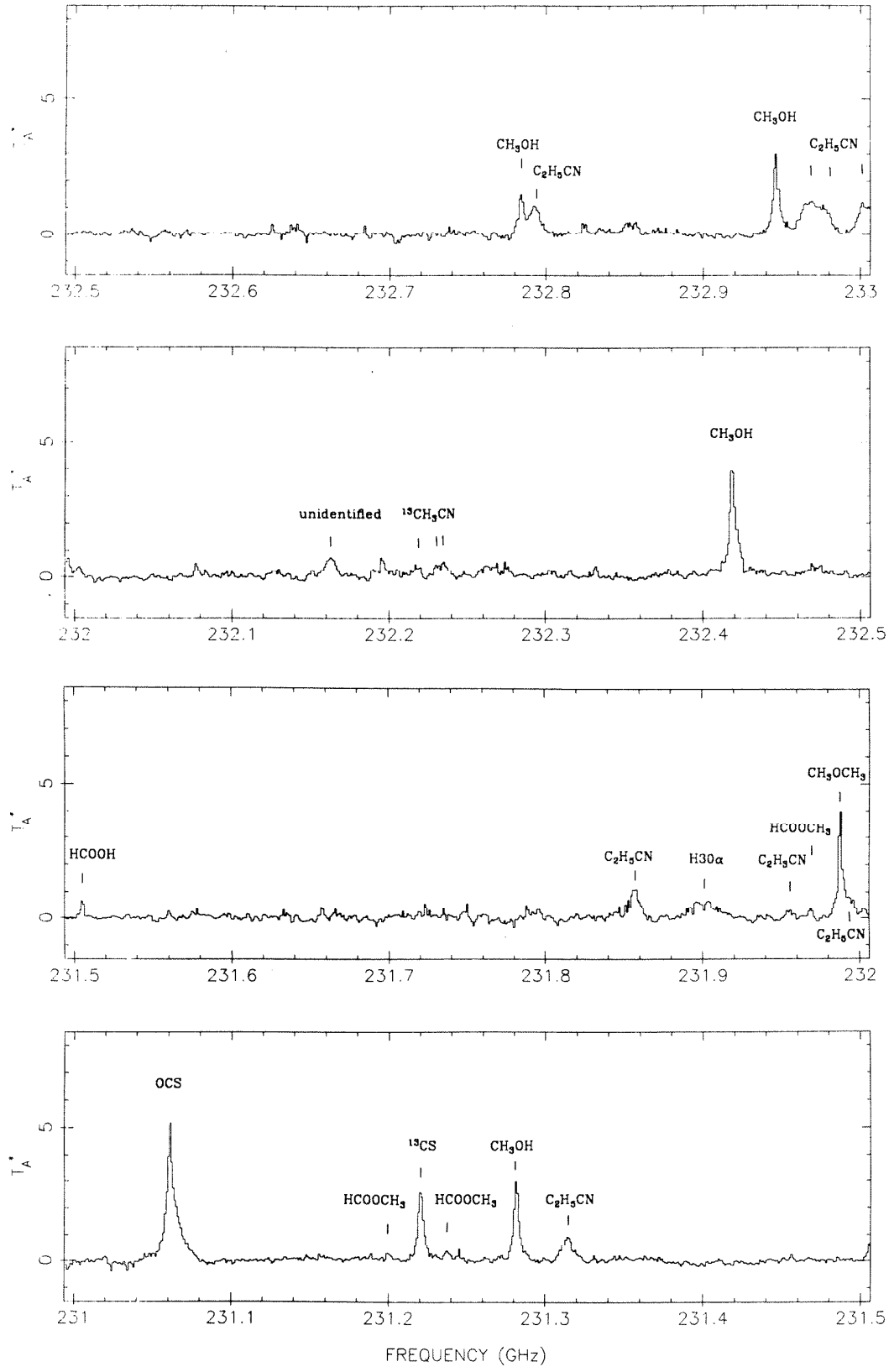
T_A^*
5
0
CH_3OH
C_2H_5CN
CH_3OH
C_2H_5CN
232.5
232.6
232.7
232.8
232.9
233
unidentified
$^{13}CH_3CN$
CH_3OH
232
232.1
232.2
232.3
232.4
232.5
HCOOH
C_2H_5CN
H30α
C_2H_5CN
$HCOOCH_3$
CH_3OCH_3
C_2H_5CN
231.5
231.6
231.7
231.8
231.9
232
OCS
^{13}CS
$HCOOCH_3$
$HCOOCH_3$
CH_3OH
C_2H_5CN
231
231.1
231.2
231.3
231.4
231.5
FREQUENCY (GHz)

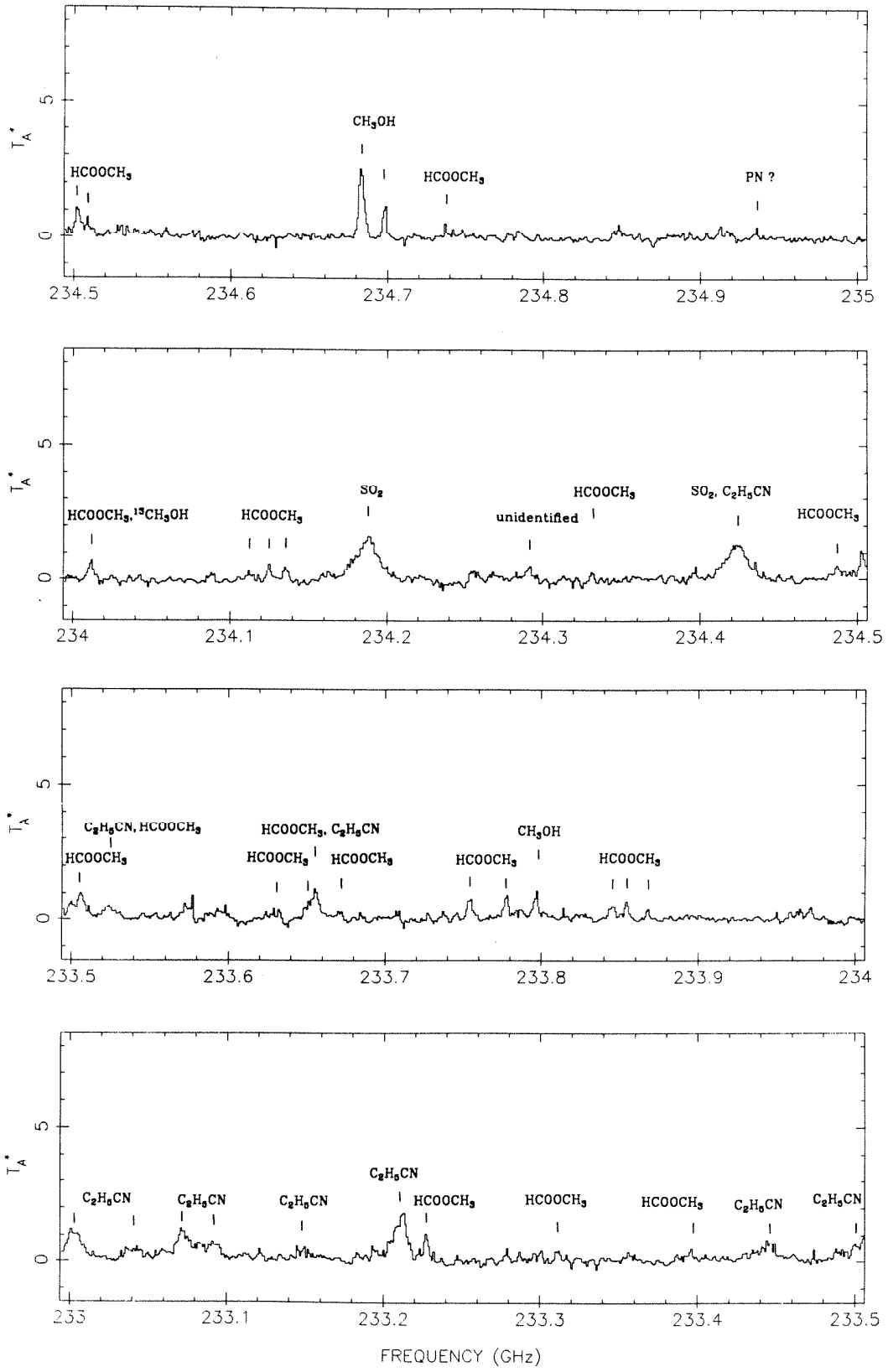
T_A^*
5
0
CH_3OH
$HCOOCH_3$
$HCOOCH_3$
PN ?
234.5
234.6
234.7
234.8
234.9
235
$HCOOCH_3$, $^{13}CH_3OH$
$HCOOCH_3$
SO_2
unidentified
$HCOOCH_3$
SO_2, C_2H_5CN
$HCOOCH_3$
234
234.1
234.2
234.3
234.4
234.5
C_2H_5CN, $HCOOCH_3$
$HCOOCH_3$
$HCOOCH_3$, C_2H_5CN
$HCOOCH_3$
$HCOOCH_3$
CH_3OH
$HCOOCH_3$
$HCOOCH_3$
233.5
233.6
233.7
233.8
233.9
234
C_2H_5CN
C_2H_5CN
C_2H_5CN
C_2H_5CN
$HCOOCH_3$
$HCOOCH_3$
$HCOOCH_3$
C_2H_5CN
C_2H_5CN
233
233.1
233.2
233.3
233.4
233.5
FREQUENCY (GHz)

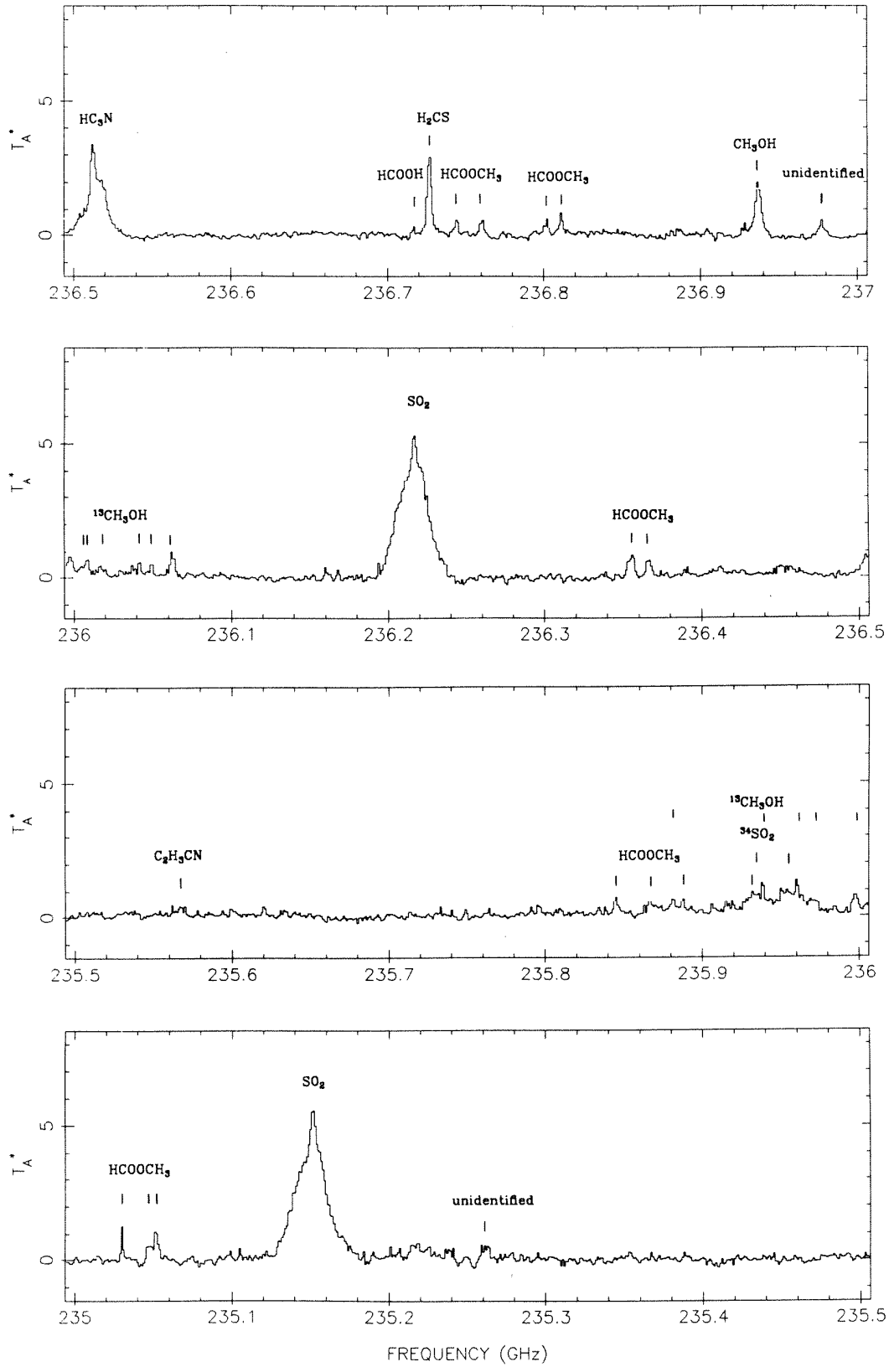
HC3N
H2CS
HCOOH
HCOOCH3
HCOOCH3
CH3OH
unidentified
SO2
13CH3OH
HCOOCH3
C2H3CN
13CH3OH
34SO2
HCOOCH3
SO2
HCOOCH3
unidentified
TA*
FREQUENCY (GHz)

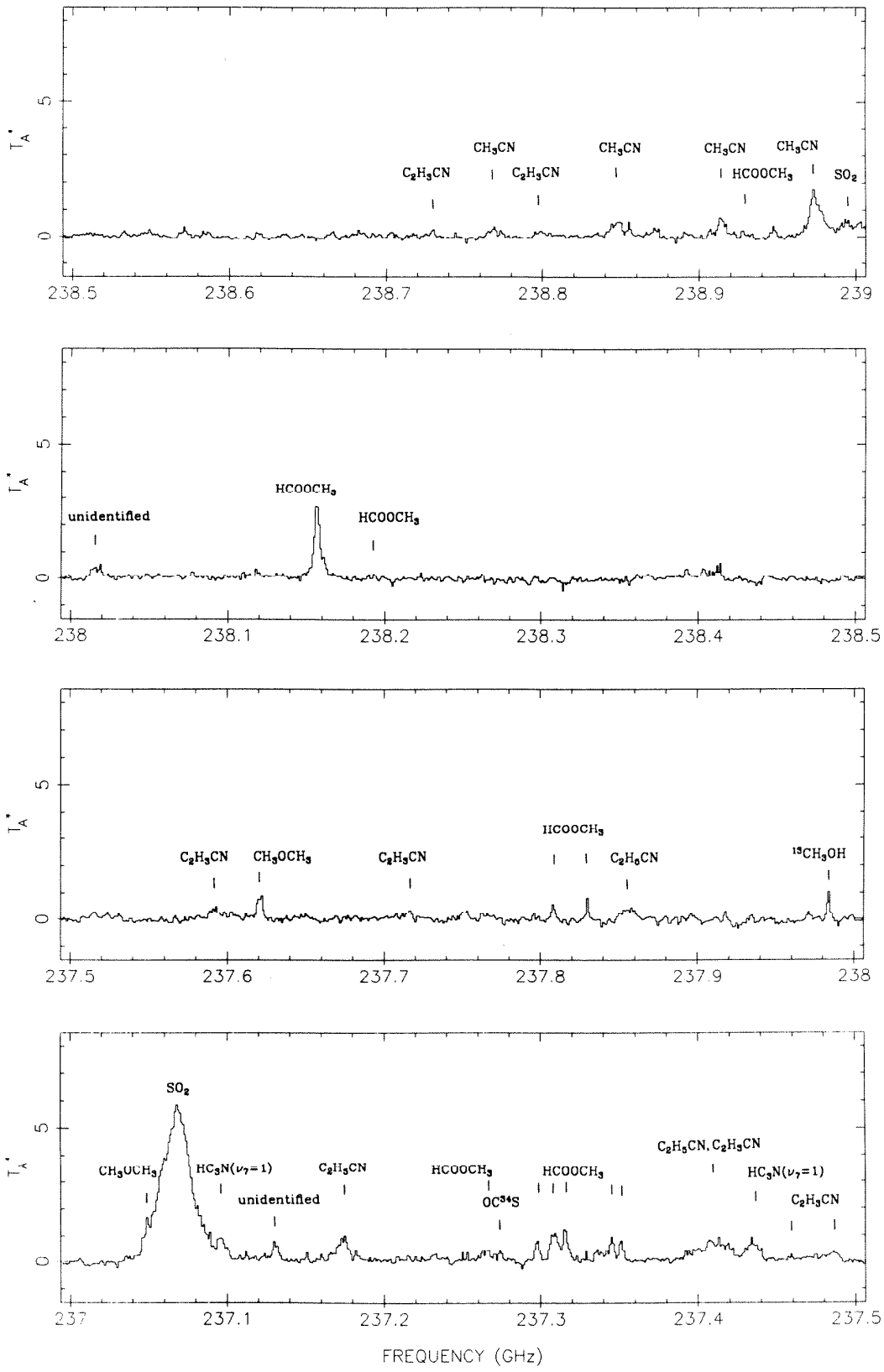
T_A^*
5
0
C_2H_3CN
CH_3CN
C_2H_3CN
CH_3CN
CH_3CN
$HCOOCH_3$
CH_3CN
SO_2
238.5
238.6
238.7
238.8
238.9
239
unidentified
$HCOOCH_3$
$HCOOCH_3$
238
238.1
238.2
238.3
238.4
238.5
C_2H_3CN
CH_3OCH_3
C_2H_3CN
$HCOOCH_3$
C_2H_3CN
$^{13}CH_3OH$
237.5
237.6
237.7
237.8
237.9
238
SO_2
CH_3OCH_3
$HC_3N(\nu_7=1)$
unidentified
C_2H_3CN
$HCOOCH_3$
$OC^{34}S$
$HCOOCH_3$
C_2H_3CN, C_2H_3CN
$HC_3N(\nu_7=1)$
C_2H_3CN
237
237.1
237.2
237.3
237.4
237.5
FREQUENCY (GHz)

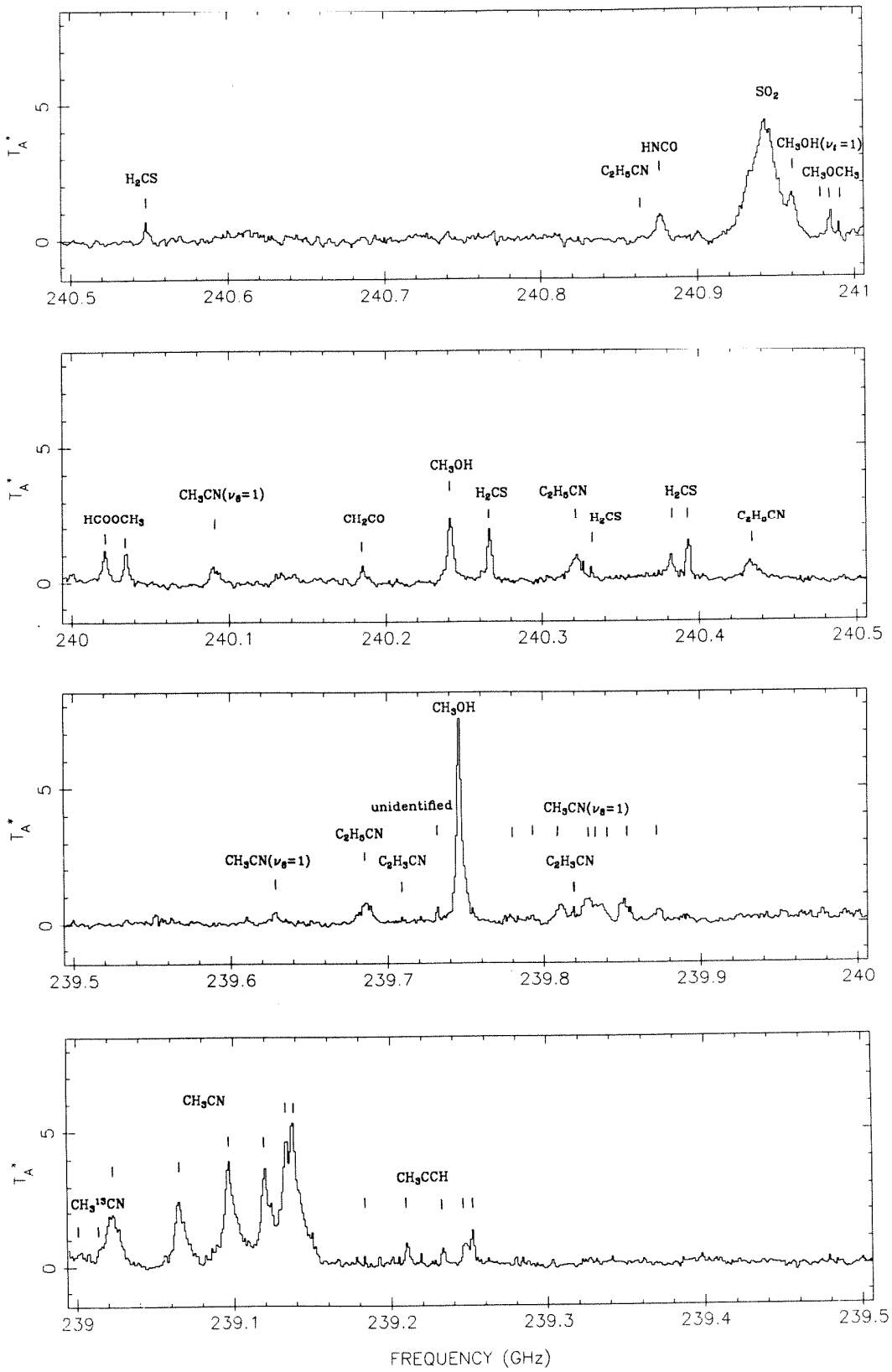
T_A^*
H_2CS
C_2H_5CN
HNCO
SO_2
$CH_3OH(\nu_t=1)$
CH_3OCH_3
240.5
240.6
240.7
240.8
240.9
241
$HCOOCH_3$
$CH_3CN(\nu_8=1)$
CH_2CO
CH_3OH
H_2CS
C_2H_5CN
H_2CS
H_2CS
C_2H_5CN
240
240.1
240.2
240.3
240.4
240.5
CH_3OH
unidentified
$CH_3CN(\nu_8=1)$
C_2H_5CN
$CH_3CN(\nu_8=1)$
C_2H_3CN
C_2H_3CN
239.5
239.6
239.7
239.8
239.9
240
CH_3CN
CH_3CCH
$CH_3{}^{13}CN$
239
239.1
239.2
239.3
239.4
239.5
FREQUENCY (GHz)

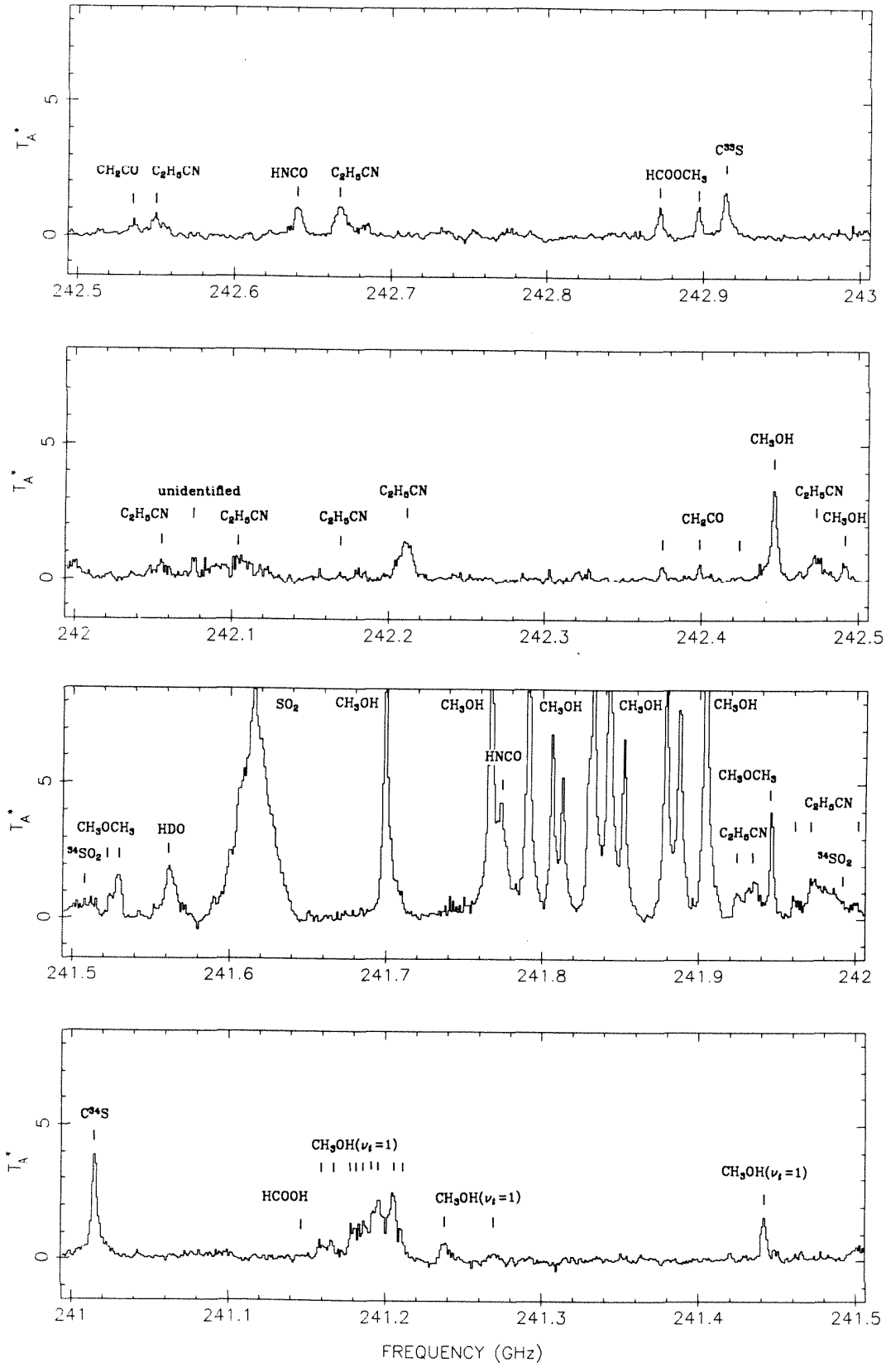
T_A^*
5
0
CH_2CO C_2H_5CN
HNCO C_2H_5CN
$HCOOCH_3$
$C^{33}S$
242.5 242.6 242.7 242.8 242.9 243
unidentified
C_2H_5CN C_2H_5CN C_2H_5CN C_2H_5CN
CH_2CO
CH_3OH
C_2H_5CN CH_3OH
242 242.1 242.2 242.3 242.4 242.5
SO_2 CH_3OH CH_3OH CH_3OH CH_3OH CH_3OH
HNCO
CH_3OCH_3
C_2H_5CN
CH_3OCH_3 HDO
$^{34}SO_2$
C_2H_5CN
$^{34}SO_2$
241.5 241.6 241.7 241.8 241.9 242
$C^{34}S$
$CH_3OH(\nu_t=1)$
HCOOH
$CH_3OH(\nu_t=1)$
$CH_3OH(\nu_t=1)$
241 241.1 241.2 241.3 241.4 241.5
FREQUENCY (GHz)

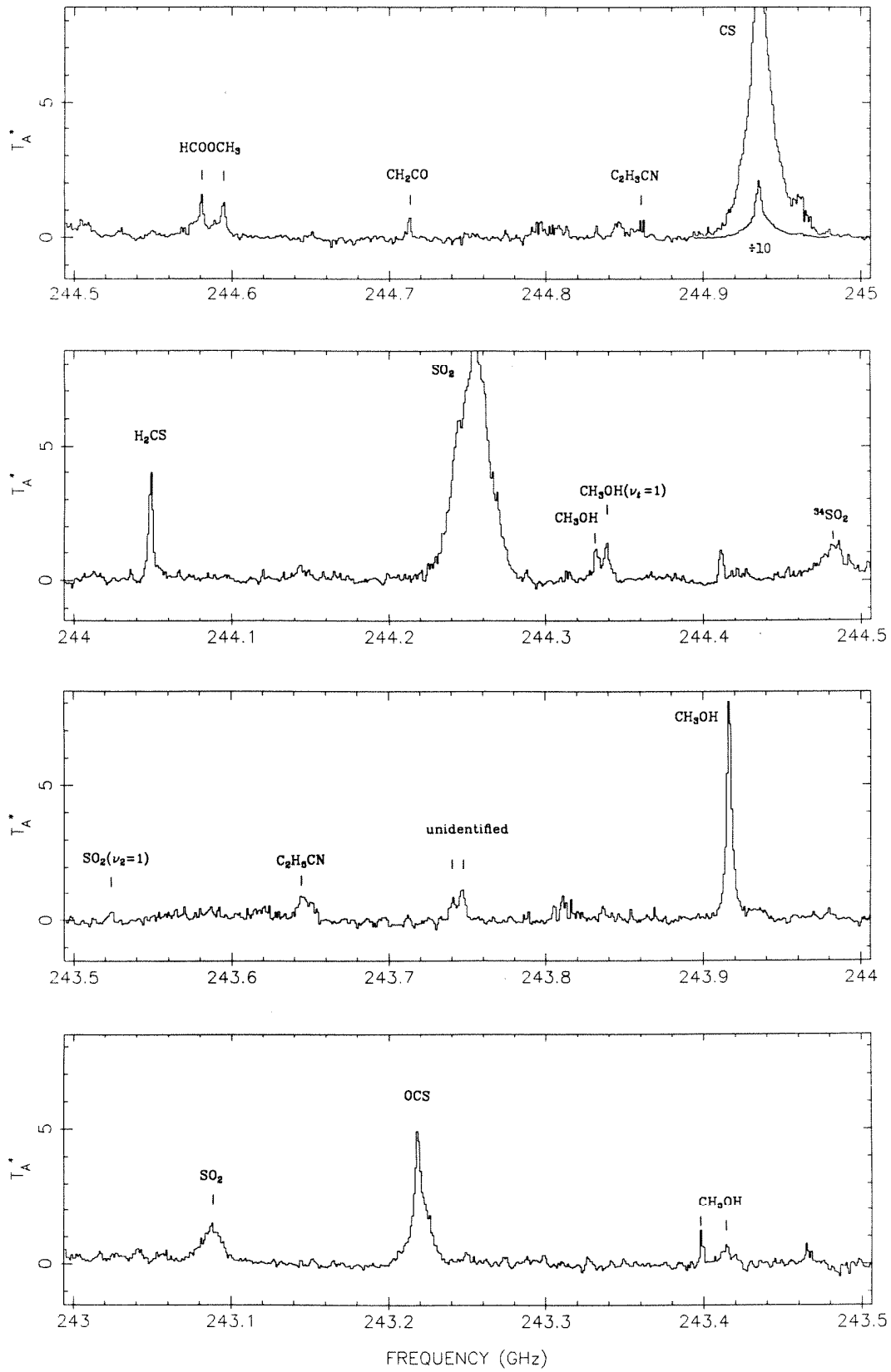
CS
HCOOCH3
CH2CO
C2H3CN
÷10
SO2
H2CS
CH3OH(νt=1)
CH3OH
34SO2
CH3OH
unidentified
SO2(ν2=1)
C2H3CN
OCS
SO2
CH3OH
T*A
5
0
244.5
244.6
244.7
244.8
244.9
245
244
244.1
244.2
244.3
244.4
244.5
243.5
243.6
243.7
243.8
243.9
244
243
243.1
243.2
243.3
243.4
243.5
FREQUENCY (GHz)

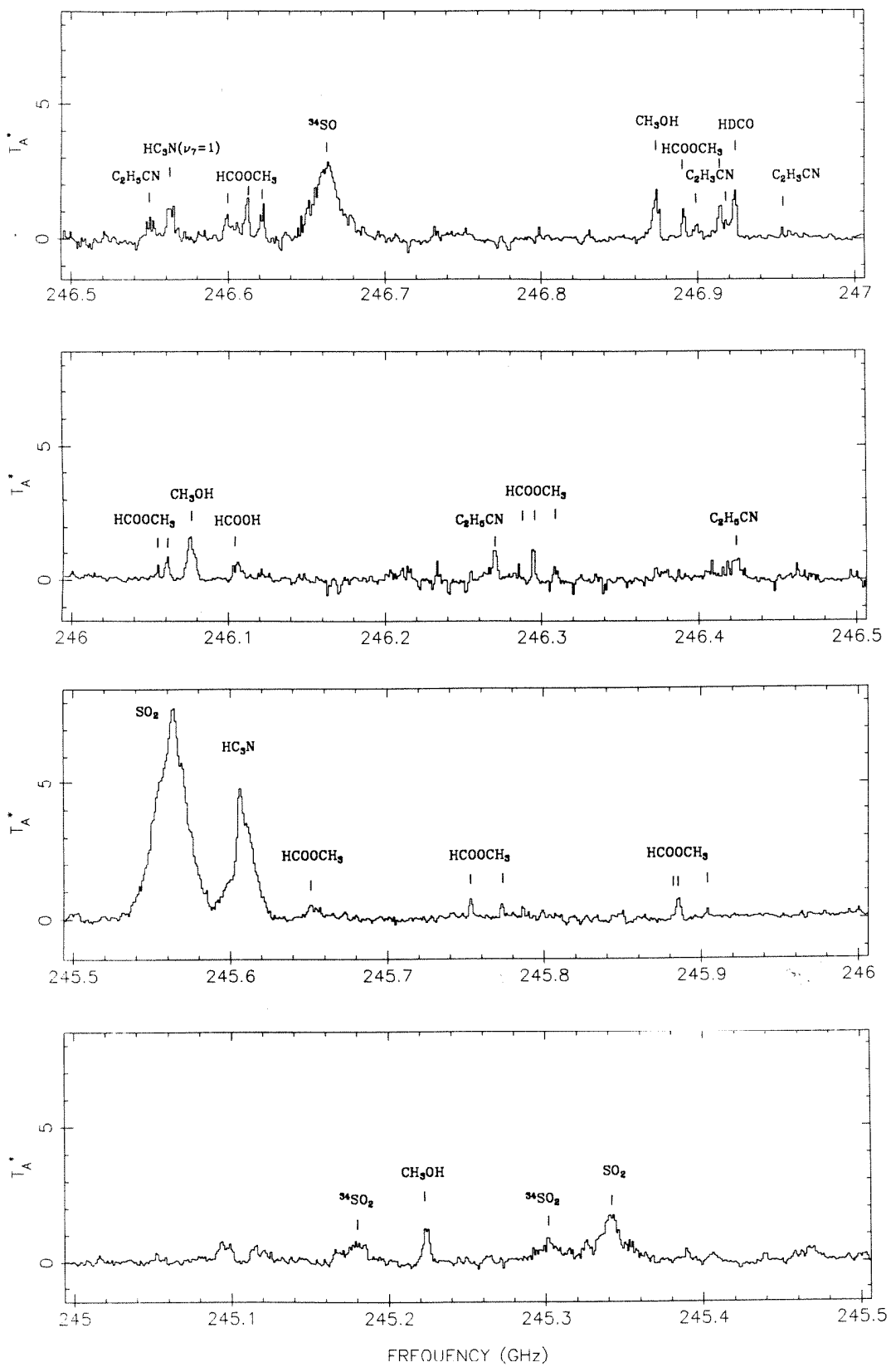
T_A^*
5
0
C_2H_5CN
$HC_3N(\nu_7=1)$
$HCOOCH_3$
^{34}SO
CH_3OH
$HCOOCH_3$
HDCO
C_2H_3CN
C_2H_3CN
246.5
246.6
246.7
246.8
246.9
247
$HCOOCH_3$
CH_3OH
HCOOH
C_2H_5CN
$HCOOCH_3$
C_2H_5CN
246
246.1
246.2
246.3
246.4
246.5
SO_2
HC_3N
$HCOOCH_3$
$HCOOCH_3$
$HCOOCH_3$
245.5
245.6
245.7
245.8
245.9
246
$^{34}SO_2$
CH_3OH
$^{34}SO_2$
SO_2
245
245.1
245.2
245.3
245.4
245.5
FREQUENCY (GHz)

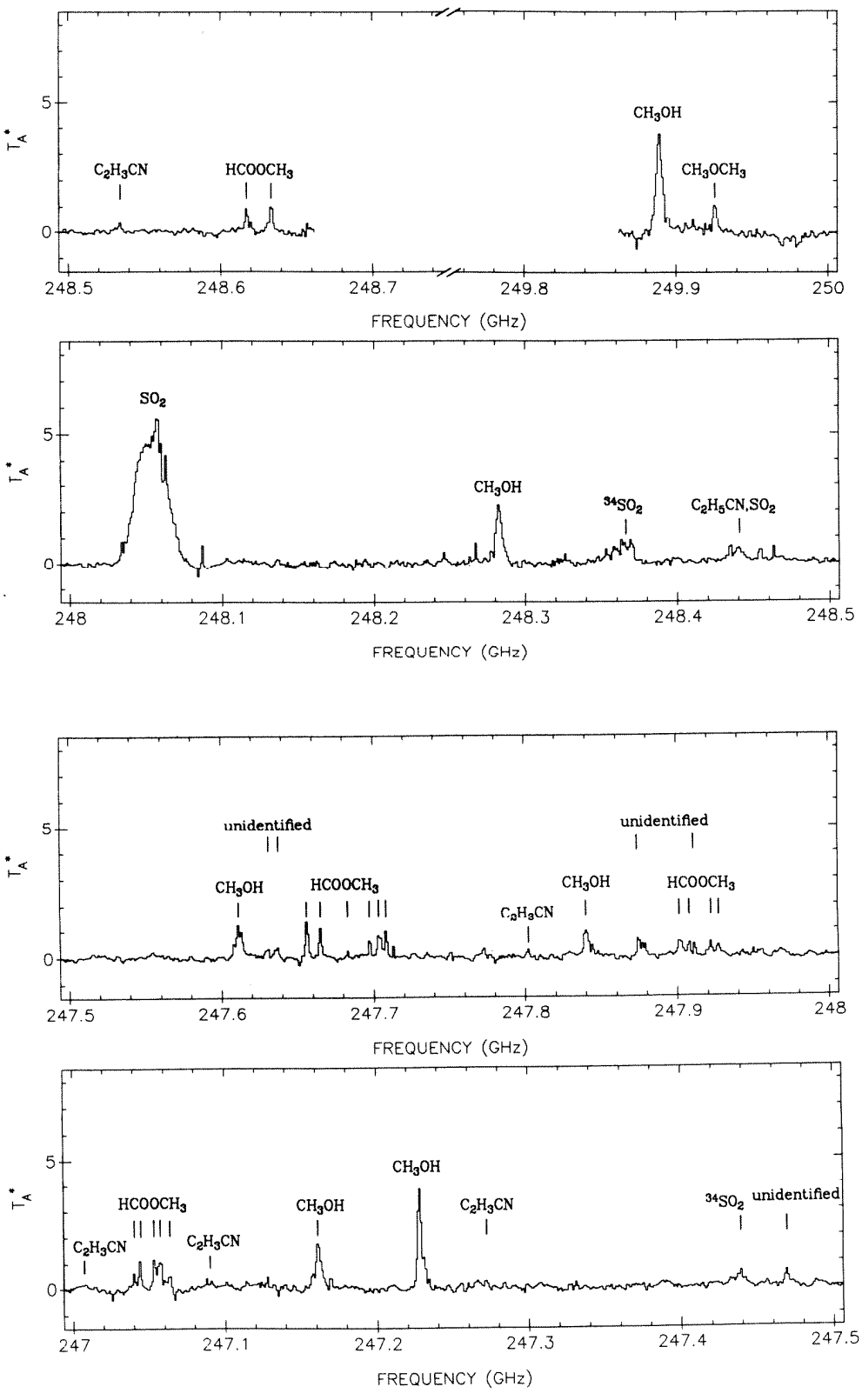
T_A^*
5
0
C_2H_3CN
$HCOOCH_3$
CH_3OH
CH_3OCH_3
248.5
248.6
248.7
249.8
249.9
250
FREQUENCY (GHz)
SO_2
CH_3OH
$^{34}SO_2$
C_2H_5CN,SO_2
248
248.1
248.2
248.3
248.4
248.5
FREQUENCY (GHz)
unidentified
CH_3OH
$HCOOCH_3$
C_2H_3CN
CH_3OH
unidentified
$HCOOCH_3$
247.5
247.6
247.7
247.8
247.9
248
FREQUENCY (GHz)
$HCOOCH_3$
C_2H_3CN
C_2H_3CN
CH_3OH
CH_3OH
C_2H_3CN
$^{34}SO_2$
unidentified
247
247.1
247.2
247.3
247.4
247.5
FREQUENCY (GHz)

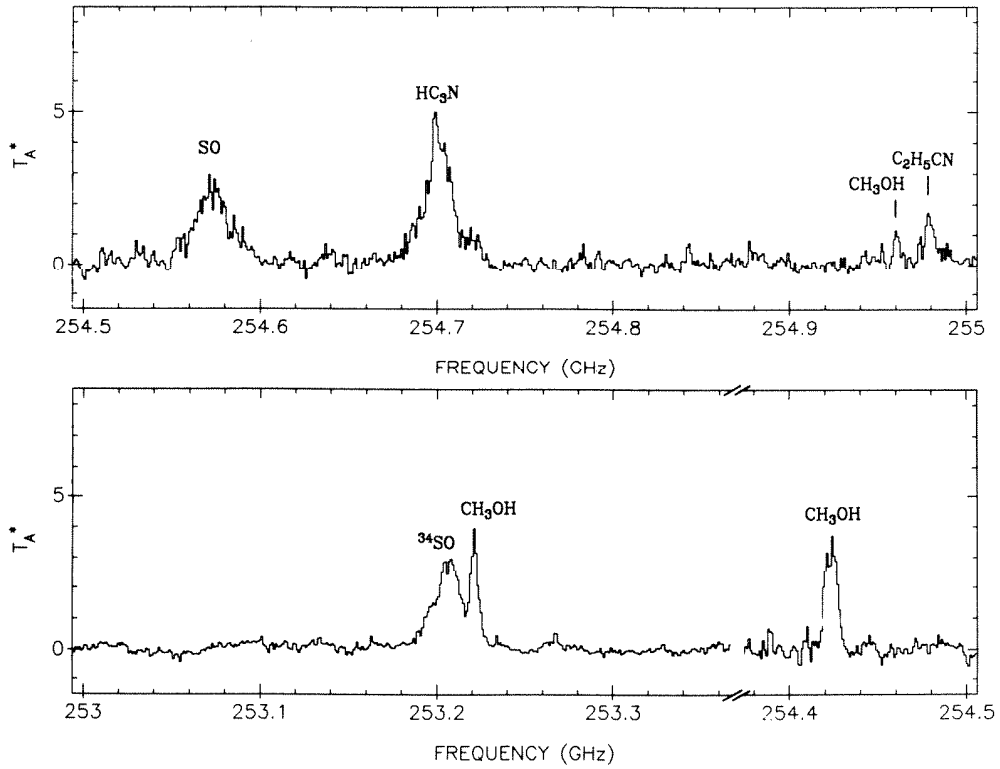
SO
HC3N
CH3OH
C2H5CN
T*A
5
0
254.5
254.6
254.7
254.8
254.9
255
FREQUENCY (GHz)
34SO
CH3OH
CH3OH
253
253.1
253.2
253.3
254.4
254.5
FREQUENCY (GHz)

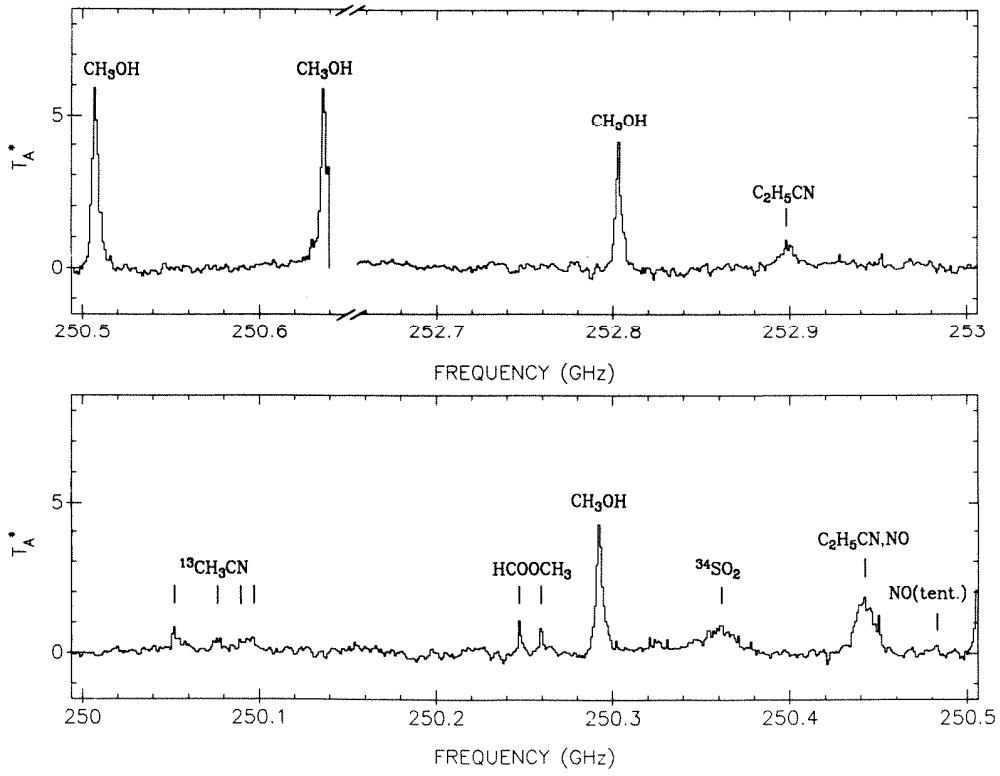
CH3OH
CH3OH
CH3OH
C2H5CN
T*A
5
0
250.5
250.6
252.7
252.8
252.9
253
FREQUENCY (GHz)
13CH3CN
HCOOCH3
CH3OH
34SO2
C2H5CN,NO
NO(tent.)
250
250.1
250.2
250.3
250.4
250.5
FREQUENCY (GHz)

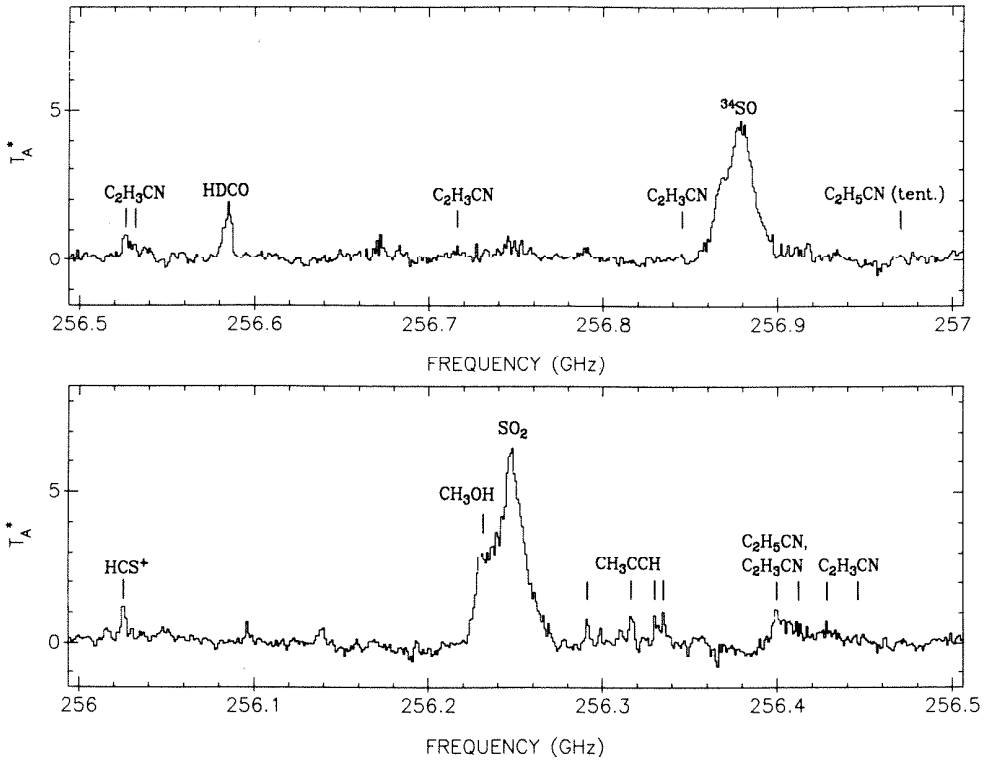
T_A^*
5
0
C_2H_3CN
HDCO
C_2H_3CN
C_2H_3CN
^{34}SO
C_2H_5CN (tent.)
256.5
256.6
256.7
256.8
256.9
257
FREQUENCY (GHz)
HCS$^+$
CH_3OH
SO_2
CH_3CCH
C_2H_5CN,
C_2H_3CN
C_2H_3CN
256
256.1
256.2
256.3
256.4
256.5
FREQUENCY (GHz)

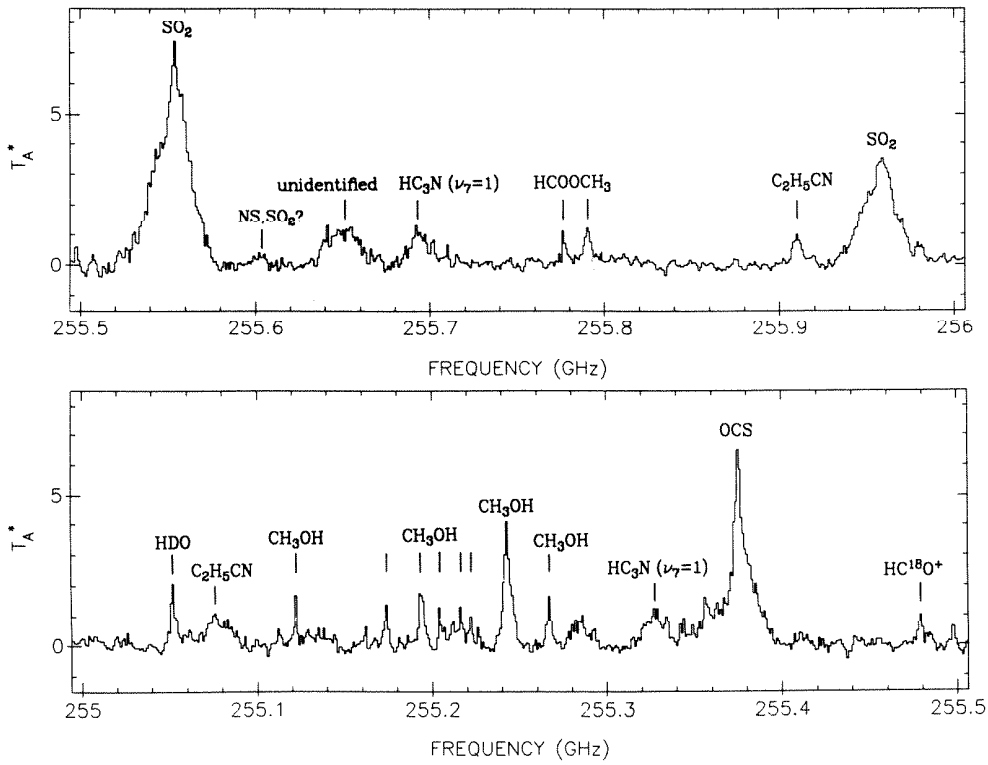
T_A^*
5
0
SO_2
NS,SO_2?
unidentified
HC_3N (ν_7=1)
$HCOOCH_3$
C_2H_5CN
SO_2
255.5
255.6
255.7
255.8
255.9
256
FREQUENCY (GHz)
HDO
C_2H_5CN
CH_3OH
CH_3OH
CH_3OH
CH_3OH
HC_3N (ν_7=1)
OCS
$HC^{18}O^+$
255
255.1
255.2
255.3
255.4
255.5
FREQUENCY (GHz)

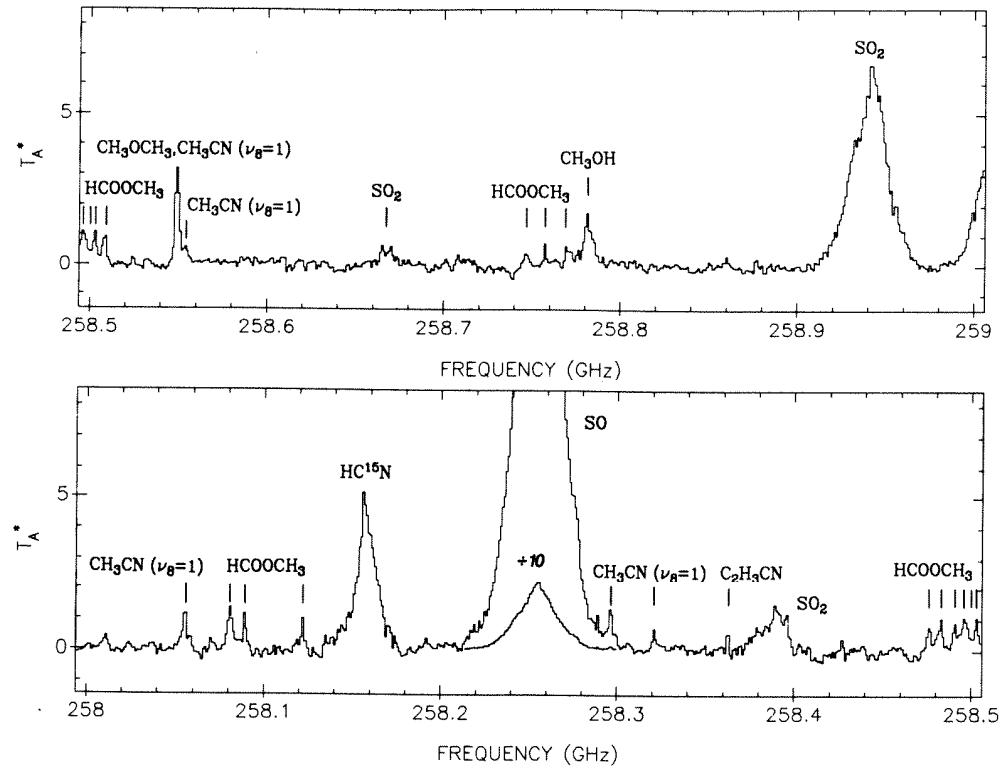
SO2
CH3OCH3,CH3CN (ν8=1)
HCOOCH3
CH3CN (ν8=1)
SO2
HCOOCH3
CH3OH
T*A
FREQUENCY (GHz)
SO
HC15N
+10
CH3CN (ν8=1)
HCOOCH3
CH3CN (ν8=1)
C2H3CN
SO2
HCOOCH3
T*A
FREQUENCY (GHz)

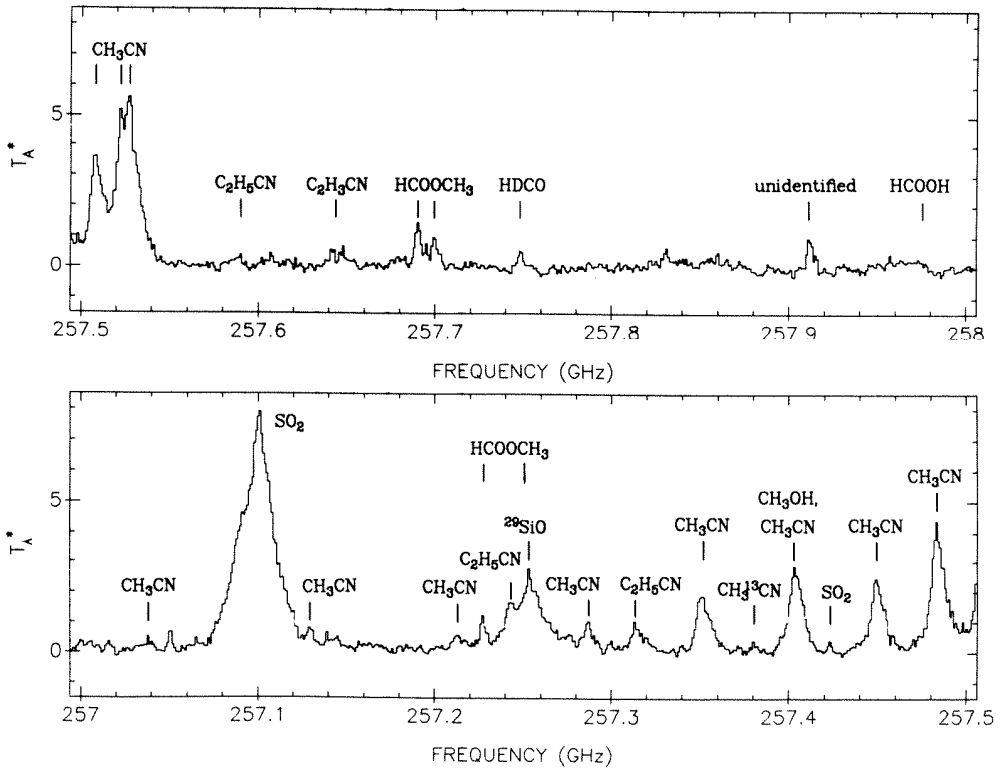
CH3CN
C2H5CN
C2H3CN
HCOOCH3
HDCO
unidentified
HCOOH
T*A
FREQUENCY (GHz)
SO2
HCOOCH3
29SiO
C2H5CN
CH3OH,
CH3CN
CH3CN
CH3CN
CH3CN
CH3CN
CH3CN
CH3CN
C2H5CN
CH3CN
CH3 13CN
SO2
T*A
FREQUENCY (GHz)

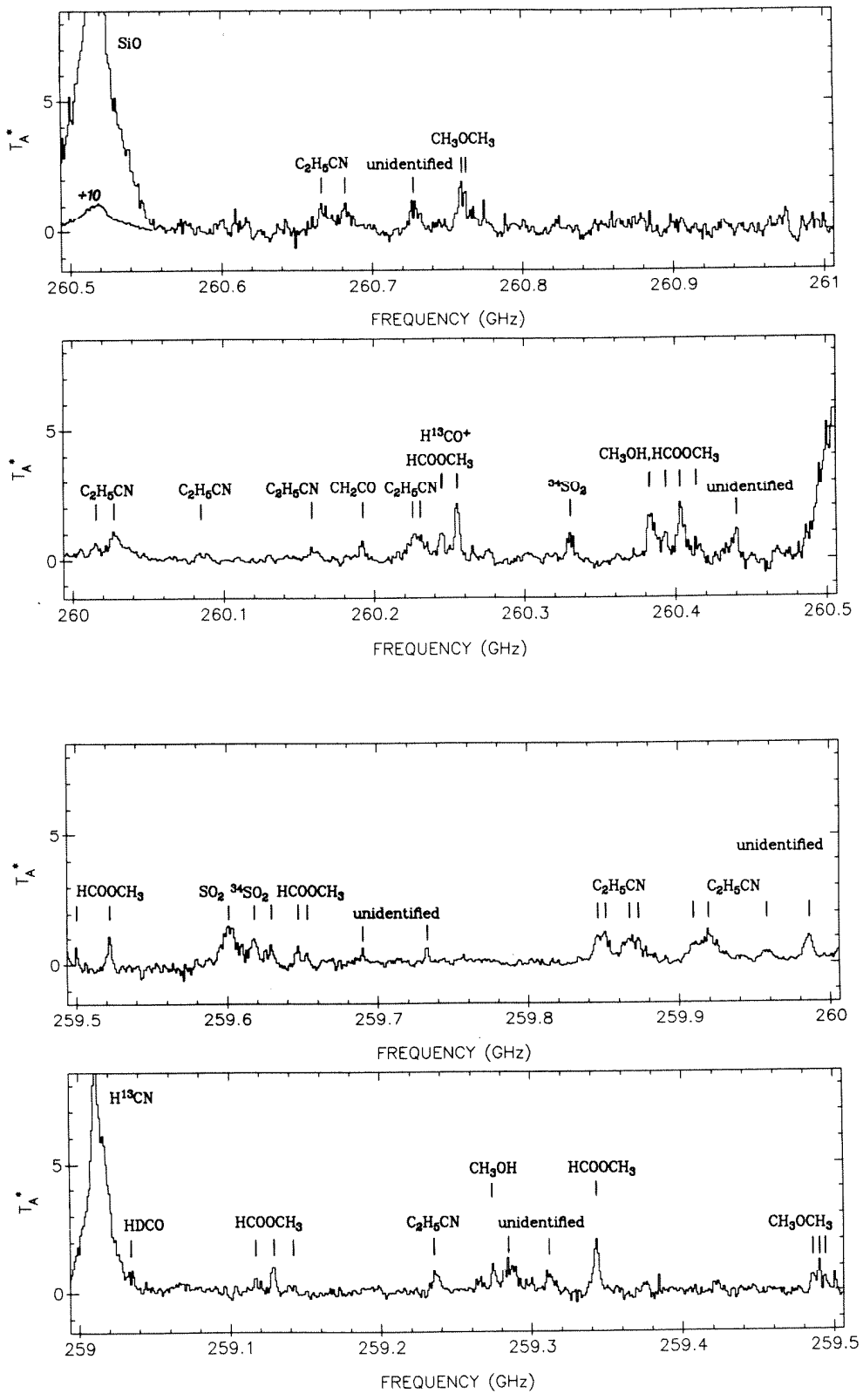
SiO
+10
C_2H_5CN
unidentified
CH_3OCH_3
T_A^*
FREQUENCY (GHz)
$H^{13}CO^+$
$HCOOCH_3$
$CH_3OH,HCOOCH_3$
$^{34}SO_2$
CH_2CO
$HCOOCH_3$
SO_2
$^{34}SO_2$
$H^{13}CN$
HDCO

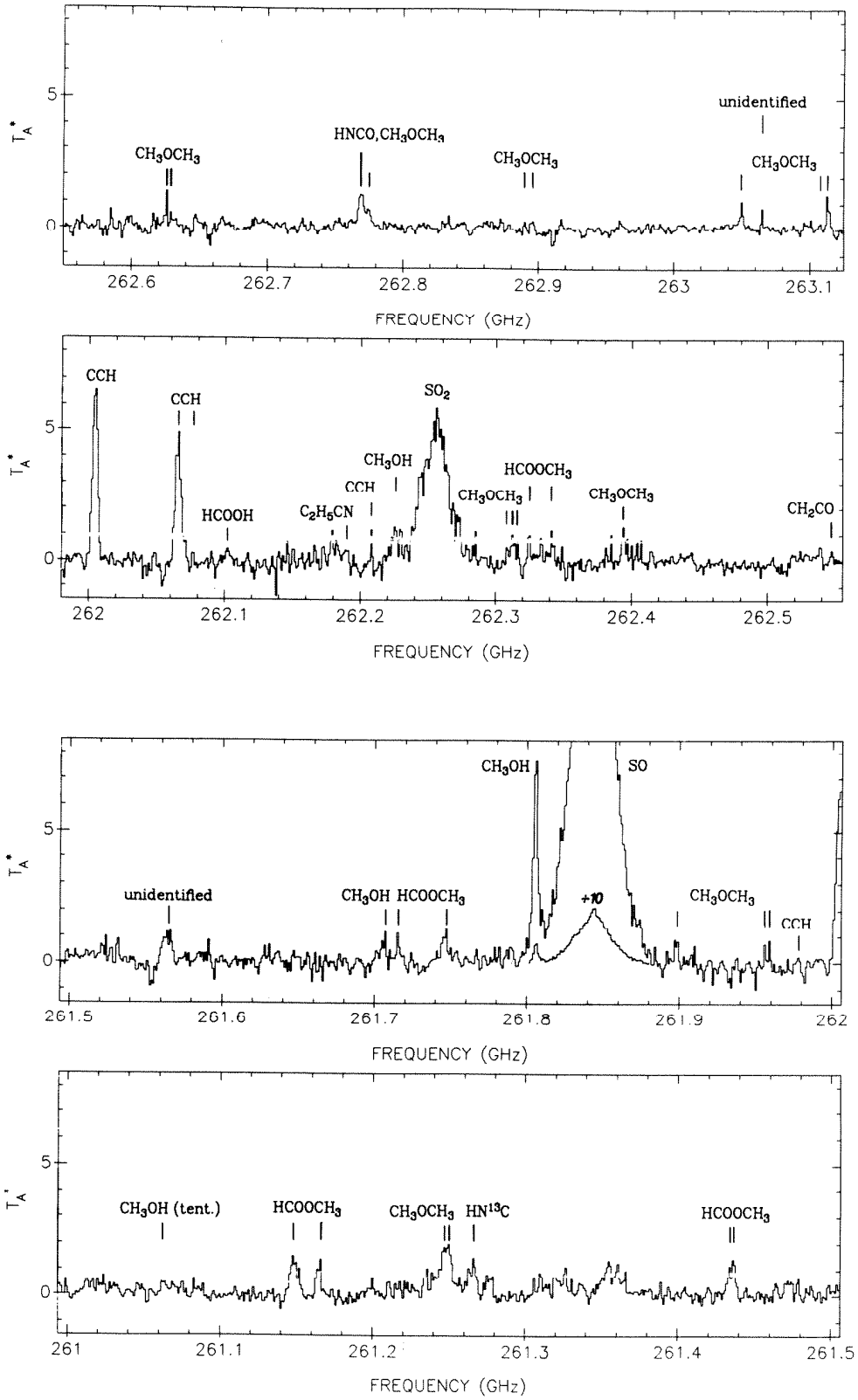
T_A^*
5
0
CH_3OCH_3
$HNCO, CH_3OCH_3$
CH_3OCH_3
unidentified
CH_3OCH_3
262.6
262.7
262.8
262.9
263
263.1
FREQUENCY (GHz)
CCH
CCH
HCOOH
C_2H_5CN
CCH
CH_3OH
SO_2
CH_3OCH_3
$HCOOCH_3$
CH_3OCH_3
CH_2CO
262
262.1
262.2
262.3
262.4
262.5
FREQUENCY (GHz)
unidentified
CH_3OH $HCOOCH_3$
CH_3OH
SO
+10
CH_3OCH_3
CCH
261.5
261.6
261.7
261.8
261.9
262
FREQUENCY (GHz)
T_A'
CH_3OH (tent.)
$HCOOCH_3$
CH_3OCH_3
$HN^{13}C$
$HCOOCH_3$
261
261.1
261.2
261.3
261.4
261.5
FREQUENCY (GHz)

APPENDIX B - LABORATORY RESULTS

In addition to the laboratory spectra discussed below, two major improvements in the instrumentation utilized in the study of molecular rotational spectra have been made during the course of this work. We shall briefly describe the nature of the new instrumentation, a frequency agile laser-based far-infrared local oscillator developed at the Jet Propulsion Laboratory (JPL) and a unique magnetic ion-confinement DC discharge cell first constructed at Duke University, before beginning an interpretation of the spectra obtained, in part, with such equipment.

B1.1 On the Generation of Tunable Far-Infrared Laser Sidebands and the Pure Rotational Spectrum of $X^2\Pi$ OH*

Because of the nearly complete lack of tunable coherent sources of radiation at submillimeter and far-infrared (FIR) wavelengths, this region has often been referred to as the gap in the electromagnetic spectrum. In recent years, however, several techniques have been developed which promise to open up this important spectral region. For example, the extension and harmonic generation of conventional microwave sources has produced spectrometers capable of continuous operation to above 1000 GHz, but the sensitivity of such instruments drops rapidly with frequency (Krupnov 1979; Helminger, Messer, and De Lucia 1983). Laser-based methods, which could cover the entire FIR region, have therefore received a great deal of attention.

Non-linear mixing techniques such as difference frequency generation from high-power CO_2 lasers in GaAs (Aggarwal *et al.* 1974), parametric oscillation (Bridges and Van Tran Nguyen 1973), and stimulated Raman scattering (Bonek and Korecky 1974) have all produced small quantities of tunable FIR radiation. More recently, Evenson *et al.* (1984) have created spectroscopically useful

*Condensed from Farhoomand *et al.* (1985a,b) and Blake *et al.* (1986).

amounts of tunable FIR radiation (~200 nW) by mixing two low-power CO_2 lasers in a metal-insulator-metal (MIM) diode. The limited tuning range of the individual infrared transitions means that a large number of laser lines, including isotopic species, must be available to provide complete coverage in the FIR. Alternatively, similar power levels (~100 nW) have been produced by mixing FIR molecular lasers and conventional microwave sources in both open (Fetterman *et al.* 1978) and closed (Bicanic, Zuiberg, and Dymanus 1978) mixer mounts. We report here the generation of copious amounts of continuously tunable laser sidebands by mixing radiation from an optically pumped FIR molecular laser with that from millimeter-wave klystrons in a GaAs Schottky-barrier diode mounted in an open structure corner cube mixer. The wide tuning range of these sidebands is limited only by the frequency ranges of the millimeter-wave (or microwave) sources used.

Figure B1.1 shows the optical layout of our laser sideband system. A commercial CO_2 pumped far-infrared molecular laser (Apollo FIR laser system, model number 560) is used as the fixed frequency source. The CO_2 laser is stabilized using an external Fabry-Perot etalon whose piezoelectric translator (PZT) is dithered by a 25 Hz sawtooth. One percent of the CO_2 power is sampled by a ZnSe beam splitter and sent through the etalon. The signal generated by the etalon at the dither frequency is then detected with a liquid nitrogen cooled HgCdTe detector and fed into a lock-in amplifier, the dc output of which controls the PZT stack of the CO_2 laser.

The FIR laser output passes through a polarizing Michelson interferometer similar to that originally proposed by Martin and Pulpett (1970). The analyzer polarizer and the path difference are set to pass the laser radiation without attenuation or polarization change. The polarizers are polyester-backed wire grids and exhibit a 10% loss. An off-axis parabolic mirror focuses the Michelson

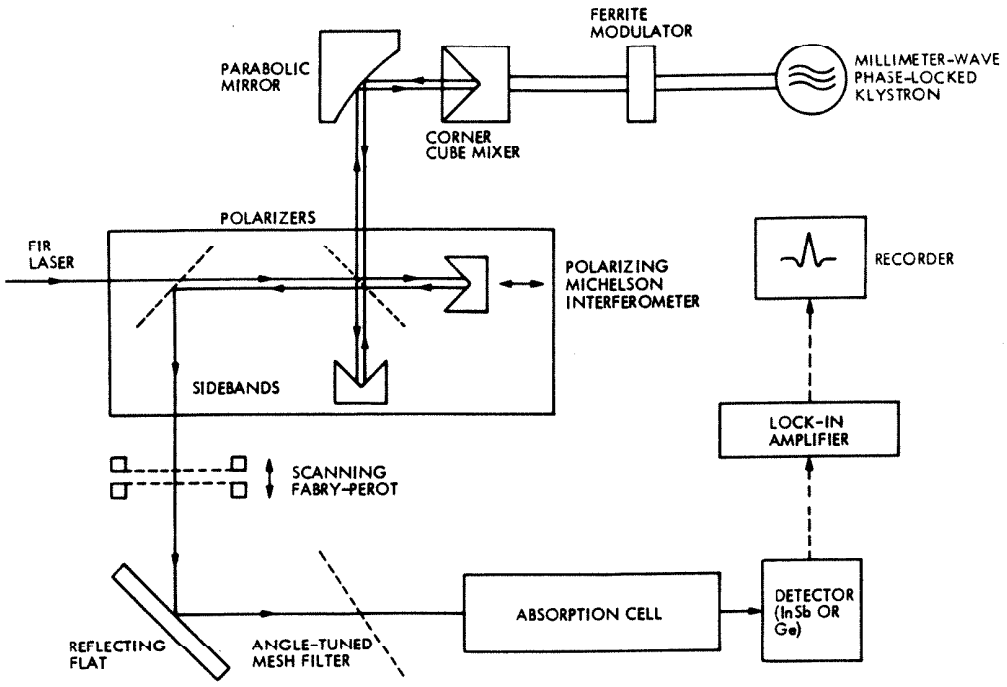

Figure B1.1: Optical layout of the JPL far-infrared laser sideband system.

output onto the mixer. The laser radiation is quasi-optically collected and coupled onto the mixer by a 1.7 mm long gold plated phosphor bronze whisker antenna (~4λ at about 700 GHz), which contacts a GaAs Schottky-barrier diode located at the apex of an open structure corner cube similar to that originally proposed by Sauter and Schultz (1977; Krautle, Sauter, and Schultz 1977). The diode (Mattauch lot #1V1, 5 fF capacitance, 7 Ω spreading resistance) was soldered onto a post which passes through the center of the corner cube's V-band waveguide, thereby intercepting millimeter-wave radiation to be mixed with the laser. The millimeter-wave radiation is produced by klystrons phase-locked to a stabilized X-band source. A ferrite modulator chopped the klystron power reaching the diode at a frequency best suited to the detector used to monitor the sidebands.

The unused laser power and the sideband power returns along the same optical path to the interferometer. The interferometer path difference is tuned so that the sideband polarization is rotated by 90° as it passes through the interferometer while the laser polarization is unrotated. This polarization behavior is accomplished when

$$2l = 2n\,\lambda_{laser} = (2m + 1)\,\lambda_{sideband} \qquad \text{(B1.1)}$$

where l is the path difference between the two arms of the interferometer and m and n are integers. Since the sideband wavelength is not necessarily harmonically related to the laser wavelength, the path length difference is tuned to optimize performance. The tuning is not critical since the transmittance of the Michelson interferometer is sinusoidal with l.

If the polarization of the laser is initially oriented 90° with respect to the diode antenna, the relation for l can be modified so that the first pass through the interferometer produces a 90° polarization change. On the return pass, the laser power undergoes a reciprocal polarization shift while the polarization of the sidebands remains unchanged. Thus, the optical path of the laser and sidebands is the same regardless of the laser polarization.

In an ideal Michelson interferometer, the sideband power would all be reflected through the output port. However, because of the imperfect polarizers and possible misalignment of the interferometer, some laser power leaks through along with the sidebands. To isolate the sideband radiation from this residual laser power, the output radiation is sent through a Fabry-Perot interferometer with a finesse of about 15. When scanned, the Fabry-Perot interferometer separates the laser as well as the upper and lower sidebands from each other. In order to further reduce the laser power level reaching the detector, an angle tunable free-standing mesh filter is employed. Such a filter is,

essentially, a very sharp notch (reject) filter whose rejection frequency is tunable by means of varying the radiation's angle of incidence (Chen 1970; Pickett, Farhoomand, and Chiou 1983).

Initially, experimental efforts were devoted to the generation and characterization of the laser sidebands as a function of several variables of the system. For this purpose, the FIR laser was operated at the 693 GHz formic acid line as the center frequency, and a 93 GHz klystron provided the tunable millimeter-wave source. The klystron power was modulated at 1 kHz, and an InSb hot-electron bolometer was placed after the tunable mesh filter with its output sent to a lock-in amplifier. Linear sweeps of the Fabry-Perot clearly indicated the generation of both sidebands with a signal-to-noise ratio of better than 100. With maximum klystron power, only 50 mV of constant voltage diode bias was needed to optimize the sideband signal. Lower klystron power settings required higher external biasing for optimum sideband generation, as expected. The effect of klystron power on the sideband output was studied by monitoring the klystron level with a second diode (Baytron model #1N-58) placed after the 10dB coupler used to phase-lock the millimeter-wave tubes. The result is the saturation curve shown in Figure B1.2. The dependence of the sideband power on the incident laser power was also determined by attenuating the laser radiation with calibrated mesh filters, resulting in the linear curve also shown in Figure B1.2. In all cases, it was made certain that the InSb detector was in its linear region. These results are all consistent with those reported by Bicanic (1983).

In order to determine the absolute sideband power generated, the InSb detector was calibrated against a Scientech thermopile power meter (model 361) at four different laser frequencies, namely 604, 693, 762, and 1397 GHz. A report by Foote *et al.* (1981) indicates that the Scientech power meter response

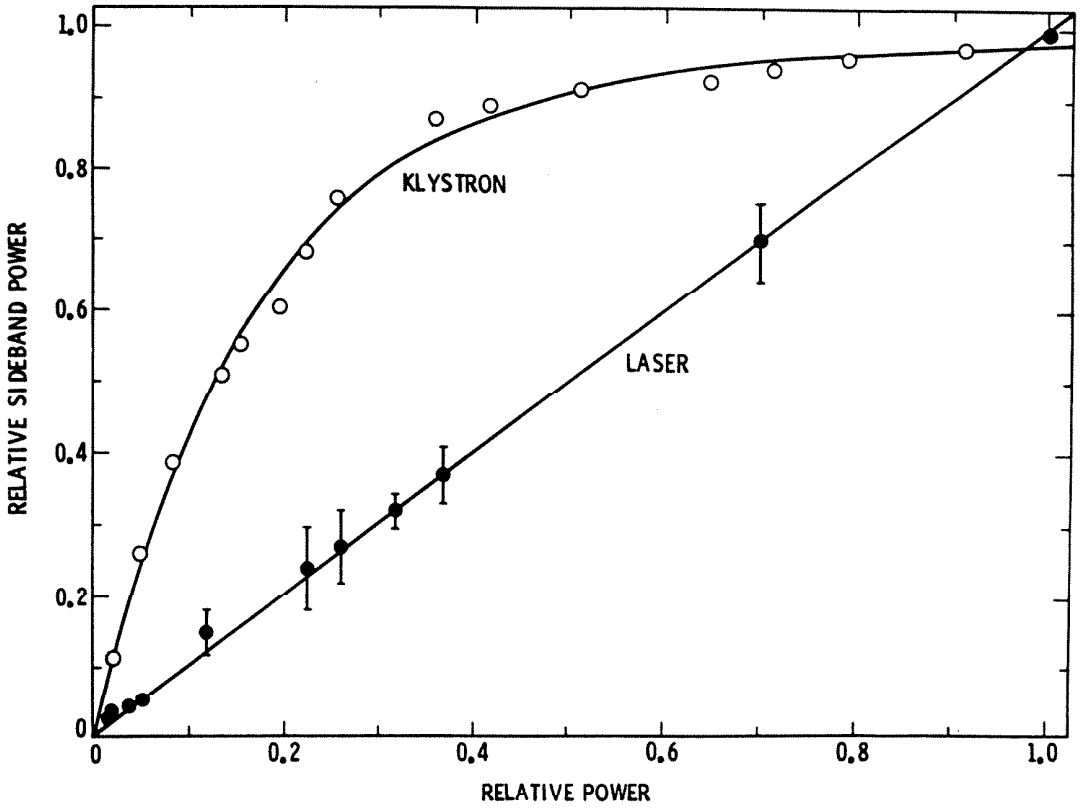

Figure B1.2: Relative sideband power vs. klystron power (○) and vs. laser power (●) at a center frequency of 693 GHz.

at 671 GHz is 0.52 ± 0.25 and at 1363 GHz is 0.575 + 0.125 of the actual irradiated power. As an additional check on relative power, a Nicolet FIR Fourier transform spectrometer was used to determine the spectral response of our InSb detector referenced to a pyroelectric detector. The Nicolet results cover a frequency range from 450 to 1650 GHz and are within 3% to 10% of the four fixed point laser results. Therefore, the dominant error bar associated with all of our absolute power measurements is the ± 20% uncertainty of the Scientech power meter reading. Using the calibrated InSb detector the incident laser power at 693 GHz was measured to be 4 mW, and the laser sideband radiation at 600 and 786 GHz was measured to be 3.0 μW.

As an intermediate step to generating sidebands in the THz region, the FIR laser was operated at the 762 GHz formic acid line. With the entire set-up

unchanged, the upper and lower sidebands at 854 and 668 GHz were readily observed. The sideband characteristics were similar to the lower frequency results and were quite reproducible. In order to test the system at higher frequencies the FIR laser was then operated on the difluoromethane line at 1627 GHz and the methanol line at 1839 GHz. Because of the rapid roll-off of the InSb detector at frequencies above 1000 GHz, a Ge bolometer cooled to 2.2°K served as the detector for these measurements. The Schottky diode antenna was left the same as before, 1.7 mm long, due to the mechanical constraints of our existing corner cube structure. At these frequencies the antenna length was 9.2 λ and 10.4 λ, respectively. A reduction in coupling efficiency of the laser radiation was therefore expected. In addition, due to the shorter wavelength, the system was much less forgiving to instability and misalignment. The sidebands were, however, relatively easy to generate. Figure B1.3 shows a portion of a linear Fabry-Perot sweep verifying the generation of the 1839 GHz (163 μm) laser sidebands at 1746 (172 μm) and 1932 GHz (155 μm). With the Ge bolometer calibrated against the InSb detector, we found that 22 mW of laser power at 1627 GHz produced about 2.5 μW of sideband power at 1532 GHz, while 3 mW of laser power generated approximately 100 nW of sideband power at 1932 GHz. The somewhat lower efficiency is attributed mainly to the excessive length of the diode antenna.

Nevertheless, the new system is more efficient than previously reported results even at high frequencies under adverse coupling conditions between the laser radiation and the Schottky diode mixer. The conversion efficiency ranges from about 0.075 % at 693 GHz where the coupling is optimum to about 0.003 % at 1839 GHz where the diode antenna is excessively long (10.4 λ). This enhanced efficiency is in part due to the use of the Michelson interferometer to separate the sidebands from the carrier and in part due to the improved mount for the Schottky-barrier diode.

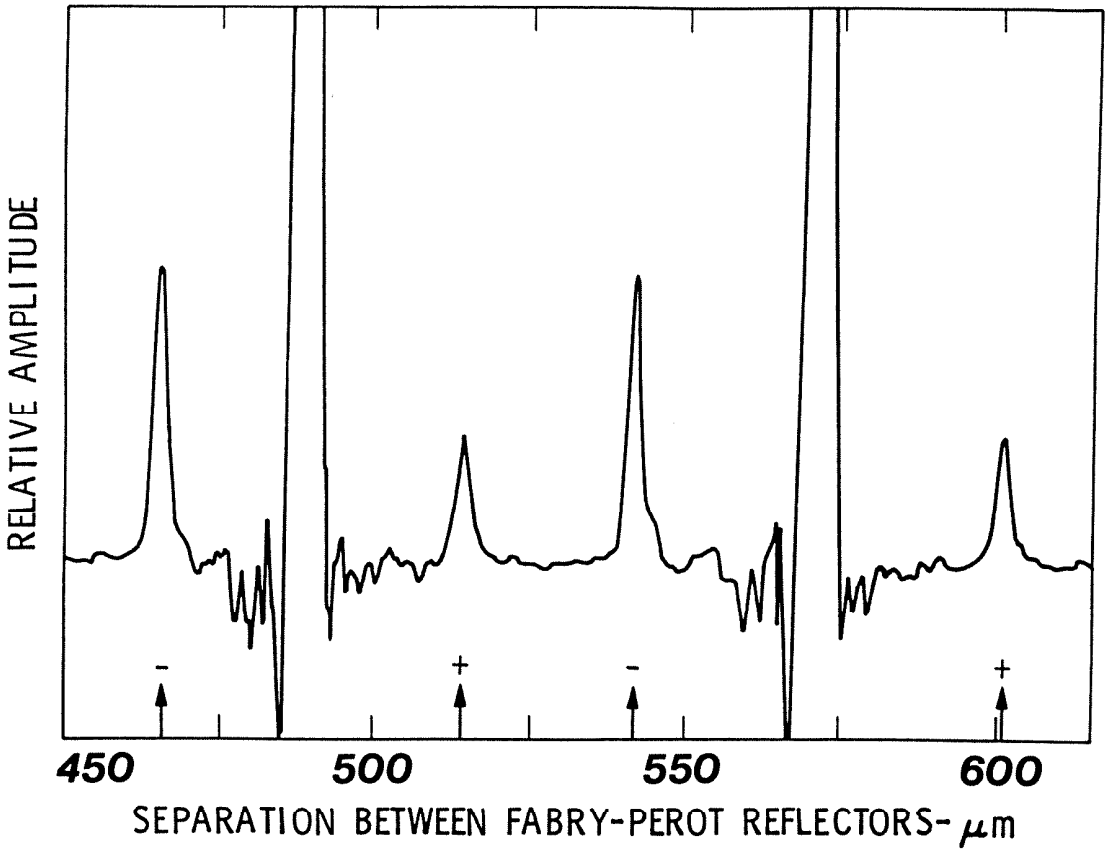

Figure B1.3: A portion of the linear Fabry-Perot sweep at the 1839 GHz (163 μm) center frequency. The upper and lower sidebands at 1932 GHz (155 μm) and 1746 GHz (172 μm) are marked by arrows and + and - signs, respectively. The horizontal axis is an absolute scale in μm showing the separation between the Fabry-Perot reflectors.

To demonstrate the tunability and monochromaticity of the generated sideband radiation, several submillimeter rotational absorption lines have been measured with this system. Specifically, we have recorded, for the first time, the direct (zero-field) spectra of the FIR pure rotational transitions of both stable and transient species such as OH, HDO, and NH_3. The work on the fundamental OH radical is of particular importance, and shall be described here as an example of the power and versatility of the laser sideband spectrometer. In addition to being a widespread constituent of the interstellar medium, OH also regulates stratospheric chlorine and nitrogen oxide catalytic ozone destruction cycles via reactions with HCl and NO_2. Because of its importance to so many

systems, and because it is relatively easy to generate in the laboratory, OH has long served as the prototypical free radical for a number of spectroscopic techniques and theoretical models. Perhaps the most well studied transitions are the microwave lambda doublets first detected in the laboratory by Dousmanis, Sanders, and Townes (1955); subsequently detected astronomically eight years later by Weinreb *et al.* (1963).

It is only recently, however, that the far-infrared (FIR) pure rotational transitions of OH shown in Figure B1.4 have become accessible to laboratory and astronomical study. Spectral lines in this region are important because they provide powerful, and often unique, probes into the chemical and physical nature of the interstellar gas (Phillips and Huggins 1981, Watson 1982). For example, thermal FIR emission from OH at 119 and 84 μm in Orion has shown that the hydroxyl radical abundance is increased dramatically by the passage of shock fronts through molecular clouds (Watson *et al.* 1985), a feature not observable with the lambda-doubling transitions. As noted in Chapter 1, searches for various species in the relatively unexplored FIR region must rely on the presence of accurate laboratory rest frequencies. To date, the bulk of the limited data on transient species has been provided by laser magnetic resonance (LMR) studies due to the almost complete lack of tunable sources of radiation at FIR wavelengths. In this pioneering technique atomic or molecular transitions are tuned into resonance with various fixed frequency FIR lasers by applying a variable magnetic field to the sample (Evenson 1981). As such, zero-field frequencies are not directly measured, but must be reconstructed from fits of the magnetic field data using sophisticated effective Hamiltonians. Errors in the zero-field transition frequencies are therefore higher than can be obtained with swept frequency techniques. In addition, the method is inapplicable to non-magnetic molecules like CO or NH_3.

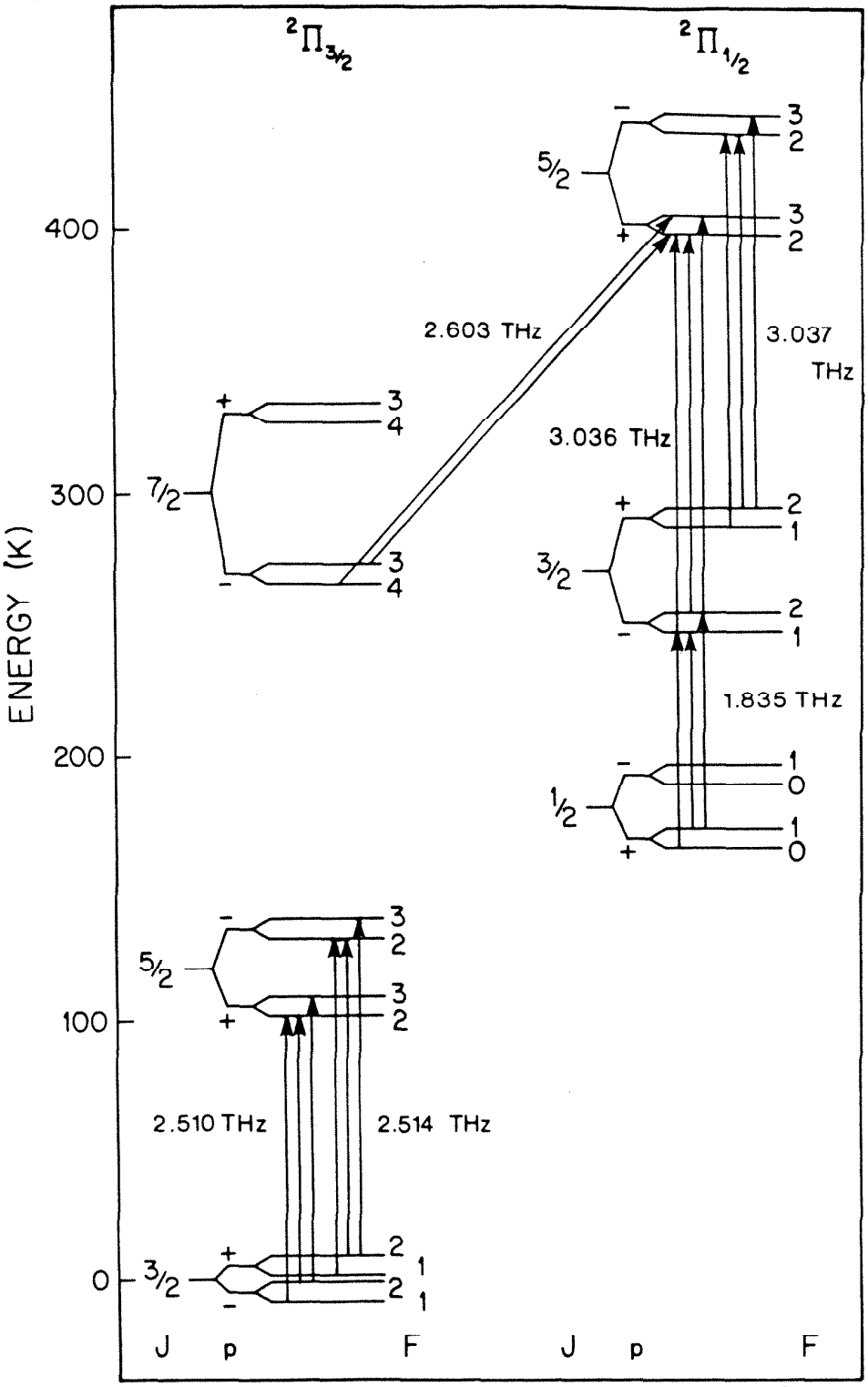

Figure B1.4: Energy level diagram of the lowest rotational states of the OH radical. The hyperfine and lambda-doubling splittings have been exaggerated here for clarity. Arrows mark the observed transitions.

We have therefore measured the fundamental rotational transition frequencies of the OH radical both as a test of the sensitivity and generality of the laser sideband technique, and to more precisely characterize the pure rotational spectrum of OH. The high accuracy of these measurements verifies the predictions of previous LMR work, and will be of use to the generation of FIR heterodyne receivers which, unlike current astronomical instruments, will be able to fully resolve the OH line profiles in the interstellar medium.

As noted above, in the initial characterization of the sideband source a Fabry-Perot with a finesse of about 15 was used in conjunction with an angle-tuned mesh filter to reduce laser leakage from the Michelson interferometer, but in these experiments a single Fabry-Perot with a finesse of approximately 80 sufficed. After passing through a free-space absorption cell which produced the OH, the sideband radiation was detected by a Ge bolometer operating at 2.2° K. Supplying the Schottky diode with a square wave bias voltage in the 50 - 500 Hz range amplitude modulated the sideband power to provide a phase sensitive signal. Since this technique monitors the total power received by the detector, a true line shape is produced. Tone-burst (frequency) modulation of the klystron may also be employed, which yields a second derivative line shape.

Lasing transitions of CH_2F_2 at 1891.3 and 2448.0 GHz, and of CH_3OH at 2522.8 and 3195.2 GHz, have been mixed with klystrons in the 50 - 90 GHz range to produce the tunable FIR radiation utilized in these experiments. Figure B1.5 shows a typical spectrum of the $\Omega = 3/2$, $J^P = 3/2^- \rightarrow 5/2^+$ transition, while Figure B1.4 shows an energy level diagram of the OH radical and the transitions studied in this work, which are listed in Table B1.1. The lambda-doubling and hyperfine splittings have been exaggerated for clarity in Figure B1.4. In most cases the nuclear hyperfine splittings are easily resolved. The hyperfine and lambda-doubling intervals of the OH rotational transitions are known to an

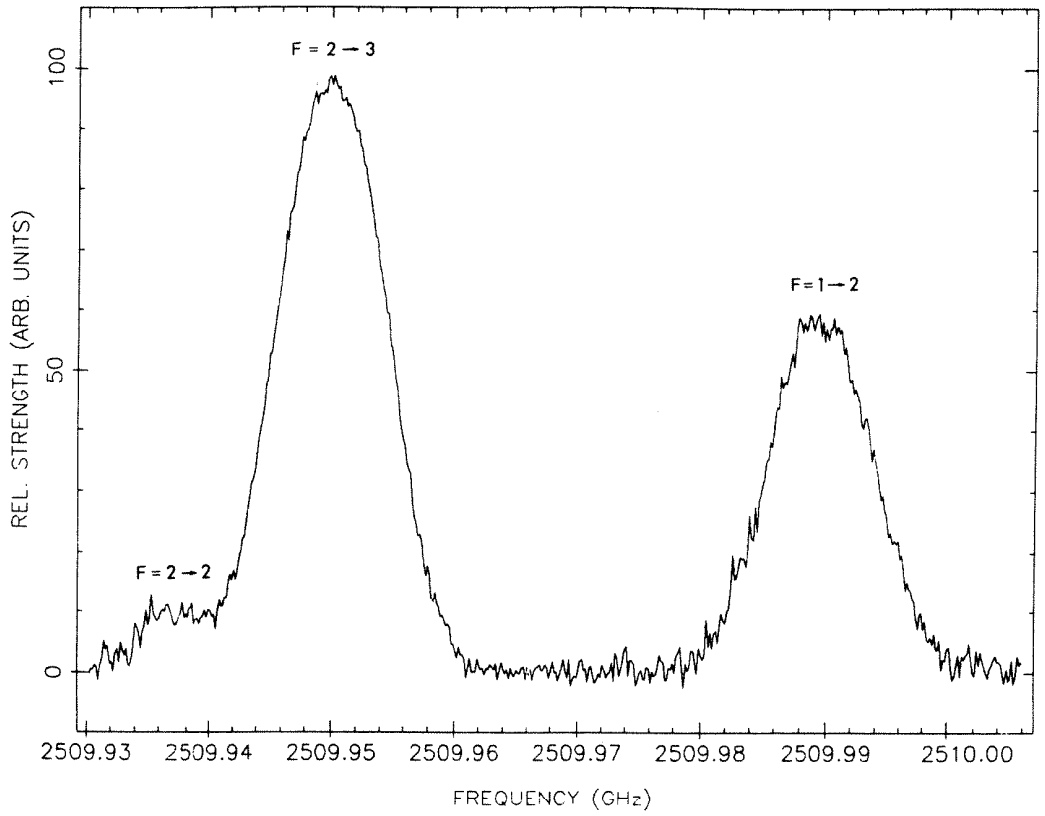

Figure B1.5: Observed spectrum of the $J^P = 3/2^- \rightarrow 5/2^+$ transition obtained by averaging four sweeps taken with a 1 second time constant. Amplitude modulation of the laser sidebands produces a true line shape profile.

accuracy of c.a. 5 kHz from the beam maser work of Meerts and Dymanus (1975). We have therefore obtained the frequencies listed in Table B1.1 by fitting the overall spectrum with Gaussian components whose separations are fixed to the hyperfine splittings measured previously. The quality of the data is such, however, that unrestricted fits of the $J^P = 3/2^- \rightarrow 5/2^+$ transitions reproduce the beam maser hyperfine splittings to within 200 kHz. Thus, the error bars quoted in Table B1.1 apply to the measured frequency of the entire pattern and not to the individual splittings of the hyperfine and lambda-doubling components. Table B1.1 also lists the predicted zero-field transition frequencies of Brown *et al.* (1982), derived from extensive set of LMR measurements (Brown *et al.* 1981). As can be seen, our measured frequencies lie slightly above the LMR

predictions but within their 3 MHz error bars in all cases. Identification of the astronomical features at 2509.9 and 2514.3 GHz as OH is therefore quite secure.

Table B1.1
Observed Spin-Rotation Transition Frequencies
of $^2\Pi_{1/2}$ and $^2\Pi_{3/2}$ OH

	Transition[a]		Measured Frequency (σ)	Observed - Calculated	LMR Predictions[b] (σ)
Ω	$J^{P'} \rightarrow J^{P''}$	$F' \rightarrow F''$	(MHz)	(MHz)	(MHz)
1/2	$3/2^- \rightarrow 1/2^+$	1 → 1	1834735.51(0.5)	0.22	1834734.7(3.0)
		2 → 1	1834747.35(0.5)	0.22	1834746.6(3.0)
		1 → 0	1834750.42(0.5)	0.22	1834749.6(3.0)
3/2	$5/2^+ \rightarrow 3/2^-$	2 → 2	2509935.44(0.5)	-0.02	2509933.7(3.0)
		3 → 2	2509949.43(0.5)	-0.02	2509947.7(3.0)
		2 → 1	2509988.61(0.5)	-0.02	2509986.9(3.0)
3/2	$5/2^- \rightarrow 3/2^+$	2 → 2	2514298.83(0.5)	-0.02	2514297.1(3.0)
		3 → 2	2514317.17(0.5)	-0.01	2514315.5(3.0)
		2 → 1	2514353.96(0.5)	-0.01	2514352.3(3.0)
1/2 → 3/2	$5/2^+ \rightarrow 7/2^-$	2 → 3	2603399.52(0.5)	-0.06	2603402.(>3.0)
		3 → 4	2603424.86(0.5)	-0.01	2603428.(>3.0)
1/2	$3/2^- \rightarrow 5/2^+$	2 → 2	3036257.77(0.5)	-0.07	3036260.(>3.0)
		1 → 2	3036269.61(0.5)	-0.07	3036272.(>3.0)
		2 → 3	3036275.58(0.5)	-0.07	3036278.(>3.0)
1/2	$3/2^+ \rightarrow 5/2^-$	2 → 2	3036573.51(0.5)	-0.08	3036576.(>3.0)
		1 → 2	3036643.73(0.5)	-0.07	3036646.(>3.0)
		2 → 3	3036645.05(0.5)	-0.06	3036647.(>3.0)

[a] Quantum numbers for the upper state are denoted by primes and those for the lower state by double primes. Superscripts on the J quantum numbers indicate the parity of the states according to Brown *et al.* (1982).

[2] Taken from Brown *et al.* (1982). σ in MHz.

The major uncertainty in these experiments is that of the FIR laser frequency as the klystrons are referenced to an extremely stable 5 MHz source. The uncertainties stem from the broad gain profiles of FIR lasers and are manifested as follows:

1) The lasing frequencies of individual FIR systems may differ significantly from the reported values because of differences in resonator geometry, CO_2 pump power, etc.

2) As determined mainly by the stability of a particular FIR cavity, the fractional accuracies reported may not be applicable to different FIR systems.

For example, we have found that for lower frequency HCOOH and CH_3F lasers the measured frequency may be altered approximately ± 0.3 - 0.5 MHz by adjusting the FIR cavity length to produce a 10 % drop in the output power level. These measurements were performed using the corner cube as a harmonic mixer. Inguscio *et al.* (1984) have obtained similar results with higher frequency laser lines used to record the LMR spectra of Si atoms for which they report a fractional accuracy of 2×10^{-7}. Therefore, to fully utilize the high resolution capabilities of this technique it is essential to monitor the laser frequencies used in each experiment.

For this purpose we initially used the J = 16 → 17 and 21 → 22 lines of CO at 1956.0 and 2528.2 GHz as a calibration standard in order to determine our absolute laser frequencies. The frequencies of these transitions are known to about 200 kHz from fits combining results from previous millimeter-wave spectroscopy with the recent high J measurements of Evenson (1985) using another tunable FIR spectrometer. Successive measurements were performed, alternating between the OH and CO lines to insure the consistency of the generated sideband frequencies. Other molecules, namely, the asymmetric rotors SO_2 and HDO, which have a much richer FIR spectrum than CO, were used in the same manner as further insurance of the stability of the system. The 0.5 MHz error bar assigned to the measured frequencies listed in Table B1.1 is the maximum standard deviation of the independent measurements performed on each

separate molecule mentioned above over a period of time. The average standard deviation of all these measurements is 0.3 MHz. In addition, fitting errors imposed by the spectral line widths of OH at these frequencies ($\Delta\nu_{Doppler} \sim 6$ MHz) also limits the accuracies to within 0.5 MHz. Using CO and HDO as the reference molecules, our CH_2F_2 and CH_3OH lasing frequencies lie within 1-3 MHz of the reported values (Peterson, Scalabrin, and Evenson 1980). Other possible systematic errors in the line frequency measurements include frequency shifts induced by Zeeman broadening by the earth's magnetic field and Stark effect shifts from the electric discharge source. We have determined, however, that these effects are negligible under the conditions of our experiment.

A simultaneous, weighted least-squares fit including the laser sideband measurements and a selected set of the available microwave Λ-doubling transitions, high resolution infrared measurements, and high-J optical data has been performed to evaluate an optimized set of molecular constants for OH, which are listed in Table B1.2. The optical term values of Coxon (1980), which we have used for states with J + 1/2 = 21 and J + 1/2 = 31, have been assigned an uncertainty of 0.020 cm^{-1}, while the sixteen infrared combination differences obtained from the difference frequency laser work of Amano (1984) have an estimated accuracy of 0.001 cm^{-1}. Frequencies for the Λ-doubling lines have been taken from Beaudet and Poynter (1978), who analyzed the rotational spectrum of OH with a three-state Hamiltonian of the type first described by Dousmanis, Sanders, and Townes (1955).

We have chosen, however, to analyze the combined data set using an effective two-state Hamiltonian as applied by Coxon (1980), whose constants are also listed in Table B1.2. Within the larger pure rotational structure, the hyperfine interactions have been modeled by the $^2\Pi$ Hamiltonian of Meerts and Dymanus (1975). As one can see, the constants listed in Table B1.2 are, in

Table B1.2
Optimized constants for the $X^2\Pi$ state of OH

Constant	Present (σ) (MHz)	Coxon[a] (σ) (MHz)
A	-4168684.47(93)	-4168731.7(348)
A_D	11.634(84)	-
B	555547.329(85)	555546.63(102)
D	57.2349(77)	57.2085(71)
H	$4.319(26) \times 10^{-3}$	$4.23607(145) \times 10^{-3}$
L	$-4.42(19) \times 10^{-7}$	$3.83734(908) \times 10^{-7}$
γ	-3517.000[b]	-3594.097(5519)
γ_D	0.679(29)	0.7396(240)
p	7053.2686(13)	7051.56099(354)
p_D	-1.55047(14)	-1.55075(43)
p_H	$1.546(37) \times 10^{-4}$	$1.670(005) \times 10^{-4}$
p_L	$3.7(34) \times 10^{-8}$	$2.0(33) \times 10^{-8}$
q	-1160.07750(41)	-1159.55593(151)
q_D	0.441971(23)	0.4418957(875)
q_H	$-8.238(29) \times 10^{-5}$	$-8.3507(402) \times 10^{-5}$
q_L	$1.348(85) \times 10^{-8}$	$1.46(10) \times 10^{-8}$
a	86.1119(25)	86.1109(37)
b^F	-73.2593(52)	-73.1524(63)
c	130.652(11)	130.6390(152)
d	56.6845(39)	58.1137(159)
d_D	-0.02279(18)	-0.02285(14)
C_I	-0.09978(61)	-0.10024(85)
C_I'	0.00671(18)	0.00649(11)

[a]Taken from Coxon (1980). σ in MHz. [b]From Amano (1984).

general, quite similar though a number of them disagree at the 1σ level. The present constants are considerably more precise, however, and have allowed the pure rotational spectrum of the OH radical to be predicted to better than 10 MHz throughout the FIR and mid-IR spectral regions. All transitions below a J of 7/2 have estimated uncertainties of less than 1 MHz. The observed - calculated rms error for the microwave and far-infrared lines is only 62 kHz, while that for the infrared combination differences is less than 0.0036 cm^{-1}. The low overall rms error of approximately 0.97 MHz demonstrates that the high-resolution spectroscopic capabilities traditionally associated with microwave spectroscopy have been extended into the far-infrared region.

B1.2. Ion Abundance Enhancement via Magnetic Confinement*

Previous laboratory microwave work on molecular ions has been conducted in the positive columns of long, large-diameter normal glow discharge cells. However, it has been known for some time that the concentration of positive ions in a glow discharge is highest in the negative glow region, not the positive column, and that the negative glow is relatively short under normal conditions (Von Engel 1955). The characteristics of the negative glow region, indeed nearly the entire discharge, are determined primarily by cathode phenomena. In normal glow discharges, the voltage drop and current density remain constant as the discharge current is increased and the cathode area covered by the plasma increases proportionally. In an anomalous glow discharge the plasma covers the entire cathode and an increase in discharge current also increases the current density and the voltage across the cathode drop. The larger cathode drop voltage of an anomalous glow discharge increases the length of the negative glow and shortens the positive column by increasing the energy and range of electrons that leave the cathode (Von Engel 1955). Brewer and Westhaver (1937) have shown that the length of the negative glow is equal to the range of such fast electrons arriving from the cathode drop. In a normal glow discharge at pressures near 1 torr this range is typically a few centimeters and is proportional to the electron energy. In long, narrow tubes at low pressures, however, scattering and loss of high-energy electrons to the cell wall reduces the length of the negative glow to substantially less than the range of these electrons. The effective range of the fast electrons, and thereby the length of the negative glow region, may be significantly affected by the application of longitudinal or transverse magnetic fields, as Thomson and Thomson (1928) noted in their classic text.

*Adapted from De Lucia *et al.* (1983).

Figure B1.6 shows a typical I-V curve of the ion apparatus, which is characteristic of an anomalous glow discharge. Maniv, Westwood, and Scanlon (1982) have shown that the voltage-current characteristics of a low-pressure anomalous glow sputtering discharge are given by

$$V_a = B \bullet I^{2/3} + V_o \qquad \text{(B1.2)}$$

where V_a is the applied voltage, V_o is the minimum voltage required to maintain the discharge, and B is a constant which depends upon the gas and pressure. The best fit of eq. (B1.2) to the discharge data is also shown in Figure B1.6. The low operating pressure and large cathode drop of the new apparatus give each electron sufficient energy to ionize many (~100) molecules and a range that can exceed the electrode separation (~1.5m). Ball (1972) has experimentally verified that significant numbers of fast electrons reach the anode with nearly all of their cathode drop energy in a large diameter anomalous glow discharge operating at 10 mTorr in pure Ar with an anode-to-cathode separation of 9.25cm. However, he also concludes that the angular distribution of these electrons is ~10°. The optimum spectroscopic use of the ionizing potential of the fast electrons would be to concentrate them along a long, narrow path through which the microwave radiation propagates. To do this, we have applied a longitudinal magnetic field of several hundred Gauss along the axis of a small diameter tube. The cyclotron radius of electrons with several thousand volts of transverse energy is only a few centimeters at these field strengths, and scattered electrons as well as those with initial trajectories not parallel to the axis of the discharge are therefore confined to the microwave field interaction region.

Measurements taken with no applied magnetic field, in addition to longitudinal and transverse magnetic fields, served to determine the location of the ions that produced the observed signals. Recall that increasing the potential drop

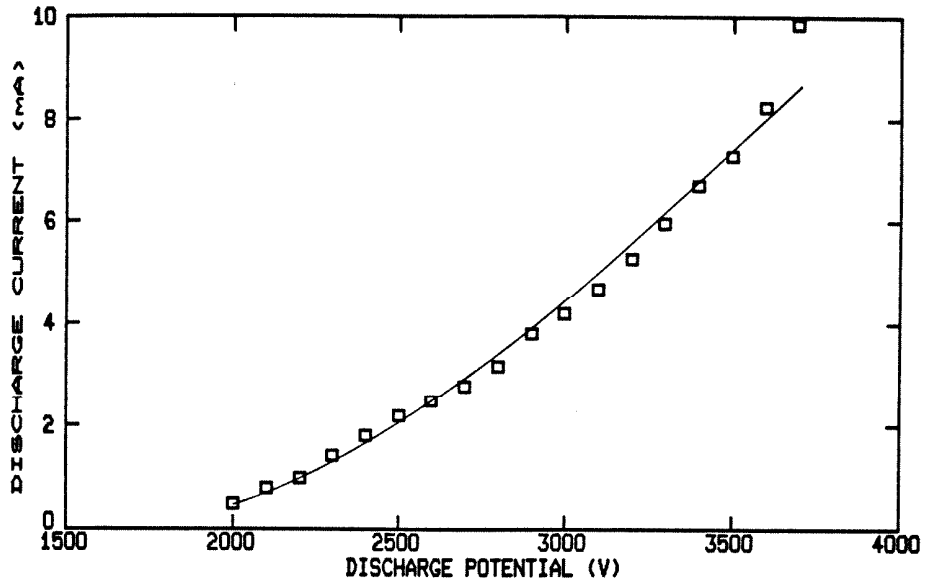

Figure B1.6: Current-voltage characteristic of the ion apparatus at a pressure of 6 mTorr in argon. This pressure is measured near the pump, and the pressure in the cathode region is probably several times larger.

across the discharge increases the length of the negative glow at the expense of the positive column. Thus, a plot of discharge potential versus signal strength should show a monotonic increase of the line intensity with the discharge voltage if the ions were produced in the negative glow. Figure B1.7 shows just such a dependence of the HCO^+ signal strength in a 5 mTorr 1:1 mixture of $CO:H_2$. In addition, the negative glow is a nearly field-free region (Von Engel 1955), and ions observed in this region would be expected to show little or no Doppler shift due to their drift velocity. Observations of NO^+ (Bowman, Herbst, and De Lucia 1982) and HOC^+ (Blake *et al.* 1983) have experimentally verified this.

Figure B1.8 shows the distance from the cathode to the optical end of the negative glow and the relative HCO^+ signal strength as a function of the solenoidal magnetic field. It can be seen that a field of ~150 Gauss is required to stretch the negative glow region to fill the entire cell. When the magnetic field strength is raised to values above that necessary to extend the negative

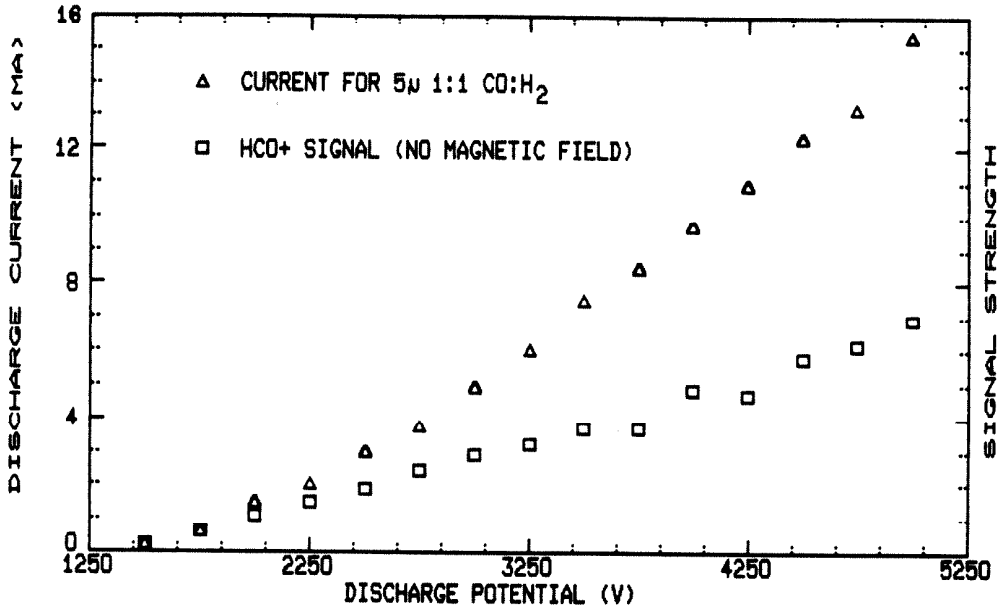

Figure B1.7: Field-free dependence of the HCO^+ *signal strength on the discharge potential.*

glow to the anode, the HCO^+ signal grows by an additional factor of two before saturation occurs. The additional enhancement beyond that due to lengthening of the ion-rich negative glow is most likely caused by an increased density of ionizing electrons. A transverse magnetic field deflects the fast ionizing electrons, causing the negative glow to terminate and the positive column to fill the tube from the anode to the point of deflection. Figure B1.9 illustrates that the strength of the observed HCO^+ signal is nearly proportional to the optical length of the negative glow as controlled by the location of a translatable, transverse magnetic field.

The new low pressure magnetic field technique has been tested in 1.5 and 4 inch diameter tubes with HCO^+, NNH^+, HOC^+, and NO^+. It has now become the "work horse" sample cell in the laboratory, with investigators in many countries having used the magnetic confinement technique to study a wide range of ions such as ArH^+ (Bowman *et al.* 1983), H_2D^+ (Bogey *et al.* 1984a; Warner *et al.* 1984), $HOCO^+$ (Bogey *et al.* 1984b), and H_3O^+ (Plummer, Herbst, and De Lucia

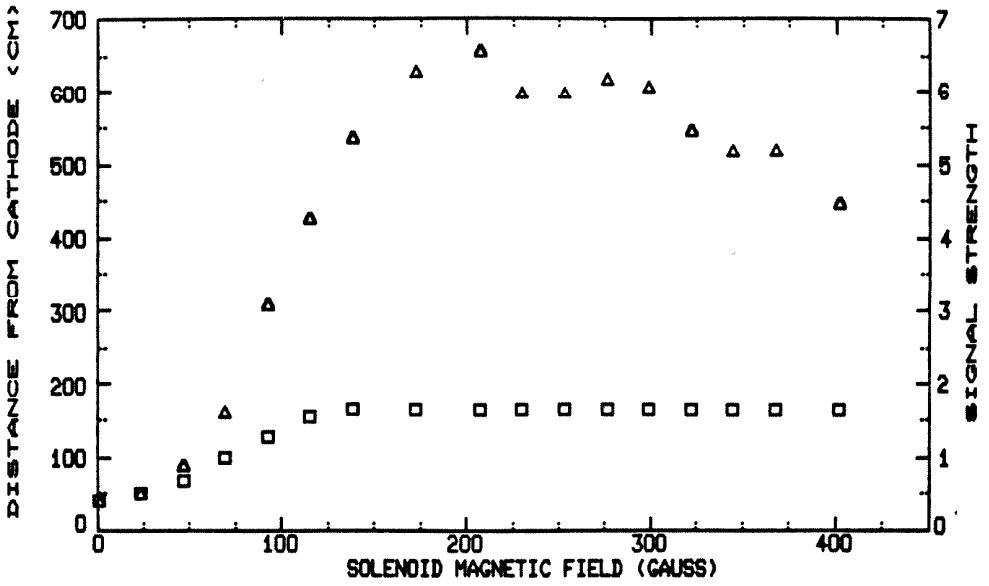

Figure B1.8: Distance from the end of the cathode to the end of the negative glow ▪ and HCO^+ signal strength Δ as a function of the magnetic field.

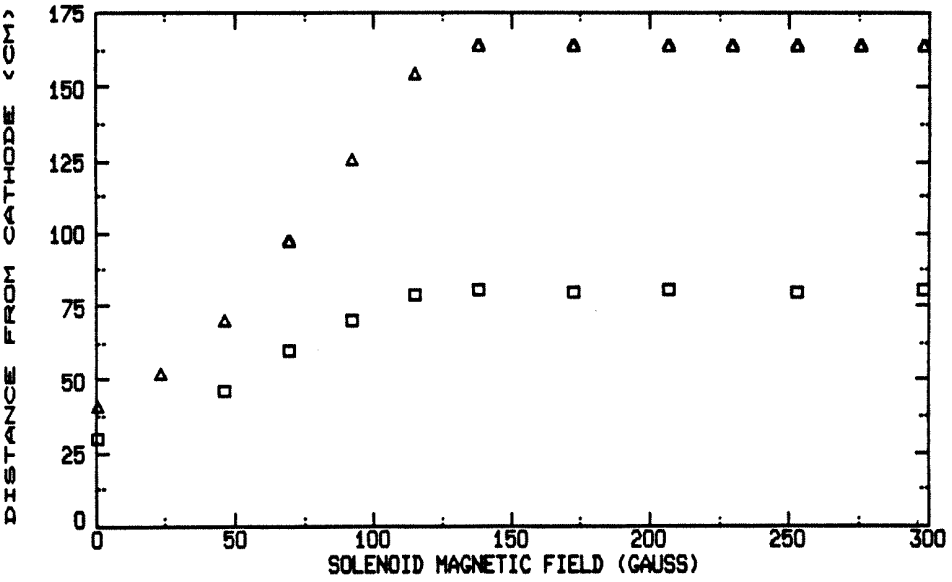

Figure B1.9: Distance from the cathode to the end of the negative glow Δ and to the point where deflection of the fast electrons reduces the observed signal strength by a factor of two ▪. The distance from the cathode to the beginning of the negative glow is approximately 15cm.

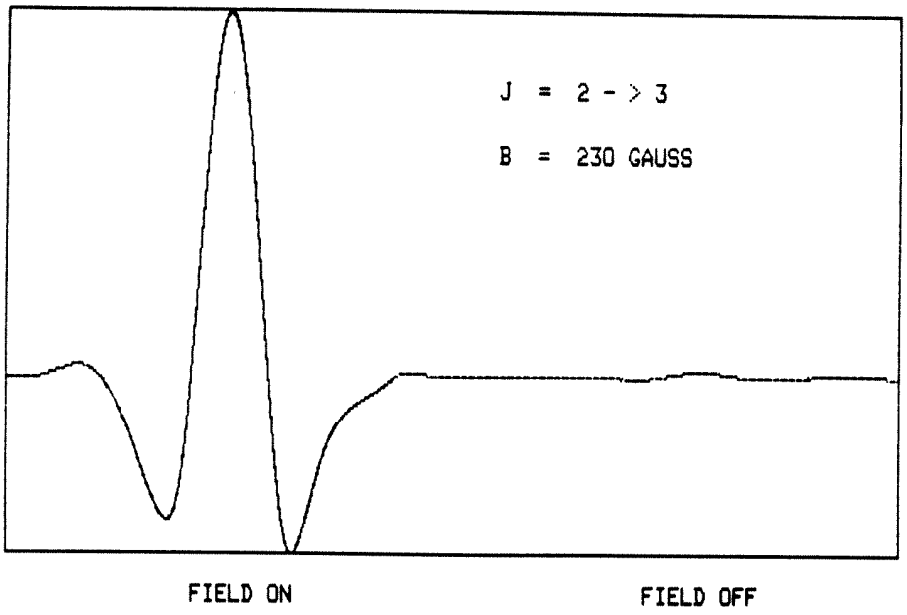

Figure B1.10: Additional enhancement for the HNN^+ ion due to the application of the magnetic field.

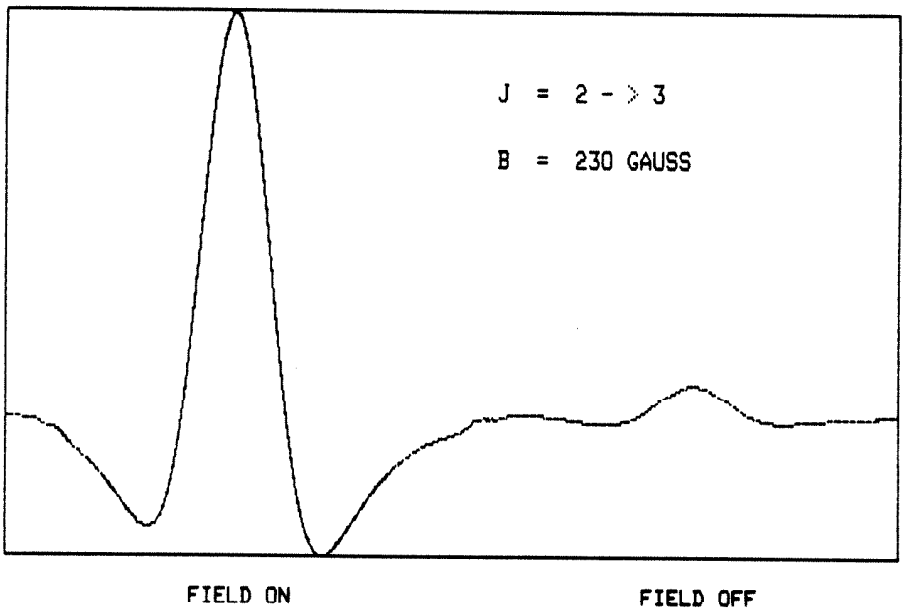

Figure B1.11: Additional enhancement for the HCO^+ ion due to the application of the magnetic field.

1985; Bogey *et al.* 1985) in both the infrared and microwave regions. In all cases an enhancement of roughly two orders of magnitude over observations in conventional glow discharges has been found. This enhancement is strongly dependent on the discharge mode, in that *no enhancement is found in normal glow discharges*. Most of the enhancement in signal-to-noise is due to the increased density of ions in the new cell, but, compared with previous microwave investigations, the larger absorption coefficients at shorter millimeter and submillimeter wavelengths and the absence of plasma discharge noise make substantial contributions as well. Furthermore, since the enhancement is specific to ions, this technique rapidly separates spectra due to ions from those due to neutrals. Figures B1.10 and B1.11 show the enhancement in signal strength due to the magnetic field for the $J = 2 \rightarrow 3$ transitions of NNH^+ and HCO^+ at 279.5 and 267.5 GHz in the 1.5 inch diameter cell. Although recorded digitally for display purposes, both transitions are observable on an oscilloscope with a signal-to-noise of several hundred. Figure B1.12 shows the enhancement of both HCO^+ and HNN^+ as a function of the solenoidal magnetic field. Similar experiments conducted with the 4 inch cell further confirm the picture outlined above. In the absence of the magnetic field, the negative glow was longer and the signals stronger than in the smaller diameter tube, as would be expected because a larger deflection is required to remove the electrons from the cell. As was also expected, the magnetic field enhancement in the 4 inch diameter tube was smaller than in the 1.5 inch cell. Estimates of the peak HCO^+ concentration in both cells are $n_{HCO^+} \gtrsim 10^{11}$ cm^{-3}, corresponding to a fractional abundance of $f(HCO^+) \gtrsim 10^{-4}$.

A simple estimate of the maximum enhancement in ion abundance via magnetic confinement in a low pressure cylindrical region of length L may be made as follows. Assume that a parallel flux of fast electrons N(0) enters the negative glow region of radius R and collides with the ambient neutral gas, whose density

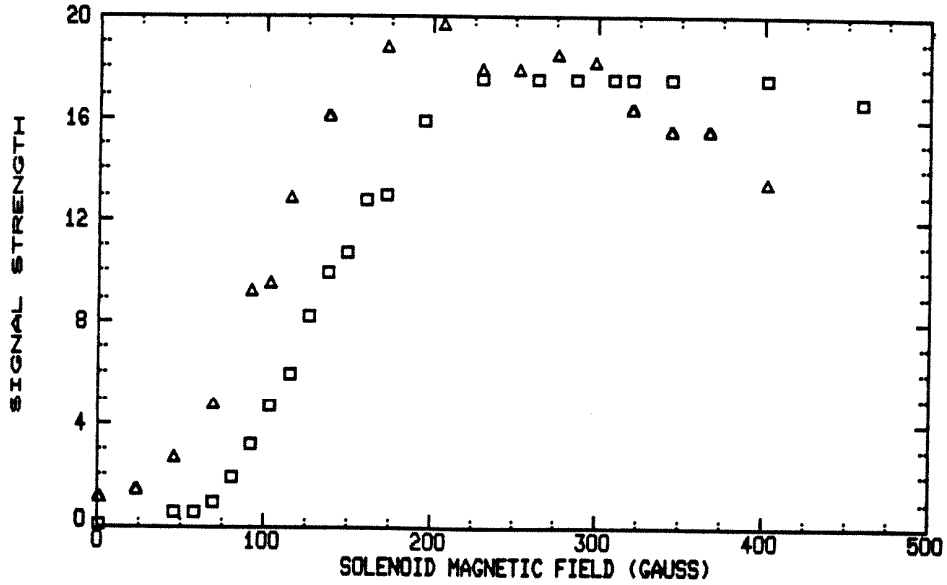

Figure B1.12: Abundance enhancement of both HNN^+ (•) and HCO^+ (Δ) as a function of the magnetic field.

is n mol cm^{-3}. Figure B1.13 illustrates the basic geometry. Assume further that because of the low pressure any collision, be it elastic, inelastic, or ionizing, is sufficient to deflect electrons from the beam and onto the wall, requiring that $\lambda_{mfp}(\text{electron}) > R$. In this limit the flux of fast electrons at x is given by

$$N(x) = N(0)e^{-n\sigma_T x} = N(0)e^{-x/\lambda} \qquad \text{(B1.3)}$$

where $\sigma_T = \sigma_{ion} + \sigma_{el} + \sigma_{inel}$ and $\lambda^{-1} = n\sigma_T$. The total ion production rate Γ (ions produced per area-time) in a length L is then

$$\Gamma = \int_{x=0}^{x=L} \sigma_{ion} n N(x) dx = \int_{x=0}^{x=L} \sigma_{ion} n N(0) e^{-x/\lambda} dx \quad , \qquad \text{(B1.4)}$$

which is simply

$$\Gamma = \sigma_{ion} n N(0)(-\lambda)e^{-x/\lambda}\Big|_0^L = \sigma_{ion} N(0)[1 - e^{-n\sigma_T L}]/\sigma_T \qquad \text{(B1.5)}$$

where σ_{ion} is the reaction cross section for ionization of the gas by fast electrons and σ_T is the total cross section for electron-gas collisions. In the short

length limit ($n\sigma_T L << 1$), we see that $\Gamma = \sigma_{ion} n N(0) L$, which simply reflects that fact that N(0) has not yet begun to decrease significantly. For $n\sigma_T L > 1$, the case applicable here, the total ion production rate is $\Gamma = \sigma_{ion} N(0) / \sigma_T$. Qualitatively, the initial flux of fast electrons is either turned into ions or wall-stuck electrons.

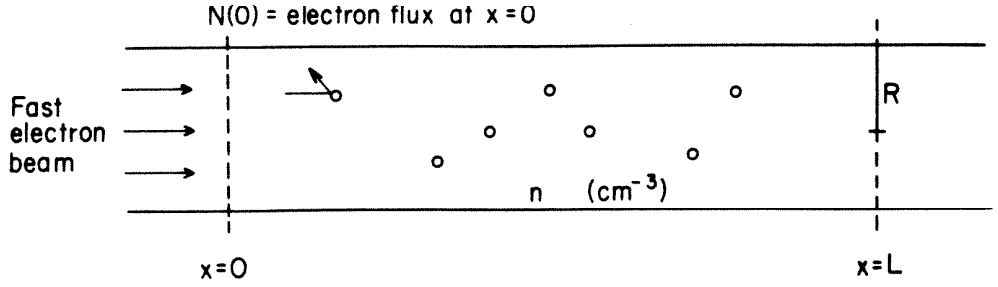

Figure B1.13: Enhancement geometry based on a cylindrical region bombarded by a parallel flux of fast electrons.

Now assume a sufficiently strong longitudinal magnetic field is applied such that *no* electrons can be scattered out of the narrow beam or the area covered by the microwave radiation. If we ignore inelastic collisions and if the cell is sufficiently long, then the high-energy electrons can utilize their entire energy to ionize large numbers of the neutral gas-phase molecules in the microwave radiation interaction region. Since N(x) = N(0) in this limit, the enhanced total ion production rate Γ' is

$$\Gamma' = \int_{x=0}^{x=L} \sigma_{ion} n N(0) dx = \sigma_{ion} n N(0) L \quad , \qquad \text{(B1.6)}$$

where the maximum L is defined such that the energy lost is equal to the initial energy E of the fast electrons. Let E_{ion} be the energy lost per ionizing collision (~30 eV). The energy loss rate in a given volume per electron density (ergs s^{-1}) is then $E_{ion} \sigma_{ion} n v_{elec}$, while the total energy loss Δ is

$$\Delta = \int_{x=0}^{x=L} \frac{dE}{dx} dx = \int_{x=0}^{x=L} E_{ion}\sigma_{ion} n dx = E_{ion}\sigma_{ion} nL. \qquad (B1.7)$$

Setting this equal to the total electron energy E we find that

$$L = \frac{E}{E_{ion}\sigma_{ion} n} \qquad (B1.8)$$

and

$$\Gamma' = N(0)\frac{E}{E_{ion}} . \qquad (B1.9)$$

If the magnetic field does not affect the ion loss processes, then the enhancement in ion signal strength is just Γ/Γ', or

$$\text{Enhancement} = \frac{\Gamma}{\Gamma'} = \frac{E}{E_{ion}} \bullet \frac{\sigma_T}{\sigma_{ion}} . \qquad (B1.10)$$

For "typical" values of $\sigma_T \sim 3\sigma_{ion}$ and $E/E_{ion} \sim 100$ (Von Engel 1955), we see that the expected maximum enhancement is ~300, which is slightly greater than that actually observed. If $\sigma_{ion} \sim 10^{-16}$ cm^2 and $n \sim 10^{15}$ mol cm^{-3} then

$$L = 100/(10^{-16} \bullet 10^{15}) = 10 \text{ meters.}$$

These calculations imply that larger enhancements could be obtained in the new cell if its length were increased from the original value of ~1.5 meters.

B2.1. Rotational Constants and Interstellar Chemistry of HOC^+*

Rest frequencies of the three new HOC^+ transitions measured in this work, with rotational quantum numbers J = 1 → 2, 2 → 3, and 3 → 4, are listed in Table B2.1 along with the rotational constants B_0 and D_0 obtained from a least-squares fit of the data. In order to correct for possible Doppler shifts, the J = 2 → 3 transition was observed with both relative directions of the microwave beam and ion drift velocity by placing the detector at different ends of the cell. Because of the low field nature of the negative glow and the rapid pumping scheme employed, the net direction of the ion flow was opposite to that expected from the electrode polarity. The derived values of B_0 and D_0 predict a frequency of 89,487.387(28) MHz for the J = 0 → 1 transition, in agreement with the value of 89,487.414(15) MHz obtained by Gudeman and Woods (1982). As expected, the centrifugal distortion constant of HOC^+ is substantially larger than that of HCO^+.

Table B2.1
Measured Rotational Transitions of HOC^+ (MHz)

Transition J'' → J'	Observed[a]	Obs. - Calc.[b]
1 → 2	178972.051	0.034
2 → 3	268451.094	-0.038
3 → 4	357921.987	0.012

[a]- Includes shift to cancel Doppler effect caused by ion drift velocity and vacuum pump.
[b]- Fitted constants are B_0 = 44,743.9235(140) MHz and D_0 = 114.89(54) kHz.

Woods *et al.* (1983) have recently observed and tentatively identified a weak emission feature in Sgr B2 as the J = 1 → 0 transition of HOC^+. The near coincidence of a formic acid line with this transition (< 2 MHz) requires that either the J = 3 → 2 or J = 4 → 3 lines at 268.5 or 357.9 GHz be searched for and

*From Blake *et al.* (1983).

detected in order to verify the identification of Woods *et al.* Assuming the correctness of their identification, Woods *et al.* obtain an HCO^+/HOC^+ abundance ratio of 330. Using a model containing approximately 20 ion-molecule reactions they conclude that the large abundance ratio is due primarily to the selective depletion reaction

$$HCO^+ + H \rightarrow HCO^+ + H \quad , \qquad \text{(B2.1)}$$

from which they infer the existence of a significant atomic hydrogen content in dense molecular clouds. The H atom abundance required in this analysis is greater than that of CO, in conflict with the ion-molecule predictions discussed in Chapter 4 (Prasad and Huntress 1980; Leung, Herbst, and Heubner 1984). Basic to the analysis of Woods *et al.* is the assumption that the reaction between CO and H_3^+ produces equal amounts of HCO^+ and HOC^+. While certainly not impossible, this assumption disagrees with the phase space theory of reactive collisions (Light 1967) which predicts the more exothermic pathway ($HCO^+ + H_2$) to be dominant. The phase space theory is supported by recent experimental work on collision-induced dissociation patterns by Illies, Jarrold, and Bowers (1982,1983), which indicates that the reaction between CO and H_3^+ produces between 1 and 11% $HOC^+ + H_2$. Additionally, conditions in the laboratory microwave experiments (traces of CO and H_2 in Ar) were such that reaction (B2.1) is of little significance. If the reaction between CO and H_3^+ did produce equal amounts of HCO^+ and HOC^+, then the abundance ratio in the glow discharge cell should have been on the order of unity. However, simultaneous measurements of the HCO^+/HCO^+ line intensities indicated a ratio of ~50-100 in the magnetic confinement cell. Thus, an HCO^+/HCO^+ ratio of ~50-100 in the interstellar medium can be generated simply by the difference in production rates if the lowest values of Illies, Jarrold, and Bowers are accepted, and the atomic hydrogen abundance in dense molecular clouds need not be as large as

suggested by Woods *et al.*

B2.2. Transition Frequencies and Molecular Constants of CN*

CN has a $^2\Sigma$ ground electronic state with a spin one nucleus, N. Thus, the rotational energy levels are split into doublets by the spin-rotation interaction, each level of which is further split into a triplet by the nuclear magnetic and quadrupole effects. The small fine and hyperfine constants of CN create the energy ordering $E_{rot} >> E_{sr} >> E_{hfs}$, implying that Hund's case $b_{\beta J}$ is the basis in which the rotational Hamiltonian is most nearly diagonal. A proper coupling scheme for this extensively studied case is

$$\vec{N} + \vec{S} = \vec{J} \qquad \text{(B2.2a)}$$

$$\vec{J} + \vec{I} = \vec{F}. \qquad \text{(B2.2b)}$$

The zero-field Hamiltonian may therefore be separated into a sum of pure rotation, spin-rotation, and hyperfine terms (Dixon and Woods 1977)

$$H = H_{rot} + H_{sr} + H_{hfs} \quad , \qquad \text{(B2.3)}$$

where

$$H_{rot} = Y_{01}N(N+1) + Y_{11}(\nu+\tfrac{1}{2})N(N+1) + Y_{21}(\nu+\tfrac{1}{2})^2N(N+1) + Y_{02}N^2(N+1)^2 + Y_{12}(\nu+\tfrac{1}{2})N^2(N+1)^2 \qquad \text{(B2.4)}$$

$$H_{sr} = \gamma_\nu \vec{N} \cdot \vec{S} \qquad \text{(B2.5)}$$

$$H_{hfs} = b_\nu \vec{I} \cdot \vec{S} + c_\nu I_z S_z + \frac{eqQ_\nu}{4} T_0^{(2)}(I) \quad . \qquad \text{(B2.6)}$$

*Adapted from Skatrud *et al.* (1983).

In the above equations, N is the angular momentum of the rotation of the molecular framework, S is the electron spin, and z is the molecular axis. In addition, γ_v is the spin-doubling constant, b_v and c_v are the Frosch and Foley (1952) magnetic hyperfine parameters, and $T_0^{(2)}(I)$ is the molecule-fixed zeroth component of the quadrupole moment tensor. Here we have identified the coefficients of the power series in v and N with the five Dunham constants $Y_{l,m}$ rather than the mechanical constants B_e, α_e, etc. The use of the five Dunham constants instead of the four individual sets of B_v and D_v reduces the number of parameters by three, and is made possible by the extensive set of data obtained. Because the CN ground state is $^2\Sigma$, however, the $Y_{l,m}$ should be viewed as effective constants which may be contaminated by admixtures with other electronic states. The fine structure constant γ_v and the hyperfine constants b_v, c_v, and eqQ_v have been left as functions of the vibrational state. The nuclear spin-rotation term $C_I I \cdot N$ is not included as the constants noted above are sufficient to fit the data to within the experimental uncertainty.

The matrix elements used to model the fine and hyperfine interactions were calculated using a derivation by Dixon and Woods (1977). Because the rotational matrix elements are diagonal in N and are much larger than any other interaction, elements off-diagonal in N can be neglected to an excellent approximation. J blocks in a given N are weakly coupled by the Fermi contact and spin-dipolar hyperfine interactions, but F is still a good quantum number in the zero-field case. Thus, the Hamiltonian factors into, at worst, 2 x 2 F matrices which couple adjacent J blocks. Figure B2.1 outlines the form of the CN Hamiltonian in this limit. Diagonalization of the F blocks produces the energy eigenvalues of the $^2\Sigma$ Hamiltonian H and leads to a non-linear relation between the quantum mechanical operators Θ_i and the molecular constants c_i. A first-order expansion of the true energy levels $E(c_i)$ about an approximate value of c_i, denoted as c_i^o, gives

$$E(c_i) = E(c_i^o) + \sum_i \frac{\partial E}{\partial c_i^o} \delta c_i \ . \qquad \text{(B2.7)}$$

This "linearized" equation is the basis for the least-squares analysis (Cook, De Lucia, and Helminger 1972) in which the initial guesses c_i^o are used to construct the Hamiltonian matrix, and the differences Δ_i between the observed and predicted frequencies generate the linear correction terms δc_i. The new molecular constants are then used to reconstruct the Hamiltonian matrix and the process is repeated until a negligible change in the calculated frequencies results.

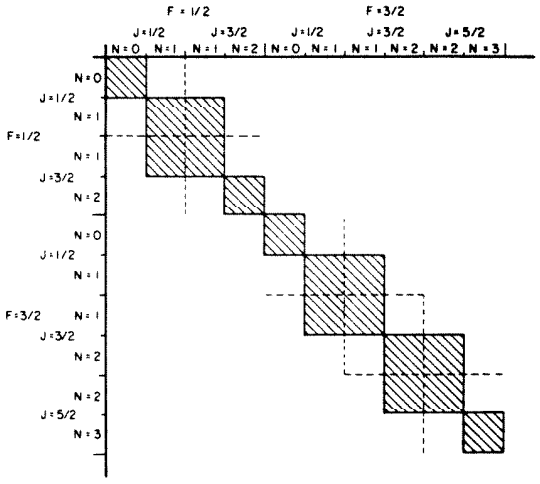

Figure B2.1: Form of the effective CN rotational Hamiltonian assuming that $E_{rot} >> E_{sr} >> E_{hfs}$.

The observed transition frequencies, along with the residuals from the non-linear least-squares fit, are listed in Table B2.2. The 14 ν=0 and ν=1 frequencies of the N = 0 → 1 transition measured by Dixon and Woods have been included in the data set. The variance of the fit is 40 kHz, which is within the experimental uncertainty of the measurements. The ν=3 transitions have been assigned a statistical weight of 1/2 relative to the rest of the data because

Table B2.2
Observed Rotational Frequencies (MHz) for $X^2\Sigma^+$ CN

Transition N J F → N' J' F'	Weight	Observed Frequency	Obs.-Calc.	Transition N J F → N' J' F'	Weight	Observed Frequency	Obs.-Calc.
v=0							
0 1/2 3/2 — 1 1/2 1/2	1	113144.190[a]	0.068	2 5/2 3/2 — 3 5/2 3/2	1	339446.777	-0.002
0 1/2 1/2 — 1 1/2 3/2	1	113170.535[a]	0.033	2 5/2 5/2 — 3 5/2 5/2	1	339475.904	0.009
0 1/2 3/2 — 1 1/2 3/2	1	113191.325[a]	0.038	2 5/2 7/2 — 3 5/2 7/2	1	339516.658	-0.032
0 1/2 1/2 — 1 3/2 3/2	1	113488.142[a]	0.016	2 3/2 5/2 — 3 5/2 5/2	1	340008.097	-0.062
0 1/2 3/2 — 1 3/2 5/2	1	113490.985[a]	0.042	2 3/2 3/2 — 3 5/2 3/2	1	340019.602	-0.023
0 1/2 1/2 — 1 3/2 1/2	1	113499.643[a]	0.014	2 3/2 5/2 — 3 5/2 7/2	1	340031.544	-0.023
0 1/2 3/2 — 1 3/2 3/2	1	113508.934[a]	0.023	2 3/2 1/2 — 3 5/2 3/2	1	340035.408[b]	-0.027
1 3/2 3/2 — 2 3/2 3/2	1	226314.540	-0.012	2 3/2 3/2 — 3 5/2 5/2			
1 3/2 5/2 — 2 3/2 5/2	1	226359.871	-0.016	2 5/2 5/2 — 3 7/2 7/2	1	340247.770[b]	0.001
1 1/2 3/2 — 2 3/2 3/2	1	226632.190	0.014	2 5/2 7/2 — 3 7/2 9/2			
1 1/2 3/2 — 2 3/2 5/2	1	226659.575	0.032	2 5/2 5/2 — 3 7/2 5/2	1	340261.818	0.030
1 1/2 1/2 — 2 3/2 1/2	1	226663.703	0.018	2 5/2 7/2 — 3 7/2 7/2	1	340265.025	0.013
1 1/2 1/2 — 2 3/2 3/2	1	226679.382	0.041	3 5/2 7/2 — 4 7/2 9/2	1	453390.057	0.045
1 3/2 3/2 — 2 5/2 5/2	1	226874.166	-0.017	3 5/2 3/2 — 4 7/2 5/2	1	453391.668[b]	0.018
1 3/2 5/2 — 2 5/2 7/2	1	226874.745	-0.019	3 5/2 5/2 — 4 7/2 7/2			
1 3/2 1/2 — 2 5/2 3/2	1	226875.897	0.001	3 7/2 7/2 — 4 9/2 9/2	1	453606.740[b]	0.029
1 3/2 3/2 — 2 5/2 3/2	1	226887.352	-0.047	3 7/2 9/2 — 4 9/2 11/2			
1 3/2 5/2 — 2 5/2 5/2	1	226892.119	-0.032				
v=1							
0 1/2 3/2 — 1 1/2 1/2	1	112101.674[a]	0.077	1 3/2 1/2 — 2 5/2 3/2	1	224785.301	-0.054
0 1/2 1/2 — 1 1/2 3/2	1	112128.989[a]	-0.008	1 3/2 3/2 — 2 5/2 3/2	1	224796.360	-0.040
0 1/2 3/2 — 1 1/2 3/2	1	112148.510[a]	0.035	1 3/2 5/2 — 2 5/2 5/2	1	224800.896	-0.022
0 1/2 1/2 — 1 3/2 3/2	1	112442.813[a]	0.021	2 3/2 5/2 — 3 5/2 5/2	1	336875.457	-0.056
0 1/2 3/2 — 1 3/2 5/2	1	112445.020[a]	0.028	2 3/2 3/2 — 3 5/2 3/2	1	336886.753	-0.064
0 1/2 1/2 — 1 3/2 1/2	1	112453.891[a]	0.054	2 3/2 5/2 — 3 5/2 7/2	1	336898.488	-0.025
0 1/2 3/2 — 1 3/2 3/2	1	112462.282[a]	0.012	2 3/2 1/2 — 3 5/2 3/2	1	336902.422[b]	0.001
1 3/2 3/2 — 2 3/2 3/2	0.5	224230.333	-0.069	2 3/2 3/2 — 3 5/2 5/2			
1 3/2 5/2 — 2 3/2 5/2	0.5	224274.624	-0.036	2 5/2 5/2 — 3 7/2 7/2	1	337112.397[b]	0.037
1 1/2 3/2 — 2 3/2 3/2	1	224544.192	-0.005	2 5/2 7/2 — 3 7/2 9/2			
1 1/2 3/2 — 2 3/2 5/2	1	224571.192	0.015	2 5/2 5/2 — 3 7/2 5/2	1	337125.917	-0.043
1 1/2 1/2 — 2 3/2 1/2	1	224575.648	0.058	2 5/2 7/2 — 3 7/2 7/2	1	337129.028	-0.049
1 1/2 1/2 — 2 3/2 3/2	1	224591.097	0.022				
v=2							
1 1/2 3/2 — 2 3/2 3/2	0.5	222449.743	0.001	1 3/2 5/2 — 2 5/2 5/2	0.5	222702.996	-0.020
1 1/2 3/2 — 2 3/2 5/2	1	222476.403	0.011	2 3/2 5/2 — 3 5/2 5/2	1	333733.144	0.037
1 1/2 1/2 — 2 3/2 1/2	1	222481.049	-0.014	2 3/2 3/2 — 3 5/2 3/2	1	333744.249	0.013
1 1/2 1/2 — 2 3/2 3/2	0.5	222496.503	0.057	2 3/2 5/2 — 3 5/2 7/2	1	333755.759	0.012
1 3/2 3/2 — 2 5/2 5/2	1	222686.588[b]	0.051	2 3/2 1/2 — 3 5/2 3/2	1	333759.727[b]	0.022
1 3/2 5/2 — 2 5/2 7/2				2 3/2 3/2 — 3 5/2 5/2			
1 3/2 1/2 — 2 5/2 3/2	1	222688.082	0.017	2 5/2 5/2 — 3 7/2 5/2	1	333980.111	0.002
1 3/2 3/2 — 2 5/2 3/2	0.5	222698.742	0.079	2 5/2 7/2 — 3 7/2 7/2	1	333983.194	0.013
v=3							
1 1/2 3/2 — 2 3/2 3/2	0.5	220348.754	0.038	1 3/2 3/2 — 2 5/2 3/2	0.5	220594.476	0.055
1 1/2 3/2 — 2 3/2 5/2	0.5	220375.080	-0.065	1 3/2 5/2 — 2 5/2 5/2	0.5	220598.361	-0.051
1 1/2 1/2 — 2 3/2 1/2	0.5	220380.030	-0.068	2 3/2 5/2 — 3 5/2 7/2	0.5	330603.183	-0.022
1 1/2 1/2 — 2 3/2 3/2	0.5	220395.322	0.084	2 3/2 1/2 — 3 5/2 3/2	0.5	330607.123[b]	-0.065
1 3/2 3/2 — 2 5/2 5/2	0.5	220582.388[b]	-0.102	2 3/2 3/2 — 3 5/2 5/2			
1 3/2 5/2 — 2 5/2 7/2				2 5/2 5/2 — 3 7/2 7/2	0.5	330811.612	0.118
1 3/2 1/2 — 2 5/2 3/2	0.5	220583.953	-0.118	2 5/2 7/2 — 3 7/2 9/2			

[a] Observed transition frequencies from Dixon and Woods (1977).

[b] These unresolved lines were entered into the fit by using the intensity weighted hyperfine splittings predicted by the rest of the data.

these lines had significantly smaller signal-to-noise ratios. Fitting the vibrational states individually gives slightly better fits and lower rms deviations, but the redundancy is much smaller and the better fit may simply be due to the

reduced statistical significance. Table B2.3 presents the derived constants and their uncertainties. In some cases the uncertainties in the constants are slightly larger than those calculated by Dixon and Woods (1977), which is not surprising in that fits of seven data points to six parameters have limited statistical significance. The variation of the fine and hyperfine constants with ν could have been fitted by a "Dunham-type" expansion, but here each vibrational state is fitted individually. Figures B2.2 - B2.5 show a monotonic progression at the 1σ level for all the fine and hyperfine interactions except for the quadrupole coupling constants.

Table B2.3
Spectral Constants of $X^2\Sigma^+$ CN for ν = 0, 1, 2, and 3

	Value (MHz)	σ (MHz)		Value (MHz)	σ (MHz)
Y_{01}	56954.0231	0.0053	γ_2	212.316	0.029
Y_{11}	-520.7118	0.0057	b_2	-32.489	0.042
Y_{21}	-0.8230	0.0013	c_2	60.93	0.11
Y_{02}	-0.19137	0.00021	eqQ_2	-1.010	0.048
Y_{12}	-0.00061	0.00018	γ_3	209.388	0.048
γ_0	217.4993	0.0068	b_3	-31.869	0.066
b_0	-33.987	0.016	c_3	61.18	0.13
c_0	60.390	0.046	eqQ_3	-1.195	0.092
eqQ_0	-1.270	0.039			
γ_1	215.070	0.012			
b_1	-33.185	0.022			
c_1	60.598	0.049			
eqQ_1	-1.170	0.039			

Table B2.4 lists the calculated rest frequencies and relative intensities of the fine and hyperfine transitions of CN in the ν = 0, 1, 2, and 3 states below 500 GHz that are of interest to the astronomical community. The relative intensities were computed from the equation (Cook, De Lucia, and Helminger 1972):

$$\langle N'SJ'IF'|\mu^{(1)}|NSJIF\rangle \propto \left[(2J+1)(2J'+1)(2F+1)(2F'+1)\right]^{\frac{1}{2}} \begin{Bmatrix} N' & J'S \\ J & N1 \end{Bmatrix} \begin{Bmatrix} J'F'I \\ FJ1 \end{Bmatrix} \quad \text{(B2.8)}$$

Table B2.4
Calculated Frequencies (MHz) and Relative Intensities for $X^2\Sigma^+$ CN

N J F --> N' J' F'	INTENSITY	FREQUENCY	FREQUENCY	FREQUENCY	FREQUENCY
		v = 0	v = 1	v = 2	v = 3
0 1/2 1/2 1 1/2 1/2	1.23	113123.337	112082.120	111037.792	109990.246
0 1/2 1/2 1 1/2 3/2	9.88	113170.502	112128.997	111084.496	110036.768
0 1/2 1/2 1 3/2 1/2	9.88	113499.629	112453.837	111404.580	110352.004
0 1/2 1/2 1 3/2 3/2	12.35	113488.126	112442.792	111393.982	110341.654
0 1/2 3/2 1 1/2 1/2	9.88	113144.122	112101.597	111056.059	110007.457
0 1/2 3/2 1 1/2 3/2	12.35	113191.287	112148.475	111102.763	110053.980
0 1/2 3/2 1 3/2 1/2	1.23	113520.414	112473.315	111422.847	110369.215
0 1/2 3/2 1 3/2 3/2	9.88	113508.911	112462.270	111412.249	110358.865
0 1/2 3/2 1 3/2 5/2	33.33	113490.943	112444.992	111395.574	110342.800
1 1/2 1/2 2 3/2 1/2	4.94	226663.685	224575.590	222481.063	220380.098
1 1/2 1/2 2 3/2 3/2	6.17	226679.341	224591.075	222496.446	220395.238
1 1/2 3/2 2 3/2 1/2	0.62	226616.520	224528.713	222434.358	220333.575
1 1/2 3/2 2 3/2 3/2	4.94	226632.176	224544.197	222449.742	220348.716
1 1/2 3/2 2 3/2 5/2	16.67	226659.543	224571.177	222476.392	220375.145
1 3/2 1/2 2 3/2 1/2	0.62	226287.393	224203.873	222114.274	220018.339
1 3/2 1/2 2 3/2 3/2	0.49	226303.049	224219.357	222129.658	220033.480
1 3/2 1/2 2 5/2 3/2	10.00	226875.896	224785.355	222688.065	220584.071
1 3/2 3/2 2 3/2 1/2	0.49	226298.896	224214.918	222124.873	220028.689
1 3/2 3/2 2 3/2 3/2	1.20	226314.552	224230.402	222140.256	220043.830
1 3/2 3/2 2 3/2 5/2	0.53	226341.919	224257.381	222166.906	220070.259
1 3/2 3/2 2 5/2 3/2	3.20	226887.399	224796.400	222698.663	220594.421
1 3/2 3/2 2 5/2 5/2	16.80	226874.183	224783.640	222686.341	220582.346
1 3/2 5/2 2 3/2 3/2	0.53	226332.519	224247.680	222156.931	220059.896
1 3/2 5/2 2 3/2 5/2	2.80	226359.887	224274.660	222183.581	220086.325
1 3/2 5/2 2 5/2 3/2	0.13	226905.366	224813.678	222715.338	220610.486
1 3/2 5/2 2 5/2 5/2	3.20	226892.151	224800.918	222703.016	220598.412
1 3/2 5/2 2 5/2 7/2	26.67	226874.764	224784.090	222686.665	220582.578
2 3/2 1/2 3 5/2 3/2	6.67	340035.281	336902.301	333759.619	330607.125
2 3/2 3/2 3 5/2 3/2	2.13	340019.625	336886.817	333744.236	330591.984
2 3/2 3/2 3 5/2 5/2	11.20	340035.525	336902.492	333759.757	330607.224
2 3/2 5/2 3 5/2 3/2	0.09	339992.258	336859.838	333717.586	330565.555
2 3/2 5/2 3 5/2 5/2	2.13	340008.158	336875.513	333733.107	330580.795
2 3/2 5/2 3 5/2 7/2	17.78	340031.567	336898.513	333755.746	330603.205
2 5/2 3/2 3 5/2 3/2	0.53	339446.779	336320.819	333185.829	330041.393
2 5/2 3/2 3 5/2 5/2	0.10	339462.679	336336.494	333201.350	330056.633
2 5/2 3/2 3 7/2 5/2	12.70	340248.573	337113.200	333967.786	330812.395
2 5/2 5/2 3 5/2 3/2	0.10	339459.994	336333.579	333198.151	330053.468
2 5/2 5/2 3 5/2 5/2	0.75	339475.894	336349.254	333213.672	330068.708
2 5/2 5/2 3 5/2 7/2	0.10	339499.303	336372.255	333236.312	330091.118
2 5/2 5/2 3 7/2 5/2	1.55	340261.788	337125.960	333980.109	330824.470
2 5/2 5/2 3 7/2 7/2	17.49	340247.625	337112.249	333966.830	330811.437
2 5/2 7/2 3 5/2 5/2	0.10	339493.281	336366.082	333230.023	330084.541
2 5/2 7/2 3 5/2 7/2	1.17	339516.690	336389.083	333252.663	330106.952
2 5/2 7/2 3 7/2 5/2	0.03	340279.175	337142.788	333996.460	330840.303
2 5/2 7/2 3 7/2 7/2	1.55	340265.012	337129.077	333983.181	330827.271
2 5/2 7/2 3 7/2 9/2	23.81	340247.874	337112.442	333966.968	330811.537
3 5/2 3/2 4 7/2 5/2	9.52	453391.571	449213.775	445022.978	440819.089
3 5/2 5/2 4 7/2 5/2	1.17	453375.671	449198.101	445007.457	440803.850
3 5/2 5/2 4 7/2 7/2	13.12	453391.708	449213.881	445023.054	440819.144
3 5/2 7/2 4 7/2 5/2	0.02	453352.262	449175.100	444984.817	440781.439
3 5/2 7/2 4 7/2 7/2	1.17	453368.299	449190.881	445000.415	440796.733
3 5/2 7/2 4 7/2 9/2	17.86	453390.011	449212.176	445021.336	440817.422
3 7/2 5/2 4 7/2 5/2	0.36	452589.777	448421.395	444241.021	440048.088
3 7/2 5/2 4 7/2 7/2	0.03	452605.814	448437.176	444256.618	440063.382
3 7/2 5/2 4 9/2 7/2	13.89	453607.236	449427.033	445233.498	441026.699
3 7/2 7/2 4 7/2 5/2	0.03	452603.940	448435.106	444254.300	440061.120
3 7/2 7/2 4 7/2 7/2	0.46	452619.977	448450.887	444269.897	440076.414
3 7/2 7/2 4 7/2 9/2	0.03	452641.689	448472.182	444290.818	440097.103
3 7/2 7/2 4 9/2 7/2	0.91	453621.399	449440.744	445246.777	441039.732
3 7/2 7/2 4 9/2 9/2	17.60	453606.634	449426.429	445232.890	441026.090
3 7/2 9/2 4 7/2 7/2	0.03	452637.115	448467.522	444286.109	440092.149
3 7/2 9/2 4 7/2 9/2	0.63	452658.827	448488.817	444307.030	440112.837
3 7/2 9/2 4 9/2 7/2	0.01	453638.537	449457.379	445262.989	441055.466
3 7/2 9/2 4 9/2 9/2	0.91	453623.772	449443.064	445249.102	441041.824
3 7/2 9/2 4 9/2 11/2	22.22	453606.772	449426.536	445232.967	441026.145

which neglects the slight mixing associated with elements off-diagonal in J.

Using a high resolution FTS between 4000 and 11,000 cm^{-1}, Cerny *et al.* (1978) have published a detailed analysis of the red system of CN in which they observed many lines with very high rotational excitation in several vibrational states, allowing a large set of rotation-vibration constants to be determined. Table B2.5 presents a comparison of the optical and microwave B_ν and γ_ν constants. For both sets of the optically derived constants, it can be seen that differences between vibrational states are calculated much more accurately than the absolute values. The microwave constants are of great precision since they have been determined from a highly accurate and substantially redundant data set.

Table B2.5
Comparison of Microwave and Optical Results on CN

Constant	Microwave(σ) (MHz)	Optical(σ) (MHz)	Difference (MHz)
B_0	56693.461(3)	56693.256(129)	0.205
B_1	56171.110(5)	56170.910(132)	0.200
B_2	55647.106(5)	55646.905(132)	0.201
B_3	55121.435(15)	55121.183(141)	0.252
γ_0	217.500(5)	222.36(99)	-4.86
γ_1	215.071(12)	220.86(99)	-5.79
γ_2	212.332(18)	218.01(138)	-5.68
γ_3	209.386(57)	215.55(135)	-6.16

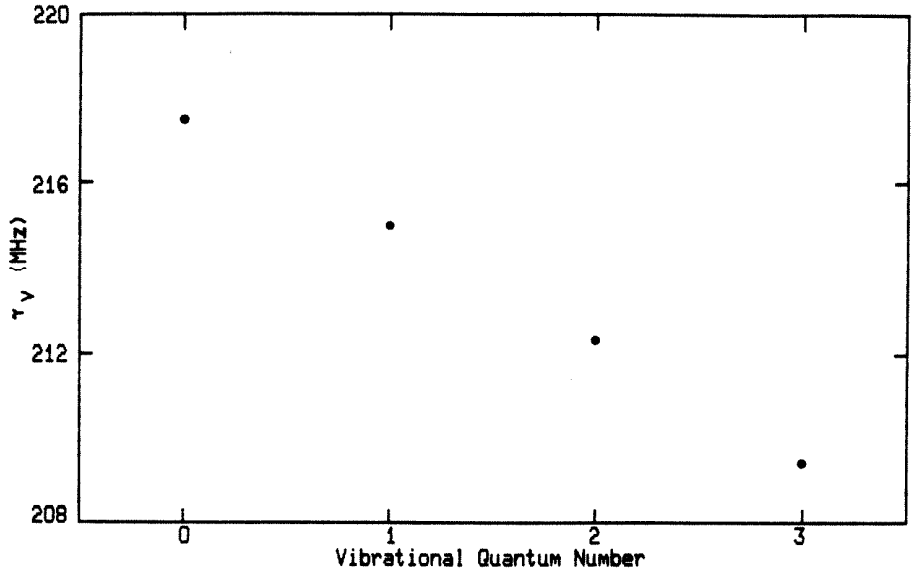

Figure B2.2: The spin-rotation constant γ_v as a function of vibrational state. The error bars are too small to show on this figure.

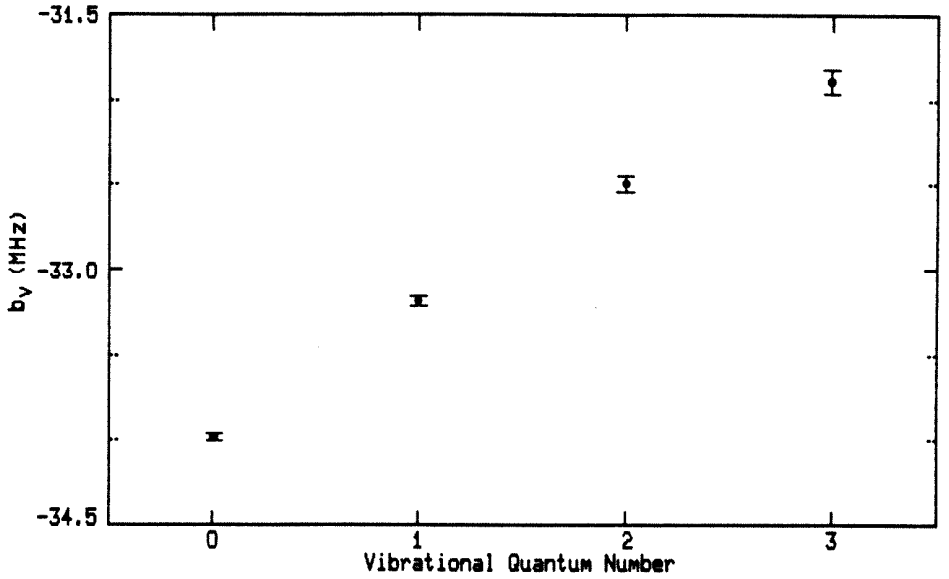

Figure B2.3: The magnetic coupling constant b_v as a function of vibrational state. The error bars shown are 1σ.

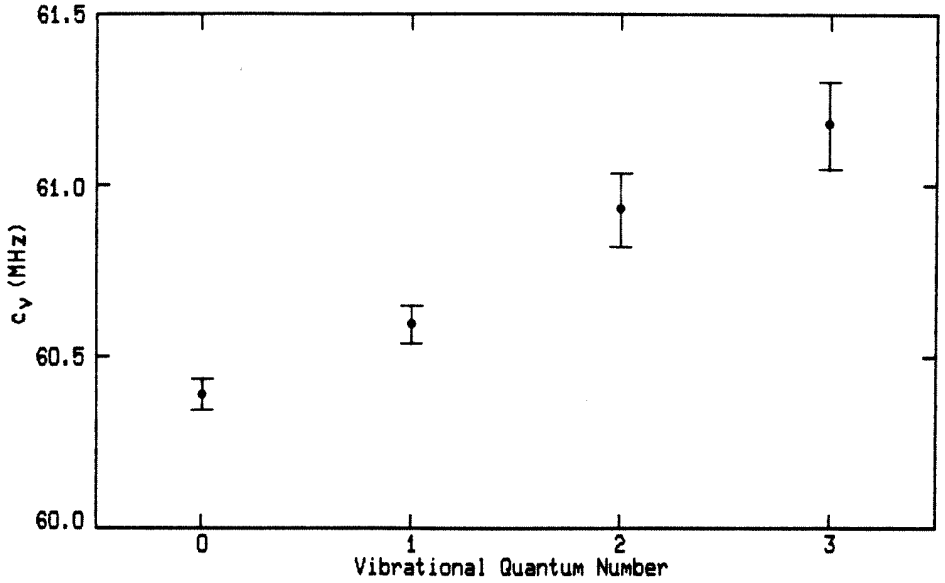

Figure B2.4: The magnetic coupling constant c_v as a function of vibrational state. The error bars shown are 1σ.

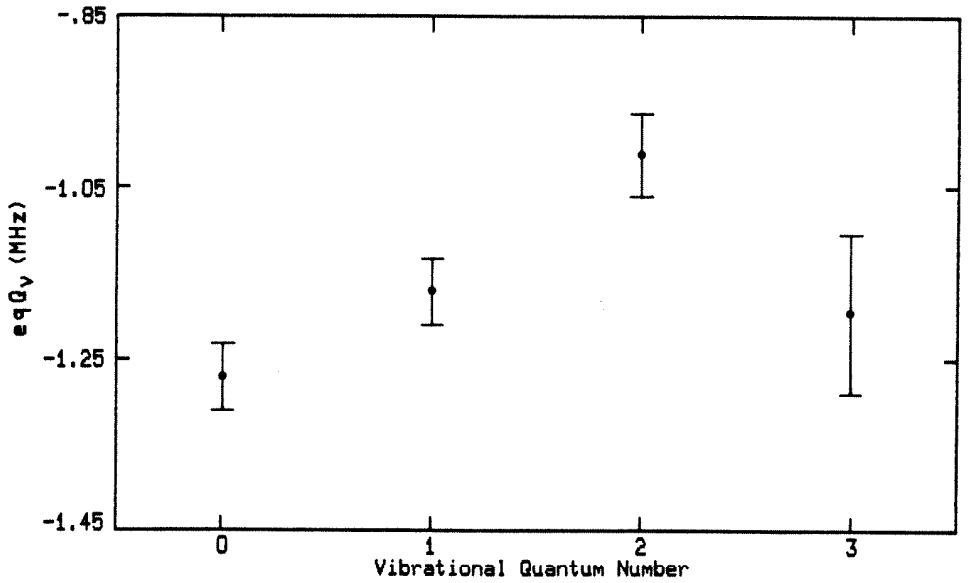

Figure B2.5: The electric quadrupole coupling constant eqQ_v as a function of vibrational state. The error bars shown are 1σ.

B2.3. Transition Frequencies and Molecular Constants of HCO*

HCO is a light, nearly prolate asymmetric rotor with one unpaired electron and one non-zero nuclear spin, and is therefore somewhat similar to CN theoretically. Thus, a coupling scheme appropriate for a discussion of its rotational spectrum is

$$\vec{N} + \vec{S} = \vec{J} \qquad \text{(B2.9a)}$$

$$\vec{J} + \vec{I} = \vec{F}, \qquad \text{(B2.9b)}$$

where N is the rotational angular momentum of the molecular framework, S is the electron spin, and I is the nuclear spin of the hydrogen nucleus. Each rotational level $N_{K_pK_o}$ is split into a doublet by the spin-rotation interaction, the levels of which are further split into doublets by the magnetic hyperfine interactions, with the final levels being characterized by the quantum numbers $F = J \pm 1/2$. The effective zero-field Hamiltonian may be split into the terms (Bowater, Brown, and Carrington 1972)

$$H_{eff} = H_{rot} + H_{cd} + H_{sr} + H_{srcd} + H_{hfs} \quad , \qquad \text{(B2.10)}$$

where H_{rot} is the rigid asymmetric rotor Hamiltonian, H_{cd} corrects for the rotational distortion effects absent in H_{rot}, H_{sr} describes the electron spin-rotation interaction, H_{srcd} contains the centrifugal distortion corrections to H_{sr}, and H_{hfs} is the magnetic hyperfine coupling between the unpaired electron and the hydrogen nucleus.

As HCO has been studied by several high-resolution techniques (ESR, LMR, centimeter microwave spectroscopy, etc.), the terms in the above Hamiltonian have been studied by a number of authors. Its spectrum is also similar to that

*As appeared in Blake *et al.* (1984).

of the HO_2 free radical and this analysis closely follows that of HO_2 by Charo and De Lucia (1982). However, as noted below, there are some significant differences. Watson's A-reduced Hamiltonian has been used for H_{rot} and H_{cd}, as in the previous extensive studies of light, singlet asymmetric rotors at the Duke University Microwave Facility (De Lucia *et al.* 1971). The A and S reduced Hamiltonians for H_{sr} and H_{srcd} have been presented by Brown and Sears (1979), who show that only four, not five, quadratic spin-rotation parameters are determinable for molecules with a single plane of symmetry. For consistency with the choice of H_{rot} and H_{cd}, the A-reduced forms of H_{sr} and H_{srcd} must be used. In the principle axis system of the molecule, H_{sr} may be written as

$$H_{sr} = \frac{1}{2}\sum_{\alpha,\beta}\varepsilon_{\alpha\beta}(N_\alpha S_\beta + S_\beta N_\alpha) \quad . \tag{B2.11}$$

Explicit forms of the matrix elements of the effective spin-rotation Hamiltonian have been given by Raynes (1964) and Bowater, Brown, and Carrington (1972). In our analysis of HCO, we have found it necessary to add an additional term to H_{srcd}. Earlier work on HO_2 and NO_2 (Bowman and De Lucia 1982) had shown that only terms through K^4 were necessary. However, we have found that for HCO, an additional term of the form

$$\langle NKSJ|H^{(6)}_{srcd}|NKSJ\rangle = H^s_K\left[\frac{J(J+1) - N(N+1) - S(S+1)}{2N(N+1)}\right]K^6$$

is required.

The magnetic hyperfine Hamiltonian H_{hfs} is simply

$$H_{hfs} = a_H\vec{S}\cdot\vec{I} + \vec{S}\cdot\underset{\approx}{T}\cdot\vec{I} \quad , \tag{B2.12}$$

where the first term depicts the isotropic Fermi contact interaction between the electron and proton spins, while the second term arises from the anisotropic

dipolar coupling of these spins.

The coupling scheme of eqs. (B2.9) determines the basis in which the effective Hamiltonian is most nearly diagonal. In the absence of external fields, F is a constant of the motion and therefore no matrix elements off-diagonal in F are present. Thus, a direct approach in which the Hamiltonian matrix is assembled into blocks with a common value of F, and then diagonalized, could be used. Unfortunately, this approach requires the diagonalization of many matrices with large dimension (~100 x 100). Symmetry principles and approximation methods are therefore employed.

In the HO_2 analysis of Charo and De Lucia (1982), the hyperfine Hamiltonian could be separated from the total Hamiltonian and treated by perturbation theory because

$$E_{rot} \gtrsim E_{sr} \gg E_{hfs} . \qquad \text{(B2.13)}$$

After removing the small hyperfine contributions to the observed transition frequencies, calculation of the asymmetric rotor energy levels including the spin-rotation was then based on the diagonalization of the Hamiltonian $H_o = H_{eff} - H_{hfs}$, which is diagonal in J. The eigenvector matrix from this analysis was used to rotate H_{hfs} into the asymmetric rotor basis, wherein the matrix elements of H_{hfs} were calculated to determine the final energy levels. This procedure neglects hyperfine matrix elements off-diagonal in J, which could be handled via second-order perturbation theory when necessary (e.g., elements diagonal in N and K for K = 0). In HCO, however, the interactions are such that

$$E_{rot} \gg E_{sr} \gtrsim E_{hfs} , \qquad \text{(B2.14)}$$

and it is difficult to completely separate the hyperfine structure from the total Hamiltonian via perturbation theory. Energy levels with the same value of N and

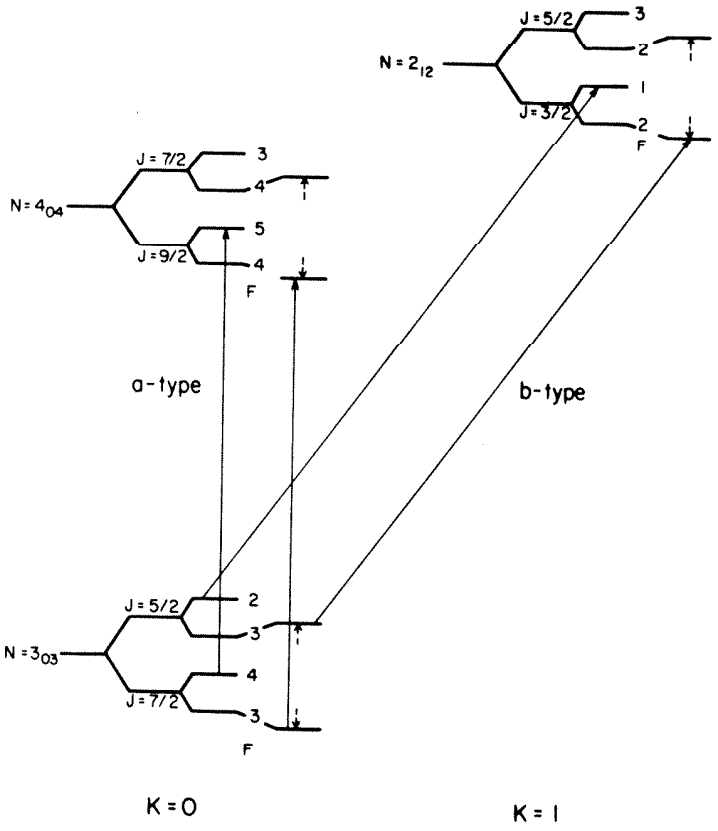

Figure B2.6: Illustration of the effects of the hyperfine perturbations for the $N_{K_pK_o} = 3_{03}$ rotational level of HCO.

F are coupled and perturbed by magnetic hyperfine elements off-diagonal in J, the perturbation being proportional to

$$\frac{(\text{ hyperfine matrix element })^2}{\Delta E} \qquad \text{(B2.15)}$$

in the second-order approximation, where ΔE is the separation of the energy levels. The large value of a_H and the small value of ΔE in HCO create large perturbations and render second-order theory inadequate. Figure B2.6 illustrates the effects of the hyperfine perturbation on the energy levels of and transitions from the $N_{K_pK_o} = 3_{03}$ rotational level. As is clear from the figure, in a-type transitions the perturbed energy levels move in the same direction and thus to some extent cancel each other, while for $K_p = 0 \rightarrow 1$ b-type transitions the perturbations add - creating large shifts of up to 150 MHz. Fortunately, of the four

strongly allowed transitions between the fine and hyperfine components of the rotational levels, only two are affected by the large hyperfine perturbations, as Figure B2.6 shows. The other two transitions may be treated in an analogous manner to the HO_2 study, and it is this set of data that has been used to calculate the rotation/spin-rotation constants of HCO.

After the hyperfine structure is removed, the remaining J blocks of H_o have dimensions of $4J+2 \times 4J+2$. In order to reduce the problem further, a modified Wang transformation, appropriate for doublet states, is applied to H_o as suggested by Raynes (1964). This judicious use of symmetry ideally reduces each J block into a set of four submatrices of dimension $J+1/2$. However, for molecules like HCO and HO_2 which lack C_{2v} symmetry, $\varepsilon_{ab} + \varepsilon_{ba} \neq 0$, and the matrix elements of this part of H_{sr} couple the four submatrices. Perturbation theory is used to include this small effect, with corrections applied to the transition frequencies arising from ε_{ab} inserted before the non-linear least-squares analysis. As Brown and Sears (1979) have noted, the values of ε_{ab} and ε_{ba} are not independent. Therefore, only the matrix elements of ε_{ab} were included in the Hamiltonian.

Figure B2.7 shows an energy level diagram of the HCO free radical and the transitions studied in this work, which are listed in Table B2.6. The large zero-field data set acquired has allowed the complex spectrum of this light asymmetric rotor with unpaired electronic spin and magnetic hyperfine structure to be completely analyzed to within experimental accuracy (<0.1 MHz) for the first time. In all cases, the nuclear hyperfine splittings are easily resolved. As discussed above, the hyperfine splittings and the rotation/spin-rotation structure of the molecule are analyzed separately. First, the observed hyperfine splittings were used to calculate the hyperfine constants a_H, T_{bb}, and T_{cc} in a weighted least-squares fit. At higher values of N, it is possible for imprecise knowledge

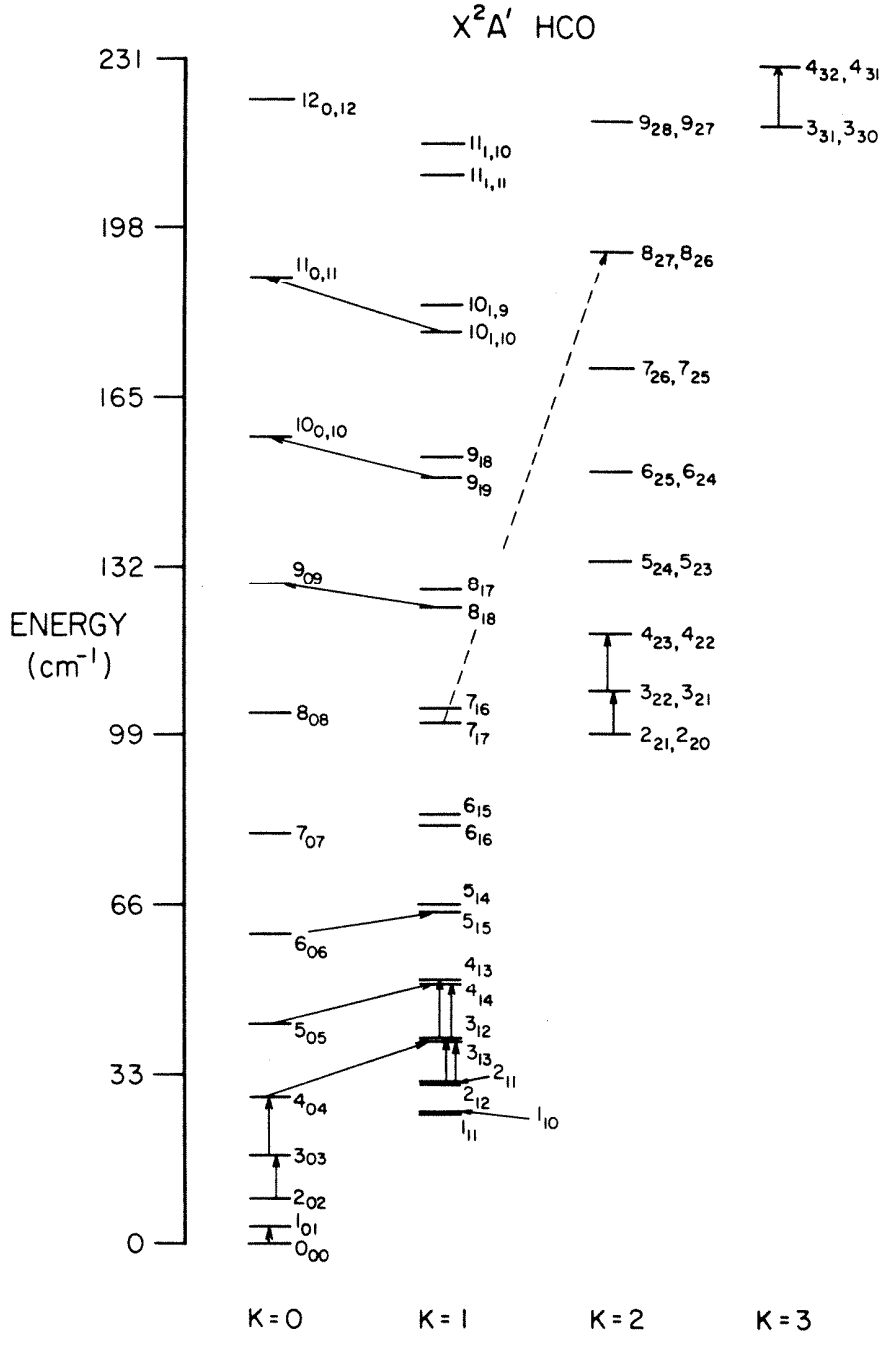

Figure B2.7: Energy level diagram of HCO from the constants of this work, excluding the fine and hyperfine splittings. Solid arrows mark the transitions observed.

(from the rotation/spin-rotation fit) of the energy denominator of eq. (B2.15) to perturb this calculation. This problem can be eliminated by fitting for the sum of the observed hyperfine splittings in each of the $8_{18} \rightarrow 9_{09}$, $9_{19} \rightarrow 10_{0,10}$, and $10_{1,10} \rightarrow 11_{0,11}$ rotational transitions. Such a procedure cancels any errors that might arise from this source and the 42 measured hyperfine splittings are reduced to 39 independent data points. The constants calculated from the hyperfine analysis are shown in Table B2.8. The rms deviation of the data points taken from Table B2.6 is ~100 kHz. There is some evidence that this could be reduced further by the inclusion of distortion terms into the hyperfine Hamiltonian, but the small size of these effects would not seem to justify it at present.

The results of this analysis were then used to calculate theoretical line frequencies from which the hyperfine contributions had been eliminated. Table B2.7 shows these frequencies and Table B2.8 presents the spectral constants that resulted from the combined rotation/spin-rotation and hyperfine fits. The variance of the rotation/spin-rotation fit is ~50 kHz. We do not directly fit for A, B, C, ε_{aa}, ε_{bb}, and ε_{cc}, but rather linear combinations of these constants. Table B2.9 presents the fitted linear combinations used and their numerical values from which the six rotation/spin-rotation constants listed above are calculated. Good statistical redundancy for the calculation of the constants was obtained from the large data set acquired and the results are generally insensitive to the details of the data set or to reasonable selections of terms to be retained in the Hamiltonian.

In addition to our new millimeter and submillimeter observations, we have also included in our weighted analysis the previous microwave data and the LMR measurement of Cook *et al.* (1976) of the $7_{17} \rightarrow 8_{26}$ transition. This latter data point is necessary to allow the independent calculation of A and Δ_K. As a result, the values of these constants depend upon this measurement, while the

Table B2.6
Observed Transition Frequencies (MHz) of X^2A HCO

Transition	J	F	Observed Frequency	Transition	J	F	Observed Frequency
3_{03}←2_{02}	7/2←5/2	4←3	260060.329	4_{22}←3_{21}	7/2←5/2	4←3	348864.210
		3←2	260082.192			3←2	348870.264
3_{03}←2_{02}	5/2←3/2	3←2	260133.586	4_{23}←3_{22}	9/2←7/2	5←4	345655.582
		2←1	260155.769			4←3	345663.584
3_{13}←2_{12}	7/2←5/2	4←3	255341.122	4_{23}←3_{22}	7/2←5/2	4←3	348778.174
		3←2	255358.430			3←2	348784.214
3_{13}←2_{12}	5/2←3/2	3←2	256875.347	4_3←3_3	9/2←7/2	5←4	344177.558
		2←1	256892.171			4←3	344186.067
3_{12}←2_{11}	7/2←5/2	4←3	263911.659	4_3←3_3	7/2←5/2	4←3	351482.848
		3←2	263927.215			3←2	351485.316
3_{12}←2_{11}	5/2←3/2	3←2	265334.325	3_{13}←4_{04}	5/2←7/2	3←4	328009.806
		2←1	265348.661			2←3	328085.568
3_{21}←2_{20}	7/2←5/2	4←3	258202.056	3_{13}←4_{04}	7/2←9/2	4←5	331180.457
		3←2	258216.096			3←4	331259.705
3_{21}←2_{20}	5/2←3/2	3←2	264343.220	4_{14}←5_{05}	7/2←9/2	4←5	236286.654
		2←1	264350.121			3←4	236363.280
3_{22}←2_{21}	7/2←5/2	4←3	258166.583	4_{14}←5_{05}	9/2←11/2	5←6	238668.347
		3←2	258180.460			4←5	238748.777
3_{22}←2_{21}	5/2←3/2	3←2	264309.081	5_{15}←6_{06}	9/2←11/2	5←6	143080.025
		2←1	264316.003			4←5	143161.676
4_{04}←3_{03}	9/2←7/2	5←4	346708.493	5_{15}←6_{06}	11/2←13/2	6←7	144956.679
		4←3	346725.172			5←6	145042.054
4_{04}←3_{03}	7/2←5/2	4←3	346787.898	9_{09}←8_{18}	17/2←15/2	9←8	143985.560
		3←2	346804.597			5←6	144138.270
4_{14}←3_{13}	9/2←7/2	5←4	340798.216	9_{09}←8_{18}	19/2←17/2	10←9	143191.199
		4←3	340812.078			9←8	143340.336
4_{14}←3_{13}	7/2←5/2	4←3	341671.586	$10_{0,10}$←9_{19}	19/2←17/2	10←9	242117.059
		3←2	341685.256			9←8	242181.559
4_{13}←3_{12}	9/2←7/2	5←4	352204.257	$10_{0,10}$←9_{19}	21/2←19/2	11←10	241420.880
		4←3	352214.661			10←9	241481.891
4_{13}←3_{12}	7/2←5/2	4←3	352967.885	$11_{0,11}$←$10_{1,10}$	21/2←19/2	11←10	341210.057
		3←2	352978.060			10←9	341242.607
4_{22}←3_{21}	9/2←7/2	5←4	345743.972	$11_{0,11}$←$10_{1,10}$	23/2←21/2	12←11	340634.955
		4←3	345752.037			11←10	340664.020

Table 2.7
Hyperfine Corrected Transition Frequencies (MHz) of X^2A HCO

Transition	J	Frequency Used in Analysis	Observed -Calculated	Transition	J	Frequency Used in Analysis	Observed -Calculated
1_{01}←0_{00}	3/2←1/2	86671.38	0.09	4_{13}←3_{12}	9/2←7/2	352204.34	0.02
1_{01}←0_{00}	1/2←1/2	86811.35	-0.24	4_{13}←3_{12}	7/2←5/2	352978.17	0.11
1_{10}←1_{11}	1/2←1/2	2726.05	-0.20	4_{22}←3_{21}	9/2←7/2	345744.32	-0.01
1_{10}←1_{11}	3/2←3/2	2890.89	0.07	4_{22}←3_{21}	7/2←5/2	348870.95	-0.01
2_{11}←2_{12}	3/2←3/2	8343.73	1.01	4_{23}←3_{22}	9/2←7/2	345655.92	0.00
2_{11}←2_{12}	5/2←5/2	8623.22	-0.46	4_{23}←3_{22}	7/2←5/2	348784.87	-0.07
3_{12}←3_{13}	5/2←5/2	16801.01	0.97	4_3←3_3	9/2←7/2	344178.34	0.01
3_{12}←3_{13}	7/2←7/2	17194.99	0.92	4_3←3_3	7/2←5/2	351487.85	0.01
3_{03}←2_{02}	7/2←5/2	260060.47	-0.04	3_{13}←4_{04}	5/2←7/2	328086.99	0.01
3_{03}←2_{02}	5/2←3/2	260155.22	-0.04	3_{13}←4_{04}	7/2←9/2	331180.90	-0.03
3_{13}←2_{12}	7/2←5/2	255341.47	0.04	4_{14}←5_{05}	7/2←9/2	236364.60	0.00
3_{13}←2_{12}	5/2←3/2	256891.86	0.04	4_{14}←5_{05}	9/2←11/2	238668.93	0.00
3_{12}←2_{11}	7/2←5/2	263911.82	0.00	5_{15}←6_{06}	9/2←11/2	143162.93	-0.01
3_{12}←2_{11}	5/2←3/2	265349.13	-0.03	5_{15}←6_{06}	11/2←13/2	144957.34	0.06
3_{21}←2_{20}	7/2←5/2	258202.77	-0.03	9_{09}←8_{18}	17/2←15/2	144137.16	0.01
3_{21}←2_{20}	5/2←3/2	264353.37	-0.04	9_{09}←8_{18}	19/2←17/2	143190.45	0.04
3_{22}←2_{21}	7/2←5/2	258167.30	0.00	$10_{0,10}$←9_{19}	19/2←17/2	242180.49	-0.02
3_{22}←2_{21}	5/2←3/2	264319.26	0.05	$10_{0,10}$←9_{19}	21/2←19/2	241420.12	-0.01
4_{04}←3_{03}	9/2←7/2	346708.58	-0.05	$11_{0,11}$←$10_{0,10}$	21/2←19/2	341241.57	0.00
4_{04}←3_{03}	7/2←5/2	346804.37	-0.01	$11_{0,11}$←$10_{0,10}$	23/2←21/2	340634.19	0.00
4_{14}←3_{13}	9/2←7/2	340798.42	0.02	8_{26}←7_{17}	15/2←13/2	2777038.60	0.00
4_{14}←3_{13}	7/2←5/2	341685.04	0.02				

Table B2.8
Zero-field Molecular Constants of X^2A HCO obtained in this work

Parameter	Value(σ) (MHz)	Parameter	Value(σ) (MHz)
A	729366.331[a]	ε_{aa}	11633.879[a]
B	44787.895[a]	ε_{bb}	19.032[a]
C	41930.640[a]	ε_{cc}	-206.096[a]
Δ_N	0.11815(17)	ε_{ab}	201.0(10)
Δ_{NK}	0.4553(16)	Δ_N^s	0.0021(5)
Δ_K	920.36(15)	Δ_{NK}^s	-0.186(17)
δ_N	0.01190(4)	Δ_K^s	-52.93(16)
δ_K	4.59(15)	H_K^s	0.504(14)
H_{KN}	-0.01302(16)		
a_H	388.89(12)	T_{bb}	2.57(13)
T_{aa}	11.19[b]	T_{cc}	-13.76(13)

[a]These parameters are calculated from Table B2.9.
[b]Calculated from T_{bb} and T_{cc} ($T_{aa} + T_{bb} + T_{cc} = 0$).

statistical uncertainty in A and Δ_K depend upon its reported uncertainty (2 MHz).

A comparison of the derived constants with those previously published is complicated by several factors. In large multiparameter fits such as those required for HCO, the correlation among the constants is significant and the contribution of higher-order constants to transition frequencies of even low N transitions is important. Thus, lower-order constants that were derived (Bowater, Brown, and Carrington 1971; Austin *et al.* 1974; Boland, Brown, and Carrington 1977; Boland *et al.* 1978) from the few previously available microwave data points are, in fact, complicated combinations of constants. In recognition of this problem, attempts were made to calculate several of the higher-order constants from other sources of information such as force fields or optical data. Unfortunately, some of the constrained constants are wrong not only in magnitude, but in some cases even in sign. As a result, some very significant

differences exist between earlier results and the constants of Table B2.8. Recently, Brown, Sears, and Radford (Brown 1982) have analyzed an extensive new set of FIR LMR data, with the resulting constants listed in Brown, Dumper, and Lowe (1983). Although their results are generally similar to ours, there remain a few differences.

Table B2.9
Fitted Linear Combinations of the
Rotation/Spin-Rotation constants listed in Table B2.8

Parameter	Value(σ) (MHz)
A - 1/2(B + C)	686007.063(160)
1/2(B + C)	43359.268(8)
1/2(B - C)	1428.628(580)
$-1/3(\varepsilon_{aa} + \varepsilon_{bb} + \varepsilon_{cc})$	-3815.605(19)
$-1/6(2\varepsilon_{aa} - \varepsilon_{bb} - \varepsilon_{cc})$	-3909.137(16)
$1/2(\varepsilon_{bb} - \varepsilon_{cc})$	112.564(4)

The inclusion of the new spin-rotation centrifugal distortion term H_K^s is important to the fit. It reduces the rms deviation of the fit by approximately an order of magnitude and makes significant contributions to the spin splittings of the higher K states. It might be concluded that HCO would not require higher-order spin-rotation centrifugal distortion terms because ε_{aa} for HCO is smaller than ε_{aa} for HO_2. However, this conclusion does not take into account that HCO undergoes substantially more bending distortion than does HO_2. This can be seen by comparing the relative sizes of Δ_K for HO_2 (~123 MHz) and HCO (~920 MHz). A careful inspection of the residuals in the earlier HO_2 analysis reveals a small, but systematic with K splitting error. Presumably, the H_K^s is in fact required, but to a lesser degree for HO_2.

B2.4. The Rotation-Distortion and Internal Rotation Constants of $HCOOCH_3$*

As a result of the recently completed spectral line surveys such as the one presented in this thesis, it has become increasingly evident that certain interstellar molecules are responsible for an inordinate share of the observed interstellar millimeter and submillimeter emission lines. For example, in the spectral scan of Orion from 72.2-91.1 GHz by Johansson *et al.* (1984), of a total of 170 lines 32 were assigned to methyl formate ($HCOOCH_3$) alone. It was therefore expected that methyl formate should contribute substantially to the line count in the OVRO spectral line survey as well. However, the assignment of spectral emission lines at these higher frequencies is more difficult because of a paucity of laboratory data even for basic stable molecules. As part of the long-term program at the Duke University Microwave Facility of measuring the near millimeter-wave spectra (100 GHz - 1 THz) of important interstellar molecules, we present here the laboratory millimeter and submillimeter spectrum of methyl formate in its ground (ν_t=0) symmetric (A) and antisymmetric (E) torsional states. Over 300 lines have been measured in the frequency range between 140 and 550 GHz involving transitions up to a rotational quantum number of J=50. Using these lines and some previous data at lower frequencies, we have determined the rotation-distortion and internal rotation constants of methyl formate in its (ν_t=0) A and E torsional states to a high degree of accuracy. These constants have been used in turn to predict the frequencies of ~20,000 lines of methyl formate in the range 1-600 GHz. This work has resulted in the assignment of over 250 new transitions in Orion to methyl formate, transitions that were initially ***unidentified*** (c.f. Appendix A).

Prior to this work, the rotational spectrum of methyl formate had been studied at lower frequencies by several investigators. Curl (1959) measured 29

*Adapted and condensed from Plummer *et al.* (1984).

lines at frequencies in the range 8-30 GHz and determined the molecular structure via isotopic studies, while Bauder (1979) measured 200 lines at frequencies up to 58 GHz and predicted the frequencies of many other lines with rotational quantum numbers of $J \lesssim 12$. More recently, DeMaison *et al.* (1983) have measured and assigned more than 100 new lines of methyl formate, principally in the region between 220-240 GHz. These authors did not include predictions of the frequencies of unmeasured transitions.

Previous laboratory studies have involved transitions of both the A (symmetric) and E (degenerate,antisymmetric) sublevels of the ground (ν_t=0) torsional state of methyl formate. This molecule undergoes internal rotation and must, in general, be analyzed by theories that explicitly take account of the internal rotation, or torsional, motion (Lin and Swalen 1959). The use of such theories for transitions involving high rotational quantum numbers can result in difficulty in fitting the spectra (DeMaison *et al.* 1983). We have found that even high J transitions belonging to the symmetric (A) sublevel of the ground (ν_t=0) torsional state can be fitted to within experimental accuracy ($\lesssim$0.1 MHz) by a theory based solely on a semirigid asymmetric top Hamiltonian of a type used previously (Cook, De Lucia, and Helminger 1972). We have therefore fitted the A and E symmetry states separately, with only the E state lines requiring a theory that explicitly accounts for the internal rotation. Our measured frequencies are presented in Table B2.10, the final column of which lists the residual from the standard asymmetric rotor analysis described below. We note that the deviations for the E sublevel can be quite large ($\Delta\nu \gtrsim 25$ MHz), even for states with low J and K.

TABLE B2.10

TRANSITIONS USED IN THE ANALYSIS [a]

A Sublevel

ASSIGNMENT	FREQUENCY	RESIDUAL
1(0, 1) - 0(0, 0)	12219.209	0.008
1(1, 1) - 0(0, 0)	25290.161	-0.020
1(1, 0) - 1(0, 1)	14681.231	0.008
2(0, 2) - 1(1, 1)	11227.499	0.009
2(0, 2) - 1(0, 1)	24298.476	0.006
2(1, 1) - 1(1, 0)	26048.515	-0.004
2(1, 1) - 2(0, 2)	16431.284	0.011
3(0, 3) - 2(0, 2)	36104.845	0.057
3(0, 3) - 2(1, 2)	24504.165	0.013
3(1, 3) - 2(0, 2)	45758.761	0.050
3(2, 1) - 3(1, 2)	37580.838	0.017
3(2, 2) - 3(1, 3)	46542.205	0.015
4(0, 4) - 3(0, 3)	47536.992	0.070
4(1, 4) - 3(1, 3)	45397.442	0.063
4(1, 3) - 3(2, 2)	14903.145	0.018
4(2, 3) - 3(2, 2)	48767.021	0.031
4(2, 2) - 3(2, 1)	50105.020	-0.025
4(3, 2) - 3(3, 1)	49134.704	0.075
5(1, 5) - 4(1, 4)	56531.706	-0.014
6(1, 5) - 5(2, 4)	46580.275	0.020
6(2, 4) - 5(3, 3)	10718.577	0.007
6(1, 5) - 6(0, 6)	36949.301	0.013
6(2, 4) - 6(1, 5)	34682.823	0.019
7(3, 4) - 6(4, 3)	8910.032	0.021
8(2, 6) - 7(3, 5)	44202.823	0.011
9(3, 7) - 8(4, 4)	14012.303	0.013
9(3, 6) - 9(2, 7)	54821.929	0.096
10(3, 7) - 10(2, 8)	52964.135	-0.016
11(2, 9) - 11(2, 10)	52800.900	0.020
12(3, 9) - 12(3, 10)	24649.431	0.010
13(0, 13) - 12(0, 12)	142817.018	0.008
13(0, 13) - 12(1, 12)	142626.196	-0.040
13(1, 12) - 12(2, 11)	149074.288	0.008
13(1, 12) - 12(1, 11)	153518.691	0.001
13(1, 13) - 12(1, 12)	142735.136	0.007
13(1, 13) - 12(0, 12)	142925.860	-0.043
13(2, 12) - 12(2, 11)	151956.555	-0.036
13(2, 11) - 12(2, 10)	164968.621	0.016
13(2, 12) - 12(1, 11)	156400.954	-0.047
13(3, 10) - 12(3, 9)	168513.715	0.002
13(3, 11) - 12(3, 10)	158704.356	-0.016
13(4, 9) - 12(4, 8)	164223.789	-0.006
13(4, 10) - 12(4, 9)	161273.350	0.013
13(5, 9) - 12(5, 8)	161152.436	-0.030
13(5, 8) - 12(5, 7)	161458.193	0.002
13(6, 8) - 12(6, 7)	160585.792	-0.041
13(6, 7) - 12(6, 6)	160601.972	-0.046

13(7, 6) - 12(7, 5)	160193.480	0.103
13(7, 7) - 12(7, 6)	160192.962	0.103
13(8, 5) - 12(8, 4)	159942.878	-0.058
13(9, 4) - 12(9, 3)	159777.031	-0.022
13(10, 3) - 12(10, 2)	159662.732	-0.010
13(11, 2) - 12(11, 1)	159582.068	0.001
13(11, 2) - 12(10, 3)	450044.224	-0.006
13(3, 10) - 13(2, 11)	57537.987	-0.050
14(11, 3) - 13(10, 4)	462303.149	-0.040
14(4, 10) - 14(4, 11)	11216.260	0.000
16(10, 6) - 15(9, 7)	459109.849	0.123
16(4, 12) - 16(4, 13)	25759.832	0.005
17(0, 17) - 16(0, 16)	185178.113	-0.019
17(0, 17) - 16(1, 16)	185158.974	0.040
17(1, 17) - 16(1, 16)	185169.547	-0.005
17(1, 16) - 16(1, 15)	195145.560	0.014
17(1, 17) - 16(0, 16)	185188.775	0.026
17(1, 16) - 16(2, 15)	194458.741	-0.005
17(2, 16) - 16(2, 15)	194871.012	0.049
17(2, 16) - 16(1, 15)	195557.798	0.034
17(9, 8) - 16(8, 9)	443498.306	0.027
17(10, 7) - 16(9, 8)	471308.597	-0.057
17(11, 6) - 16(10, 7)	499024.121	-0.019
17(17, 0) - 17(16, 1)	455836.181	-0.094
18(0, 18) - 17(0, 17)	195774.604	-0.022
18(0, 18) - 17(1, 17)	195764.006	-0.002
18(1, 18) - 17(1, 17)	195769.849	0.000
18(1, 18) - 17(0, 17)	195780.465	-0.001
18(4, 14) - 18(4, 15)	48120.276	-0.011
18(17, 1) - 18(16, 2)	455799.028	-0.046
20(0, 20) - 19(0, 19)	216967.334	0.000
20(1, 20) - 19(1, 19)	216965.991	0.112
20(1, 19) - 19(1, 18)	226778.745	0.029
20(2, 18) - 19(2, 17)	237305.972	-0.009
20(2, 19) - 19(2, 18)	226718.688	-0.011
20(8, 12) - 19(7, 13)	451310.227	0.003
20(5, 15) - 20(5, 16)	25530.745	0.011
20(17, 3) - 20(16, 4)	455695.443	0.120
21(1, 20) - 20(1, 19)	237350.386	0.000
21(1, 20) - 20(2, 19)	237266.791	-0.119
21(2, 19) - 20(2, 18)	247665.359	0.002
21(2, 20) - 20(2, 19)	237315.082	-0.010
21(2, 20) - 20(1, 19)	237398.579	0.011
21(2, 19) - 20(3, 18)	246038.887	0.025
21(3, 19) - 20(3, 18)	247053.453	-0.006
21(3, 19) - 20(2, 18)	248679.964	0.010
21(3, 18) - 20(3, 17)	260255.080	-0.044
21(4, 17) - 20(4, 16)	271544.733	-0.017
21(4, 18) - 20(4, 17)	255789.405	0.001
21(5, 16) - 20(5, 15)	271532.798	-0.005
21(5, 17) - 20(5, 16)	261165.400	-0.005
21(6, 15) - 20(6, 14)	265024.759	-0.045
21(6, 16) - 20(6, 15)	262340.541	0.017
21(7, 14) - 20(7, 13)	261746.580	0.011
21(7, 15) - 20(7, 14)	261433.707	-0.040
21(8, 14) - 20(8, 13)	260392.731	-0.002

21(8, 13) - 20(8, 12)	260415.333	0.011
21(8, 14) - 20(7, 13)	462730.286	0.061
21(9, 13) - 20(9, 12)	259646.531	-0.013
21(9, 12) - 20(9, 11)	259647.705	0.027
21(10, 11) - 20(10, 10)	259128.128	-0.039
21(17, 4) - 21(16, 5)	455626.380	0.045
22(7, 15) - 21(6, 16)	447746.972	-0.041
22(17, 5) - 22(16, 6)	455544.297	0.094
23(7, 16) - 22(6, 17)	460826.503	-0.157
23(17, 6) - 23(16, 7)	455447.479	-0.068
24(17, 7) - 24(16, 8)	455334.891	-0.022
25(7, 19) - 24(6, 18)	459572.246	0.019
25(8, 18) - 24(7, 17)	505916.944	0.082
26(17, 9) - 26(16, 10)	455055.613	0.051
27(16, 12) - 26(16, 11)	332113.370	0.079
27(17, 11) - 26(17, 10)	331943.363	0.048
27(18, 10) - 26(18, 9)	331809.715	0.028
27(20, 8) - 26(20, 7)	331625.030	-0.007
27(21, 7) - 26(21, 6)	331564.665	-0.033
27(23, 5) - 26(23, 4)	331492.007	-0.080
27(24, 4) - 26(24, 3)	331475.285	-0.081
27(26, 2) - 26(26, 1)	331473.023	0.063
27(17, 10) - 27(16, 11)	454885.594	0.007
28(3, 25) - 27(4, 24)	330653.474	0.072
28(4, 24) - 27(4, 23)	343443.944	-0.031
28(5, 24) - 27(5, 23)	340754.756	0.024
28(6, 23) - 27(6, 22)	348065.967	0.030
28(8, 21) - 27(8, 20)	350457.580	-0.001
28(10, 18) - 27(10, 17)	347628.388	-0.136
28(10, 19) - 27(10, 18)	347617.010	0.006
28(12, 17) - 27(12, 16)	345985.352	-0.016
28(13, 16) - 27(13, 15)	345466.941	-0.019
28(15, 14) - 27(15, 13)	344759.053	-0.010
28(17, 12) - 27(17, 11)	344322.969	0.051
28(19, 10) - 27(19, 9)	344051.340	0.034
28(20, 9) - 27(20, 8)	343958.362	0.017
28(21, 8) - 27(21, 7)	343887.467	0.007
28(22, 7) - 27(22, 6)	343835.114	-0.039
28(23, 6) - 27(23, 5)	343798.647	-0.019
28(25, 4) - 27(25, 3)	343764.760	0.000
28(26, 3) - 27(26, 2)	343764.139	0.080
28(27, 2) - 27(27, 1)	343772.431	-0.057
28(17, 11) - 28(16, 12)	454693.127	0.013
29(3, 26) - 28(4, 25)	341421.330	-0.016
29(7, 22) - 28(7, 21)	373164.421	0.059
29(11, 19) - 28(11, 18)	359350.585	-0.032
29(11, 18) - 28(11, 17)	359351.992	-0.025
30(1, 29) - 29(1, 28)	332576.219	0.064
30(3, 27) - 29(4, 26)	352103.280	0.078
30(7, 24) - 29(7, 23)	375741.624	-0.025
30(7, 23) - 29(7, 22)	387882.419	0.029
30(8, 23) - 29(8, 22)	376305.084	0.031
30(8, 22) - 29(8, 21)	379600.540	-0.026
30(9, 22) - 29(9, 21)	374814.976	0.023
30(9, 21) - 29(9, 20)	375267.572	-0.051
30(15, 16) - 29(15, 15)	369659.289	0.024

30(20, 11) - 29(20, 10)	368641.467	0.029
30(22, 9) - 29(22, 8)	368474.435	0.023
30(24, 7) - 29(24, 6)	368384.176	0.023
30(17, 13) - 30(16, 14)	454233.208	-0.091
31(3, 28) - 30(4, 27)	362730.846	-0.012
31(7, 25) - 30(7, 24)	387817.112	0.023
31(7, 24) - 30(7, 23)	402331.899	0.033
31(8, 24) - 30(8, 23)	389140.636	0.012
31(9, 23) - 30(9, 22)	387814.167	-0.056
31(9, 22) - 30(9, 21)	388565.703	-0.043
31(15, 17) - 30(15, 16)	382130.687	-0.008
32(1, 31) - 31(1, 30)	353728.559	-0.079
32(3, 29) - 31(4, 28)	373324.941	0.023
32(7, 26) - 31(7, 25)	399681.086	-0.029
32(7, 25) - 31(7, 24)	416322.224	0.063
32(8, 25) - 31(8, 24)	401873.811	0.033
32(8, 24) - 31(8, 23)	408605.464	0.008
32(9, 24) - 31(9, 23)	400830.187	0.101
32(9, 23) - 31(9, 22)	402042.551	0.026
32(10, 23) - 31(10, 22)	399049.495	0.001
32(10, 22) - 31(10, 21)	399184.848	0.012
32(13, 20) - 31(13, 19)	395710.562	-0.047
32(14, 19) - 31(14, 18)	395096.242	0.121
32(15, 18) - 31(15, 17)	394617.027	-0.068
32(15, 18) - 31(15, 17)	394617.047	-0.048
32(16, 17) - 31(16, 16)	394238.675	-0.001
32(17, 16) - 31(17, 15)	393937.152	0.026
33(1, 32) - 32(1, 31)	364302.395	-0.040
33(7, 27) - 32(7, 26)	411329.888	-0.036
33(7, 26) - 32(7, 25)	429712.109	0.050
33(15, 19) - 32(15, 18)	407119.055	0.000
34(1, 33) - 33(1, 32)	374874.404	-0.075
34(3, 31) - 33(4, 30)	394459.449	0.023
34(7, 28) - 33(7, 27)	422768.630	0.008
34(7, 27) - 33(7, 26)	442410.058	-0.043
35(0, 35) - 34(0, 34)	375759.233	-0.142
35(1, 34) - 34(1, 33)	385444.566	-0.119
35(3, 32) - 34(4, 31)	405012.755	-0.075
35(7, 29) - 34(7, 28)	434010.321	-0.002
35(7, 28) - 34(7, 27)	454366.413	-0.048
36(4, 33) - 35(3, 32)	415584.281	0.003
37(13, 25) - 36(13, 24)	459067.443	0.032
37(13, 24) - 36(13, 23)	459068.819	0.067
38(1, 37) - 37(1, 36)	417143.531	0.004
38(4, 34) - 37(4, 33)	446660.246	-0.004
38(4, 34) - 37(5, 33)	446570.383	-0.013
38(5, 33) - 37(6, 32)	456093.589	-0.034
38(5, 34) - 37(5, 33)	446624.930	0.032
38(5, 33) - 37(5, 32)	457227.937	-0.034
38(5, 34) - 37(4, 33)	446714.760	0.007
38(7, 31) - 37(7, 30)	485987.991	-0.030
38(8, 30) - 37(8, 29)	494831.422	0.004
38(9, 29) - 37(9, 28)	488623.148	-0.078
38(10, 28) - 37(10, 27)	479741.528	-0.019
38(11, 27) - 37(11, 26)	475513.076	0.041
38(13, 26) - 37(13, 25)	471825.707	-0.004

38(13, 25) -	37(13, 24)	471828.274	-0.028
38(14, 24) -	37(14, 23)	470731.236	-0.044
38(15, 23) -	37(15, 22)	469884.976	0.011
38(16, 22) -	37(16, 21)	469217.917	-0.045
38(18, 20) -	37(18, 19)	468254.283	-0.017
38(20, 18) -	37(20, 17)	467619.972	0.015
38(22, 16) -	37(22, 15)	467199.889	-0.005
38(23, 15) -	37(23, 14)	467048.387	0.024
38(24, 14) -	37(24, 13)	466927.888	0.002
38(25, 13) -	37(25, 12)	466834.018	0.013
38(27, 11) -	37(27, 10)	466712.258	-0.018
39(1, 38) -	38(1, 37)	427705.706	0.061
39(3, 36) -	38(3, 35)	447194.934	-0.031
39(4, 36) -	38(4, 35)	447193.730	-0.031
39(4, 35) -	38(4, 34)	457161.410	0.055
39(5, 35) -	38(5, 34)	457139.786	0.060
39(5, 35) -	38(4, 34)	457194.209	-0.020
40(1, 39) -	39(1, 38)	438265.646	0.078
40(1, 40) -	39(1, 39)	428602.606	0.038
40(2, 38) -	39(2, 37)	447960.966	0.041
40(3, 37) -	39(3, 36)	457733.711	-0.058
40(4, 37) -	39(4, 36)	457733.009	-0.059
40(4, 36) -	39(5, 35)	467634.574	-0.013
40(15, 26) -	40(14, 27)	391152.863	-0.062
40(15, 25) -	40(14, 26)	391151.801	0.080
41(1, 41) -	40(1, 40)	439164.751	0.014
41(1, 40) -	40(1, 39)	448823.285	0.052
42(1, 42) -	41(1, 41)	449724.631	0.010
42(1, 41) -	41(1, 40)	459378.636	0.060
42(15, 28) -	42(14, 29)	388860.702	0.077
42(15, 27) -	42(14, 28)	388855.980	-0.091
43(1, 43) -	42(1, 42)	460282.127	-0.035
43(1, 42) -	42(1, 41)	469931.601	0.066
43(15, 29) -	43(14, 30)	387562.388	0.125
43(15, 28) -	43(14, 29)	387553.659	-0.012
44(1, 44) -	43(1, 43)	470837.367	0.060
44(16, 29) -	43(16, 28)	544773.793	-0.021
44(17, 28) -	43(17, 27)	543901.481	0.043
44(18, 27) -	43(18, 26)	543198.000	0.022
44(15, 30) -	44(14, 31)	386152.257	-0.062
44(15, 29) -	44(14, 30)	386136.414	-0.003
45(15, 31) -	45(14, 32)	384622.631	-0.015
45(15, 30) -	45(14, 31)	384593.773	0.014
46(15, 31) -	46(14, 32)	382913.278	0.032
47(4, 43) -	46(4, 42)	541246.458	-0.034
47(15, 33) -	47(14, 34)	381170.128	-0.062
48(15, 34) -	48(14, 35)	379230.572	-0.079
49(2, 47) -	48(2, 46)	542832.304	0.124
49(15, 35) -	49(14, 36)	377138.813	-0.087
49(15, 34) -	49(14, 35)	376875.248	0.077
50(1, 49) -	49(1, 48)	543730.288	-0.160
50(15, 36) -	50(14, 37)	374889.539	-0.009
50(15, 35) -	50(14, 36)	374450.171	0.060

TABLE B2.10 - continued

E Sublevel

TRANSITION	FREQUENCY	PERTURBATION
1(1 0)- 1(1 1)	1610.906	1.76
1(0 1)- 0(0 0)	12218.155	-0.02
1(1 0)- 1(0 1)	14676.764	0.88
1(1 1)- 0(0 0)	25284.035	-0.88
2(0 2)- 1(0 1)	24296.523	-0.03
2(1 2)- 1(1 1)	22827.767	0.58
2(1 1)- 1(1 0)	26044.834	-0.56
2(1 1)- 2(0 2)	16425.070	0.34
2(1 2)- 1(0 1)	35893.643	-0.29
2(0 2)- 1(1 1)	11230.657	0.84
3(1 2) 3(1 3)	9647.158	0.32
3(0 3)- 2(0 2)	36102.287	0.03
3(1 3)- 2(1 2)	34156.907	0.16
3(1 2)- 2(1 1)	38976.132	-0.10
3(2 2)- 2(2 1)	36678.594	24.10
3(2 1)- 2(2 0)	37182.133	-24.05
3(1 2)- 3(0 3)	19298.933	0.23
3(2 2)- 3(1 3)	46517.293	-7.44
3(2 1)- 3(1 2)	37576.548	7.32
3(1 3)- 2(0 2)	45754.045	-0.08
3(0 3)- 2(1 2)	24505.103	0.22
4(1 3)- 4(1 4)	16037.314	0.19
4(0 4)- 3(0 3)	47534.170	0.03
4(1 4)- 3(1 3)	45395.830	0.08
4(2 3)- 3(2 2)	48768.242	5.05
4(2 2)- 3(2 1)	50094.974	-4.99
4(3 2)- 3(3 1)	49151.779	21.02
4(3 1)- 3(3 0)	49155.218	-20.96
4(1 3)- 4(0 4)	23550.758	0.15
4(2 3)- 4(1 4)	49889.745	-2.44
4(2 2)- 4(1 3)	35885.475	2.32
4(1 4)- 3(0 3)	55047.553	-0.06
4(0 4)- 3(1 3)	37882.362	0.09
4(1 3)- 3(2 2)	14915.870	7.73
5(1 4)- 5(1 5)	23923.885	0.08
5(1 5)- 4(1 4)	56529.919	0.04
5(1 4)- 5(0 5)	29401.529	0.08
5(2 4)- 5(1 5)	54140.188	-0.99
5(0 5)- 4(1 4)	51052.202	-0.04
6(1 5)- 6(1 6)	33164.244	-0.05
6(2 4)- 6(2 5)	8570.747	1.08
6(1 5)- 6(0 6)	36927.862	-0.01
6(2 4)- 6(1 5)	34671.762	0.53
6(1 5)- 5(2 4)	46579.827	1.08
7(1 6)- 7(1 7)	43528.061	-0.12
7(2 5)- 7(2 6)	14267.298	0.62
7(1 6)- 7(0 7)	45989.383	-0.06
7(2 5)- 7(1 6)	35974.324	0.39
8(2 6)- 8(2 7)	21663.139	0.37

8(2 6)- 8(1 7)	38958.634	0.28
8(3 5)- 8(2 6)	57612.663	2.56
9(2 7)- 9(2 8)	30670.575	0.20
9(2 7)- 9(1 8)	43829.185	0.18
9(3 6)- 9(2 7)	54810.958	1.10
10(3 7)- 10(3 8)	10466.111	1.47
10(2 8)- 10(1 9)	50674.718	0.07
10(3 7)- 10(2 8)	52952.379	0.67
11(2 9)- 11(2 10)	52761.823	-0.05
11(3 8)- 11(3 9)	16618.312	0.86
11(3 8)- 11(2 9)	52543.396	0.45
11(9 3)- 11(8 4)	235025.830	-10.80
12(3 9)- 12(3 10)	24625.169	0.53
12(3 9)- 12(2 10)	53974.704	0.34
12(9 4)- 12(8 5)	234898.990	-10.62
13(0 13)- 12(0 12)	142815.471	0.03
13(1 12)- 12(1 11)	153512.698	0.01
13(2 11)- 12(2 10)	164955.675	-0.07
13(3 11)- 12(3 10)	158693.673	0.05
13(3 10)- 12(3 9)	168495.015	-0.16
13(9 5)- 12(9 4)	159782.762	7.89
13(9 4)- 12(9 3)	159766.825	-8.04
13(10 4)- 12(10 3)	159670.865	7.95
13(10 3)- 12(10 2)	159654.876	-8.03
13(11 3)- 12(11 2)	159592.303	7.74
13(11 2)- 12(11 1)	159576.651	-7.92
13(9 5)- 13(8 6)	234735.650	-10.43
13(0 13)- 12(1 12)	142624.476	0.02
13(1 12)- 12(2 11)	149065.244	0.01
14(9 6)- 14(8 7)	234529.390	-10.21
15(9 7)- 15(8 8)	234273.120	-10.01
16(9 8)- 16(8 9)	233959.010	-9.93
17(0 17)- 16(0 16)	185176.804	0.00
17(1 17)- 16(1 16)	185168.224	0.01
17(1 16)- 16(1 15)	195139.867	0.02
17(2 16)- 16(2 15)	194864.970	0.02
17(9 9)- 17(8 10)	233578.520	-10.09
17(1 17)- 16(0 16)	185187.425	-0.02
17(0 17)- 16(1 16)	185157.596	0.03
18(0 18)- 17(0 17)	195773.352	-0.01
18(1 18)- 17(1 17)	195768.588	0.01
18(9 10)- 18(8 11)	233122.160	-10.82
18(1 18)- 17(0 17)	195779.165	-0.05
18(0 18)- 17(1 17)	195762.736	0.01
19(4 16)- 18(4 15)	233212.750	0.06
19(5 15)- 18(5 14)	236743.680	0.39
19(6 14)- 18(6 13)	236800.520	5.35
19(6 13)- 18(6 12)	237807.630	-5.27
19(7 13)- 18(7 12)	235865.870	33.22
19(7 12)- 18(7 11)	235887.180	-33.14
19(8 11)- 18(8 10)	235029.940	-13.13

19(9 10)- 18(9 9)	234486.410	-11.21
19(10 10)- 18(10 9)	234134.600	11.11
19(10 9)- 18(10 8)	234112.330	-11.16
19(11 9)- 18(11 8)	233867.110	10.90
19(11 8)- 18(11 7)	233845.250	-10.96
19(12 8)- 18(12 7)	233670.980	10.52
19(12 7)- 18(12 6)	233649.880	-10.58
19(13 7)- 18(13 6)	233524.630	9.80
19(13 6)- 18(13 5)	233504.980	-9.85
19(14 6)- 18(14 5)	233414.430	8.85
19(14 5)- 18(14 4)	233396.680	-8.90
19(15 5)- 18(15 4)	233331.210	7.70
19(15 4)- 18(15 3)	233315.780	-7.73
19(16 4)- 18(16 3)	233268.590	6.29
19(16 3)- 18(16 2)	233256.010	-6.29
19(17 3)- 18(17 2)	233222.180	4.75
19(9 11)- 19(8 12)	232579.430	-12.79
19(3 17)- 18(2 16)	229590.410	0.01
20(1 19)- 19(1 18)	226773.130	0.00
20(2 19)- 19(2 18)	226713.060	0.05
20(2 18)- 19(2 17)	237297.470	0.03
20(3 18)- 19(3 17)	236355.930	0.05
20(8 13)- 19(8 12)	247704.319	16.20
20(8 12)- 19(8 11)	247682.629	-16.23
20(9 12)- 19(9 11)	247063.622	11.75
20(9 11)- 19(9 10)	247040.576	-11.78
20(10 11)- 19(10 10)	246623.194	11.60
20(10 10)- 19(10 9)	246600.002	-11.61
20(11 10)- 19(11 9)	246308.227	11.41
20(11 9)- 19(11 8)	246285.337	-11.48
20(12 9)- 19(12 8)	246076.790	10.93
20(12 8)- 19(12 7)	246054.817	-11.04
20(13 8)- 19(13 7)	245903.677	10.25
20(13 7)- 19(13 6)	245883.099	-10.33
20(15 6)- 19(15 5)	245672.976	8.06
20(15 5)- 19(15 4)	245656.779	-8.14
20(16 5)- 19(16 4)	245597.303	6.66
20(16 4)- 19(16 3)	245583.971	-6.67
20(18 2)- 19(18 1)	245491.773	-3.27
20(19 2)- 19(19 1)	245468.455	1.39
20(19 1)- 19(19 0)	245465.669	-1.39
20(9 12)- 20(8 13)	231938.660	-17.32
20(9 11)- 20(8 12)	231955.220	17.55
20(2 19)- 19(1 18)	226856.820	0.02
20(1 19)- 19(2 18)	226629.350	0.02
20(3 18)- 19(2 17)	238926.800	-0.01
20(2 18)- 19(3 17)	234726.530	0.02
21(1 20)- 20(1 19)	237344.870	0.02
21(2 20)- 20(2 19)	237309.540	0.05
21(3 19)- 20(3 18)	247044.076	0.01
21(3 18)- 20(3 17)	260244.445	0.04

21(4 18)- 20(4 17)	255776.104	0.02
21(4 17)- 20(4 16)	271524.688	-0.02
21(5 17)- 20(5 16)	261148.864	0.11
21(5 16)- 20(5 15)	271505.883	-0.01
21(6 16)- 20(6 15)	262324.850	1.12
21(6 15)- 20(6 14)	265002.610	-1.00
21(7 15)- 20(7 14)	261436.730	16.78
21(7 14)- 20(7 13)	261715.481	-16.70
21(8 14)- 20(8 13)	260404.025	21.17
21(8 13)- 20(8 12)	260384.280	-21.12
21(9 13)- 20(9 12)	259653.011	12.45
21(9 12)- 20(9 11)	259629.241	-12.45
21(10 12)- 20(10 11)	259137.933	12.01
21(10 11)- 20(10 10)	259113.912	-12.06
21(11 11)- 20(11 10)	258769.903	11.82
21(11 10)- 20(11 9)	258746.199	-11.89
21(12 10)- 20(12 9)	258499.283	11.39
21(12 9)- 20(12 8)	258476.446	-11.45
21(13 9)- 20(13 8)	258296.299	10.67
21(13 8)- 20(13 7)	258274.949	-10.68
21(14 8)- 20(14 7)	258142.087	9.68
21(14 7)- 20(14 6)	258122.658	-9.75
21(15 7)- 20(15 6)	258024.239	8.55
21(15 6)- 20(15 5)	258007.148	-8.54
21(16 6)- 20(16 5)	257933.832	7.00
21(16 5)- 20(16 4)	257919.889	-6.94
21(17 5)- 20(17 4)	257865.087	5.35
21(17 4)- 20(17 3)	257854.460	-5.28
21(18 4)- 20(18 3)	257813.513	3.53
21(18 3)- 20(18 2)	257806.542	-3.44
21(19 3)- 20(19 2)	257775.827	1.54
21(19 2)- 20(19 1)	257772.702	-1.58
21(9 13)- 21(8 14)	231187.690	-26.00
21(9 12)- 21(8 13)	231200.140	26.18
21(0 21)- 20(1 20)	227559.930	-0.04
21(2 20)- 20(1 19)	237393.190	0.03
21(1 20)- 20(2 19)	237261.200	0.02
22(9 14)- 22(8 15)	230315.800	-39.40
22(9 13)- 22(8 14)	230312.310	39.58
23(9 15)- 23(8 16)	229318.630	-53.18
25(1 24)- 25(0 25)	230435.730	-0.10
25(2 24)- 25(1 25)	230440.760	-0.03
26(1 25)- 26(0 26)	240162.780	0.04
26(2 25)- 26(1 26)	240165.610	0.08
27(2 25)- 27(1 26)	231511.030	-2.43
28(2 26)- 28(2 27)	241334.840	0.09
28(1 27)- 27(1 26)	311412.050	-0.82
28(2 27)- 27(2 26)	311412.700	0.53
28(8 21)- 27(8 20)	350442.250	0.48
28(8 20)- 27(8 19)	351823.454	-0.21
28(9 20)- 27(9 19)	348909.476	5.71

28(9 19)- 27(9 18)	349048.536	-5.61
28(10 19)- 27(10 18)	347628.342	17.66
28(10 18)- 27(10 17)	347604.557	-17.63
28(11 18)- 27(11 17)	346687.487	14.16
28(11 17)- 27(11 16)	346659.820	-14.17
28(12 17)- 27(12 16)	346001.628	13.51
28(12 16)- 27(12 15)	345974.609	-13.54
28(13 16)- 27(13 15)	345486.430	12.61
28(13 15)- 27(13 14)	345460.973	-12.85
28(14 15)- 27(14 14)	345091.462	11.82
28(14 14)- 27(14 13)	345067.730	-11.91
28(15 14)- 27(15 13)	344783.579	10.50
28(15 13)- 27(15 12)	344762.571	-10.51
28(16 13)- 27(16 12)	344541.294	8.94
28(16 12)- 27(16 11)	344523.488	-8.87
28(17 12)- 27(17 11)	344349.455	7.11
28(17 11)- 27(17 10)	344335.302	-7.04
28(18 11)- 27(18 10)	344197.310	5.08
28(18 10)- 27(18 9)	344187.205	-5.02
28(19 10)- 27(19 9)	344076.904	2.82
28(19 9)- 27(19 8)	344071.156	-2.92
28(2 26)- 28(1 27)	241335.670	0.04
29(0 29)- 28(0 28)	312283.830	0.18
29(3 26)- 29(2 27)	230936.320	-0.04
29(4 26)- 29(3 27)	231232.050	-0.05

a Transitions below 100 GHz taken from Bauder (1979). All frequencies in MHz.

The data for the symmetric (A) torsional sublevel were analyzed via a standard Hamiltonian for asymmetric top molecular spectra of the type (Watson 1968)

$$H_{eff} = H_{rot} + H_{dist}^{(4)} + H_{dist}^{(6)} + H_{dist}^{(8)} + H_{dist}^{(10)} \quad , \qquad (B2.16)$$

where H_{rot} is the rigid body rotational Hamiltonian and the four other elements are centrifugal distortion terms involving angular momentum operators raised to the total exponent shown in the superscript. We have previously discussed in detail the application of this theory (Cook, De Lucia, and Helminger 1972). Utilizing the above Hamiltonian, we were able to fit our data augmented with the lower frequency transitions of Bauder (1979) to an rms deviation of 51 kHz, which is of the same magnitude as our experimental accuracy. This treatment is applicable to rotational transitions in the symmetric (A) sublevel of the ground torsional state only. An attempt to use the same approach for transitions involving the E sublevel measured by Bauder (1979) was less successful.

It was found, however, that a similar model in which the internal rotation interactions in the E sublevel are handled via a perturbation theory of the type described by Herschbach (1959) can account quite nicely for the observed spectra. Because of the large rotational energies involved for the highest J states in the present data set, it has been necessary to include terms in the perturbation expansion up to 9th order. Details of the fitting procedure may be found in Plummer (1985). We note that several of the higher-order matrix elements listed by Herschbach (1959) contain errors in their coefficients and signs. The current (7/1/85) rms error of the E sublevel fit is about 140 kHz, slightly worse than the A sublevel fit but an order of magnitude better than the rms of 1.44 MHz reported by DeMaison *et al.* (1983). The largest problems appear to be with the $\Delta J=0$ Q-branch transitions for which the internal rotation perturbations are most severe. It appears that inclusion of centrifugal distortion terms into the

Table B2.11
Rotation-Distortion and Internal Rotation Constants of $HCOOCH_3$

Constant[a]	A sublevel Value(σ)[b] (MHz)	E sublevel Value[c] (MHz)
	Rotation-Distortion Constants	
A	19985.7623(36)	19980.441
B	6914.7577(5)	6913.683
C	5304.4681(4)	5304.512
$\Delta_J \times 10^5$	617.8100(766)	599.20
$\Delta_{JK} \times 10^3$	-17.1981(118)	-23.261
$\Delta_K \times 10^3$	82.3578(237)	75.834
$\delta_J \times 10^4$	19.5022(33)	
$\delta_K \times 10^3$	7.6605(187)	
$H_J \times 10^8$	1.654(32)	
$H_{JK} \times 10^7$	17.3189(3358)	
$H_{KJ} \times 10^6$	4.8512(974)	
$H_K \times 10^6$	4.2214(767)	
$h_J \times 10^9$	8.422(141)	
$h_{JK} \times 10^6$	1.0091(107)	
$h_K \times 10^5$	1.2204(328)	
$L_{JJK} \times 10^{10}$	-1.0719(1555)	
$L_{JK} \times 10^9$	-1.4668(540)	
$l_{KJ} \times 10^9$	-1.2372(1437)	
$P_{JJK} \times 10^{15}$	-3.938(1194)	
$P_{JK} \times 10^{13}$	-4.7594(8445)	
$P_{KJ} \times 10^{12}$	2.3953(2338)	
$P_{KKJ} \times 10^{13}$	-5.200(1530)	
$p_{JJK} \times 10^{14}$	-1.221(140)	
$p_{KKJ} \times 10^{12}$	-3.7764(5929)	
	Internal Rotation Parameters	
	F = 168529.9 MHz	
	V_3 = 399.33249 cm^{-1}	
	s = 31.5715	
	ρ_a = 0.074703	

notes: a-Rotation-distortion constants from Hamiltonian described by Cook, De Lucia, and Helminger (1972), b-Number of significant figures required to reproduce spectrum, c-E sublevel analysis is preliminary, a more complete description may be found in Plummer (1985).

internal rotation Hamiltonian will reduce the residual rms to within our experimental accuracy, however (Plummer 1985). The molecular rotation, centrifugal distortion, and internal rotation constants determined from our least-squares

analysis are listed in Table B2.11.

With the molecular constants shown in Table B2.11 and their associated uncertainties, we have predicted transition frequencies and uncertainties in the predicted frequencies for ~20,000 transitions of methyl formate in its ν_t=0 A and E sublevels involving $J \lesssim 50$ in the frequency range 1-600 GHz. Not all of these transitions are of sufficient strength to be of interest astronomically, and to select a more useful subset of the total data set we have imposed an upper frequency limit of 500 GHz, an upper limit for energy excitation of 350 cm^{-1}, and an intensity criterion. Our intensity criterion for the rather crowded spectrum is to calculate "blend strengths" by multiplying the dipole strength S (Gordy and Cook 1970) for each transition by the relevant dipole moment squared (μ_a^2 or μ_b^2, see Bauder 1979), and then summing this quantity for all lines falling within 1.5 MHz of each other. A lower limit of 2.0 was imposed on the "blend strengths." In addition, weak individual lines of blends have been omitted.

Even so, some 5400 transitions of the original 20,000 remain after this selection procedure is applied. Roughly 90% of the A type transitions have predicted uncertainties of 30 kHz or less, 99% have predicted uncertainties of 100 kHz or less, and 100% have predicted uncertainties under 600 kHz. Statistical errors in the E type predicted frequencies are slightly larger, but have a similar distribution. Our predicted uncertainties have been checked by experimental measurements of selected lines and found to be accurate. The list of predicted transition frequencies is excessively long to be included in this appendix, but is available from the author upon request.

References for Appendix B

Aggarwal, R.L., Lax, B., Fetterman, H.R. Tannenwald, R.E. and Clifton, B.J. 1974, *J. Appl. Phys.* **45**, 3972.

Amano, T. 1984, *J. Mol. Spec.*, **103**, 436.

Austin, J.A., Levy, D.H., Gottlieb, C.A., and Radford, H.E. 1974, *J. Chem. Phys.*, **60**, 207.

Ball, D.J. 1972, *J. Appl. Phys.*, **43**, 3047.

Bauder, A. 1979, *J. Phys. Chem. Ref. Data*, **8**, 583.

Beaudet, R.A. and Poynter, R.L. 1978, *J. Phys. Chem. Ref. Data*, **7**, 311.

Bicanic, D.D., Zuiberg, B.F.J., and Dymanus, A. 1978, *Appl. Phys. Lett.*, **32**, 367.

Bicanic, D.D. 1983, *Infrared and Millimeter Waves, Vol. 7*, ed. J. Button (Academic: New York), 243.

Blake, G.A., Helminger, P., Herbst, E., and De Lucia, F.C. 1983, *Ap. J.(Letters)*, **264**, L69.

Blake, G.A., Sastry, K.V.L.N., and De Lucia, F.C. 1984, *J. Chem. Phys.*, **80**, 95.

Blake, G.A., Farhoomand, J., and Pickett, H.M. 1986, *J. Mol. Spec.*, in press.

Bogey, M., Demuynck, C., Denis, M., Destombes, J.L., and Lemoine, B. 1984a, *Astr. Ap.*, **137**, L15.

Bogey, M., Demuynck, C., and Destombes, J.L. 1984b, *Astr. Ap.*, **138**, L11.

Bogey, M., Demuynck, C., Denis, M, and Destombes, J.L. 1985, *Astr. Ap.*, in press.

Boland, B.J., Brown, J.M., and Carrington, A. 1977, *Mol. Phys.*, **34**, 453.

Boland, B.J., Brown, J.M., Carrington, A., and Nelson, A.C. 1978, *Proc. R. Soc. Lond. Ser. A*, **360**, 507.

Bonek, E. and Korecky, H. 1974, *Appl. Phys. Lett.*, **25**, 740.

Bowater, I.C., Brown, J.M., and Carrington, A. 1971, *J. Chem. Phys.*, **54**, 4957.

Bowater, I.C., Brown, J.M., and Carrington, A. 1972, *Proc. R. Soc. Lond. A*, **333**, 265.

Bowman, W.C. and De Lucia, F.C. 1982, *J. Chem. Phys.*, **77**, 92.

Bowman, W.C., Herbst, E., and De Lucia, F.C. 1982, *J. Chem. Phys.*, **77**, 4261.

Bowman, W.C., Plummer, G.M., Herbst, E., and De Lucia, F.C. 1983, *J. Chem. Phys.*, **79**, 2093.

Brewer, A.C. and Westhaver, J.W. 1937, *J. Appl. Phys.*, **8**, 779.

Bridges, T.J. and Van Tran Nguyen 1973, *Appl. Phys. Lett.*, **23**, 107.

Brown, J.M. and Sears, T.J. 1979, *J. Mol. Spec.*, **75**, 111.

Brown, J.M., Kerr, C.M.L., Wayne, F.D., Evenson, K.M., and Radford, H.E. 1981, *J. Mol. Spec.*, **86**, 544.

Brown, J.M. 1982, private communication.

Brown, J.M., Schubert, J.E., Evenson, K.M., and Radford, H.E. 1982, *Ap. J.*, **258**, 899.

Brown, J.M., Dumper, K.M., and Lowe, R.S. 1983, *J. Mol. Spec.*, **97**, 441.

Cerny, D., Bacis, R., Guelachvilli, and Roux, R. 1978, *J. Mol. Spec.*, **73**, 154.

Charo, A. and De Lucia, F.C. 1982, *J. Mol. Spec.*, **94**, 426.

Chen, C. 1970, *IEEE Trans. MTT* **MTT-18**, 627.

Cook, J.M., Evenson, K.M., Howard, C.J., and Curl, R.F., Jr. 1976, *J. Chem. Phys.*, **64**, 1381.

Cook, R.L., De Lucia, F.C., and Helminger, P. 1972, *J. Mol. Spec.*, **41**, 123.

Coxon, J.A. 1980, *Can. J. Phys.*, **58**, 933.

Curl, R.F. 1959, *J. Chem. Phys.*, **30**, 1529.

De Lucia, F.C., Cook, R.L., Helminger, P., and Gordy, W. 1971, *J. Chem. Phys.*, **55**, 5334.

De Lucia, F.C., Herbst, E., Plummer, G.M., and Blake, G.A. 1983, *J. Chem. Phys.*, **78**, 2312.

DeMaison, J., Boucher, D., Dubrille, A., and Van Eijck, B.P. 1983, *J. Mol. Spec.*, **102**, 260.

Dixon, T.A. and Woods, R.C. 1977, *J. Chem. Phys.*, **67**, 3956.

Dousmanis, G.C., Sanders, T.M.Jr., and Townes, C.H. 1955, *Phys. Rev.*, **100**, 1735.

Evenson, K.M. 1981, *Faraday Disc. Chem. Soc.*, **71**, 7.

Evenson, K.M., Jennings, D.A., and Peterson, F.R. 1984, *Appl. Phys. Lett.*, **44**, 576.

Evenson , K.M. 1985, private communication.

Farhoomand, J., Blake, G.A., Frerking, M.A., and Pickett, H.M. 1985a, *J. Appl. Phys.*, **57**, 1763.

Farhoomand, J., Blake, G.A., and Pickett, H.M. 1985b, *Ap. J.(Letters)*, **291**, L19.

Fetterman, H.R., Tannenwald, P.E., Clifton, B.J., Fitzgerald, W.D., and Erickson, N.R. 1978, *Appl. Phys. Lett.* **33**, 151.

Foote, F.B., Hodges, D.T., and Dyson, H.B. 1981, *Int. J. of Infra. and Milli. Waves*, **2**, 773.

Frosch, R.A. and Foley, H.M. 1952, *Phys. Rev.*, **88**, 1337.

Gordy, W. and Cook, R.L. 1970, *Microwave Molecular Spectra* (Wiley Interscience: New York).

Gudeman, C.S. and Woods, R.C. 1982, *Phys. Rev. Lett.*, **48**, 1344.

Helminger, P., Messer, J.K., and De Lucia, F.C. 1983, *Appl. Phys. Lett.*, **42**, 309.

Herschbach, D.R. 1959, *J. Chem. Phys.*, **31**, 91.

Illies, A.J., Jarrold, M.F., and Bowers, M.T. 1982, *J. Chem. Phys.*, **77**, 5847.

Illies, A.J., Jarrold, M.F., and Bowers, M.T. 1983, *J. Am. Chem. Soc.*, **105**, 2562.

Inguscio, M., Evenson, K.M., Beltran-Lopez, H., and Ley-Koo, E. 1984, *Ap. J.(Letters)*, **278**, L127.

Johansson, L.E.B., Andersson, C., Ellder, J., Friberg, P., Hjalmarson, A., Hoglund, B., Irvine, W.M., Olofsson, H., and Rydbeck, G. 1984, *Astr. Ap.*, **130**, 227.

Krautle, H., Sauter, E., and Schultz, G.V. 1977, *Infrared Physics*, **17**, 477.

Krupnov, A.F. 1979, *Modern Aspects of Microwave Spectroscopy*, edited by G.W. Chantry (Academic: New York), 217.

Leung, C.M., Herbst, E., and Huebner, W.F. 1984, *Ap. J. Suppl.*, **56**, 231.

Light, J.C. 1967, *Discuss. Faraday Soc.*, **44**, 14.

Lin, C.C. and Swalen, J.D. 1959, *Rev. Mod. Phys.*, **31**, 841.

Maniv, S., Westwood, W.D., and Scanlon, P.J. 1982, *J. Appl. Phys.*, **53**, 856.

Martin, D.H. and Pulpett, E. 1970, *Infrared Physics*, **10**, 105.

Meerts, W.L. and Dymanus, A. 1975, *Can. J. Phys.*, **53**, 2123.

Peterson, F.R., Scalabrin, A., and Evenson, K.M. 1980, *Int. J. of Infra. and Milli. Waves*, **1**, 111.

Phillips, T.G. and Huggins, P.J. 1981, *Ap. J.*, **251**, 533.

Pickett, H.M., Farhoomand, J., and Chiou, A.E. 1983, *IEEE-MTT Symposium Digest*, 106.

Plummer, G.M., Herbst, E., De Lucia, F.C., and Blake, G.A. 1984, *Ap. J. Suppl.*, **55**, 633.

Plummer, G.M. 1985, Ph.D. Thesis, Duke University.

Plummer, G.M., Herbst, E., and De Lucia, F.C. 1985, *J. Chem. Phys.*, in press.

Prasad, S.S. and Huntress, W.T., Jr. 1980, *Ap. J. Suppl.*, **43**, 1.

Raynes, W.T. 1964, *J. Chem. Phys.*, **41**, 3020.

Sauter, E. and Schultz, G.V. 1977, *IEEE Trans. MTT*, **MTT-25**, 468.

Skatrud, D.D., De Lucia, F.C., Blake, G.A., and Sastry, K.V.L.N. 1983, *J. Mol. Spec.*, **99**, 35.

Thomson, J.J. and Thomson, G.P. 1928, *Conductivity of Electricity through Gases* (Cambridge University Press).

Von Engel, A. 1955, *Ionized Gases* (Oxford University Press).

Warner, H. E., Connor, W. T., Petrmickl, R. H., and Woods, R. C. 1984, *J. Chem. Phys.*, **81**, 2514.

Watson, D.M. 1982, Ph.D. Thesis, University of California, Berkeley.

Watson, D.M., Genzel, R., Townes, C.H., and Storey, J.W.V. 1985, *Ap. J.*, **298**, in press.

Watson, J.K.G. 1968, *J. Chem. Phys.*, **48**, 4517.

Weinreb, S., Barret, A.H., Meeks, M.L., and Henry, J.C. 1963, *Nature*, **200**, 829.

Woods, R.C., Gudeman, C.S., Dickman, R.L., Goldsmith, P.F., Huguenin, G.R., Irvine, W.M., Hjalmarson, A., Nyman, L-A., and Olofsson, H. 1983, *Ap. J.*, **270**, 583.